2022

Structural and petrologic insights into the emplacement of effusive silicic lavas: Inyo Domes, California

Shelby L. Isom
West Virginia University, sli0005@mix.wvu.edu

Structural and petrologic insights into the emplacement of effusive silicic lavas: Inyo Domes, California

Shelby Lee Isom

Dissertation submitted to the
Eberly College of Arts and Sciences
at West Virginia University

in partial fulfillment of the requirements
for the degree of

Doctor of Philosophy
in
Geology

Graham D.M. Andrews, Ph.D., WVU, Chair
Jaime Toro, Ph.D., WVU
Kathleen C. Benison, Ph.D., WVU
Shikha Sharma, Ph.D., WVU
Alan G. Whittington, Ph.D., University of Texas at San Antonio

Morgantown, West Virginia
2022

Keywords: silicic lava, Inyo Volcanic Chain, Long Valley, effusive, obsidian

ABSTRACT

Structural and petrologic insights into the emplacement of effusive silicic lavas: Inyo Domes, California

Shelby Lee Isom

The Long Valley volcanic region, eastern California, USA is most famous for the caldera-forming eruption which produced the Bishop Tuff ~760,000 years ago. Over the last 3,000 years volcanism has been focused in the western margin of the region through punctuated eruptions of silicic lavas and domes. Three simultaneous effusive silicic eruptions, ~600 years ago, generated three lava domes: Obsidian Dome; Glass Creek Dome; and Deadman Dome which erupted onto vastly different topographies. These domes are exceptionally unique as they erupted variable amounts of two textural and chemical endmember lavas (crystal-rich and crystal-poor) that intimately mixed. The overarching goal of this dissertation is to investigate the magmatic genesis and emplacement styles of these young effusive silicic lava domes.

The first chapter of this dissertation investigates the petrogenesis of the three 600-year-old Inyo Domes, concluding they originated from variable mixing of several long-lived, complex, contiguous, magmatic plumbing systems. The second chapter characterizes brittle and brittle-ductile structures preserved across the upper surface of Obsidian Dome, challenging the long-standing theory that the upper surface of silicic lavas is dominated by ductile folding. The third chapter utilizes morphologies classified from analog modeling to characterize the upper surface of Obsidian Dome and Glass Creek Dome to assess the control of underlying topography and crystallinity on lava emplacement rates.

ACKNOWLEDGEMENTS

This dissertation would have not been possible without the unwavering support, understanding, and friendship of Dr. Graham Andrews. Graham trusted my scientific judgement allowing me to grow and think independently about the science that we are doing. However, he was always there with a helping hand or encouraging insight when I needed it most. The opportunity to come to West Virginia has changed my life in more ways than I can count. Thank you, Dr. Andrews.

Thank you to my family for always supporting me, even when that meant I was moving to the opposite side of the country. I love you all so much. Specifically, I must thank the most influential and inspiring women of my life. First, my sister, who paved the path as a first-generation college student, giving me the courage to follow. I've marveled at your tenacity and passion for science since we were kids, I'm so very lucky I have you to look up to. To my mother, Connie, who instilled in me fierce determination and taught me to walk through this world with empathy. Thank you so much for giving me the best parts of you. Finally, my childhood friend Beth who has always been an unwavering beacon of support and love since we were 8-years-old. You have always supported my pursuit of higher education, thank you for pushing me to start that Master's program. My life would be very different if for not that nudge you gave me to pursue my passion for science.

I am forever thankful for the WVU Geology & Geography Department. West Virginia has felt like home since the minute I arrived. I will always cherish the lifelong friends and many beers we shared at Brewpub. Specifically, to C&C, thank you for you for the love, laughs, and for always being there with an encouraging word.

Finally, thank you to my husband, Tyler, who I never thought I'd be lucky enough to find in West Virginia. You are my goofy light at the end of the tunnel. Thank you for always giving me perspective and putting a smile on my face when I was struggling. I promise we can get back to fishing, hiking, and exploring, soon. I love you.

This work is dedicated to my Grandparents, Ken and Wanda Isom. They ignited my love for the outdoors at an early age. My grandpa was always on the hunt for the perfect rock or wildflowers to bring back to my grandma at the end of each day we spent up at our family cabin in Idaho. Thank you for everything. You are dearly missed.

TABLE OF CONTENTS

INTRODUCTION

Future eruptions occurring within the Long Valley volcanic region, eastern California, USA are inevitable. The region is tectonically and volcanically active, evidenced by earthquake swarms and mass tree kills from CO_2 emissions that record movement of magma in the shallow crust (Hill, 1996). Following the large-volume, caldera-forming eruption of the Bishop Tuff (760 ka; Hildreth, 1979), the region has been dominated by small-volume (<5 km^3), effusive, silicic eruptions, the youngest of which occurring along the Inyo and Mono Volcanic Chains (Hildreth, 2004). Future eruptions will be in similar form (Magnan et al., 2018). The individual chapters of this dissertation address the overarching goal of constraining eruption dynamics of small volume silicic lavas from magma genesis to eruption and emplacement, to cooling and solidification. As detailed case studies, I use the three 0.6 ka Inyo Domes of eastern California: Obsidian Dome, Glass Creek Dome, and Deadman Dome.

Chapter 1:

The Origins and Implications of Feldspar Antecrysts in Silicic Lavas and Domes of the Inyo Chain, Long Valley Caldera, eastern California dives into the complex semi-contiguous, magma plumbing system that generated the youngest eruptions in the Long Valley volcanic region. This chapter sets the stage describing the Long Valley volcanic region and where the Inyo Volcanic Chain fits in to the regional volcanic history. The 0.6 ka Inyo Domes erupted two texturally opposing (crystal-rich and crystal-poor) lavas which are distributed variably across the upper surface of each dome. There is an increase in the proportion of crystal-rich lava erupted as you move south towards two older lavas, 41 ka Northwest dacites and 113 ka West Moat rhyolites. These older lavas are texturally similar to the crystal-rich lava of the young Inyo Domes. Past research has suggested this crystal-rich endmember found at each lava over the span of ~113 kyrs is a remobilized portion of the residual Bishop Tuff mush. This chapter utilizes quantitative whole rock, mineral, and glass data and semi-quantitative mineral data to investigate the textural and compositional similarities of these temporally separate lavas occurring along the N-S Inyo Chain. Ultimately this research works to elucidate if the crystal-rich portion of these lavas is genetically related to a residual crystal cumulate of the Bishop Tuff. This chapter is close to submission to *Geochemistry, Geophysics, Geosystems* (*G^3*), with USGS co-authors Dawn Ruth and Dawnika Blatter, and Graham Andrews.

Chapter 2:

Making Sense of Brittle Deformation in Silicic Lavas: Insights from Obsidian Dome, California is focused on the upper surface of the northern most Inyo Dome: Obsidian Dome. This chapter comprehensively documents the brittle and brittle-ductile structures and deformation across the surface of Obsidian Dome, with particular emphasis on the temporal and spatial evolution of structures. Key to this study was the creation of a digital field mapping workflow where we imaged the upper surface with a quadcopter drone generating high-resolution orthorectified images and then used those images to map the lithofacies contacts and structural measurements across the upper surface. We also highlight previously non-described explosive phenomenon at Obsidian Dome that occurred away from the active vent throughout the lava's eruption and reveal that brittle deformation and local explosivity are linked processes. This study has been resubmitted to *Geosphere* following a first set of positive reviews.

This study is an outgrowth of "The Fold Illusion" a paper published in *Earth and Planetary Science Letters* (Andrews et al., 2021) for which I am a co-author. Both studies were born through the observation that brittle and brittle-ductile deformation is preserved in small to large scale structures across the surface of silicic lavas. Whereas past research is focused on the ductile syn-emplacement dynamics of lavas suggesting their upper surfaces are folds. This fold theory (Fink, 1980) is utilized in many works to hypothesize viscosity and composition of terrestrial lavas. The Fold Illusion challenges the long standing "fold theory" by reinterpreting structures and modeling the timescale of cooling and the inevitable tensile fracturing of the upper surface. It concluded that the upper surface of silicic lavas transition from ductile to brittle deformation in less than 10 hours.

Chapter 3:

Characterization and Comparison of Emplacement Processes: Glass Creek Dome and Obsidian Dome, California, USA, utilizes the same field techniques in Chapter 2 and compositional data collected in Chapter 1 to compare the surface morphology, flow front structures, and calculated flow rates between Obsidian Dome and Glass Creek Dome. Each dome was emplaced on different topography and are comprised of two compositionally and texturally distinct lavas. They are perfect case studies to investigate the control of composition (crystal-rich versus crystal-poor) and underlying topography on the emplacement styles of silicic lavas. Using

orthorectified images, field data, and Google Earth we classified the upper surface of Obsidian Dome and Glass Creek Dome according to the morphological domains of Fink and Griffiths (1998). We document flow front structures and measure flow front thicknesses to estimate yield strengths, which we compare to the yield strengths derived from analog models. This study combines field observations and quantitative geochemical data and compares it with observations at active silicic lavas and morphologies derived through modeling. We find that flow front structures and upper surface morphologies correlate across both domes. Furthermore, we note the thicker regions of the domes record the fastest emplacement timescales and these regions are classified as lobate morphologies with flow front structures often containing banded obsidian and microcrystalline rhyolite.

The culmination of these individual chapters works to illuminate the entire history of three young silicic lavas from magma genesis to eruption and emplacement.

CHAPTER 1: THE ORIGINS AND IMPLICATIONS OF FELDSPAR ANTECRYSTS IN SILICIC LAVAS AND DOMES OF THE INYO CHAIN, LONG VALLEY CALDERA, EASTERN CALIFORNIA

Authors: Shelby L. Isom, Dawn Ruth, Dawnika Blatter, Graham D.M. Andrews, and Holly D. Pettus.

Corresponding author: Shelby L. Isom

Projected journal: Geochemistry, Geophysics, Geosystems

Keywords: Long Valley caldera, Bishop Tuff, mush, Inyo Domes

Abstract

The chemical evolution of intracontinental, crustal magma bodies that produce large volume (>300 km^3) silicic eruptions is exhaustively researched. However, intracontinental small volume (<1 km^3) silicic lava eruptions are uncommon and research into their plumbing systems is scarce. The Long Valley caldera is known for its cataclysmic, large-volume (~600 km^3) caldera-forming eruption which produced the Bishop Tuff ~760 ka. Since then, protracted Long Valley silicic magmatism has been attributed to a residual crystal mush from the Bishop Tuff eruption. This study examines the similarities and differences between the crystal cargoes of Middle and Late Pleistocene lavas (0.6 ka, 41 ka, and 113 ka) along the N-S trending Inyo Chain on the northwestern margin of the Long Valley caldera, and their relationship with the Bishop Tuff magmatic system. In doing so we attempt to elucidate the spatial and temporal continuity of small volume silicic magma plumbing systems. We attribute the crystal-rich lavas of this study to a crystal cumulate unrelated to the Bishop Tuff magma chamber, whereas the crystal-poor lavas originated from a separate source possibly related to the adjacent Mono Volcanic Chain. We envisage the shallow (~12 km depth) crust beneath the northwestern moat of the Long Valley caldera to be comprised of several semi-contiguous reservoirs, which are reenergized through time by thermal recharge. We speculate that the emplacement of the Inyo dike promoted magma-mixing and piecemeal eruptions of the compositionally and texturally contrasting Inyo lavas.

1.0 INTRODUCTION

The Long Valley volcanic region is tectonically and volcanically active, containing some of the youngest and most active volcanoes in California, and monitoring by the USGS California Volcano Observatory is ongoing through the region (Mangan et al., 2018). The volcanic region includes the voluminous Bishop Tuff that erupted from the Long Valley caldera ~760,000 years ago, the Mammoth Mountain complex, the Mono Volcanic Chain, and the Inyo Volcanic Chain (Bailey, 1989, 1976; Hildreth, 1981). The most recent eruptions in Long Valley occurred along the Inyo Chain ~600 years ago when three silicic lava domes erupted simultaneously (Wood, 1983; Miller, 1985). According to the USGS California's Exposure to Volcanic Hazards Scientific Investigation Report, three to five million people yearly travel through the volcanic region, skiing the flanks of Mammoth Mountain or traveling to the Yosemite Valley, ~13,000 flights pass over the region daily, and ~63,000 people live close to these domes in the surrounding towns (e.g., Mammoth Lakes; Fig. 1A; Mangan et al., 2018).

Understanding and quantifying the petrogenesis of the youngest eruptions in the region is paramount as the next potential volcanic threat within the Long Valley volcanic region is projected to be along the extensional N-S lineament of the Mono-Inyo Chain. Past researchers have considered the magmatic system that could have contributed to the 0.6 ka Inyo Chain eruptions, suggesting residual Bishop Tuff crystal mush is responsible for its crystal-rich component (Sampson & Cameron, 1987; Vogel et al., 1989; Varga et al., 1990; Reid et al., 1997; Hildreth, 2004).

The overarching goal of this study is to elucidate the spatial and temporal continuity of small volume silicic magma plumbing systems near the Inyo Chain. Specifically, this work investigates the textural and compositional similarities and the spatial and temporal relationships between the youngest Inyo Domes rhyolites (~0.6 ka), the Northwest dacites (~41-26 ka), and the West Moat rhyolites (~160-113 ka) and their possible genetic relationship to an unerupted residual crystal cumulate of the Bishop Tuff (Mahood et al., 2010; Miller, 1985; Wood, 1983).

2.0 GEOLOGIC BACKGROUND

The Long Valley volcanic region is defined by temporal, spatial, and compositional shifts in volcanism from its inception (~4.4 Ma) through the most recent eruptions (Hildreth, 2004). The region sits in the transtensional basin between the Sierra Nevada Mountains and the Basin and Range province promoting decompression melting in the underlying mantle in response to the thinning crust (Hildreth, 2004; Riley et al., 2012).

Beginning ~4.4 Ma, basaltic magmatism dominated eastern central California with dacitic volcanism focused in the Long Valley volcanic region from ~3.5-2.5 Ma (Bailey, 2004). At ~2.2 Ma the mafic magmatism ceased, and volcanism shifted to the northeastern edge of LONG VALLEY with the production of the high-silica, crystal-poor rhyolites of Glass Mountain (Fig. 1A), which continued until ~0.79 Ma (Hildreth, 2004). The caldera forming eruption, which produced the Bishop Tuff, initiated ~760 Ka resulting in the collapse and creation of the Long Valley caldera. The Long Valley caldera lies at the center of the Long Valley volcanic region (Fig. 1A). The Bishop Tuff plinian eruption evacuated ~600 km^3 of rhyolitic ash-flows and ash fallout. The Bishop Tuff pumice is compositionally and texturally zoned from 1-25% phenocrysts over a silica range of 73-78 wt.% and 2-600 ppm Ba (Hildreth, 1979). Hildreth (2004) notes the absence of mafic magmatism and enclaves suggesting the large silicic system of the Bishop Tuff prevented any mafic to intermediate magma from reaching the surface.

Following the eruption of the Bishop Tuff, from ~750 ka to ~250 ka, the Long Valley volcanic region experienced interspersed periods of rhyolitic volcanism, likely responding to mafic underplating, producing lavas and domes all with elevated Ba concentrations (>500 ppm and up to 1550 ppm) erupting in the center of the Long Valley caldera (Hildreth, 2004). The Early Rhyolites (~750-650 ka) consist of several lavas and tuffs that erupted onto the western floor of the Long Valley caldera from 13 vents (Hildreth, 2004). Magmatism shifted to the western margin of the Long Valley caldera from ~230 to 8 ka with the simultaneous eruptions of the Mammoth Mountain dome complex and its mafic periphery (~230 to 8 ka), the West Moat rhyolites (~160 to 97 ka), and the Northwest wall trachydacite chain or “Northwest dacites” (~41 to 26 ka; Hildreth, 2004; Mahood et al., 2010). The Mammoth Mountain dome complex is made up of 37 basalt, trachyandesite, and trachydacite lavas and 25 alkalic rhyodacite eruptive units defined by Hildreth et al (2014) and Hildreth & Fierstein (2016). During the early 1980s and mid-1990s seismic

swarms occurred and carbon dioxide was emitted from the flanks of Mammoth Mountain. This activity was attributed to the intrusion of a small (<0.01 km^3) magma body into the shallow crust (Hill, 1996). Interestingly, seismic reflection surveys of the area identify a low-velocity zone at ~4.5 km depth, which possibly extends to ~10 km depth shallowly dipping to the northeast in the western moat of the Long Valley caldera (Hill et al., 1985). This low-velocity zone potentially represents a magma reservoir at depth.

The West Moat rhyolites are defined by three crystal-rich rhyolitic lava domes (~1 km^3) and a crystal-rich rhyolitic coulee (~4 km^3; Hildreth et al., 2004). The West Moat Coulee erupted ~161 ka adjacent to the Mammoth Mountain complex and just to the north of the town of Mammoth Lakes (Fig. 1A). The Mammoth Knolls Dome and Dry Creek Dome are crystal-rich high-silica rhyolitic domes which erupted at the edge of the Mammoth Mountain periphery, on top of the West Moat Coulee ~113 ka. The fourth West Moat rhyolite dome, Deer Mountain, erupted ~113 ka, slightly west and north of the Mammoth Knolls and Dry Creek domes. The simultaneously erupted Mammoth Mountain suite is alkaline distinguishing it from the West Moat rhyolites which are subalkaline, much like the early rhyolites within the Long Valley caldera (Hildreth, 2004). Additionally, the Mammoth Knolls and Dry Creek domes have higher silica contents but are depleted in barium whereas Deer Mountain and the West Moat Coulee are enriched in barium with lower silica contents (Hildreth, 2004).

The Northwest wall trachydacite chain (Northwest dacites) erupted concurrently from four WNW-aligned vents, crosscutting the northwestern edge of the Long Valley caldera producing crystal-rich trachydacite from ~41 to 26 ka (Mahood et al., 2010). The Northwest wall trachydacite chain includes several crystal-rich trachydacitic lavas which decrease in silica content and young towards the caldera (Fig. 1A).

During the initial eruptions of the Northwest dacites magmatism was also focused in the north with the eruptions of the N-S aphyric rhyolitic Mono Chain (Kelleher & Cameron, 1990; Marcaida et al., 2019). Located near and around Mono Lake, the Mono Domes are made up of 28 silicic domes and coulees with the youngest eruption, Negit Island, occurring within the center of Mono Lake ~ 350 years ago creating an island of lavas topped by a cinder cone (Stine, 1987; Marcaida et al., 2019). All Mono Domes and coulees are barium depleted, aphyric, high-silica

rhyolites apart from the ~40 ka "Dome 12" which is the only dacitic dome in the Mono Chain (Kelleher & Cameron, 1990).

Erupting to the south along the same N-S lineament of the Mono Chain is the Inyo Volcanic Chain. Seven silicic lava domes and several phreatic explosion craters define the Inyo Volcanic Chain (Fig. 1B). From north to south the five large domes and two smaller domes are Wilson Butte, Obsidian Dome, Cratered Dome, Glass Creek Dome, Caldera Wall Dome, North Deadman Dome, and Deadman Dome (Wood, 1983; Miller, 1985). North Deadman Dome is the oldest lava amongst the Inyo Volcanic Chain with a hypothesized age of ~4 ka (Miller, 1985). The northern most dome of the Inyo Volcanic Chain is the aphyric Wilson Butte which erupted ~1.3 ka and has been hypothesized to originate from the same magma system as the Mono Domes (Vogel et al., 1989). Two small domes, <0.001 km^3, Cratered Dome and Caldera Wall Dome, have not been dated but are covered with tephra from the youngest Inyo Volcanic Chain eruptions suggesting they are at least older than ~0.6 ka (Hildreth, 2004).

The rupturing of the Hartley Springs fault is suggested to have initiated the emplacement of a magmatic dike ~0.6 ka producing the youngest three silicic lava domes, Obsidian Dome, Glass Creek Dome, and Deadman Dome (Fig. 1B; Bursik & Sieh, 1989). Glass Creek Dome erupted upon a glacial moraine and flowed over it and down to the south abutting against the oldest (~41 ka) Northwest dacite lava. Additionally, explosive cratering occurred between Obsidian Dome and Glass Creek Dome and at the southern extent of the Inyo Volcanic Chain resulting in three large craters, North Crater, South Crater, and Deer Mountain Crater (Bailey, 1976; Fink, 1985; Fink & Pollard, 1983). The Deer Mountain crater intruded through fragmenting and cratering the top of the ~113 ka Deer Mountain dome.

The lavas investigated in this study have been associated with temporally separate phases of volcanism that occurred in the western area of the Long Valley volcanic region, however they all lie in the same N-S lineament, share similar modal mineralogy, textural characteristics, and chemical compositions (FIG 2; Bailey, 2004; Hildreth, 2004).

2.1 Deposit Morphology

Four lithofacies defined by their proportion and size of vesicles (fine vesicular pumice, coarse vesicular pumice, obsidian, and dense microcrystalline rhyolite) were characterized by Manley & Fink, 1987 and are observed at each Inyo Dome in variable volumetric proportions

(Sampson, 1987). The brecciated fringes of the youngest Inyo Domes are dominated by fractured blocks (<5 m) of fine vesicular pumice and obsidian is generally confined to the flow fronts. The microcrystalline rhyolite is observed over the center of the domes appearing as larger (>10 m), more coherent blocks (Fig. 1B).

Within the lithofacies two distinct textures are identified, often intimately mixed, across the youngest Inyo Domes (Obsidian Dome: OBD; Glass Creek Dome: GCD; and Deadman Dome: DMD) albeit in different proportions (Fig. 2B; Sampson, 1987). These two distinct textures were named "coarsely porphyritic rhyolite" denoting the lava with a crystallinity of 25 to 40% and "finely porphyritic rhyolite" is the lava with a crystallinity of <23% crystals (Bailey et al., 1976; Sampson, 1987; Sampson & Cameron, 1987). However, in this study we distinguish the rhyolites based solely on crystallinity forgoing the textural term "porphyritic" as the lavas containing <5% crystals do not contain two crystal size populations. Thus, we have expanded and simplified the original endmember unit names into crystal-rich (x-r) with >12% crystals, crystal-medium (x-m) with 6 to 12% crystals, and crystal-poor (x-p) with 0.5 to 6% crystals (Fig. 2). Large alkali feldspar and plagioclase megacrysts (≥5mm) are indicative of the x-r and x-m lavas and are absent from the x-p lavas. These new crystallinity categories for the different Inyo Domes units follow the same textural classification as Hildreth & Wilson, 2007 for the Bishop Tuff.

The x-p lava dominates the fringes of the domes with mixing of both endmembers concentrated between the two distinct zones resulting in the x-m lava (Fig. 2). The x-p lava constitutes ~99% of the lava at Obsidian Dome and forms a strongly creased and brecciated fringe at the distal margins of the other domes (~40% of GCD, ~20% of DMD), and the tephra from all of domes (Sampson, 1987). Furthermore, all the older domes: Wilson Butte (WB), Cratered Dome (CD), Caldera Wall Dome (CWD), and North Deadman Dome (NDMD) are crystal-poor and do not contain a crystal-rich textural member (Fig. 2).

Two older crystal-rich lavas, Deer Mountain (DM) and the Northwest dacites (NWD), are not considered part of the Inyo Volcanic Chain but fall within the N-S lineament (Fig. 2A). The DM lava at the southern terminus of Inyo Volcanic Chain is crystal-rich and contains feldspar megacrysts, first noted by Sampson & Cameron, 1987. The Northwest dacites are also crystal-rich and contain feldspar megacrysts (Bailey, 1989).

3.0 METHODS

3.1 Sample Collection and Preparation

We collected samples from the Inyo Volcanic Chain during two field work campaigns in 2018 and 2019 (Fig. 2A). We focused on sampling rocks of the variable crystallinities (x-p, x-m, x-r), at the three youngest Inyo Domes (OBD, GCD, DMD). We collected samples from Deer Mountain (DM) and the Northwest dacites (NWD) to compare textural and compositional similarity with the Inyo Domes. We collected a sample from the oldest unit within the Northwest dacites, which has the highest silica concentration (Mahood et al., 2010). Furthermore, we collected samples from the two smallest Inyo Domes that sit directly north, (Cratered Dome, CD) and south (Caldera Wall Dome, CWD) of GCD (Fig. 2A).

Of the collected samples, 28 thin sections were made of the texturally different lavas at OBD, GCD, and DMD. One thin section was made for DM, NWD, CD, CWD for comparative petrography. We completed the initial petrographic analysis at West Virginia University in the Volcano and Petrology lab using the petrographic microscope with attached digital camera.

3.2 Analytical Methods

Based on petrographic analysis, we sent thirteen rock samples to the Peter Hooper GeoAnalytical Lab at Washington State University for XRF and ICP-MS bulk geochemical analysis of major and trace elements. Analytical precision for rare earth elements is typically better than 5% (relative standard deviation) and ~10% for the rest of the trace elements. All analyses are compared with USGS and international rock standards and the results were deemed to be within the standards. Analyzed samples include the lavas of various crystallinities from OBD, GCD, and DMD and one sample each from the DM, CD, CWD, and NWD (Appendix 1: Table 1).

Major element chemistry and high-resolution (256 pixels) Back-scattered Electron (BSE) images and Energy Dispersive X-Ray Spectroscopy (EDS) maps were collected on a Tescan Vega3 Tungsten Filament Scanning Electron Microscope (SEM) with two Oxford X-MaxN 150 mm^3 energy dispersive spectrometers at the U.S. Geological Survey, Menlo Park, CA. An accelerating voltage of 15 kV with a 420 nm spot size and working distance of 15 mm were used to collect BSE images and EDS maps for identification of variable crystal populations, textures, and zoning and to identify areas of interest to collect semi-quantitative compositional data (Fig. 3).

The JEOL JXA 8530 F+ Electron Probe Microanalyzer (EPMA) at the U.S. Geological Survey, Menlo Park was used for quantitative mineral and glass chemistry. An accelerating voltage of 15 kV was used for all phases and the beam current and beam diameter were varied depending on the phase: for amphibole we used a beam current of 15 nA and a focused beam, for oxides a 20nA beam current and a focused beam, for feldspars a 10 nA beam current and a 5 μm diameter beam, and for glass a 3nA beam current and a 5 μm diameter beam. Peak counting times for major elements ranged from 10 to 20 seconds and from 20 to 60 seconds for trace elements. For feldspar and glass analyses a first pass peak count time of 10 seconds was used to mitigate migration of Na and K. All analytical conditions and quantitative compositional data can be found in Appendix 1: Table 2 through 7.

3.3 Geothermobarometry

We calculated temperatures for all textual units of the 0.6 ka Inyo Domes, the Northwest dacites, and the West Moat rhyolite, DM, using two geothermometers (Table 1). We used the plagioclase – alkali feldspar-liquid thermobarometer of Putirka, 2008 for both size populations of the plagioclase and alkali feldspar minerals. We utilized the K_D value of 0.1 ± 0.05 as a check for equilibrium; all K_D's that fell out of this range are not considered. EPMA derived glass compositions were used as the liquid composition in the thermometry and barometry. Standard inherent error of each thermobarometer, amphibole-liquid and albite-liquid are ± 30 °C and ± 23 °C, respectively.

Amphibole compositions and whole rock and glass analyses were used to calculate pressure using amphibole-liquid geobarometer (Putirka, 2016). We used the K_D value of 0.28 ± 0.11 as a check for equilibrium and all values that fell out of this range are not considered. Standard error for pressure estimates is large, ± 400 MPa for amphibole-liquid and albite-liquid ± 300 MPa. The large standard error for pressure estimates is noted and considered in subsequent interpretations.

4.0 RESULTS

4.1 Petrography & Mineralogy

4.1.1 0.6 ka Inyo Domes

The minerals found within all texture groups of the youngest Inyo Domes lavas (listed by modal abundance) are plagioclase, sanidine, biotite, oxides, orthopyroxene, ± amphibole, zircon, apatite, ± quartz, ± clinopyroxene, ± allanite (Table 2; Sampson & Cameron, 1987).

There are two feldspar (plagioclase and sanidine) size populations (≥5 mm and ≤2.5 mm) in the x-r and x-m lavas.

The ≥5 mm plagioclase and sanidine feldspar megacrysts are anhedral to subhedral. Under cross polarized light (XPL) the plagioclase megacrysts display albite and tartan twinning and the sanidine megacrysts display Carlsbad twinning. EDS x-ray maps show normal zonation, Na-rich rims, of the ≥5 mm plagioclase (Fig. 3A). The ≥5 mm sanidine is less abundant and often observed mantling resorbed plagioclase cores (Fig. 3C). Poikilitic sanidine megacrysts display sieve textures, resorption, and dissolution features with inclusions of amphibole, biotite, oxides, and pyroxene (Fig. 4B & 4C).

Overall, the ≥5 mm plagioclase and sanidine are heavily fractured (Fig. 4D). The ≤2.5 mm feldspars in all textural units (x-p, x-m, x-r) are anhedral to subhedral. Resorbed-looking rounded plagioclase cores are observed mantled by sanidine rims (Fig. 5E). Most ≤2.5 mm plagioclase within the x-r and x-m lavas are normally zoned (Fig. 5B & 5G). Mafic phases (i.e., pyroxene or biotite) and oxides are observed nucleating on the ≤2.5 mm plagioclase and sanidine (Fig. 5J).

Quartz phenocrysts are identified in only the x-r GCD and DMD lavas. Quartz occurs between 1 to 4 mm in size, is anhedral and heavily fractured (Fig. 6B). In plane polarized light (PPL) the eutaxitic groundmass, microlites, and vesicle flow bands mantle the rounded quartz phenocrysts.

Biotite are ~100 μm to 1 mm subhedral to anhedral crystals in all textural units and is commonly heavily fractured (Fig. 6A&D). Resorption features in the larger (~1 mm) crystals are observed along with mineral inclusions of apatite and hematite. Melt inclusions are present but are commonly crystallized (Fig. 6E).

Amphibole occurs as ~500 μm to ~2 mm crystals only in the x-m and x-r lavas. It is generally euhedral to subhedral with resorption and embayment common (Fig. 6C). Occasionally melt inclusions are observed, but do not occur as frequently as in biotite. Mineral overgrowths and inclusions of apatite and oxides is observed. Clinopyroxene phenocrysts (~150 μm to 500 μm) are generally found in the x-p lavas. They are euhedral but fractured and commonly have oxide inclusions (Fig. 6F).

Ilmenite and magnetite oxides litter the groundmass of all textural units. They are generally subhedral to anhedral and occur as inclusions within plagioclase, sanidine, and the mafic minerals (Fig. 6D). Minor amounts of zircon (in all textural units) and allanite (only in x-m and x-r) are found as inclusions in phenocrysts and in the groundmass, and usually range in size between ~250 μm and ~500 μm.

Crystal clots of normally zoned plagioclase (dominant phase) with variable amounts and sizes of biotite, oxides, and ± amphibole range in sizes from 2.5 mm to ~10 mm and are identified in the x-m and x-r lavas. (Figs. 3A-C).

The groundmass for all textural units is defined as eutaxitic with vesicles of variable size and shape depending upon the lithofacies in which the crystals are hosted. Stretched to flattened cigar-shaped vesicles of variable sizes are observed.

4.1.2 Small Inyo Domes

The small domes (>0.65 ka), Cratered Dome and Caldera Wall Dome are x-p. CD and CWD share similar major mineral phases, by order of abundance they are plagioclase and sanidine feldspars (≤2.5 mm), clinopyroxene, biotite and oxides with minor apatite and ± zircon (Table 2). Plagioclase and sanidine are subhedral to anhedral and fractured and complex plagioclase to sanidine sector zoning is observed (Fig. 5I). Additionally, like the ≤2.5 mm 0.6 ka Inyo feldspars, plagioclase resorbed cores are mantled by sanidine rims (Fig. 5C). Biotite is scarce and when observed it is embayed. Oxides are subhedral and commonly observed as inclusions in feldspars. Apatite microlites are observed in the groundmass of both CD and CWD. CD's groundmass is dense, with few vesicles and when observed they are rounded and sometimes interconnected, but not stretched of flattened. The groundmass of CWD is vesiculated with large, stretched, and flattened vesicles.

4.1.3 Northwest dacites

The textural and mineral data collected for NWD in this study is from the northern most lava nearest to GCD (Fig. 2A). The x-r NWD contains, by order of abundance, plagioclase, biotite, oxides, clinopyroxene, orthopyroxene, and sanidine and minor amounts of zircon and apatite (Table 2).

The sanidine and plagioclase feldspars occur in two size populations (≥5 mm and ≤2.5 mm) with both appearing anhedral and heavily fractured (Fig. 7C). Under XPL plagioclase displays albite twinning and is often normally zoned (Fig. 7B). Poikilitic plagioclase megacrysts display sieve textures (e.g., Fig. 7E), resorption, and dissolution features with inclusions of clinopyroxene (Fig. 7D). Biotite phenocrysts range from ~250 μm to 1 mm and are often observed embayed, anhedral, and commonly replaced by oxides and apatite. Clinopyroxene (~250 μm) is more abundant than orthopyroxene (~1 mm), but both are subhedral, fractured and commonly embayed. Ilmenite and magnetite oxides are subhedral and generally occur as phenocrysts and as overgrowths or inclusions in plagioclase feldspars and biotite. Crystal clots of normally zoned plagioclase, pyroxene, biotite, and oxides are observed (Fig. 7A). The groundmass is glassy and dominated by plagioclase microlites (Fig. 7B).

4.1.4 West Moat rhyolites

The textural and mineral data for the West Moat rhyolites is from a sample collected from the northern most West Moat rhyolite, Deer Mountain (Fig. 2A). The mineral phases observed, by order of abundance, are plagioclase, sanidine, amphibole, biotite, oxides, quartz with minor amounts of apatite and zircon (Table 2).

The x-r DM lava contains two size populations of both the plagioclase and sanidine feldspars (≥5 mm and ≤2.5 mm). The ≥5 mm plagioclase and sanidine are sieve textured, anhedral, and fractured (Fig. 7F). The ≥5 mm sanidine is observed being mantled by plagioclase (Fig. 7I). The ≤2.5 mm anhedral plagioclase exhibit normal zoning and albite twinning under XPL. The ≤2.5 mm sanidine is anhedral and can exhibit Carlsbad twinning.

The biotite phenocrysts (~250 μm to 1 mm) are anhedral, fractured, and commonly host melt inclusions (Fig. 7G). Biotite also appears embayed with inclusions of apatite and oxides. Amphibole (~1 mm in length) is subhedral with sparse embayments and appears to be replaced by biotite in several crystals. Magnetite and ilmenite oxides occur in the groundmass and as inclusions

in all the major mineral phases. Ilmenite phenocrysts (~100 μm) often display exsolution lamellae. Crystal clots (~2 mm) of plagioclase, biotite, oxides, and pyroxene are observed (Fig. 7J). Considering all the samples in the study, the megacrysts within the DM x-r lava are the most fractured and inconsistently zoned displaying normal, reverse, and complex zonations (e.g., Fig. 7F).

4.2 Whole Rock

Whole rock data collected from this study is compiled with data from Bailey, 2004; Hildreth et al., 2014; Sampson & Cameron, 1987; Varga et al., 1990; Vogel et al., 1989 to illustrate the similarities and differences between the (4 ka to 0.6 ka) Inyo Domes, the (41-26 ka) Northwest dacites, the (160-113 ka) West Moat rhyolites, and the (760 ka) Bishop Tuff.

4.2.1 Major & Minor Element Compositions

There is a distinct compositional variation between the texturally contrasting x-r and x-p lavas of the youngest Inyo Domes, consistent with the observations of Sampson & Cameron (1987) and Vogel et al. (1989). Silica concentration increases with age when comparing the x-p and x-r lavas with the x-p lavas having higher total alkali versus silica concentration totals than the x-r lavas (Fig. 8). Comparatively, the x-p and x-r Bishop Tuff whole rock data clusters at lower total alkali versus silica concentration totals slightly overlapping the x-r West Moat rhyolites (Fig. 8). Major element variation diagrams show the x-r and x-p rhyolites can occur on separate but parallel continuous trends, with the x-p rhyolite having a larger range in silica content (~69.4 - 74 wt.%) than the x-r rhyolite (~71.5 wt.%) (Fig. 9A). The x-p continuous trend appears to have an upper and lower limit with the x-m lava from Obsidian Dome straddling each endmember (Fig. 9C). Overall, the rhyolites generally fall together in a continuous trend with both the Inyo domes and West Moat rhyolites having low- and high-silica endmembers (Fig. 9D). The dacites (NWD) erupted over about fourteen thousand years with the youngest eruptions having the lowest SiO_2 contents (Mahood et al., 2010). Furthermore, record a progressive decrease in SiO_2 and increase in FeO, CaO, and TiO_2 with age (Fig. 9B). An observable liquid line of descent is noted from x-r dacites to x-p and x-r the rhyolites (Fig. 9E).

4.2.2 Trace Elements

Trace element variation diagrams display the same independent x-r and x-p parallel trends (Fig. 10C). Observed barium concentrations within all textural members (x-p, x-m, x-r) lie along

the same trend clustering together in high- and low-barium groups agreeing with the observation of Vogel et al., 1989 (Fig. 10A). The low-barium (<400 ppm) group consists of a x-p sample from Obsidian Dome and one of the small domes whereas the x-p older Inyo Domes and x-r younger West Moat rhyolites are even more depleted in barium (<300 ppm) (Fig. 10A). The high-barium group includes the dacites, x-p and x-r 0.6 ka Inyo rhyolites, and the older West Moat rhyolites. The x-p 0.6 Inyo lavas and the Northwest dacites are enriched in zirconium plotting away from a clustering of the x-r rhyolites and the older Inyo Domes (Fig. 10B). Consistently, the older Inyo Dome (Wilson Butte) and youngest West Moat rhyolite are the most depleted in barium and zirconium. When comparing barium concentration with weight % K_2O a trend emerges with increasing barium from the older Inyo Domes to the oldest Northwest dacites at a consistent weight % K_2O value (~5.2 wt.%) (Fig. 10C). Whereas the x-r rhyolites cluster at lower weight % K_2O with the youngest and most silica rich Northwest dacites having the lowest weight % K_2O (Fig. 10C).

4.3 Glass Chemistry

Quantitative groundmass glass chemistry illustrates the compositional similarities between the (~4 ka to 0.6 ka) Inyo Domes, the (~41-26 ka) Northwest dacites, the (~160-113 ka) West Moat rhyolites (Fig. 9B).

The glass from every textural unit of the 0.6 ka Inyo lavas overlaps the older Inyo and younger West Moat rhyolite whole rock data, with the x-r glass having the highest silica concentrations of all lavas investigated (Fig. 9E). Much like the whole rock data the x-p 0.6 ka Inyo glass ranges in silica content from 70.5 to 76 wt.% with the lower silica concentration overlapping the glass of the NWD (dacite) (e.g., Fig. 6D). The dacite glasses clusters at two silica concentrations, ~63 wt.% and ~71.5 wt.% with the higher SiO_2 overlapping the 0.6 ka Inyo rhyolites (Fig. 9B). Consistently, several glass analyses from the 41 ka NWD and the x-p 0.6 ka OBD have overlapping oxide concentrations (Fig. 9).

Generally, all lavas investigated fall along the same liquid line of decent when comparing CaO concentrations with the x-r glass of NWD being the least evolved and the x-r glass of GCD and OBD being the most evolved (Fig. 9E). There are overall compositional similarities between all the Inyo Domes, the Northwest wall dacites, and the West Moat rhyolites.

4.4 Mineral Chemistry

Quantitative mineral chemistry was determined for both size populations of feldspars, oxides, amphibole, and pyroxene. SEM EDS-derived semi-quantitative chemical compositions were used for biotite, amphibole, and pyroxene. The various textural units of the (~4 ka to 0.6 ka) Inyo Domes, the Northwest dacites (~41 to 26 ka), and the West Moat rhyolites (~113 ka) all share similar mineral compositions.

4.4.1 Feldspar

Plagioclase feldspars (≤2.5 mm) in all 0.6 ka Inyo units (x-p, x-m, x-r) are commonly mantled by Ba-rich sanidine (Fig. 5A). Furthermore, sanidine (≤2.5 mm) from the x-p 0.6 ka Inyo and small Inyo lavas are zoned in barium with Ba-rich rims (Fig. 5C). The sanidine (≥ 5mm) display more complex zoning and do not have straightforward Ba-enriched rims like that of the small sanidine.

The orthoclase component of both size populations reveals two general groups (Fig. 11B). The first, Or_{63-70}, includes the ≤2.5 mm population and is found at OBD, GCD, DMD, and the two x-p small domes (CD and CWD). The second sanidine group, Or_{76}, includes both size populations and occurs within all rhyolitic lavas except for the x-p small domes. The dacite falls between both groups having Or_{71-74}.

A greater compositional range in plagioclase is observed among all lavas investigated but appears to have two clusters between An_{20-30} and An_{50-70} with some intermediate compositions bridging the gap (Fig. 11C).

The first group, An_{22}, includes both size populations with the megacrysts from rhyolites DM, OBD, DMD, and dacite NWD and the smaller phenocrysts from GCD, OBD, DMD, DM and NWD. The second group, An_{26-33}, includes only the ≤2.5 mm plagioclase and is found at OBD, GCD, DMD, and the two x-p small domes (CD and CWD). Both size populations display variable concentrations An_{35-50} including all lavas except DM and the small domes. The last plagioclase group at An_{56-63} contains phenocrysts from all rhyolites and dacite lavas investigated in this study (Fig. 11C).

4.4.2 Pyroxene

Pyroxene semi-quantitative analysis reveal two clinopyroxene (cpx) and two orthopyroxene (opx) clusters among the data (Fig. 10A). The dacites, West Moat rhyolites, and

0.6 ka Inyo rhyolites contain both cpx and opx of relatively similar compositions. Generally, pyroxene is scarce in the x-r Inyo lavas. The 0.6 ka Inyo Domes have two opx groups, one which clusters with the small Inyo Domes and the other which overlaps the dacites and West Moat rhyolites (Fig. 11A).

4.4.3 Biotite

Semi-quantitative compositional biotite data show a gradient in ferrous iron concentration from the x-p to the x-m and x-r 0.6 ka Inyo lavas with the x-p lavas containing higher ferrous iron concentrations. Biotites within the West Moat rhyolites have similar compositions to the dacites and the x-r and x-m 0.6 ka Inyo lavas (Fig. 12B). Biotite was not analyzed in the NWD.

4.4.4 Amphibole

Amphibole is a major phase in the x-r lavas of the 0.6 ka Inyo lavas and the West Moat rhyolites. Both x-r lavas have amphiboles which plot in the actinolite field with amphibole compositions which cluster together (Fig. 12C). This study could not observe amphibole within the x-p Inyo lavas nor within the NWD.

4.4.5 Oxides

Oxide quantitative data confirm the presence of both ilmenite and magnetite within the 0.6 ka Inyo lavas, which agrees with previous work of Vogel et al. (1989). Overlapping ilmenite compositions occur within the x-r Inyo lavas, the Northwest dacites, and the West Moat rhyolites (Fig. 12D). Analytical time constraints leading to lack of data explains the absence of magnetite in the West Moat rhyolites and Northwest dacites in this study.

4.5 Geothermobarometry

Using the alkali feldspar-liquid geothermobarometer it was not possible to produce K_D values within the acceptable range for the sanidines of either size population (Putirka, 2008). However, it was possible to calculate temperature estimates for the plagioclase feldspars and their corresponding groundmass glasses for the 0.6 ka Inyo lavas, NWD, and DM. The plagioclase-liquid temperatures calculated in this study agree within uncertainty with oxide pair temperature calculations of Vogel et al. (1989) (Fig. 13A). The estimated temperatures of the x-p Inyo lavas and the x-r NWD lie between 900-925 ± 23 °C (Fig. 13A). Only one albite-liquid temperature for NWD dacite was in equilibrium giving the calculated temperature of ~910 ± 23 °C. Pressure estimates based on the feldspar-liquid geothermobarometer should be considered with caution

(Putirka, 2008) as variable pressure estimates were calculated for the x-p Inyo lavas, and the x-r DM lava. The variability of the barometer is highlighted by the vastly different pressure estimate for the same x-r DM sample, ~350 MPa using amphibole-liquid and ~800 MPa using plagioclase-liquid (Fig. 13A).

The amphibole-liquid geothermobarometer utilized quantitative and semi-quantitative amphibole compositions with whole rock and glass analyses from this study (Putirka, 2016). Pressure estimates for the x-r Inyo lavas and the DM lava are ~300 to 450 ± 50 MPa (Fig. 13B). Temperature estimates were similar for the x-r Inyo lavas and the x-r DM lava all falling between 775-800 °C.

5.0 DISCUSSION

Previous work has postulated that two independent reservoirs, related to the West Moat rhyolites and the aphyric Mono Chain, generated the x-r and x-p 0.6 ka Inyo lavas, respectively (Sampson & Cameron, 1987; Vogel et al., 1989). The rhyolites and dacites examined span ~160 kyrs and the origins of their crystal-rich endmember, specifically that of the 0.6 ka Inyo Domes, have long been tied to ~160 ka residual Bishop Tuff magma (i.e., Hildreth, 2004).

The data from this study confirms the chemical and textural similarities between the x-r 0.6 ka Inyo lavas and the x-r DM lavas (Sampson & Cameron, 1987) and elucidates the chemical similarities between the x-p Inyo lavas, most notably Obsidian Dome, and the Northwest dacites hypothesized to exist by previous research (e.g., Hildreth et al., 2014).

5.1 Disequilibrium Phenocrysts

Petrographic investigation into the lavas of this study reveals the overwhelmingly similar mineralogy and textures shared between the Inyo lavas, the Northwest dacites, and the Deer Mountain of the West Moat rhyolites. Resorption features, complex zonations, embayments, and fracturing suggests the sanidine and plagioclase megacrysts found in all x-r lavas are in fact antecrysts (e.g., Fig. 4). This is further demonstrated by the failure of tests for equilibrium (K_D values) during initial attempts to estimate temperature profiles (plagioclase-liquid; alkali-liquid; two-feldspar thermometry) from the temporally separate lavas. The two-feldspar and alkali feldspar-glass thermometry resulted in K_D values (< 0.15 & > 0.20) confirming the feldspars of both size groups are not in equilibrium with their host melt (glass). The only feldspars in

equilibrium with their host melts (glass or whole rock) are the small (≤2.5 mm) plagioclase phenocrysts in some of the lavas sampled (e.g., Fig. 13).

Two clusters of small plagioclase and sanidine crystals were observed in the x-p 0.6 ka Inyo lavas and the smaller Inyo Domes. These phenocrysts are not euhedral and display zonations and resorption features, but the compositional similarities suggest x-p small Inyo Domes and x-p 0.6 ka Inyo Domes shared or sampled similar magma upon eruption. Further similarities are identified when comparing the whole rock data (e.g., Fig. 9B).

Disequilibrium textures are noted in the mafic minerals, which share chemical similarities, of all the lavas investigated. The NWD, DM, and the Inyo Domes contain clinopyroxene, biotite, and ilmenite that all cluster in a narrow range of compositions (Fig. 12). Amphibole identified in the x-r and x-m 0.6 ka Inyo lavas are chemically like the amphibole of DM (Fig. 12C). Furthermore, crystal clots dominantly comprised of normally zoned plagioclase and mafic mineral phases occur within all the x-r dacites and rhyolites and possibly represent entrained portions of a crystal mush (e.g., Ellis et al., 2014). The disequilibrium phenocryst textures and chemical similarities amongst the temporally separate rhyolites and dacites suggest they mingled prior to eruption.

5.2 Is residual Bishop Tuff the source of the feldspar antecrysts?

One potential source for the antecrysts identified in the Inyo, Northwest dacites, and West Moat rhyolites is a residual 760 Ka Bishop Tuff crystal-rich mush (Hildreth, 2004; Hildreth et al., 2014). If the feldspar antecrysts identified in the Inyo, Northwest dacites, and West Moat rhyolites are liberated and entrained Long Valley type feldspars this should be reflected in similar feldspar core compositions (Wolff et al., 2015). However, the feldspar compositions, both core and rim, from this study do not overlap with the Bishop Tuff feldspars (e.g., Chamberlain et al. 2015). (Fig. 11). The large antecrystic feldspars of this study have tight compositional ranges, An_{22} and Or_{76}, which plot distinctly away from the Bishop Tuff. Specifically, the ≥5mm sanidine antecrysts plot at higher orthoclase contents than that of the Bishop Tuff (e.g., Fig 11B). Furthermore, the Bishop Tuff feldspars have consistently lower barium concentrations with respect to the lavas investigated in this study (Chamberlain et al., 2015).

We conclude that the x-r Inyo lavas, the Northwest dacites, and Deer Mountain of the West Moat rhyolites sampled the same crystal-rich mush which is not genetically related to a residual portion of the Bishop Tuff.

5.3 Conjugate Magma Reservoirs

The 0.6 ka Inyo lavas are located within a complex region of volcanism, the x-p Mono Chain to the north, x-r West Moat rhyolite and Mammoth Mountain to the south, the x-r Northwest wall trachydacite chain abutting GCD to the southeast, and the addition of a mafic component evidenced by mafic enclaves (Varga et al., 1990; Hildreth, 2004; Mahood et al., 2010) (Fig.14A).

The eruption of the West Moat rhyolites was previously attributed to a remobilized section of crystallizing Long Valley reservoir (low-velocity lens in the western caldera: Hill et al., 1985; Hildreth & Fierstein, 2016). Whereas we imagine the West Moat rhyolites were generated from a cumulate pile independent of the Bishop Tuff. Zircons within the x-r DM lava show $^{230}Th/^{238}U$ mineral isochron ages clustering at ~237 ka aligning with the earliest onset of the Mammoth Mountain mafic volcanism (~230 ka). Thus, it is possible that a cumulate pile was rejuvenated by the earliest Mammoth Mountain mafic volcanism at ~237 ka (Fig. 14A; Hildreth & Fierstein, 2016). Additionally, the origin of the Northwest dacites has been hypothesized to originate from mafic input that promoted mixing between West Moat rhyolite magma and trachydacitic magma of Mammoth Mountain (Ring, 2000; Bailey, 2004). Quantitative mineral and glass data from this study, reveal the compositional similarities between the ~41 ka Northwest dacites and ~113 ka Deer Mountain lavas. Both lavas contain feldspar antecrysts, mafic minerals, and oxides with overlapping similar compositional ranges suggesting the NWD did in fact mingle with the magma that produced the West Moat rhyolites.

5.4 Inyo Domes Magma System

The extensional, en-echelon fault system that overprints the western margin of the Long Valley caldera sets the stage for mingling and mixing of the temporally distinct magma systems examined in this study (Hildreth, 2004). The petrologic and geochemical data collected in this study and in previous work demonstrates the compositional and textural similarities between the crystal cargoes of the 0.6 ka, 41 ka, and 113 ka lavas (e.g., Sampson & Cameron, 1987).

We envisage a long-lived (~250 ka) cumulate pile in the northwest moat of the Long Valley caldera that has been thermally rejuvenated over the last ~230 ka generating the mixed and mingled

x-r lavas of this study (Fig. 14A). With respect to the x-r Inyo lavas thermal rejuvenation was accompanied by mass transfer as evidenced by mafic enclaves (e.g., Fig 2A; Varga et al., 1990) whereas no enclaves have been identified in the x-r West Moat rhyolites. Our data indicate the chemically similar x-r Inyo lavas originated from the same cumulate pile as the West Moat rhyolites (Fig. 14C). Potentially, punctuated mafic recharge generated the two temporally separate but nearly identical cumulate melts. Liberation and entrainment of the cumulate is inferred by the anhedral, resorbed feldspar antecrysts and crystal clots identified in the x-r lavas (e.g., Fig 3).

The potential source of the x-p Inyo lavas is a separate magma system to the north, possibly related to the aphyric high-silica rhyolites of the Mono Chain (Fig. 14A; Vogel et al., 1989). This system potentially has an unerupted cumulate pile that has experienced sustained mafic recharge, with little mass contribution, generating the aphyric high silica rhyolites of the Inyo Volcanic Chain. Compositional and textural similarities, temperature profiles, as well as spatial relationships indicate the possible shared parental magma of the older Inyo lavas, small Inyo domes, and the x-p 0.6 ka Inyo lavas (Fig. 14B).

Mixing of a rhyolite and dacite component is hypothesized to generate the compositional range of the x-p Inyo lavas, specifically noted at OBD (Vogel et al., 1989). Based on the compositional similarities, particularly the overlapping glass compositions of OBD and NWD, we infer that the mixing of an unerupted portion of trachydacite with the x-p rhyolite compositionally like Wilson Butte (older Inyo Dome) generated the chemical gradients in the x-p Inyo lavas (Fig. 14A).

Phases of disequilibrium melting of a fusible crystal cumulate, dominated by quartz, sanidine, and biotite, followed by crystallization can create the barium enriched sanidine rims observed within the lavas of this study (e.g., Fig 5A). Furthermore, crystal settling and compaction leading to the extraction of high-silica melt will create a chemically stratified magma reservoir with low barium concentrations within the first high-silica melts (Bachmann & Bergantz, 2004; Wolff et al., 2020). This stratification is represented in the x-p older Inyo lavas, smaller Inyo domes, and the 0.6 Inyo lavas (Fig. 14B).

The data presented in this study agrees with past research that the x-p and x-r Inyo lavas were generated from different parental magmas and housed in separate reservoirs (Sampson & Cameron, 1987; Vogel et al., 1989). Differential draw-up of variable density magma is potentially responsible for the different volumetric proportions of the x-r and x-p lavas at the three youngest

Inyo Domes (Blake & Fink, 1987). Amphibole-liquid barometry estimates suggest the x-r rhyolite magmas were housed at similar pressures, ~350 MPa (Fig. 13B). We believe this pressure profile illuminates the depth at which the cumulate pile is housed, which coincides with the low-velocity melt lens identified in the western margin of the Long Valley caldera (Hill, 1976). The emplacement of the 0.6 ka Inyo dike bulldozed through separate small reservoirs resulting in mixing and mingling with the magmas which generated the ~41 ka Northwest dacites and the ~113 Deer Mountain, West Moat rhyolite (Fig. 14A).

6.0 CONCLUSIONS

This study confirms that the petrogenesis of the two textural end-members of the 0.6 ka Inyo Domes is complex and the result of mixing and mingling of older dacitic and rhyolitic magmas. There are distinct similarities in the crystal cargoes of the (4 ka to 0.6 ka) Inyo Domes, the (41-26 ka) Northwest dacites, and the (160-113 ka) West Moat rhyolites. We cannot confirm the cumulate pile which contributed to the x-r magmas in this study to be crystallizing Long Valley residue. However, we do note that the feldspar chemistry of this study does not match those of the Bishop Tuff. The small, semi-contiguous reservoirs hypothesized herein highlight the critical role of thermal recharge in triggering intracontinental eruptions.

FUTURE WORK

The crystal clots identified within the x-r lavas potentially contain vital information about the cumulate pile from which they were derived (e.g., Ellis et al., 2014). Future work could determine, using EPMA, the quantitative chemical composition of the glass within the crystal clots and its similarities or differences to the host melt. Furthermore, quantitative compositions of the normally zoned plagioclase feldspars within the crystal clots could be compared to that of the feldspar phenocrysts. These data could then be compared to the Bishop Tuff to further understand its relationship to that of the Inyo Domes, Northwest dacites, and West Moat rhyolites.

ACKNOWLEDGEMENTS

The authors sincerely thank the United States Geological Survey – Menlo Park and the previous work by Roy A. Bailey, Wes Hildreth, and Daniel Sampson. This research was supported by the National Science Foundation through awards EAR 1725131 and EAR 1935764 to GA, INTERN to GA and SI, and the John C. and Mildred Ludlum Geology Endowment to SI. The authors benefited from field and laboratory assistants, Levi Fath and Jayden Ware.

REFERENCES

Bachmann, O., & Bergantz, G. W. (2004). On the origin of crystal-poor rhyolites: Extracted from batholithic crystal mushes. *Journal of Petrology*, *45*(8), 1565–1582. https://doi.org/10.1093/petrology/egh019

Bailey, R. A. (1989). *Geologic map of Long Valley caldera, Mono-Inyo Craters volcanic chain, and vicinity, eastern California*.

Bailey, R. A. (2004). Eruptive History and Chemical Evolution of the Precaldera and Postcaldera Basalt-Dacite Sequences, Long Valley, California: Implications for Magma Sources, Current Seismic Unrest, and Future Volcanism. *U.S. Geological Survey Profession Paper*, *1692*, 0–75. http://pubs.usgs.gov/pp/pp1692/

Bailey, R. A., Dalrymple, G. B., & Lanphere, M. A. (1976). Volcanism, structure, and geochronology of Long Valley Caldera, Mono County, California. *Journal of Geophysical Research*, *81*(5), 725–744. https://doi.org/10.1029/jb081i005p00725

Bailey, R. A. (1976). Volcanism, Structure, and Geochronology of Long Valley Caldera. *Journal of Geophysical Research*, *81*(5), 725–744.

Blake, S., & Fink, J. H. (1987). The dynamics of magma withdrawal from a density stratified dyke. *Earth and Planetary Science Letters*, *85*(4), 516–524. https://doi.org/10.1016/0012-821X(87)90145-2

Bursik, M., & Sieh, K. (1989). Range front faulting and volcanism in the Mono Basin, eastern California. *Journal of Geophysical Research*, *94*(B11). https://doi.org/10.1029/jb094ib11p15587

Chamberlain, K. J., Wilson, C. J. N., Wallace, P. J., & Millet, M. A. (2015). Micro-analytical perspectives on the bishop tuff and its magma chamber. *Journal of Petrology*, *56*(3), 605–640. https://doi.org/10.1093/petrology/egv012

Ellis, B. S., Bachmann, O., & Wolff, J. A. (2014). Cumulate fragments in silicic ignimbrites: The case of the Snake River Plain. *Geology*, *42*(5), 431–434. https://doi.org/10.1130/G35399.1

Fink, J. H. (1985). Geometry of Silicic Dikes Beneath the Inyo Domes, California. *Journal of Geophysical Research*, *90*, 11,127-11,133.

Fink, J. H., & Pollard, D. D. (1983). Structural evidence for dikes beneath silicic domes, Medicine Lake Highland volcano, California. *Geology*, *11*(8), 458–461. https://doi.org/10.1130/0091-7613(1983)11<458:SEFDBS>2.0.CO;2

Hildreth, W. (1979). The Bishop Tuff: evidence for the origin of compositional zonation in silicic magma chambers. In C. E. Chapin & W. E. Elston (Eds.), *Ash-Flow Tuffs* (Vol. 180, pp. 43–75). Geological Society of America Special Paper.

Hildreth, W. (1981). Gradients in silicic magma chambers: Implications for lithospheric magmatism. In *Journal of Geophysical Research* (Vol. 86, Issue B11). https://doi.org/10.1029/JB086iB11p10153

Hildreth, W. (2004). Volcanological perspectives on Long Valley, Mammoth Mountain, and Mono Craters: Several contiguous but discrete systems. *Journal of Volcanology and Geothermal Research*, *136*(3–4), 169–198. https://doi.org/10.1016/j.jvolgeores.2004.05.019

Hildreth, W., & Fierstein, J. (2016). Eruptive history of Mammoth Mountain and its mafic periphery, California. In *Professional Paper*. https://doi.org/10.3133/pp1812

Hildreth, W., Fierstein, J., Champion, D., & Calvert, A. (2014). Mammoth mountain and its mafic periphery- A late Quaternary volcanic field in eastern California. *Geosphere*, *10*(6), 1315–1365. https://doi.org/10.1130/GES01053.1

Hildreth, W., & Wilson, C. J. N. (2007). Compositional zoning of the bishop tuff. *Journal of Petrology*, *48*(5), 951–999. https://doi.org/10.1093/petrology/egm007

Hill, D. P. (1976). Structure of Long Valley Caldera, California, from a seismic refraction experiment. *Journal of Geophysical Research*, *81*(5), 745–753. https://doi.org/10.1029/jb081i005p00745

Hill, D. P. (1996). Earthquakes and Carbon Dioxide Beneath Mammoth Mountain, California. *Seismological Research Letters*, *67*(1), 8–15. http://pubs.geoscienceworld.org/ssa/srl/article-pdf/67/1/8/2753349/srl067001_0008.pdf

Hill, D. P., Kissling, E., Luetgert, J. H., & Kradolfer, U. (1985). Constraints on the upper crustal structure of the Long Valley- Mono Craters volcanic complex, eastern California, from seismic refraction measurements (USA). *Journal of Geophysical Research*, *90*(B13). https://doi.org/10.1029/jb090ib13p11135

Kelleher, P. C., & Cameron, K. L. (1990). The geochemistry of the Mono Craters-Mono Lake Islands Volcanic Complex, eastern California. *Journal of Geophysical Research*, *95*(B11).

Mahood, G. A., Ring, J. H., Manganelli, S., & McWilliams, M. O. (2010). New 40Ar/39Ar ages reveal contemporaneous mafic and silicic eruptions during the past 160,000 years at Mammoth Mountain and Long Valley caldera, California. *Bulletin of the Geological Society of America*, *122*(3–4), 396–407. https://doi.org/10.1130/B26396.1

Mangan, M., Ball, J., Wood, N., Jones, J. L., Peters, J., Abdollahian, N., Dinitz, L., Blankenheim, S., Fenton, J., & Pridmore, C. (2018). California's Exposure to Volcanic Hazards. *USGS Scientific Investigations Report*, *5159*, 50.

Manley, C. R., & Fink, J. H. (1987). Internal textures of rhyolite flows as revealed by research drilling. *Geology*, *15*(6), 549–552. https://doi.org/10.1130/0091-7613(1987)15<549:ITORFA>2.0.CO;2

Marcaida, M., Vazquez, J. A., Stelten, M. E., & Miller, J. S. (2019). Constraining the Early Eruptive History of the Mono Craters Rhyolites, California, Based on 238U-230Th Isochron Dating of Their Explosive and Effusive Products. *Geochemistry, Geophysics, Geosystems*, *20*(3), 1539–1556. https://doi.org/10.1029/2018GC008052

Martens, A. (2014, January 21). *Inyo Domes, CA lidar 2016 airborne lidar survey*. National Center for Airborne Laser Mapping (NCALM).

Miller, C. D. (1985). Holocene eruptions at the Inyo volcanic chain, California: Implications for possible eruptions in Long Valley caldera. *Geology*, *13*(1), 14–17. https://doi.org/10.1130/0091-7613(1985)13<14:HEATIV>2.0.CO;2

Putirka, K. D. (2008). Thermometers and barometers for volcanic systems. *Reviews in Mineralogy and Geochemistry*, *69*, 61–120. https://doi.org/10.2138/rmg.2008.69.3

Putirka, K. D. (2016). Rates and depths of magma ascent on earth: Amphibole thermometers and barometers for igneous systems and some implications for eruption mechanisms of felsic magmas at arc volcanoes. *American Mineralogist*, *101*(4), 841–858. https://doi.org/10.2138/am-2016-5506

Reid, M. R., Coath, D. I. D., Harrison, T. M., & Mckeegan, K. D. (1997). Prolonged residence times for the youngest rhyolites associated with Long Valley Caldera: 230Th-238U ion microprobe dating of young zircons. In *Earth and Planetary Science Letters* (Vol. 50).

Riley, P., Tikoff, B., & Hildreth, W. (2012). Transtensional deformation and structural control of contiguous but independent magmatic systems: Mono-inyo craters, Mammoth Mountain, and Long Valley Caldera, California. *Geosphere*, *8*(4), 740–751. https://doi.org/10.1130/GES00662.1

Ring, J. H. (2000). *Young volcanism in western Long Valley caldera, California*.

Sampson, D. E. (1987). Textural heterogeneities and vent area structures in the 600-year-old lavas of the Inyo volcanic chain, eastern California. In *Geological Society Special Publication* (pp. 89–102). https://doi.org/10.1130/SPE212-p89

Sampson, D. E., & Cameron, K. L. (1987). The Geochemistry of the Inyo Volcanic Chain: Multiple Magma Systems in the Long Valley Region, Eastern California. *Journal of Geophysical Research*, *92*, 403–421.

Stine, S. (1987). *Mono Lake; the past 4,000 years*.

Varga, R. J., Bailey, R. A., & Suemnicht, G. A. (1990). Evidence for 600 Year-Old Basalt and Magma Mixing at Inyo Craters Volcanic Chain, Long Valley Caldera, California. *Journal of Geophysical Research*, *95*, 21441–21450.

Vogel, T. A., Eichelberger, J. C., Younker, L. W., Schuraytz, B. C., Horkowitz, J. P., Stockman, H. W., & Westrich, H. R. (1989). Petrology and emplacement dynamics of intrusive and extrusive rhyolites of Obsidian Dome, Inyo craters volcanic chain, eastern California. *Journal of Geophysical Research*, *94*(B12), 17937–17956.

Wolff, J. A., Ellis, B. S., Ramos, F. C., Starkel, W. A., Boroughs, S., Olin, P. H., & Bachmann, O. (2015). Remelting of cumulates as a process for producing chemical zoning in silicic tuffs: A comparison of cool, wet and hot, dry rhyolitic magma systems. In *Lithos* (Vols. 236–237, pp. 275–286). https://doi.org/10.1016/j.lithos.2015.09.002

Wolff, J. A., Forni, F., Ellis, B. S., & Szymanowski, D. (2020). Europium and barium enrichments in compositionally zoned felsic tuffs: A smoking gun for the origin of chemical and physical

gradients by cumulate melting. *Earth and Planetary Science Letters*, *540*. https://doi.org/10.1016/j.epsl.2020.116251

Wood, S. H. (1983). Chronology of late Pleistocene and Holocene volcanics, Long Valley and Mono Basin geothermal areas, eastern California. *U.S. Geological Survey Open-File Report 83-747*, *14*, 76.

FIGURES

Table 1. Summary of petrological and geochemical characteristics of selected Long Valley lavas. This study; 1 - Bailey, 2004; 2 - Dalrymple, 1967; 3 - Hildreth, 1981; 4 - Hildreth, 2004; 5 - Hildreth et al., 2014; 6 - Mahood et al,. 2010; 7 - Miller, 1985; 8 - Sampson & Cameron, 1987; 9 - Varga et al., 1990; 10 - Wood, 1977*

Phenocryst abbreviations: Pl – plagioclase; Sa – sanidine; Qt – quartz; Bt – biotite; Opx – orthopyroxene; Cpx – clinopyroxene; Apa – apatite; Zrn – zircon; Aln – allanite.

Textural units: x-p – crystal-poor; x-m – crystal-medium; x-r – crystal-rich.

lava	unit ID	age (Kyr)	SiO_2 (wt %)	approx. volume (km^3)	Ba (ppm)	crystal content (%)	textural unit	mineral phases	feldspar megacrysts	Ba-rich rim	dating method
Bishop Tuff	BT	760 [2]	~75.5-77.3 [3]	650 [4]	2-600	1 - 25	x-r	Sa, Qt, Pl, Bt,oxides, Px, Zrn, Aln	Y	n/a	sanidine [2]
Deer Mountain (west moat rhyolites)	DM	~115 ± 1 [4]	72-73 & 76-77 [4]	4 ± 1 [4]	33-1290	20 - 30	x-r	Pl, Sa, Amp, Bt, Qt, oxides, Px, Apa, Zrn, Aln	Y	Y	sanidine [4]
northwest wall dacites	NWD	40 to 27 ± 1 [6]	61.7 - 66.4*; [1;4]	~ 1 [4]	1380-1670	20 - 30	x-r	Pl, Sa, Bt, Opx, Cpx, Apa, Zrn	Y	Y	sanidine [6]
North Deadman Dome	NDMD	4 to 6 [4]	64.6 [5]	0.04 [4]	141 [5]	2 - 3 [5]	x-p	-	N	N	-
Wilson Butte	WB	1.3 [10]	76.7 [8]	0.05 [4]	68 [9]	2 - 3 [5]	x-p	-	N	N	^{14}C [10]
Cratered Dome	CD	?	~ 73.5	0.0001 [4]	~ 350	2-3	x-p	Pl, Sa, oxides, Bt, Cpx, Zrn, Apa	N	Y	-
Caldera Wall Dome	CWD	?	~ 73	0.0001 [4]	~ 630	2-3	x-p	Pl, Sa, oxides, Bt, Cpx, Apa	N	Y	-
Obsidian Dome	OBD	0.65 ±0.05 [7]	~ 70-71.7*;[8]	1 [4]	340-1200	0 - 5 & 5-15	x-p, x-m, x-r	Pl, Sa, Bt, oxides, Opx / Amp, Cpx, Zrn, Apa, Qt	Y	Y	^{14}C [7]
Glass Creek Dome	GCD	0.65 ±0.05 [7]	~ 71.4-74 *;[8]	1 [4]	350-975	25 - 40	x-p, x-m, x-r	Pl, Sa, Bt, Amp, Qt, oxides, Opx, Cpx, Zrn, Apa, Aln, Qt	Y	Y	^{14}C [7]
Deadman Dome	DMD	0.65 ±0.05 [7]	~ 69.4-74 *;[8]	1 [4]	740-1330	25 - 40	x-p, x-m, x-r	Pl, Sa, Bt, Amp, Qt, oxides, Opx, Cpx, Zrn, Apa, Aln, Qt	Y	Y	^{14}C [7]

Table 2. Geothermobarometers used in this study. We assumed a water content of 4.0 wt% for the amphibole-melt thermobarometer from Vogel et al., 1989.

thermobarometer	crystal	"melt" composition	KD value	eqn. used	author	error
amphibole-melt	core rim	groundmass glass whole rock biotite melt inclusion	0.28 ± 0.11	5 & 7a	Putirka, 2016	± 30 °C ± 400 MPa
plag-melt	core An_{26-39} rim An_{33}	groundmass glass	0.1 ± 0.05	24a & 25a	Putirka, 2008	± 23 °C ± 300 Mpa

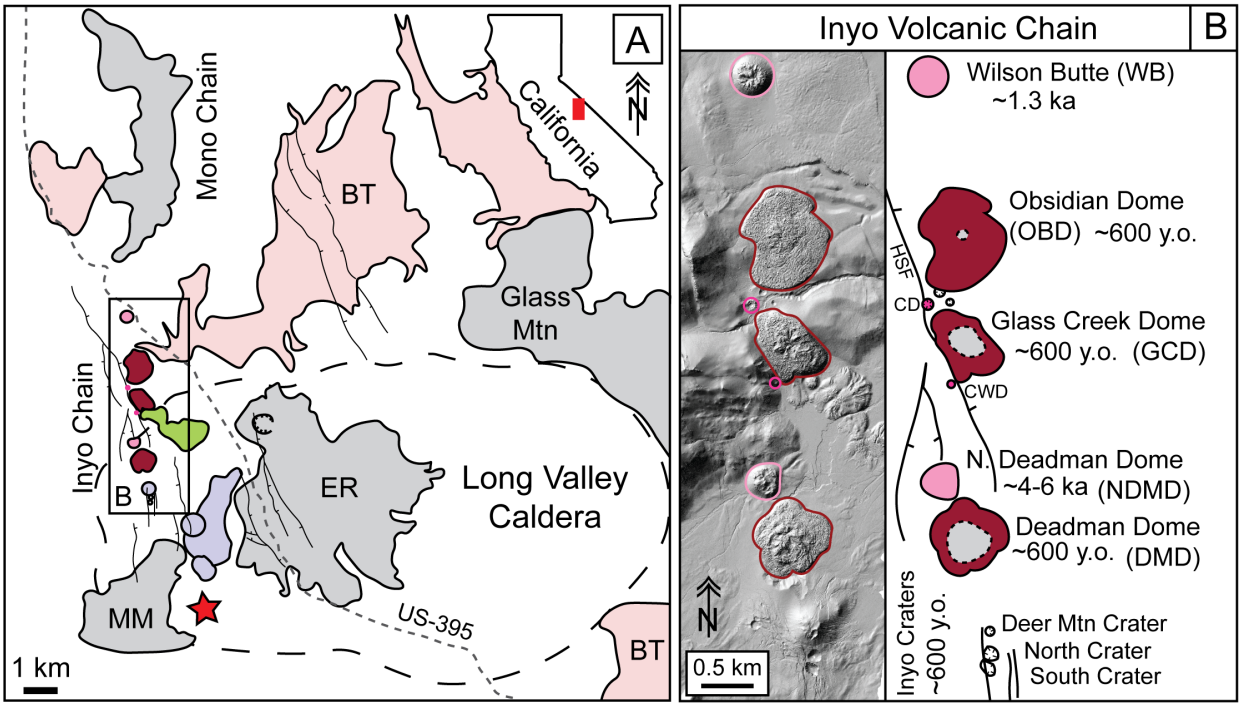

Figure 1. (A) The Long Valley volcanic region with simplified volcanic units after (Bailey, 1989). Red star indicates location of the town of Mammoth Lakes and the Long Valley caldera margin is denoted by a dashed line. The black box encompasses the lavas investigated in this study which fall along the same N-S lineament, light purple – West Moat rhyolites (~161-113 ka), light green – Northwest dacites (~41-26ka), and pink to wine reds – Inyo Volcanic Chain rhyolites. Abbreviations MM – Mammoth Mountain, ER – Early Rhyolites, BT - Bishop Tuff. Greyed out units are not considered in this study. Lighter colors indicate older units while darker colors indicate younger units.

(B) Inyo Volcanic Chain. Phreatic explosion craters are identifiable in the lidar image of the Inyo Chain, occurring between Obsidian Dome and Glass Creek Dome and further to the south. Additionally, the lidar highlights the brecciated fringes and the more coherent, blocky centers of the three youngest Inyo Domes (Martens, 2014). Wine red to pink colors indicate crystal-poor rhyolitic compositions and grey areas indicate concentrations of the crystal-rich rhyolite with the dashed outline highlighting areas of mixing between the two lavas. The Inyo Domes consist of five large silicic lava domes: Wilson Butte (WB); Obsidian Dome (OBD); Glass Creek Dome (GCD); north Deadman Dome (NDMD); and Deadman Dome (DMD) and two smaller domes: Cratered Dome (CD) and Caldera Wall Dome (CWD). The Inyo Craters: Deer Mountain Crater; North Crater; and South Crater. Ages from (Hildreth, 2004; Mahood et al., 2010; Miller, 1985; Wood, 1983). Abbreviations HSF - Hartley Spring fault.

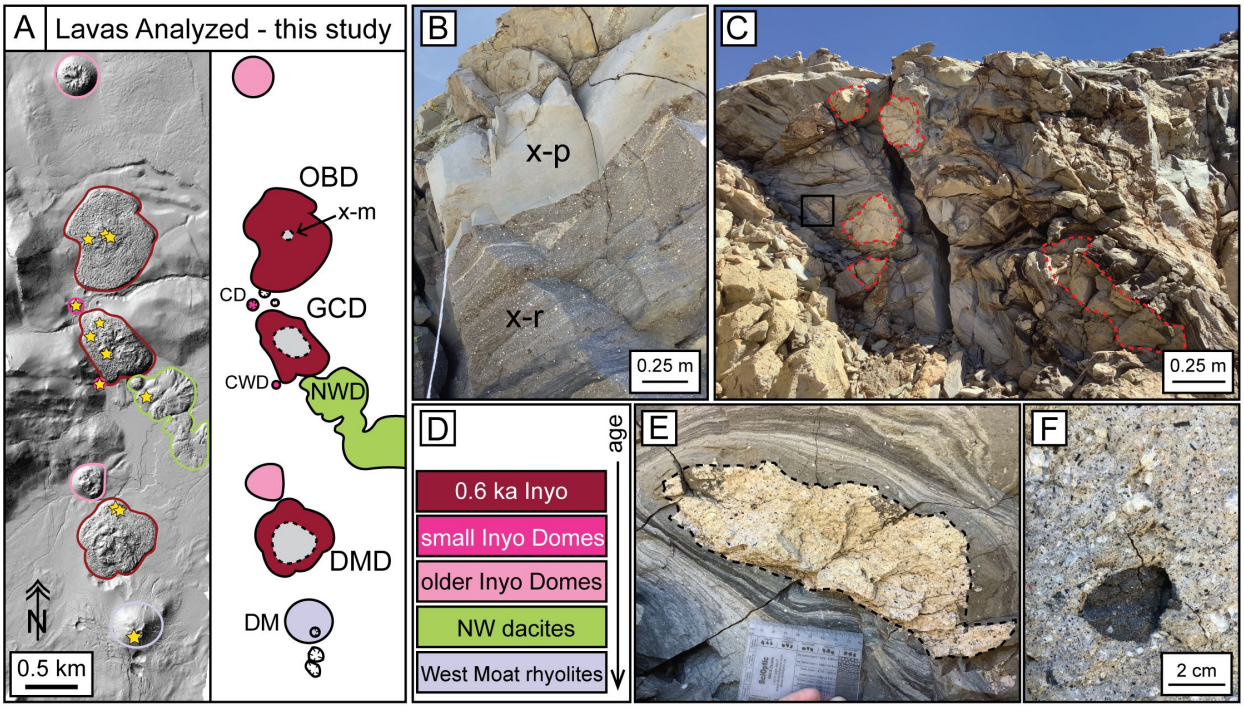

Figure 2. (A) Inset of the N-S lineament of lavas investigated in this study from Figure 1, ages and legend noted in D. Abbreviations as in Figure 1. Dashed lines indicate the intermixing between the x-p and x-m endmember lavas. The area dominated by x-r lava is shaded grey. Yellow stars indicate sample locations from this study. (B) Outcrop photo of a 0.5-meter-thick x-p lava in contact with x-r lava at GCD. (C) Outcrop at GCD, red dashed lines outline incorporated pumiceous x-r lava into banded x-p lava. Black box indicates where photo E was taken. (D) Legend. (E) Lithofacies gradients of the Inyo Domes: pumiceous, glassy, to dense within an outcrop of x-m lava. (F) Mafic inclusion within x-r pumiceous GCD lava.

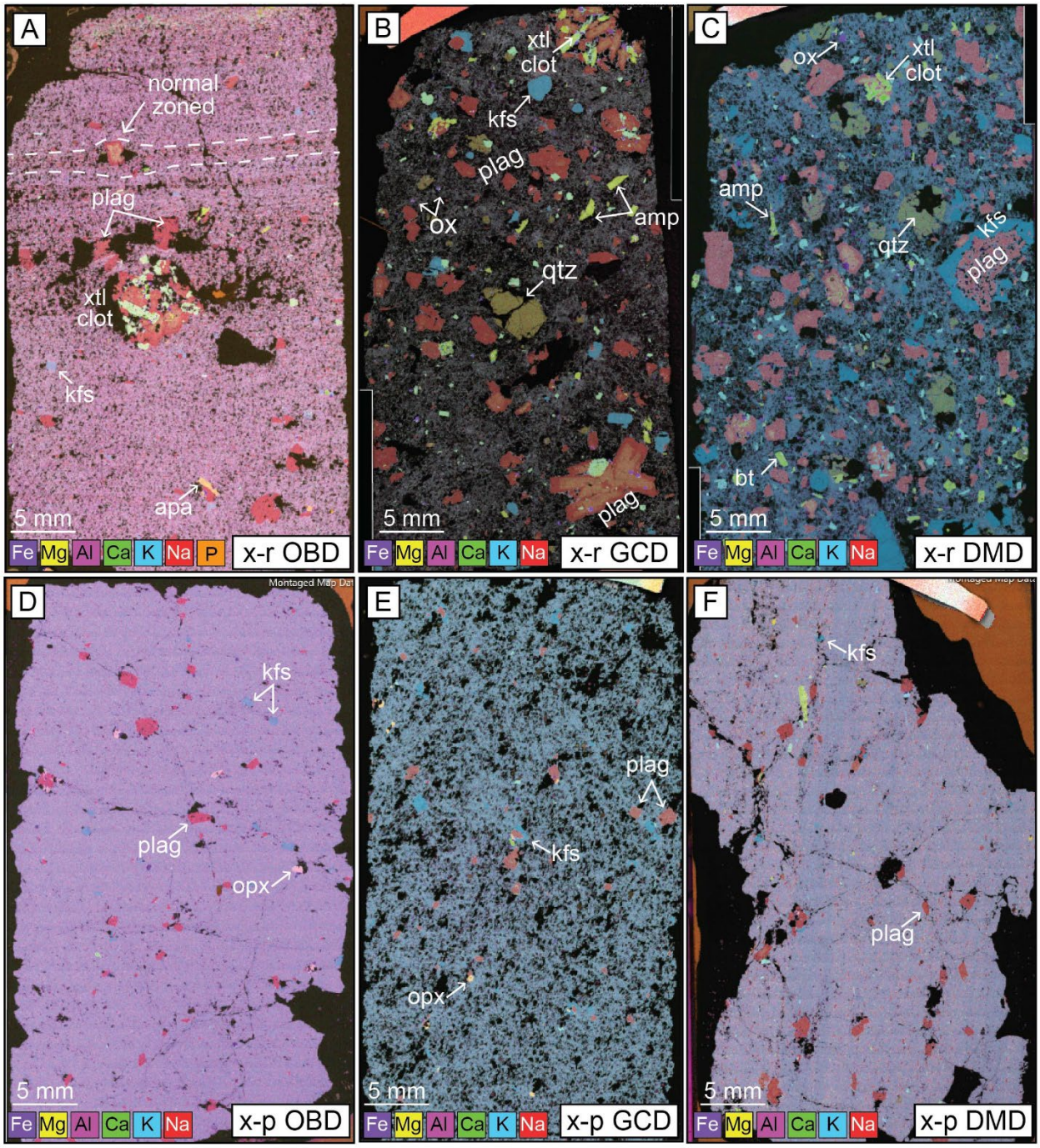

Figure 3. EDS xray maps of the x-r (A-C) and x-p (D-E) 0.6 ka Inyo lavas. Minerals: red - plagioclase (plag), blue - sanidine (kfs), green to blue - biotite (bt), purple - oxides (ox), green - amphibole (amp), brownish - quartz (qtz), pink to orange – orthopyroxene (opx), orange – apatite (apa) and crystal clots (xtl clot).

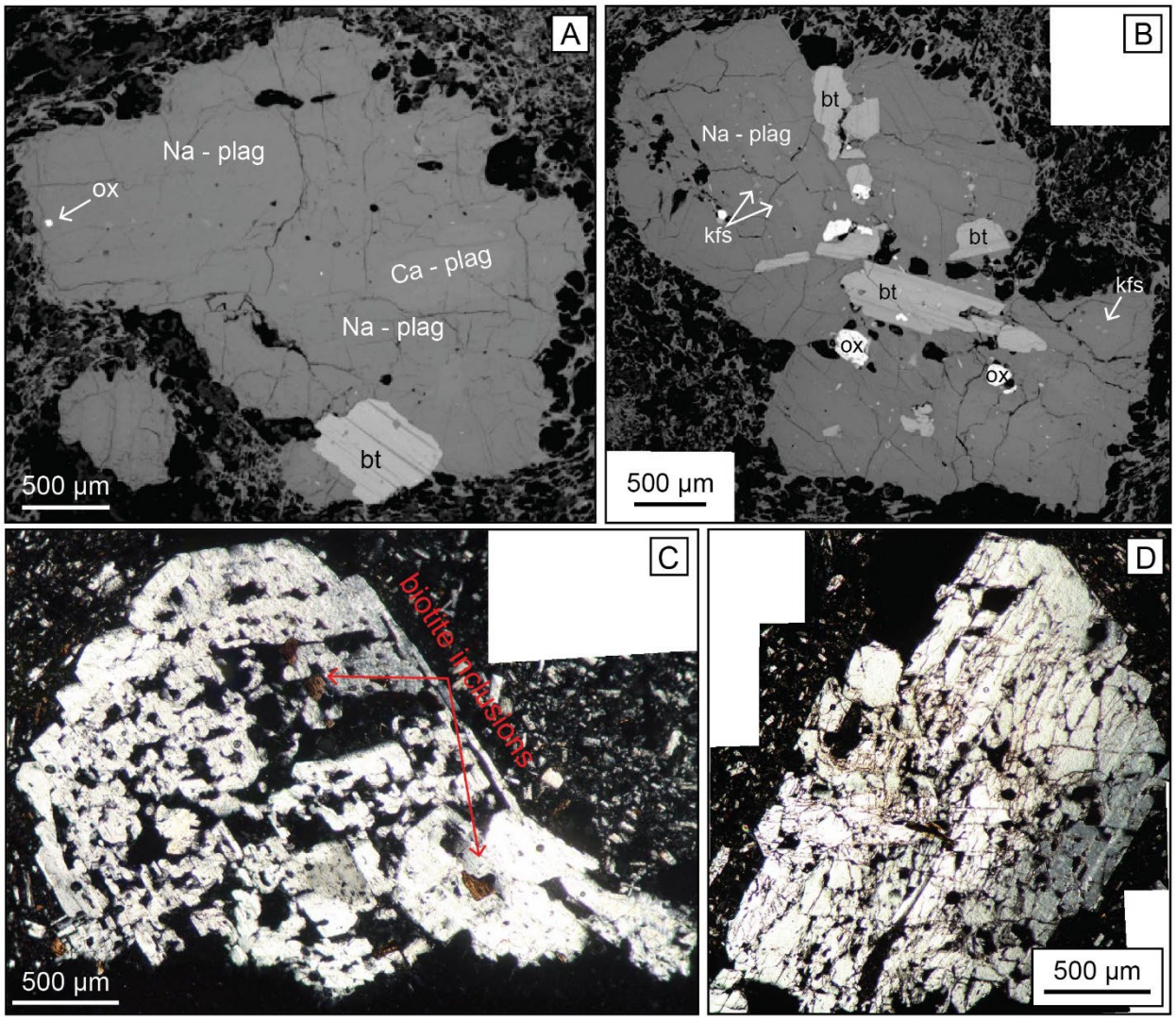

Figure 3. BSE (A&B) and XPL (C&D) images of the feldspar megacrysts (≥ 5mm) within the x-r 0.6 ka Inyo Domes. (A) Normaly zoned anhedral plagioclase. (B) Anhedral poikilitic plagioclase with chadacryts of biotite (bt) and oxides (ox). Small anhedral inclusions of sanidine (kfs) are observed throughout the crystal. (C) Sieve textured poikilitic plagioclase with biotite inclusions. (D) Heavily fractured subhedral sieve textured plagioclase.

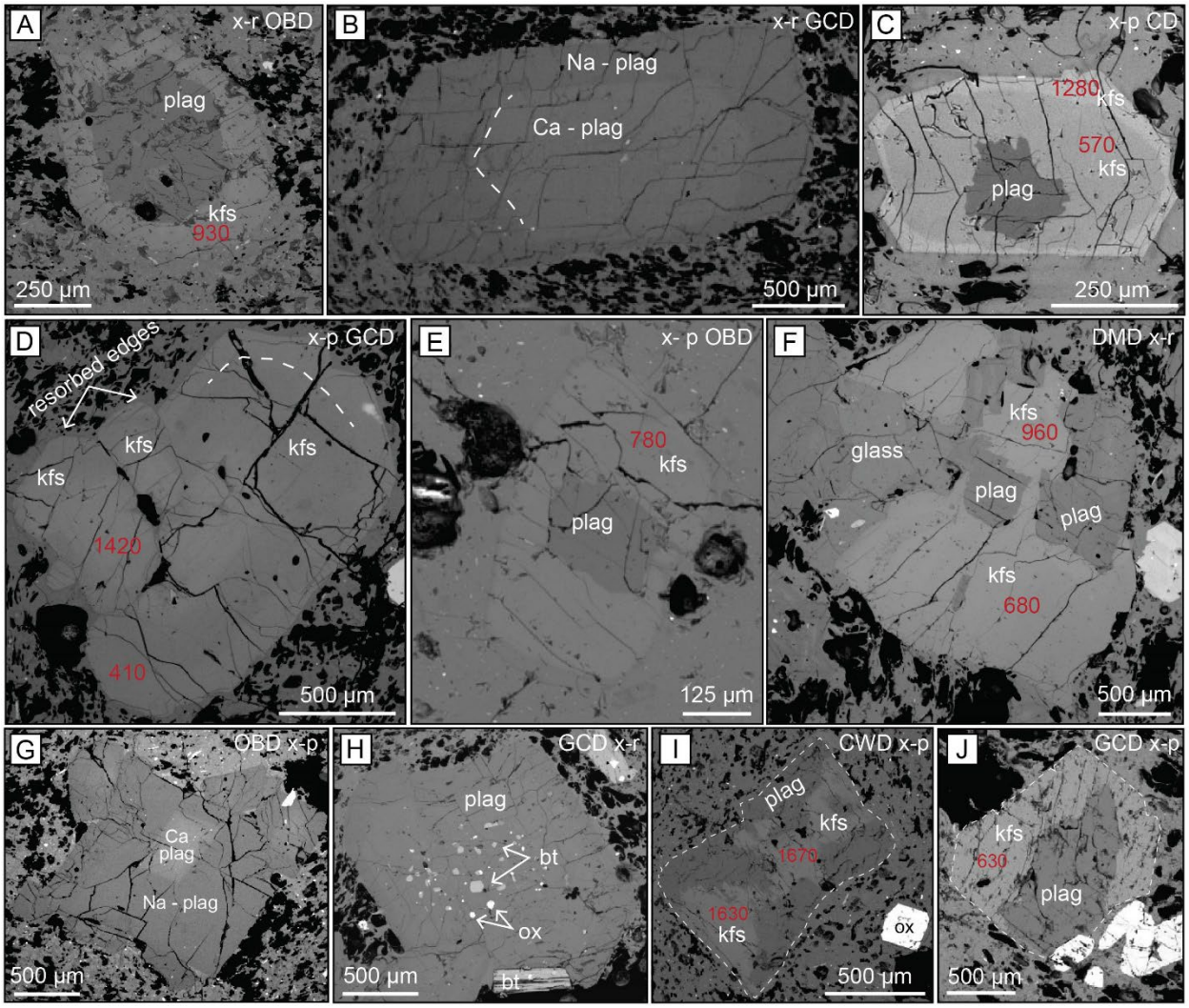

Figure 4. BSE images of the small (≤2.5 mm) sanidine and plagioclase feldspars of the Inyo Domes. Red numbers indicate semi-quantitative barium concentrations in ppm. Mineral abbreviations – plagioclase (plag), sanidine (kfs), biotite (bt), and oxides (ox). (A) Resorbed plag mantled by Ba-enriched kfs from OBD. (B) Normally zoned plag from GCD. (C) Anhedral plag core mantled by progressively enriched barium kfs from CD. (D) Resorbed anhedral kfs with variable Ba concentrations from GCD (E) Resorbed plag mantled by kfs from OBD. (F) Anhedral glomerocrysts of plag and kfs from DMD. (G) Normally zoned plag from OBD. (H) Poikilitic plag with bt and ox inclusions from GCD. (I) Sector zoned plag and Ba- enriched kfs from CWD. (J) Plag mantled with kfs from GCD.

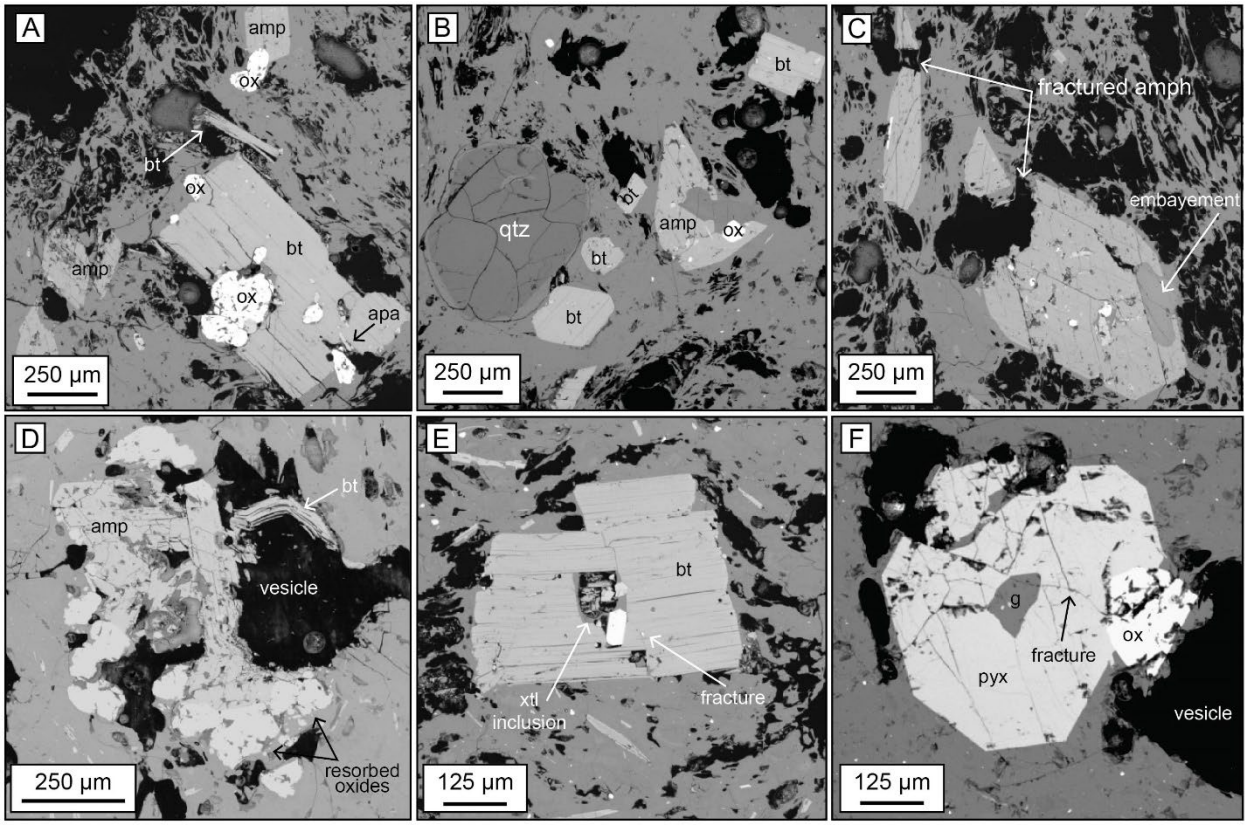

Figure 5. BSE images of the mafic minerals within the x-r (A-C) and x-p (D-F) Inyo Domes. Mineral abbreviations – biotite (bt), oxides (ox), amphibole (amp), apatite (apa), glass (g), pyroxene (pyx), quartz (qtz), and crystal inclusion (xtl inclusion). (A) Fractured bt with ox and apa inclusions. Anhedral ox and amp and fractured bt litter the groundmass. (B) Anhedral rounded qtz surrounded by anhedral bt and amp with ox inclusions. (C) Fractured amp with glass embayement. (D) Heavily resorbed, fractured ox, amp, and bt. (E) Fractured subhedral bt with mineral inclusions. (F) Fractured pyroxene with glass and ox inclusions.

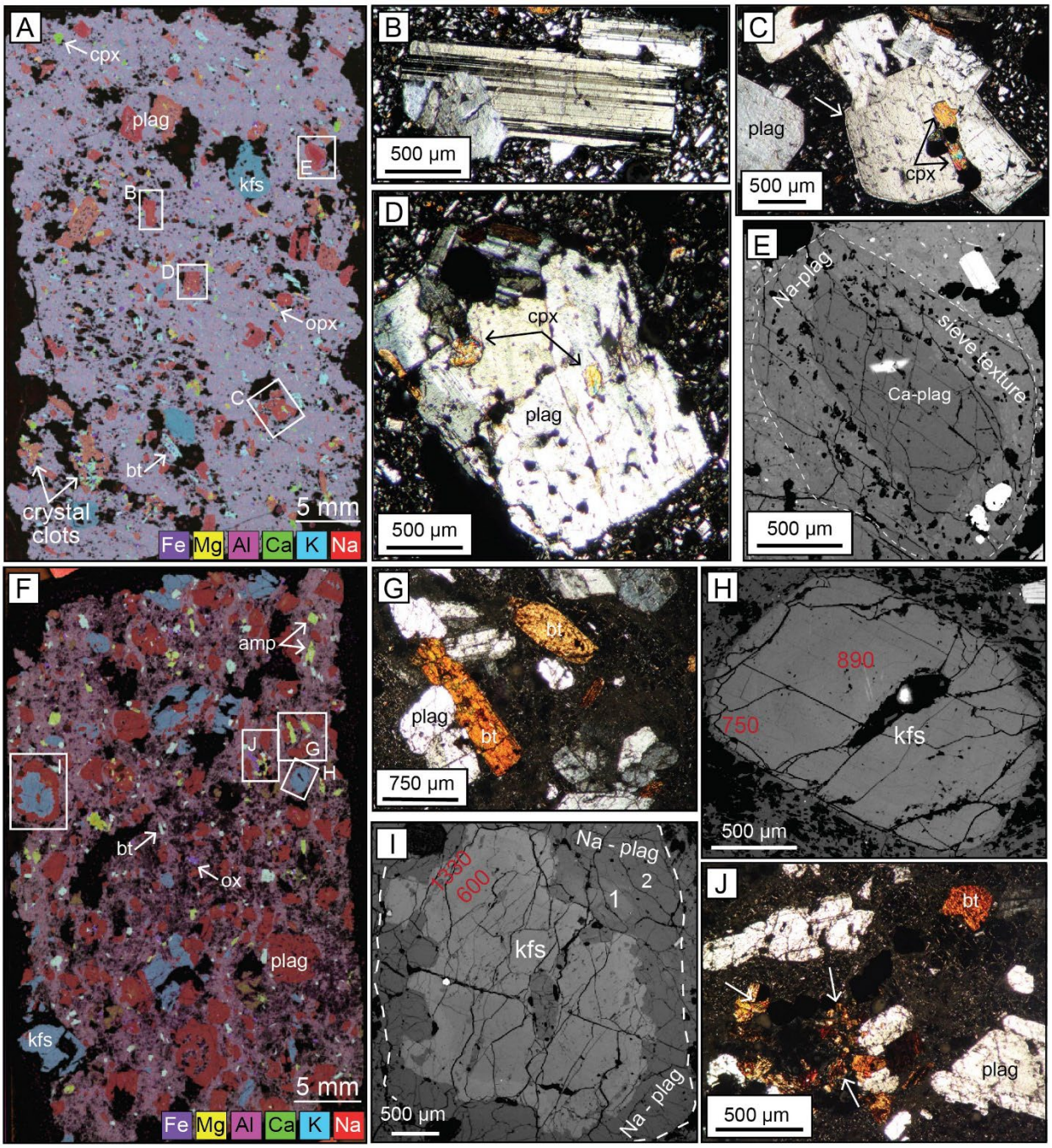

Figure 6. EDS maps , XPL and BSE images of the Northwest dacite (A-E) and Deer Mountain (F-J). Xray map (A&F) minerals: red - plagioclase (plag), blue - sanidine (kfs), green to blue - biotite (bt), purple - oxides (ox), green - amphibole (amp), brownish - quartz (qtz), yellow – orthopyroxene (opx), and green – clinopyroxene (cpx).

(A) Northwest dacite xray map, white boxes indicate location of figures B-E. (B) Albite twinning in plag. (C) Anhedral glomerycrysts of plag with cpx inclusions. (D) Sieve textured plag with cpx inclusions. (E) Normally zoned plag with sieve textured rim. (F) Deer Mountain xray map, white boxes show locations of figures (G-J). (G) Anhedral ≤2.5 mm plag with subhedral bt. (H) Subhedral zoned kfs with variable semi-quantitative barium concentrations in ppm (red numbers). (I) Anhedral barium zoned kfs (red numbers) mantled by plag. Lighter region (indicated with "1") is Ca - plag mantled by Na – plag (2). (J) White arrows indicating crystal clot of bt, ox, and plag.

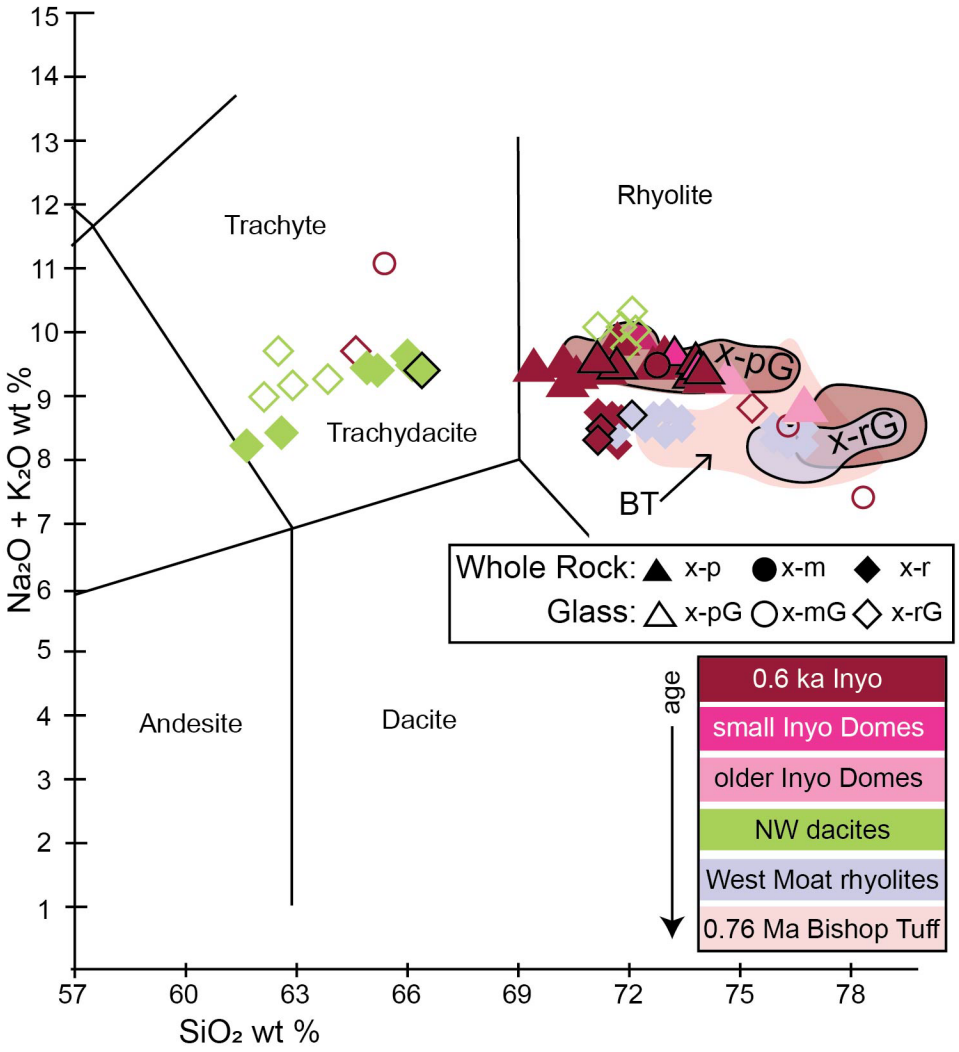

Figure 7. TAS diagram showing whole rock and groundmass glass data from this study and whole rock data from previous studies. Light pink region contains x-r and x-p Bishop Tuff (BT) whole rock data. The extent of the x-p glass (x-pG) and x-r glass (x-rG) of the 0.6 ka Inyo and West Moat rhyolites are indicated by the shaded regions. All data with heavy black outlines are from this study. Previous work from Bailey, 2004; Hildreth et al., 2014; Sampson & Cameron, 1987; Varga et al., 1990; Vogel et al., 1989.

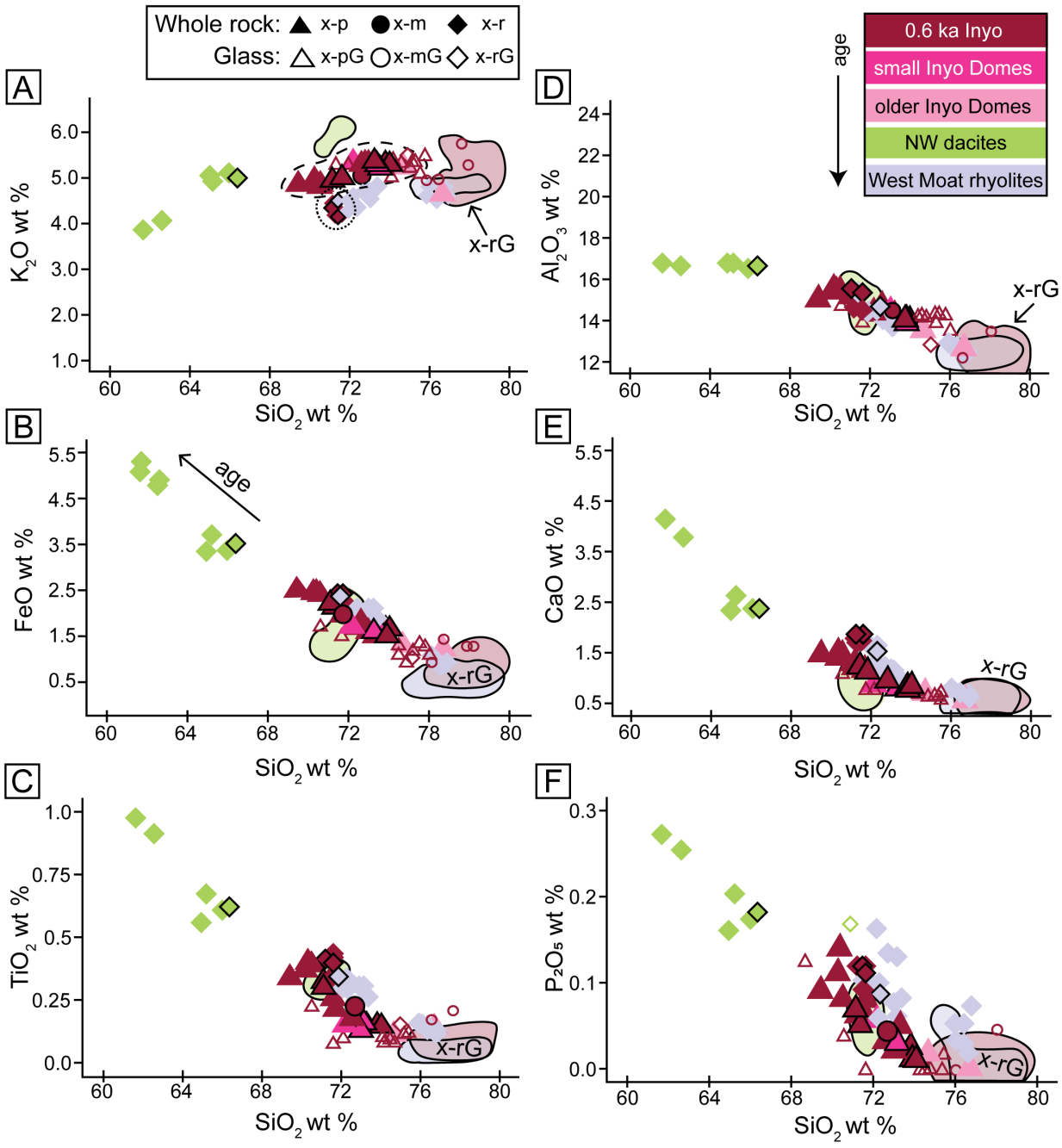

Figure 8. Major and minor element variation diagrams vs SiO2. (A) Black dashed line indicates x-p Inyo Domes trend, and the stippled black line indicates x-r Inyo Domes. The compositional extent of the x-r glass is encompassed by the shaded regions for each lava. Heavy black lines indicate all data from this study. Previous work from Bailey, 2004; Hildreth et al., 2014; Sampson & Cameron, 1987; Varga et al., 1990; Vogel et al., 1989.

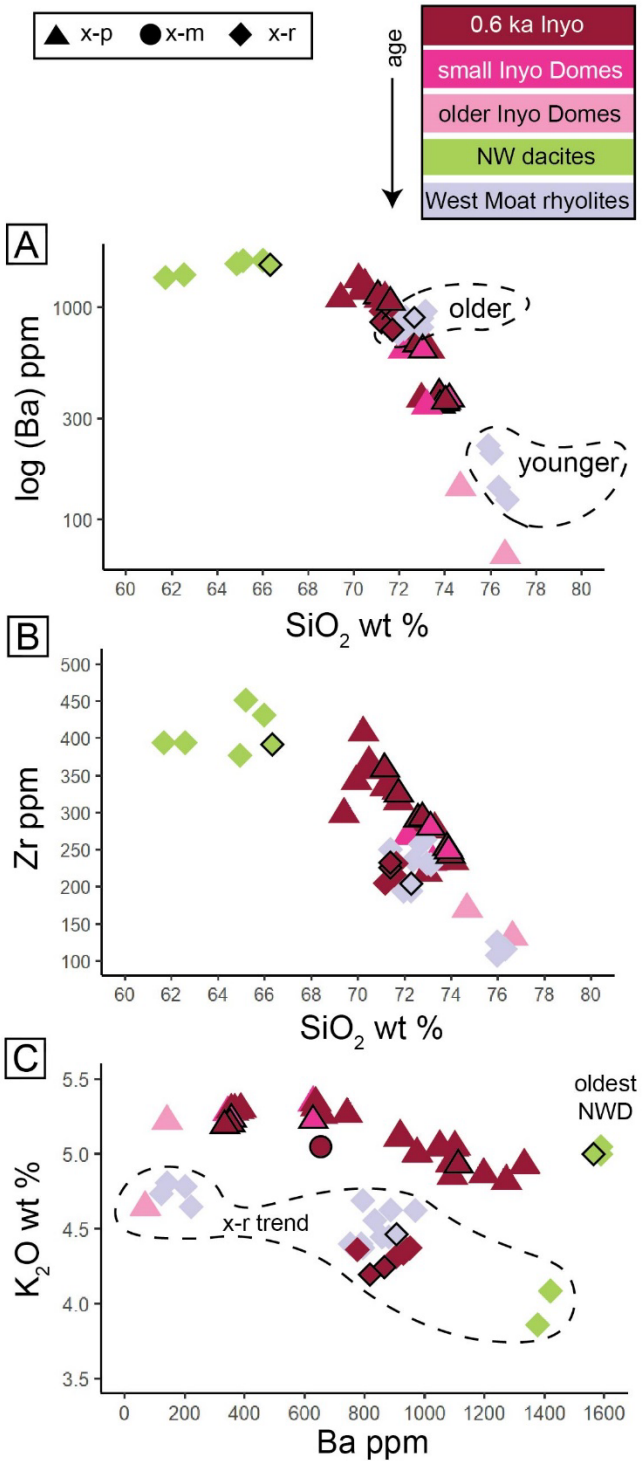

Figure 9. (A-B) Trace element variation diagrams vs SiO2 weight %, dashed outlines indicate the older and younger West Moat rhyolites. (C) Major element variation vs Ba ppm, dashed line outlines the x-r trend. Heavy black outline indicates data from this study. Previous work from Bailey, 2004; Hildreth et al., 2014; Sampson & Cameron, 1987; Varga et al., 1990; Vogel et al., 1989.

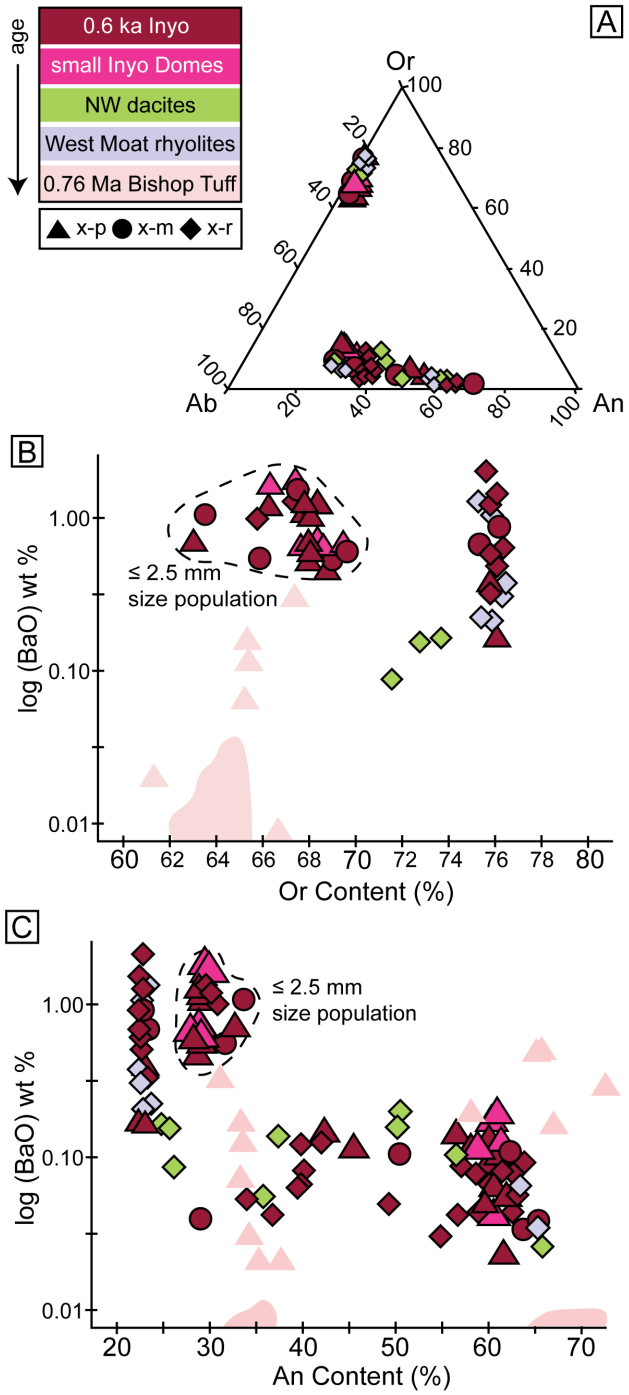

Figure 10. (A) Average quantitative feldspar compositions plotted in the Feldspar ternary. Sanidine and plagioclase are both found in all the Inyo rhyolites, the Northwest dacites, and the West Moat rhyolites. (B) Orthoclase concentrations and (C) anorthite concentrations from this study (black outline) compared to the x-r feldspar from the Bishop Tuff (light pink fields and symbols) Chamberlain et al., 2015). The dashed line encloses ≤ 2.5mm feldspar populations.

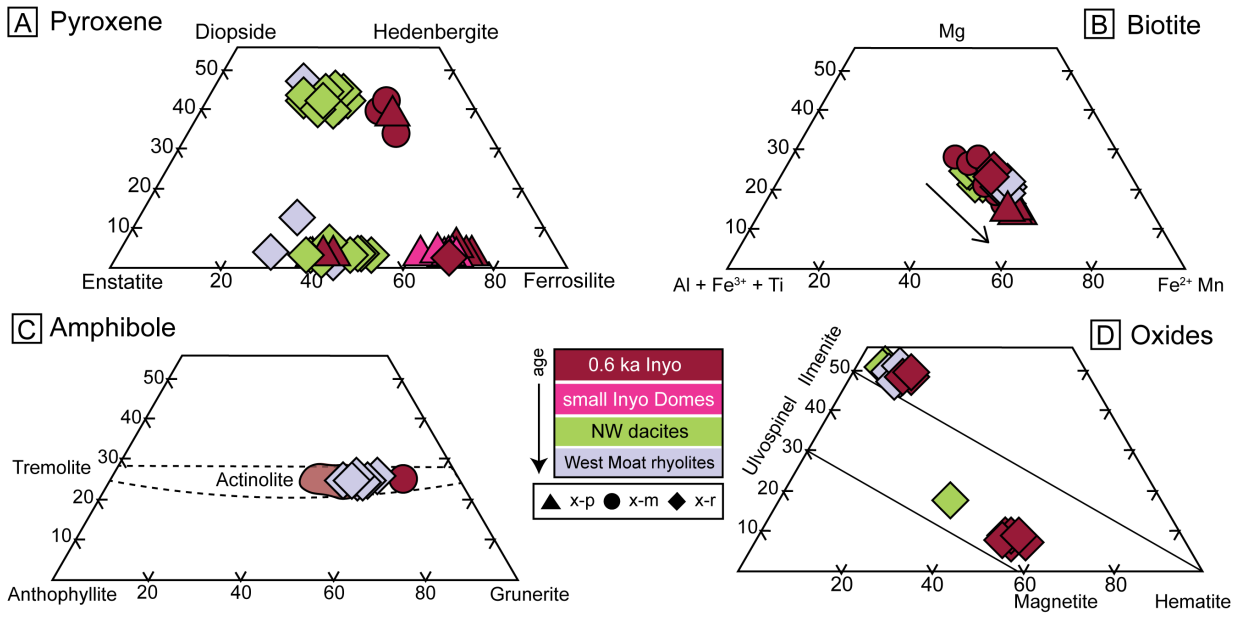

Figure 11. (A) Pyroxene ternary diagram showing semi-quantitative cpx and opx of this study. (B) Biotite ternary diagram of biotites within this study, black arrows indicates increasing ferrous iron concentrations identified in the 0.6 ka Inyo lavas. (C) Overlapping actinolite compositions of 0.6 ka Inyo and West Moat rhyolites. Shaded area demonstrates extent of x-r 0.6 ka Inyo lavas. (D) Ilmenite compositions of the x-r 0.6 ka Inyo Domes, Northwest dacites, and West Moat rhyolites.

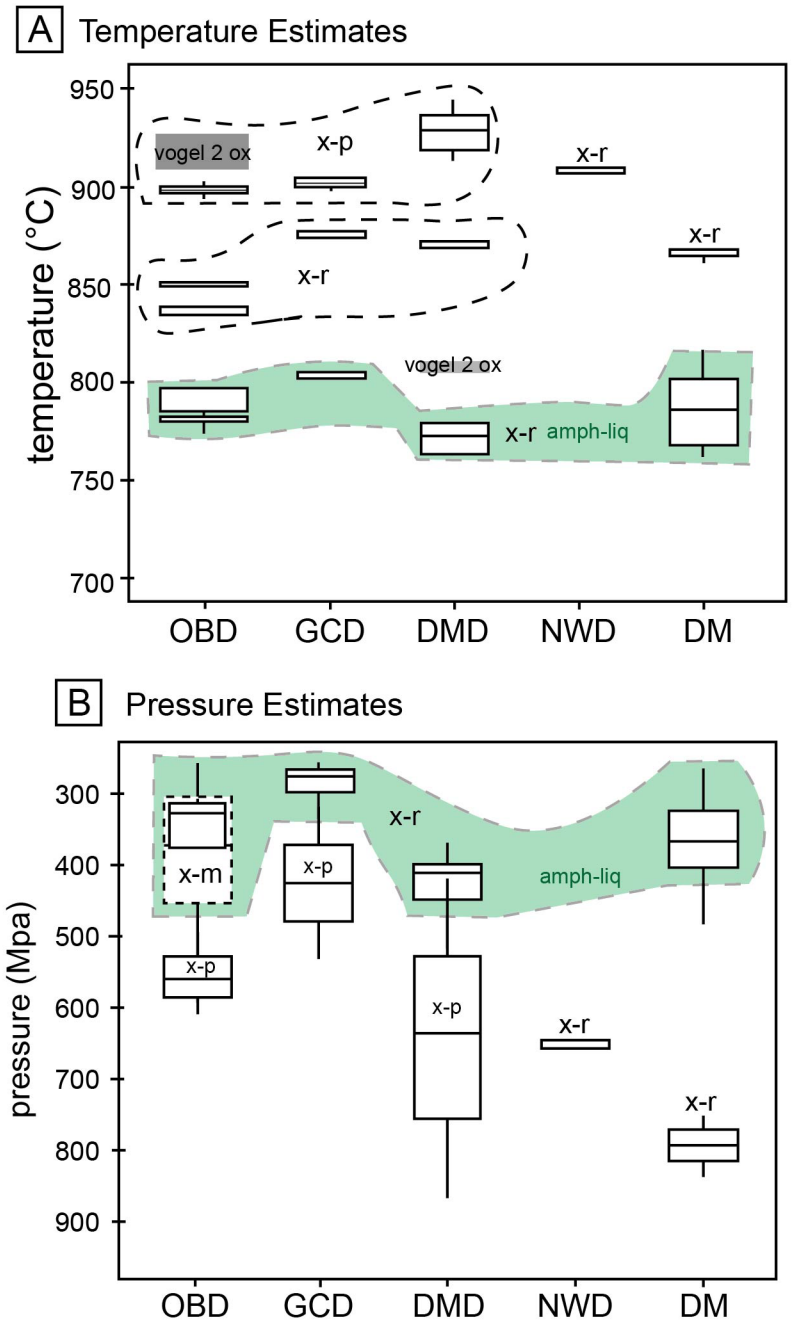

Figure 12. (A) Temperature and (B) pressure estimates using the albite-liquid and amphibole-liquid (shaded green region) geothermobarometers of Putirka, 2008, 2016 for the 0.6 ka, 41ka, 113ka lavas and their textural units investigated in this study. Dark colored boxes indicate the oxide pair temperature estimates of (Vogel et al., 1989). Whiskers on each box indicate the minimum and maximum values calculated and does not show the inherent uncertainty of each thermobarometer, see Table 2 for uncertainties.

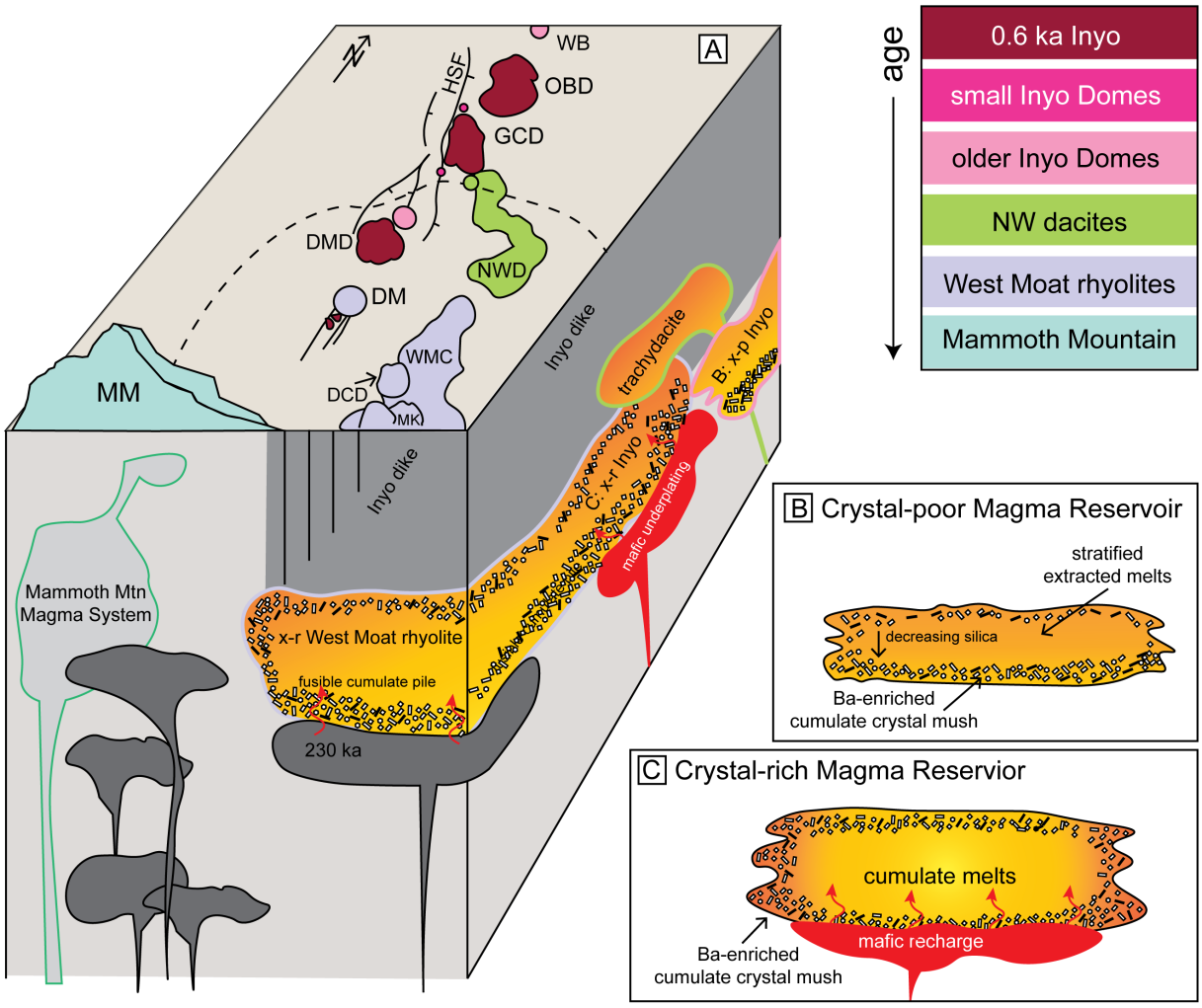

Figure 13. (A) Three-dimensional sketch examining the magma system below the west moat of the Long Valley caldera. Ground surface (map view) displays the lavas investigated in this study including the Mammoth Mountain (MM) complex. Long Valley caldera margin denoted by dashed line. Upper surface not to scale. Magma systems active (red-orange gradient) and mingling immediately prior to and after 0.6 ka Inyo Domes dike emplacement (shaded light gray). Darker grey plumes indicate non-active older intrusions. The three reservoirs which contributed to the 0.6 ka Inyo magmas are orange-yellow in color while mafic recharge/underplating is red. (B) Sketch after Wolff et al (2020) of the hypothesized x-p reservoir for all the Inyo magmas. Extracted melts are from the alkali-feldspar and quartz dominated mush aggregate at the top of the reservoir and stratify themselves with respect to density and temperature (silica concentration). (C) Sketch after Wolff et al (2020) depicting the mafic recharge that melted and liberated the fusible cumulate pile to create the x-r Inyo lavas. Earlier underplating, possibly the ~230 ka mafic Mammoth Mountain volcanism, generated the genetically similar West Moat rhyolites.

CHAPTER 2: MAKING SENSE OF BRITTLE DEFORMATION IN SILICIC LAVAS: INSIGHTS FROM OBSIDIAN DOME, CALIFORNIA

Authors: Shelby L. Isom, Graham D.M. Andrews, Stuart Kenderes, Alan G. Whittington

Corresponding author: Shelby L. Isom

Submitted to: Geosphere

Keywords: silicic lava, emplacement, obsidian, crease structures

Abstract

The absence of observable extrusive silicic lava flows has skewed research to extensively focus on prehistoric lavas, most notable the Holocene lavas in Oregon and California, USA, for information about their eruptive and emplacement dynamics. The first ever witnessed silicic lava eruptive events, Chaitén (2008) and Cordón Caulle (2011) Chile, were paramount to the volcanology community as they featured a range of emplacement processes (endogenous vs. exogenous), movement limiting modes, and eruptive behaviors (explosive vs. effusive) previously thought to act independently throughout an eruptive event. We attempt to document a continuum of brittle and brittle-ductile deformation and fracture induced outgassing during the emplacement of the ~600-year-old silicic lava, Obsidian Dome, California, USA. This study focuses on the structural geology of the upper surface mapping textural-structural relationships onto high-resolution (<10 cm^2/pixel) orthorectified color base maps. We find that the upper surface is characterized by small (<1 m) mode-I tensile fractures which grow and initiate new cracks which link together to form larger tensile fractures (1-5 m) which penetrate deeper into the lava. We record ornamentations on these fracture surfaces which allow snapshot views into the rheological and outgassing conditions during the lava's effusion. The largest fractures develop during single, large fracture events in the final stages of the lava's emplacement. Ornamentations preserved on fractured surfaces record degassing and explosive fragmentation away from the vent throughout the lava's emplacement suggesting explosive activity was occurring during the effusive emplacement.

1.0 INTRODUCTION

Extrusive silicic rocks are common throughout the geological record from a range of tectonic environments and are important hosts of epithermal mineralization. Whereas lava domes are ubiquitous at intermediate and silicic volcanoes (e.g., Mount St. Helens, USA 1980-1986; 2004-2008) and are the subject of numerous studies (e.g., Fink et al., 1990; Sparks et al., 2000; Pallister et al., 2013), direct observations of active silicic lava flows didn't occur until two Chilean eruptions, Chaitén and Cordon Caulle, in 2008 and 2011, respectively (Lara, 2009; Schipper et al., 2013). Lavas *flows* differ in that they often occur on the flanks of volcanoes (e.g., Medicine Lake volcano, California, USA) where the lava is not restricted to a deep crater and with sufficient magma supply develops to a unidirectional lava flow (a 'coulee'; e.g., the Chao dacite, Chile (de Silva et al., 1994); Big Obsidian Flow, Newberry volcano, USA (Donnelly-Nolan et al., 2011)). They also form on low-relief caldera floors where they can spread radially (e.g., Deadman Dome, California, USA; Sampson & Cameron, 1987). In both cases, silicic lava flows develop characteristic surface features such as ogives and pervasive fracturing (e.g., Andrews et al., 2021). In the absence of observed emplacement events, most studies are of ancient lavas.

This paper documents a field-based study at Obsidian Dome, California, USA (Fig. 1), to investigate the emplacement of silicic lavas through the lens of brittle deformation of the upper surface and margins. We attempt to constrain the relative timings, mechanisms, and conditions under which deformation occurred through a combination of textural and structural observations. Specifically, this study examines how different fracture types and sizes relate to one another, and whether they form a single continuous deformation process, or if they represent different processes operating at different times. In so doing, we document evidence of synchronous localized explosive processes intimately linked to the deformation.

2.0 SILICIC LAVA EMPLACEMENT MECHANISMS

Unlike intermediate composition lava domes where there are several active worldwide at any one time, most of what is known about the dynamics of rhyolitic and rhyodacitic lava flows must be inferred from prehistoric examples. Herein, we use the term 'lava' for pre-historic examples and reserve 'lava flows' for active flows. We do this to (1) avoid confusion between

active and pre-historic extrusions, and (2) because it is difficult to distinguish lava domes and lava flows in the geological record, but both are coherent lavas.

2.1 Observations at Active Silicic Lavas

The 2011-12 eruption of Cordón Caulle, Chile, was the first large volume, crystal-poor (i.e., obsidian), rhyolite lava emplacement observed throughout the entire eruptive event. It is important because it (1) featured unexpected ranges of emplacement processes (endogenous vs. exogenous; Farquharson et al., 2015; Magnall et al., 2017) and advance-limiting modes (Castruccio et al., 2013) acting contemporaneously in different parts of the lava flow, and (2) the advance continued for ~8 months after new magma ceased being erupted from the vent (Tuffen et al., 2013). Additionally, contemporaneous explosive eruptions from the advancing lava accompanied effusion ('hybrid activity'; Schipper et al., 2013; Castro et al, 2014, 2016; Castro & Walter, 2021). Hybrid activity is attributed to out-gassing through fracture networks (tuffisites) within and above the shallow conduit during the lava's effusion (Castro et al., 2014; Wadsworth et al., 2020). These observations challenge the theory ("permeable foam model") that rhyolitic lavas are degassed upon effusion and the transition into a dense glassy lava occurs by collapsing of the bubble and pore space (permeable network) (Eichelberger et al., 1986). Experimental studies demonstrate that even high porosity foams cannot support effective permeability without fracturing (Ryan et al., 2019). The outgassing pathways are sustainable until viscous relaxation closes the fracture pathways (Heap et al., 2019; Unwin et al., 2021).

2.2 Insights from Studies of Ancient Silicic Lavas

Holocene, obsidian lavas in California and Oregon, USA (e.g., Fink, 1983; Fink & Anderson, 2017), are the most comprehensively studied; additional important Late Pleistocene and Holocene examples exist in the Aeolian Islands (Italy), the Chilean Andes, Iceland, Japan, and New Zealand (e.g., Stevenson et al., 1994; Maeno & Taniguchi, 2006; Lara, 2009; Tuffen & Castro, 2009; Pallister et al., 2013; Tuffen et al., 2013; Bullock et al., 2018). Investigations of these lavas have yielded important insights into silicic lava emplacement mechanisms through detailed studies of (1) morphology (e.g., Fink, 1980a; Ramsey & Fink, 1999; Deardorff et al., 2019; Leggett et al., 2020), (2) lithology and structure (e.g., Manley & Fink, 1987; Smith & Houston, 1994; Smith, 2002; Andrews et al., 2021), and (3) microstructure and petrofabrics (e.g., Castro et al., 2002; Cañón-Tapia & Castro, 2004; Rust & Cashman, 2003; Manga et al., 2018). These observations and quantitative data provide inspiration and constraints for many

informative numerical and analog simulations (e.g., Fink & Griffiths, 1990, 1992, 1998; Merle, 1998; Lescinsky & Merle, 2005; Farrell et al., 2018; Kenderes, 2021).

2.2.1 Silicic Lava Lithostratigraphy

Despite most silicic lavas having only a simple, single chemical composition, most if not all, display two or more distinct lithofacies; that is, physically and texturally distinctive rock types. Although the lithofacies naming schemes vary between studies (Fink, 1980a; 1983; Manley & Fink, 1987; Stevenson et al., 1994; Maeno & Taniguchi, 2005; Andrews et al., 2021), the typical lithostratigraphic units identified are: (1) microcrystalline rhyolite (can be devitrified or spherulitic; bulk density ~ 2,100 kg/m^3); (2) finely vesicular pumice (FVP); (3) coarsely vesicular pumice (CVP); and (4) avesicular obsidian (bulk density >2,000 kg/m^3).

Fink (1983)'s seminal study of the Big and Little Glass Mountain lavas (~1.2 ka) at Medicine Lake volcano, California, USA, described three lithofacies (FVP, CVP, and avesicular obsidian) on the upper surfaces and at the distal margins. Furthermore, the extensive talus at the margins was inferred to obscure a laterally continuous layer of avesicular obsidian and CVP, underlain by a basal breccia. Scientific drilling at Obsidian Dome (Eichelberger et al., 1984; 1985) and Banco Bonito (~130 ka), Valles Calera, New Mexico, USA, revealed the same general lithostratigraphy (Fink & Manley, 1987; Manley & Fink, 1987; Fig. 2), and this stratigraphy was inferred to be laterally continuous within Obsidian Dome where it was correlated between boreholes near the vent and the margin (Fink & Manley, 1987; Manley & Fink, 1987; Fig. 2). Several drill cores from the Takanoobane rhyolite (~51 ka) of SW Japan (Furukawa & Uno, 2015) reveal alternating layers of CVP and obsidian in the uppermost 20 meters, with the AVL2 core resembling the observed stratigraphy of the RDO-2A core at Obsidian Dome (Fig. 2).

Similar lithofacies have been identified at silicic lavas in New Zealand (Ben Lomond rhyolite, ~100 ka; Stevenson et al., 1994) and at Showa Iwo-jima, Japan (88 years-old; Maeno & Taniguchi, 2005) where the presence of a basal breccia overlain by a rhyolite core grading upwards into obsidian is ubiquitous. Importantly, although Maeno and Taniguchi (2005) described extensive CVP at the upper surface of Showa Iwo-jima, nowhere has laterally continuous CVP at depth been demonstrated conclusively (cf. Fink, 1983), and CVP is absent from many lavas including the Ben Lomond lava (Fig. 2; Stevenson et al., 1994) and lavas in the Landmannalaugar area, Iceland (e.g., Wilson et al., 2007).

Features indicative of hybrid explosive-effusive activity identified at Chaitén and Cordón Caulle, Chile such as expansive pyroclastic ridges, tuffisite veins, and glassy to pumiceous ballistic bombs are described at Big Glass Mountain, California, USA (Castro & Walter, 2021). There, obsidian pyroclasts display similar hydrous geochemical signatures to pyroclasts from the hybrid Chaitén eruption.

2.2.2 Structural Observations

The upper surfaces of silicic lavas are dominated by a carapace of superficially erratically placed, angular boulders of avesicular obsidian and FVP (e.g., Anderson et al., 1998; Plaut et al., 2004; Leggett et al., 2020). Immediately beneath the boulders, the surface of the coherent lava is in situ FVP and avesicular obsidian that is ubiquitously disrupted by tensile fractures, the largest of which provide windows into the lava's interior. Crease structures (Anderson & Fink, 1992) are large, splayed-open fractures exposing deep into the lava, unique to silicic lavas and domes (e.g., Mount St. Helens, USA, 1980-86). Although better exposed elsewhere (e.g., Medicine Lake volcano, USA), several crease structures are present at Obsidian Dome, including ones that have been partially quarried.

Superimposed on this foundation are ~15 – 20 m-amplitude ridges and troughs that are regularly spaced, laterally continuous, arcuate (Fink, 1980b), and usually parallel to the nearest flow margin and perpendicular to the inferred flow direction. Ridges are antiformal and expose 'deeper' lithofacies like avesicular obsidian under a thin or non-existent carapace of FVP boulders. Troughs are synformal and are filled by the thick FVP boulder carapace. The ridges and troughs are termed ogives and are commonly interpreted as buckle-style folds (Fink, 1980a; Fink, 1980b; Fink, 1983; Anderson & Fink, 1992; Fink & Anderson, 2017); however, Andrews et al. (2021) demonstrated that ogives form by dilation of decimeter-scale circumferential fracture sets that form horst (ridge) and graben (trough) morphologies.

Herein we use 'brittle-ductile' to refer to deformation processes that initiated in the brittle regime (i.e., exceeding the tensile strength of the rock) and then experienced ductile flow (i.e., plastic flow where melt viscosity is the dominant physical control on rheology). The brittle-ductile transition is a dynamic boundary separating the brittle and ductile regimes at any given time and set of conditions and can be thought of as the manifestation of the silicate glass transition (T_g). The glass transition temperature (Dingwell, 1996) is a dynamic variable and strongly influenced by melt viscosity, melt composition, temperature, strain rate, and dissolved

volatile composition, primarily. Generally, silicate melts require higher temperatures and dissolved water contents, and lower strain rates to have a low effective viscosity and to flow ductilely, than to have a higher viscosity and to deform brittlely. Moreover, higher silica contents correlate with higher viscosity (Dingwell, 1996). Therefore, the location of the brittle-ductile transition is difficult to predict without being able to examine the results of the deformation (i.e., fractures).

2.2.3 Microstructures and Petrofabrics

Extensive research has been conducted on the origins and implications of flow banding (changes in crystallinity, vesicularity, or fragmentation and annealing of tuffisite) in silicic lavas including Obsidian Dome (e.g., Castro, 2005; Gonnerman & Manga, 2005; Tuffen et al., 2013). However, for the purpose of this research, and in the absence of evidence to the contrary, we assume that all flow bands are developed before or during effusion at the vent and are passive layers (i.e., weak) that faithfully record ductile deformation during lateral emplacement. Flow bands are typically steep at the upper surface and sub-horizontal elsewhere (Smith, 1996). Andrews et al. (2021) inferred that fracturing and tilting at the upper surface associated with ogives disrupted the flow banding that would otherwise have been sub-horizontal. Sub-horizontal flow banding from outcrops (e.g., Smith, 1996) and analog experiments (e.g., Merle, 1998) is interpreted to result from ductile, gravitational loading (maximum principal stress (σ_1) is vertical) and sub-horizontal (i.e., ground surface parallel) radial spreading (σ_2 and σ_3) where $\sigma_1 > \sigma_2 = \sigma_3$. This is coaxial or 'pure' shear strain. Coaxial, ductile deformation in obsidian is also recorded in the preferred orientations of microlite crystals (Castro et al., 2002; Castro & Mercer, 2004; Manga et al., 2018), vesicles (Rust et al., 2003), and magnetic fabrics (Cañón-Tapia & Castro, 2004).

2.3 This Study

Taken together, the structures observed at silicic lavas record a prolonged history of extensional, coaxial deformation: brittle and brittle-ductile at the upper surface, and ductile in the interior. However, the body of existing literature is heavily weighted towards inferences about the entire flow's behavior based on its large-scale morphology (e.g., Fink & Griffiths, 1998; Cioni & Funedda, 2005; Bullock et al., 2018; Farrell et al., 2018; Leggett et al., 2020). Few studies are directed at the upper surfaces (*cf.* Fink, 1980b; 1983; Andrews et al., 2021) and those

that do differ significantly in their interpretations (i.e., ogives are or are not folds). Therefore, *this study* focuses exclusively on the architecture and structural geology of the upper surface at Obsidian Dome, California, USA. It examines: a possible continuum of deformation, recorded in the tensile fractures ubiquitous to silicic lavas, and fracture facilitated out-gassing throughout the entirety of lava emplacement.

2.3.1 Obsidian Dome

Obsidian Dome is part of the Holocene Inyo volcanic chain nestled on the eastern side of the Sierra Nevada Mountains, eastern California, USA, in the Long Valley volcanic region. The dome sits approximately 1.5 km north of the Pleistocene Long Valley caldera margin (Fig. 1). The Inyo chain includes silicic lavas and phreatic craters above a N-S trending dike zone (Bailey, 1976; Fink, 1985; Fink & Pollard1985; Miller, 1985; Reches & Fink, 1988). Obsidian Dome is one of the three youngest domes (~650-550 years; Wood, 1977; Miller, 1985) along with Glass Creek dome and Deadman Dome, and all three are coeval with extensive pumice and ash tephra deposits that blanket the surrounding landscape. The ~600-year-old lavas and their feeder dike share different proportions of two geochemically distinct rhyolitic magmas (Sampson & Cameron, 1987). At Obsidian Dome the low-silica (~70 wt%), microcrystalline endmember is restricted to the central peak region over the inferred vent whereas the high-silica (73.5 wt%) endmember is ubiquitous at the margins (Vogel et al., 1989). Whether or not these geochemical and textural differences are sufficient to influence the emplacement of the lava is uncertain.

Obsidian Dome is a pancake-shaped silicic lava, covering an area of about 2 km^2, and has an estimated eruptive volume of 0.1 km^3 (Eichelberger et al., 1986). The dome slopes down very gradually to the east and south and has a central peak reaching ~2,608 m above sea level and about ~2,472 m above the base at the lowest elevation, eastern margin. The thickness of the flow-margins is variable between a maximum thickness of ~60 m in the northeast where the lava flowed into a paleovalley and ~20 m along the southeastern margin.

3.0 METHODS

Textural and structural data were collected over several extended visits to Obsidian Dome. In addition, <10 cm^2/pixel-resolution, structure-from-motion photogrammetric models were constructed from images collected from a drone and were used to generate digital terrain models and orthorectified color base maps. Structural and textural data, including field

photographs and samples, were gathered from the upper surface using *FieldMove* (Petroleum Experts, 2020) digital geological mapping software on ruggedized Apple *iPad 4 mini* tablets (Hama et al., 2014; Allmendinger et al., 2017).

Most of the data presented here are structural measurements collected in the field and are displayed in a series of large-scale textural-structural maps. The exceptionally rough surfaces of silicic lavas (Plaut et al., 2004) make them slow and hazardous to traverse, and lack enough relief or distinctive features to support navigation using the available 1:24,000 scale topographic maps or 1 m-resolution lidar-derived digital terrain models (DTMs). Therefore, we developed a workflow to produce color, orthorectified airphotos and accompanying DTMs of sites of interest using a small unoccupied aerial vehicle (sUAS) and then digitally mapped structural features onto those base images.

We collected GPS-located, overlapping, plan-view photographs along raster flight paths with a *DJI Phantom 4 Advanced* sUAS, following the approach of Leggett et al. (2020). This is a consumer-grade sUAS with a 20-megapixel, color, gimbal-mounted camera, and is controlled from an *Apple iPad 4 mini*. Flight paths were planned and optimized for photography using *Dronedeploy* (Drone Deploy, 2020) and *Drones Made Easy's Map Pilot* applications for *Apple iOS*, usually with fixed flight altitudes between 30 m and 50 m above the ground and designed to provide 85% overlap between adjacent images along and across flightlines. Flights were typically conducted in the late morning to take advantage of lower wind speeds and to maintain similar bright, high-angle lighting between missions.

DTMs and orthorectified airphotos were constructed by structure-from-motion (SfM) photogrammetry (e.g., Westoby et al., 2012) in *Agisoft Metashape Professional v.1.5* (Agisoft, 2019) following the approach of Leggett et al. (2020). The dense point clouds for each site returned root-mean-square errors of ±0.1 m and generated DTMs with ~5 cm-resolution. The resulting orthorectified airphotos have resolutions of ~2 - 5 cm^2 / pixel.

We mapped on to ruggedized iPad 4 mini tablets with *Midland Valley Exploration's FieldMOVE* (Petroleum Experts, 2020) installed. Additional structural measurements were collected using cell phones (*Apple iPhone 6* and *7*; *Google Android*-powered *LG X*) with *FieldMOVE Clino* installed. Most software using GPS location produce horizontal errors of 5 to 10 m, but this is mitigated by manually correcting the measurement location against the high-

resolution orthorectified base image (e.g., Allmendinger et al., 2017). Typically, *iPhone* smartphones running *FieldMOVE Clino* produce better data than *Android*-powered units (e.g., Allmendinger et al., 2017; Novakova & Pavlis, 2017; 2019; Trede et al., 2019). Comparisons of *FieldMOVE* (*iPad 2*) and *FieldMOVE Clino* (*iPhones 7* and *8*) against handheld compass-clinometers identify a mean error of ±0.25 ° in dip angle (Hama et al., 2014) and <10 ° – 23 ° in strike azimuth (Hama et al., 2014; Allmendinger et al.,2017); the azimuth value is known to be very susceptible to disturbance of the smartphone's built-in magnetometer (e.g., powerlines, batteries, etc.). We recalibrated the *iPad 4 minis* and *iPhones* regularly, occasionally confirmed strike and dip measurements with handheld compass-clinometers, and manually adjusted measurement locations to the base image.

Every structural measurement, sample, and image was recorded with spatial metadata. Using Google Earth all the *.kmz* files from each *FieldMOVE* project were initially assessed for accuracy of locations and large-scale structural patterns. The *.kmz* files contain all structural information, locations and orientations of all field photos taken, making them a powerful tool in Google Earth. Original plane.csv files from *FieldMOVE* with all planar structural measurements and locations and were imported into QGIS 3.10 for further analyses using the orthorectified base images previously generated in QGIS 3.10 as well. Data and orthorectified images were combined to create local structural maps across Obsidian Dome. Each structural map is accompanied by several stereonets displaying the attitude of the different planar features and lineations measured. All strike and dip information were compiled and analyzed using *Stereonet 11* (Allmendinger et al., 2011).

4.0 OBSERVATIONS AND DATA

4.1 Major Lithofacies

Herein we use the term *lithofacies* to refer to different textural forms and emphasize that different lithofacies readily grade into one another. Three volumetrically significant rhyolite lithofacies are recognized at Obsidian Dome. By different proportions and sizes of vesicles they are: avesicular obsidian, finely vesicular pumice (FVP), and coarsely vesicular pumice (CVP; Fink, 1983). A fourth microcrystalline rhyolite lithofacies is present directly over the vent and at depth recorded in the drill cores. It appears to be restricted to discrete flow bands within obsidian and is associated with neither FVP nor CVP.

4.1.1 Avesicular Obsidian

The avesicular obsidian is defined as variably flow banded, black, 95 % glass groundmass with small (≤2 mm-diameter), albite and sanidine, and sparse clinopyroxene, amphibole, and Fe-Ti oxide phenocrysts (Vogel et al., 1989), and sparse quartz spherulites. It is the same as the 'dense obsidian' described by Manley & Fink (1987) from the Obsidian Dome drill cores as well as outcrops at many other silicic lavas (e.g., Fig. 2). The obsidian is typically avesicular with measured porosities of ~1 – 4%, with ~0.15 to 0.22 wt.% H_2O and bulk density of ~2,300 kg/m^3 (Andrews et al., 2021). Where it is transitional with CVP, or in low-strain zones (e.g., fold hinges, dilational shear bands), large (≥1 mm-diameter), isolated vesicles form a scoriaceous texture (Fig. 3A). Scoriaceous obsidian is typically very strongly flow banded with an abundance of ductile and brittle deformation structures including: intrafolial isoclinal recumbent folds, boudins of avesicular obsidian and microcrystalline rhyolite (e.g., Fig. 3C), rotated crystals, faults, and tension gashes.

Obsidian is best exposed at Obsidian Dome around the margins of the lava, in surrounding talus, and in small, discrete masses (≤10 m-across) on the upper surface. It is typically massive at the margins and forms semi-continuous horizons separated by lenses of autobreccia (Fig. 4A-B). Obsidian on the upper surface grades laterally and upwards into the extensive carapace of FVP where faint flow banding becomes more pronounced, and the rock becomes lighter gray in color.

4.1.2 Finely Vesicular Pumice (FVP)

The upper surface of Obsidian Dome is dominated by decameter-scale angular blocks, boulders, pinnacles, and randomly rotated slabs of FVP (Fig. 3D). FVP is light beige to dark gray in color, flow banded, and contains ubiquitous small (≤0.5 mm-diameter), spherical vesicles (Fig. 3E). The measured porosities of FVP are ~30 – 40% with ~0.23 wt.% H_2O, and its bulk density is ~1,670 – 1,750 kg/m^3 (Andrews et al., 2021).

4.1.3 Coarsely Vesicular Pumice (CVP)

CVP has >40% vesicles and is a dark olive-green color with large (0.1-1 cm-diameter), often stretched and interconnected, vesicles (Fig. 3B; Fink, 1983; Manley & Fink, 1987; Fink et al., 1992). CVP has a porosity of 20 – 80% with ~ 0.14 wt.% H_2O, and a bulk density of ≤ 1,000 kg/m^3 (Andrews et al., 2021). The CVP makes up ~1% of the surface of Obsidian Dome and is

concentrated around the WSW and NW margins of the dome as positive topographic features around crease structures (Fig. 3D).

4.1.4 Lithostratigraphy at Obsidian Dome

We did not identify laterally continuous CVP layers at the flow-margins of Obsidian Dome as proposed in Fink (1983) and related models, regardless of how thick the lava was. Instead, the observed lithostratigraphy at the flow-margins of Obsidian Dome is, from the base upwards, talus obscuring the bottom ~10 to 30 m of the front followed by prominent, massive layers of obsidian (~2 to 10 m-thick; Fig. 4A) which are often interbedded with breccia, CVP, or microcrystalline rhyolite (Fig. 4B), and capped by a veneer of blocky FVP blocks (~5 m-thick).

4.2 Fractures

The different lithofacies described at Obsidian Dome are disrupted by a plethora of different-sized fractures associated with distinctive outcrop morphologies. Herein, we use the word 'fracture' purely descriptively and not genetically. A fracture is a planar or curviplanar dislocation of measurable surface area (i.e., >10 cm^2) and orientation (i.e., dip and strike) that is superimposed upon the original flow banding or surface. A fracture may be concordant with flow banding, or it may be discordant, and it may have measurable displacement across it (i.e., dilation; mode 1), along it (i.e., a fault; modes 2 or 3), or it may have neither and be of unknown mode. A fracture terminates at a tip point (in two dimensions) or a tip line (in three dimensions) and is not infinite. Finally, a fracture may be 'healed' such that it is not a mechanical weakness or open. We describe the fractures in order of increasing size (i.e., length-width-depth). We describe four classes of planar features based upon scale, morphology, and their relationships to the lithofacies and other features (Table 1). The classes are based on a qualitative assessment and form a continuum.

4.2.1 Cracks

The smallest and most ubiquitous fractures on the surface of the lava are **cracks**. They crosscut all the lithofacies but are most prevalent in the FVP where they are irregular or very weakly curviplanar. Cracks in CVP are irregular planes and those in avesicular obsidian can be irregular planar or strongly curviplanar (e.g., Fig. 4C). Everywhere they are ≤1 m in length and ≤1 m deep (Fig. 5A) and are usually open and dilated (≤20 cm-across) widening upwards. Cracks do not show plane-parallel displacement. Cracks typically occur in orthogonal sets of

intersecting vertical fractures, mutually perpendicular to sub-horizontal flow banding (Fig. 5B), lithological layering, and the upper surface (Fig. 5C). Cracks can incorporate different surface ornamentations (see below) and are themselves cross-cut by larger fractures (Fig. 4C). Only cracks are observed to be closed and healed, and only when formed in obsidian (e.g., Andrews et al. (2021)'s figure 6C).

4.2.2 Clefts

Clefts are larger than cracks with lengths of 2 to 10 m, depths of 1 to 5 m, and widths of 0.5 to 3 m, large enough to allow a person to stand within them (Fig. 6A). Cracks cross-cut and are cut by clefts. Clefts occur in all lithofacies but are best developed in avesicular obsidian (Fig. 6B) where they typically have very irregular, although generally planar, sides.

4.2.3 Crevasses

Crevasses are typically larger still but only occur in the FVP and avesicular obsidian lithofacies where they are characterized by very smooth planar margins symmetrical about a near-vertical axis (Fig. 7). Fracture depths of ≥5 m, lengths of 10 – 20 m, and widths (2 – 5 m) define crevasses; they are noteable for the upwelling of cool air as you stand atop or within them suggesting that they penetrate deep into the lava. Crevasses are the primary fracture class that define the margins of ogive structures, and therefore play a larger role in defining the surface physiography than clefts or cracks. Their surfaces are rarely, if ever, ornamented and instead nucleate later perpendicular cracks (Fig. 7A-B). Crevasses narrow and terminate towards tips buried under the FVP carapace but unlike clefts, the crevasses are empty of FVP boulders (e.g., Fig. 7C).

4.2.4 Crease Structures

The largest and least common type of fractures are crease structures that only occur in CVP and in five locations at Obsidian Dome (Fig. 8A) where the lava is estimated to be thickest (50 - 60 m). Aerial images display the stark color and textural contrast between the smooth, expansive crease structure surface in CVP and the surrounding FVP blocks (Fig. 8B). Although pumice mining operations have altered several crease structures, their general size and orientation are preserved, and show that the main fracture is not systematically orientated relative to the nearest flow fronts (Fig. 8A). Nor do the crease structures define the ogives, rather where they occur, they overprint the local ogive pattern.

The crease structures are characterized by (1) long fracture lengths (>10 m; Fig. 8B), (2) large fracture widths (>2 m), and (3) their flared shape where their very smooth curviplanar surfaces routinely rotate from near vertical at the base to sub-horizontal (Fig 8C-D). Vertical to sub-horizontal flow banding is often intersected by the curviplanar surfaces (Fig. 8E) with identical patterns, for example intrafolial folds, exposed on sides. The curviplanar surfaces of crease structures at other lavas display striations (e.g., Fink, 1980b; Anderson & Fink, 1992) but no striations are found on any of the crease structures at Obsidian Dome. The crease structure fracture surfaces are penetrated by cracks but not clefts or crevasses and are not ornamented.

4.3 Fracture Ornamentation

Cracks and clefts are often associated with fracture surface ornamentations (Table 1). Four very different types of ornamentation are identified: red oxidized surfaces, red leathery surfaces, pink tessellated surfaces, and welded breccias. To the best of our knowledge this is the first description of fracture ornamentations on the surface of silicic lavas.

4.3.1 Red Surfaces

Rust-red surfaces generally occur as thin (≤0.5 mm) veneers coating crack and cleft surfaces in any of the different lithofacies (e.g., Fig. 4C), and are very common on FVP and obsidian blocks in the carapace where they typically cover one side only. The deepest red colors occur at the flow-margins and are associated with avesicular obsidian interlayered with breccia (Fig. 4B). Many red surfaces are cut by later, smaller cracks that expose the original lithology color beneath the veneer (Fig. 4C).

4.3.2 Leathery Surfaces

Red ‘leathery’ surfaces on cracks and clefts are also thin veneers cut by later, smaller cracks but are distinctly wrinkled and contorted, and occur on all lithofacies (Fig. 9A). Different red leathery surfaces can exhibit a variety of small-scale morphologies. In some cases, there are two perpendicular sets of wrinkles where the larger are parallel to the underlying flow banding and the smaller and later wrinkles are discordant and sub-horizontal (e.g., Fig. 9A). Some wrinkles are demonstrably differential extrusions of certain flow bands across an initially planar fracture (e.g., Andrews et al. (2021)’s figure 6B).

4.3.3 Pink Tessellated Surfaces

Pink tessellated surfaces are thin (≤0.1 to 5 mm-thick) veneers of pink tuff annealed to the fracture (Fig. 9B). They occur in all lithofacies but are most readily identified in CVP where it can be concordant or discordant with flow banding. The thin layers are nearly always stretched to form polygonal wafers (tesserae) with separation of 1 – 5 mm (Fig. 9C).

4.3.4 Welded Breccias

Oxidized lapilli- to block-sized, angular to sub-rounded, obsidian clasts fill many otherwise open cracks and, especially clefts at the upper surface of Obsidian Dome. The breccias are typically tack-welded together and to the fracture walls (e.g., Fig. 4C) as well as strongly flattened and welded in narrow fractures within obsidian. The lapilli and blocks are occasionally nearly in situ and jigsaw-fit (e.g., Fig. 10A) where they are not discolored and are very angular; however, in most cases the clasts are somewhat rounded and stained with an orange veneer (Fig. 10B) and appear to be allochthonous. Where tack-welded, a finer grained orange matrix is composed of ash-sized clasts that are sub-rounded. Similar tack-welded breccias form tall pillars at the margins of the lava's upper surface (Fig. 10C).

5.0 DISCUSSION

The upper surfaces of Obsidian Dome and all other silicic lavas and domes are characterized by rough, uneven, block-strewn, irregular masses of pumice and obsidian (e.g., Anderson et al., 1998; Plaut et al., 2004; Leggett et al., 2020). Although the carapace buries much of the coherent lava, it and how it formed are important to understanding the entire lava emplacement process. This is because, unlike typical sedimentary breccias or even the marginal talus slopes at Obsidian Dome, the clasts in the upper carapace cannot have been transported very far, if at all, from where they originated (i.e. clasts are more or less in situ). Moreover, the clasts have not been liberated from the coherent lava by many of the typical forms of erosion and mechanical weathering that interfere with rocks; for example, erosion by water or ice, or disruption by root-wedging. We are confident of this because (1) Obsidian Dome is post-glacial, (2) it has no surface drainage network and allows for no standing water, and (3) it is almost completely devoid of vegetation. Thermal expansion-contraction coupled with ice-wedging are plausible mechanisms to generate some fractures post-emplacement; however, they are much more likely to accentuate pre-existing (i.e. syn-emplacement) fractures that rainwater and

snowmelt can exploit. With these caveats in mind, we discuss how the fractures, and their ornamentations inform on lava emplacement processes.

5.1 Tensile Fracturing

5.1.1 Cracks and Clefts

Cracks and clefts are mode 1 tensile fractures formed by wholly brittle (FVP, obsidian, and CVP; Fig. 6) or brittle-ductile (obsidian only; Fig. 5B) deformation. They form perpendicular to a pre-existing surface (i.e., parallel to σ_1), propagate in the σ_2 direction and dilate in the σ_3 direction (i.e., plane strain); where orthogonal fracture sets σ_2 and σ_3 are approximately equal (i.e., coaxial shear strain). The original surface that is fractured may be the top of the coherent lava (Fig. 5A) or be part of a larger fracture class. Stresses produced during the vesiculation of silicate melt to form FVP exceed the tensile strength of the melt as it becomes less hydrous (Andrews et al., 2021). Therefore, many of the smallest cracks, especially orthogonal sets and those superimposed on crevasse and crease structure faces, are probably initiated in part by volume increase associated with the formation of FVP at the upper surface.

We infer that the irregular nature of these fractures is caused by the linking of many small cracks into fewer, larger cracks and clefts. Therefore, clefts develop from growing and linking of parallel-striking cracks under the same stress state. Linkage of smaller co-striking fractures is usually achieved when opposing tips propagate past each other and then ‘hook’ through the intervening rock barrier (e.g., Lamarche et al., 2018); this is plausible at Obsidian Dome where the fractured material is mechanically isotropic.

The presence of weakly curviplanar cracks and healed cracks in obsidian, and the formation of leathery surfaces on cracks and clefts in obsidian strongly suggests that the deformation in obsidian layers was brittle-ductile. In this scenario cracks initiate in the overlying FVP by purely brittle tensile stretching and propagate downwards into melt that is above T_g (i.e., capable of viscous flow). We are confident that fractures initiate in the FVP because they are the most dilated (i.e., furthest from the tip) at the surface and (2) the tensile strength of FVP (~1.5 MPa; Andrews et al., 2021) is less than that of the low-porosity obsidian (Heap et al., 2021). There, the fracture-tip propagation is fast enough to effect a high shear strain, and locally and temporally cause the tip region of the viscous melt through the glass transition into the rigid (i.e., brittle deformation) regime causing brittle failure (e.g., Huang & Hassager, 2017). This is

somewhat analogous (albeit in reverse) to the production of pyroclasts by fragmentation of a rapidly expanding melt (e.g., Cordonnier et al., 2012; Heap et al., 2016) where the deformation rate is faster than the viscous relaxation rate (i.e., Deborah number > 1; Wadsworth et al., 2018). Upon release of the tensile stress the strain rate becomes zero and the volume returns across T_g to the ductile regime allowing the margins of the fracture to relax viscously and close together (e.g., Dingwell & Webb, 1990; Wadsworth et al., 2020). The presence of leathery surfaces on cracks and clefts in obsidian strongly suggests that despite being at elevated temperature (i.e., above T_g), some flow bands experienced more viscous relaxation than others, and moreover, these different bands alternate frequently. However, we see no evidence that they fractured differently. Minor but significant differences in dissolved water content probably best explain the different responses under the same temperature and stress conditions. DeGroat-Nelson et al. (2001) and Andrews et al. (2021) measured dissolved water contents in obsidian ranging from 0.13 – 0.22 wt. %. Even though this range is small (~0.1 wt. %) dissolved water has the greatest effect on melt viscosity when at the lowest concentrations (Dingwell, 1996; Romine & Whittington, 2015) and therefore, very small differences in water content between adjacent flow bands may yield very different responses. If this is correct, it implies that the flow banding in the otherwise homogeneous obsidian formed from a more hydrous and less hydrous component (e.g., Seaman et al., 2009).

5.1.2 Crevasses and Crease Structures

Crevasses and crease structures are different from the smaller fracture classes because they are characteristically smooth and are not ornamented. Although they are both often penetrated by cracks and clefts, the surfaces of crevasses and crease structures are notably continuous and simple. Crevasses and crease structures share some important features: (1) they both appear to 'push' through the FVP boulder carapace (e.g., Fig 7A) and do not have significant numbers of boulders resting inside them, and (2) both share having vertical σ_1 and sub-horizontal σ_2 and σ_3, where $\sigma_2 > \sigma_3$ (i.e., plane strain). However, the key difference between crevasses and crease structures is whether or not they are curviplanar. Crevasses are planar and exhibit a simple V-shaped cross-sectional profile (e.g., Fig. 7B); in contrast, crease structures are very curviplanar (Fig. 8C: Anderson & Fink, 1992). We interpret the crevasses and crease structures to be end-members on a continuum when the rheology allows for viscous relaxation (Wadsworth et al., 2018).

In this model, a single, large magnitude, tensile failure event, possibly initiated in the FVP, forms a single, large crevasse fracture and a maximum of 2 – 5 m of dilation. We infer a single fracturing event because of the absence of striations (e.g., Anderson & Fink, 1992). *If* the fracture penetrates to a depth that is below T_g during the same or a subsequent stretching event, there is the potential for viscous relaxation through horizontal flow (where σ_3 switches to become σ_1) to (1) partially close the fracture forming a curviplanar surface, and (2) to rotate the rigid ceiling upwards forming a crease structure (Fig. 11). To what degree this process may depressurize the $>T_g$ lava interior and induce spontaneous vesiculation, possibly forming CVP, is the topic of a future paper.

5.1.3 Relative Timing and Fracture Progression

Cracks form throughout the emplacement process, probably for as long as FVP forms and for the duration of flow. In both cases the tensile strength of the FVP is so low as to readily fracture at even very low differential stresses (<5 MPa). Once formed, cracks are permanent mechanical weaknesses (unless healed by welding) that are exploited by continued stretching (Byerlee's Rule; Byerlee, 1978). As cracks continue to grow and new cracks initiate, they link together to form clefts that penetrate deeper into the lava. We consider this the basic mode by which the upper surface, FVP, and top of the avesicular obsidian deform.

Superimposed upon this foundation, crevasses and crease structures form locally where the stress and rheological conditions permit and displace earlier formed cracks and clefts. Crease structures, and to a lesser degree crevasses, are located over the thickest, and presumably slowest cooling, parts of the lava (Kenderes, 2021). Taken together, this implies that they form relatively late in the emplacement of any given area of the upper surface. Both penetrate thick sections of lava into the silicate melt as single, smooth planes suggesting that a relatively strong (i.e., high yield strength) lid had to have formed before they initiated. The different sizes of crevasses and crease structures can be explained by their age relative to the gradual cooling and thickening of the lid (e.g., Park & Iversen, 1984; Stasiuk et al., 1993). In this scenario, ogives defined by crevasses form relatively late when the lid has reached a thickness 0.8 – 1.2 times the ogive spacing (Bai & Pollard, 2000). At Obsidian Dome this would equate to crevasses forming when the lid was ~8 – 12 m-thick. The non-systematic orientations of crease structures (Fig. 8A) support an interpretation where tensile stresses were independent of stretching at the margins

(i.e., the gravitational spreading of the flow) and instead represent local stress heterogeneities (Fink, 1983).

In summary, cracks initiate as FVP forms at the upper surface, and then cracks develop into clefts and new cracks form, as long as FVP is under tension. Cracks are probably the first and last fracture types to form. Crevasses and crease structures only form late in the emplacement of any given area of the upper surface when a relatively competent layer has formed and grown to ~10 m-thickness. Under these conditions older cracks and clefts are probably either healed or too shallow to prevent the build-up of stress in the competent layer. The lid fails in a single event when a high enough stress overcomes the great tensile strength; in crevasses the stress is due to continued spreading of the lava whereas in crease structures it is probably due to local heterogeneities (Fig. 11).

5.1.4 Rheological Constraints

Andrews et al. (2021) determined that T_g in this case ranges between 680 °C, 650 °C, and 614 °C for FVP, CVP, and avesicular obsidian, respectively. Both FVP and CVP form by vesiculation of silicate melt and initiate under ductile conditions and above T_g but then evolve very differently (Fink, 1983). In the case of FVP, the thermal gradient is very high, and it would cool below T_g in ~16 - 10 hours (Andrews et al., 2021). However, the tensile stresses from initial volume expansion readily exceed the tensile strength of the increasingly dry and fragile FVP carapace causing the formation of cracks in this time window and probably increase the cooling rate further by increasing the surface area. We infer that the relatively high dissolved water contents in FVP (~0.23 – 0.96 wt.%; DeGroat-Nelson et al., 2001; Andrews et al., 2021) are preserved by fracture-enhanced cooling in a positive feedback loop where exsolution of water makes the melt more fragile (i.e., increasing porosity: Heap et al., 2021) and drives volume expansion and increasing hydrostatic pressure (i.e., stress) that exceeds the decreasing tensile strength as the carapace dries and cools (Ryan et al., 2019). Repeated generation of new cracks increases the surface area and cooling rate, rapidly (10s to 100s of minutes) eventually leading to quenching of the FVP carapace and terminating volatile exsolution.

Avesicular obsidian, on the other hand, quenches before volatile exsolution in the main volume of the melt, except where we see CVP or evidence for explosive venting (e.g., tuff). Dissolved water contents in the obsidian are variable from 0.22 wt.% (the minimum for FVP)

down to 0.13 wt.% (similar to the CVP minimum) (Andrews et al., 2021). This suggests some parts of the obsidian were quenched rapidly and experienced minimal volatile loss like FVP whereas others remained above T_g long enough (hours) to lose some water before quenching (Wadsworth et al., 2018). We have not analyzed the textural evidence in the obsidian to determine whether or not it has vesiculated and then welded (e.g., Wadsworth et al., 2020). Where CVP forms, tensile stresses from initial vesiculation do not exceed the tensile strength and brittle deformation does not interfere. Instead, a volatile-rich zone inflates through local vapor-pressure and vesicles can continue to grow and (probably) nucleate until stopped by cooling-induced quenching (Manley & Fink, 1987).

Taking the lowest value for T_g (614 °C in obsidian; Andrews et al., 2021) as a minimum, ductile deformation must occur above that. Brittle deformation can occur above T_g if the strain rate is high enough and the stress great enough to exceed the strength of the glass (Dingwell, 1996). Therefore, the scene is set for range of processes including explosive fragmentation that may only occur when the rheological and stress-strain conditions are appropriate (Gonnerman, 2015). For example, crevasses evolving into crease structures. Upon formation of a competent lid continued or renewed tensile deformation is concentrated upon single, large, planar fractures (crevasses). If the fracture does not penetrate through and beyond the contemporaneous T_g isosurface (Fig. 11) the crease structure is not modified further. On the hand, if the fracture penetrates into the melt, (1) horizontal viscous relaxation across the fracture will close any void space formed by dilation and plastically deform the fracture margins forming a crease structure, and (2) allow for upward flow of melt into the space wrenched-open in the lid. We envisage this process being localized to the volume immediately around the fracture and to generate a rotational strain in the lid where melt is channeled up into the gap in the lid while simultaneously being drained from beneath the flanks of the crease structure. This explains the correlation between the changing attitude of flow banding and the curvature of the crease structure margins (Fig. 8D).

5.1.5 Implications

The existing literature on silicic lavas understates, arguably, the pervasiveness and complexity of fractures at the upper surface. This is important for understanding of lava cooling and lava flow dynamics, especially in analog and numerical models, similar to how ’a’ā lavas are modeled (e.g., Applegarth et al., 2010). Models by necessity simplify the rheological and

mechanical properties and profiles of lavas (e.g., Griffiths & Fink, 1997; Merle, 1998). However, more sophisticated models will benefit from adapting parameters that are usually fixed like yield strength, lid thickness, and viscosity. For example, with improved understanding of how the strength and thickness of the upper surface and lid evolve in response to fracturing and outgassing will yield more reasonable simulations. Similarly, cooling rate is accelerated by the fracturing process and is probably underestimated.

5.2 Outgassing and Hybrid Activity During Emplacement

We interpret the presence or absence of different ornamentations on fracture surfaces as snap shots of out-gassing processes and different rheological responses to stress during emplacement. Based on lithofacies, ornamentation, and fracture morphology we can consider a further subdivision of processes occurring within 'cold' lava (i.e., wholly below Tg) and those that incorporate 'hot' lava as well (i.e., crossing the contemporaneous T_g isosurface: Fig. 11). Hot features exhibit evidence of ductile deformation of silicate melt either as post-fracture viscous flow or vesiculation and explosive fragmentation.

Fracturing occurs during and after plastic flow of the lava. Contemporaneous fracturing and ductile flow processes are recorded by welding and healing of cracks and clefts, and the evolution of crevasses to crease structures. Moreover, these features are typically accompanied by red surface and leathery surface ornamentations. These features are subsequently cut by planar, non-ornamented cracks. Rust-red surfaces are inferred to be oxidized, probably magnetite microlites to hematite but this has not been tested, during exsolution of water across the fracture surfaces (e.g., Manley, 1996) at elevated temperature (>500 °C; e.g., Watkins & Haggerty, 1967; Saito et al., 2004). Therefore, red surfaces and red leathery surfaces must form immediately after a fracture has formed and dilated before the rock can cool significantly. Leathery surfaces are plastically deformed so must form above T_g (614 °C for obsidian). Fractures are therefore important outgassing pathways through enhanced permeability (e.g., Kushnir et al., 2017; Heap et al., 2019).

Fracture surfaces coated with tuff (pink tessellated surfaces) and lapilli-sized juvenile volcaniclastic grains are widespread but not volumetrically significant. The pink color probably results from oxidation by outgassing water vapor, but in these cases the fluid also entrained ash-sized particles. The most plausible explanation for forming ash-sized tephra is the explosive fragmentation of frothy low porosity melt indicating rapid decompression of volatile-rich melt at

the base of a fracture (Heap et al., 2021). Similar welded ash- to lapilli-size clasts are recorded within the products of effusive and hybrid lavas (e.g., Tuffen & Castro, 2009; Castro et al., 2012; Castro & Walter, 2021).

6.0 CONCLUSIONS

The textural and structural observations recorded in this study demonstrate the pervasive tensile fracturing of the upper surface of silicic lavas during emplacement. Fractures characterized by size and shape record two separate continuums of brittle and brittle-ductile deformation occurring late-stage and throughout Obsidian Dome's emplacement. We demonstrate that small scale cracks grow and link to form larger cracks and clefts in all lithofacies during the lava's effusion. We hypothesize that the largest fractures, crevasses and crease structures, lie as endmembers along a fracture continuum occurring in the final stages of lava emplacement. A single, large scale fracture event generates a crevasse whether or not this fracture penetrates deep enough (wholly through T_g) solely controls the formation of crease structures. Furthermore, ornamentation recorded on these fracture surfaces illuminate areas across the lava where fractures penetrated the brittle-ductile transition resulting in explosive fragmentation. The identified annealed to welded ash- to lapilli-sized tuff across the surface and at the margins highlights the ongoing outgassing during lava emplacement. The presence of hot ($> T_g$) fractures suggests the late-stage emplacement process governing Obsidian Dome was endogenous as witnessed at Cordón Caulle, Chile (Tuffen et al., 2013; Farquharson et al., 2015; Magnall et al., 2018). The extensional Long Valley volcanic region is active and potential eruptions are predicted along the N-S Inyo-Mono volcanic chain, where the most recent eruptions occurred. Hazard forecasting and future lava emplacement models should consider the strength of the upper surface and how it evolves to accommodate fracturing and outgassing.

ACKNOWLEDGEMENTS

The authors sincerely thank the extensive, insightful review provided by Dr. Jonathan Fink and anonymous reviewer which improved and expanded this manuscript. This research was supported by the National Science Foundation through awards EAR 1725131 and EAR 1935764 to GA and EAR 1724581 to AW, and the John C. and Mildred Ludlum Geology Endowment to SI. The authors benefitted from discussions with Kenneth Befus, Tyler Leggett, Sarah Brown, and field assistants Holly Pettus and Levi Fath.

REFERENCES

Allmendinger, R.W., Cardozo, N., and Fisher, D., 2011, Structural Geology Algorithms: Vectors and Tensors in Structural Geology: New York, Cambridge University Press, 304 p.

Allmendinger, R. W., Siron, C. R., & Scott, C. P. (2017). Structural data collection with mobile devices: Accuracy, redundancy, and best practices. Journal of Structural Geology, 102, 98–112. https://doi.org/10.1016/j.jsg.2017.07.011

Anderson, S. W., & Fink, J. H. (1992). Crease structures: indicators of emplacement rates and surface stress regimes of lava flows. Geological Society of America Bulletin, 104(5), 615–625. https://doi.org/10.1130/0016-7606(1992)104<0615:CSIOER>2.3.CO;2

Anderson, S. W., Stofan, E. R., Plaut, J. J., & Crown, D. A. (1998). Block size distributions on silicic lava flow surfaces: Implications for emplacement conditions. GSA Bulletin, 110(10), 1258–1267.

Andrews, G. D. M., Kenderes, S. M., Whittington, A. G., Isom, S. L., Brown, S. R., Pettus, H. D., Cole, B. G., & Gokey, K. J. (2021). The fold illusion: The origins and implications of ogives on silicic lavas. Earth and Planetary Science Letters, 553. https://doi.org/10.1016/j.epsl.2020.116643

Applegarth, L. J., Pinkerton, H., James, M. R., & Calvari, S. (2010). Morphological complexities and hazards during the emplacement of channel-fed 'a'ā lava flow fields: A study of the 2001 lower flow field on Etna. Bulletin of Volcanology, 72(6), 641–656. https://doi.org/10.1007/s00445-010-0351-1

Bai, T., & Pollard, D. D. (2000). Fracture spacing in layered rocks: a new explanation based on the stress transition. Journal of Structural Geology , 22, 43–57. www.elsevier.nl/locate/jstrugeo

Bailey, R. A., Dalrymple, G. B., & Lanphere, M. A. (1976). Volcanism, structure, and geochronology of Long Valley Caldera, Mono County, California. Journal of Geophysical Research, 81(5), 725–744. https://doi.org/10.1029/jb081i005p00725

Bullock, L. A., Gertisser, R., & O'Driscoll, B. (2018). Emplacement of the Rocche Rosse rhyolite lava flow (Lipari, Aeolian Islands). Bulletin of Volcanology, 80(5). https://doi.org/10.1007/s00445-018-1222-4

Byerlee, J. D. (1978). Friction of rocks. In Rock Friction and Earthquake Prediction (pp. 615–626). Birkhäuser, Basel.

Canón-Tapia, Edgardo., & Castro, Jonathan. (2004). AMS measurements on obsidian from the Inyo Domes, CA: A comparison of magnetic and mineral preferred orientation fabrics. Journal of Volcanology and Geothermal Research, 134(3), 169–182. https://doi.org/10.1016/j.jvolgeores.2004.01.005

Castro, J. M., Bindeman, I. N., Tuffen, H., & Ian Schipper, C. (2014). Explosive origin of silicic lava: Textural and δD-H2O evidence for pyroclastic degassing during rhyolite effusion. Earth and Planetary Science Letters, 405, 52–61. https://doi.org/10.1016/j.epsl.2014.08.012

Castro, J. M., Cordonnier, B., Tuffen, H., Tobin, M. J., Puskar, L., Martin, M. C., & Bechtel, H. A. (2012). The role of melt-fracture degassing in defusing explosive rhyolite eruptions at volcán Chaitén. Earth and Planetary Science Letters, 333–334, 63–69. https://doi.org/10.1016/j.epsl.2012.04.024

Castro, J. M., Manga, M., & Cashman, K. (2002). Dynamics of obsidian flows inferred from microstructures: Insights from microlite preferred orientations. Earth and Planetary Science Letters, 199(1–2), 211–226. https://doi.org/10.1016/S0012-821X(02)00559-9

Castro, J. M., Manga, M., & Martin, M. C. (2005). Vesiculation rates of obsidian domes inferred from H2O concentration profiles. Geophysical Research Letters, 32(21), 1–5. https://doi.org/10.1029/2005GL024029

Castro, J. M., & Mercer, C. (2004). Microlite textures and volatile contents of obsidian from the Inyo volcanic chain, California. Geophysical Research Letters, 31(18), 2–5. https://doi.org/10.1029/2004GL020489

Castro, J. M., & Walter, S. (2021). Hybrid rhyolitic eruption at Big Glass Mountain, CA, USA. Volcanica, 257–277.

Castruccio, A., Rust, A. C., & Sparks, R. S. J. (2013). Evolution of crust- and core-dominated lava flows using scaling analysis. Bulletin of Volcanology, 75(1), 1–15. https://doi.org/10.1007/s00445-012-0681-2

Cordonnier, B., Caricchi, L., Pistone, M., Castro, J., Hess, K. U., Gottschaller, S., Manga, M., Dingwell, D. B., & Burlini, L. (2012). The viscous-brittle transition of crystal-bearing silicic melt: Direct observation of magma rupture and healing. Geology, 40(7), 611–614. https://doi.org/10.1130/G3914.1

de Silva, S. L., Self, S., Francis, P. W., Drake, R. E., & Ramirez R., C. (1994). Effusive silicic volcanism in the Central Andes: the Chao dacite and other young lavas of the Altiplano-Puna volcanic complex. Journal of Geophysical Research, 99(B9). https://doi.org/10.1029/94jb00652

Deardorff, N., Booth, A., & Cashman, K. (2019). Remote Characterization of Dominant Wavelengths From Surface Folding on Lava Flows Using Lidar and Discrete Fourier Transform Analyses. Geochemistry, Geophysics, Geosystems. https://doi.org/10.1029/2019gc008497

Degroat-Nelson, P. J., Cameron, B. I., Fink, J. H., & Holloway, J. R. (2001). Hydrogen isotope analysis of rehydrated silicic lavas: implications for eruption mechanisms. Earth and Planetary Science Letters, 185, 331–341. www.elsevier.com/locate/epsl

Dingwell, D. B. (1996). Volcanic dilemma: Flow or blow? Science, 273(5278), 1054–1055. https://doi.org/10.1126/science.273.5278.1054

Dingwell, D. B., & Webb, S. L. (1990). Relaxation in silicate melts. European Journal of Mineralogy, 2, 427–449. http://pubs.geoscienceworld.org/eurjmin/article-pdf/2/4/427/4001861/427_gseurjmin_2_4_427_450_dingwell.pdf

Donnelly-Nolan, J. M., Stovall, W. K., Ramsey, D. W., Ewert, J. W., & Jensen, R. A. (2011). Newberry Volcano-Central Oregon's Sleeping Giant. U.S Geological Survey Fact Sheet, 3145, 1–6.

Drone Deploy, 2020, Drone Mapping Software: https://www.dronedeploy.com/ (accessed July 2019).

Eichelberger, J. C., Carrigan, C. R., Westrich, H. R., & Price, R. H. (1986). Non-explosive silicic volcanism. Nature, 323, 598–602.

Eichelberger, J. C., Lysne, P. C., Miller, C. D., & Younker, L. C. (1985). Research Drilling at Inyo Domes, California: 1984 Results. Eos, Transactions American Geophysical Union, 66(17), 1–3.

Eichelberger, J. C., Lysne, P. C., & Younker, L. W. (1984). Research drilling at Inyo Domes, Long Valley Caldera, California. Eos, Transactions American Geophysical Union, 65(39), 721–725. https://doi.org/10.1029/EO065i039p00721

Farquharson, J. I., James, M. R., & Tuffen, H. (2015). Examining rhyolite lava flow dynamics through photo-based 3D reconstructions of the 2011-2012 lava flowfield at Cordón-

Caulle, Chile. Journal of Volcanology and Geothermal Research, 304, 336–348. https://doi.org/10.1016/j.jvolgeores.2015.09.004

Farrell, J., Karson, J., Soldati, A., & Wysocki, R. (2018). Multiple-generation folding and non-coaxial strain of lava crusts. Bulletin of Volcanology, 80(12). https://doi.org/10.1007/s00445-018-1258-5

Fink, J. H. (1980a). Gravity instability in the Holocene Big and Little Glass Mountain rhyolitic obsidian flows, northern California. Tectonophysics, 66, 147–166. https://doi.org/10.1016/0040-1951(80)90043-8

Fink, J. H. (1980b). Surface folding and viscosity of rhyolite flows. Geology, 8(5), 250–254. https://doi.org/10.1130/0091-7613(1980)8<250:SFAVOR>2.0.CO;2

Fink, J. H. (1983). Structure and emplacement of a rhyolitic obsidian flow: Little Glass Mountain, Medicine Lake Highland, northern California (USA). Geological Society of America Bulletin, 94(3), 362–380. https://doi.org/10.1130/0016-7606(1983)94<362:SAEOAR>2.0.CO;2

Fink, J. H. (1985). Geometry of Silicic Dikes Beneath the Inyo Domes, California. Journal of Geophysical Research, 90, 11,127-11,133.

Fink, J. H., & Anderson, S. W. (2017). Emplacement of Holocene Silicic Lava Flows and Domes at Newberry, South Sister, and Medicine Lake Volcanoes, California and Oregon. U.S. Geological Survey Scientific Investigations Report, 5022 – I, 41. https://doi.org/https://doi.org/10.3133/sir20175022I

Fink, J. H., & Griffiths, R. W. (1998). Morphology, eruption rates, and rheology of lava domes: Insights from laboratory models. Journal of Geophysical Research: Solid Earth, 103(1), 527–545. https://doi.org/10.1029/97jb02838

Fink, J. H., Malin, M. C., & Anderson, S. W. (1990). Intrusive and extrusive growth of the Mount St Helens lava dome. Nature, 348(6300), 435–437. https://doi.org/10.1038/348435a0

Fink, J. H., & Manley, C. R. (1987). Origin of pumiceous and glassy textures in rhyolite flows and domes. In Special Paper of the Geological Society of America (Vol. 212, pp. 77–88). https://doi.org/10.1130/SPE212-p77

Fink, J. H., & Pollard, D. (1985). Inyo Dike Rotation. Science, 228(4706), 1382–1385.

Furukawa, K., & Kamata, H. (2004). Eruption and emplacement of the Yamakogawa Rhyolite in central Kyushu, Japan: A model for emplacement of rhyolitic spatter. In Earth Planets Space (Vol. 56).

Furukawa, K., & Uno, K. (2015). Origin and deformation of high porosity bands in the Takanoobane Rhyolite lava of Aso volcano, Japan. Journal of Volcanology and Geothermal Research, 305, 76–83. https://doi.org/10.1016/j.jvolgeores.2015.09.021

Gonnermann, H. M. (2015). Magma Fragmentation. Annual Review of Earth and Planetary Sciences, 43(1), 431–458. https://doi.org/10.1146/annurev-earth-060614-105206

Gonnermann, H. M., & Manga, M. (2005). Flow banding in obsidian: A record of evolving textural heterogeneity during magma deformation. Earth and Planetary Science Letters, 236(1–2), 135–147. https://doi.org/10.1016/j.epsl.2005.04.031

Griffiths, R. W., & Fink, J. H. (1997). Solidifying Bingham extrusions: A model for the growth of silicic lava domes. Journal of Fluid Mechanics, 347, 13–36. https://doi.org/10.1017/S0022112097006344

Hama, L., Ruddle, R. A., & Paton, D. (2014). Geological orientation measurements using an iPad: Method comparison. TPCG 2014 - Theory and Practice of Computer Graphics, Proceedings, 45–50. https://doi.org/10.2312/cgvc.20141207

Heap, M. J., Tuffen, H., Wadsworth, F. B., Reuschlé, T., Castro, J. M., & Schipper, C. I. (2019). The Permeability Evolution of Tuffisites and Implications for Outgassing Through Dense Rhyolitic Magma. Journal of Geophysical Research: Solid Earth, 124(8), 8281–8299. https://doi.org/10.1029/2018JB017035

Heap, M. J., Wadsworth, F. B., Heng, Z., Xu, T., Griffiths, L., Aguilar Velasco, A., Vairé, E., Vistour, M., Reuschlé, T., Troll, V. R., Deegan, F. M., & Tang, C. (2021). The tensile strength of volcanic rocks: Experiments and models. Journal of Volcanology and Geothermal Research, 418. https://doi.org/10.1016/j.jvolgeores.2021.107348

Heap, M. J., Wadsworth, F. B., Xu, T., Chen, C. feng, & Tang, C. (2016). The strength of heterogeneous volcanic rocks: A 2D approximation. Journal of Volcanology and Geothermal Research, 319, 1–11. https://doi.org/10.1016/j.jvolgeores.2016.03.013

Hildreth, W. (2004). Volcanological perspectives on Long Valley, Mammoth Mountain, and Mono Craters: Several contiguous but discrete systems. Journal of Volcanology and

Geothermal Research, 136(3–4), 169–198. https://doi.org/10.1016/j.jvolgeores.2004.05.019

Huang, Q., & Hassager, O. (2017). Polymer liquids fracture like solids. Soft Matter, 13(19), 3470–3474. https://doi.org/10.1039/c7sm00126f

Kenderes, S. M. (2021). Emplacement styles of obsidian lavas: an integrated field and laboratory study. [Doctoral dissertation, University of Missouri].

Kushnir, A. R. L., Martel, C., Champallier, R., & Arbaret, L. (2017). In situ confirmation of permeability development in shearing bubble-bearing melts and implications for volcanic outgassing. Earth and Planetary Science Letters, 458, 315–326. https://doi.org/10.1016/j.epsl.2016.10.053

Lamarche, J., Chabani, A., & Gauthier, B. D. M. (2018). Dimensional threshold for fracture linkage and hooking. Journal of Structural Geology, 108, 171–179. https://doi.org/10.1016/j.jsg.2017.11.016

Lara, L. E. (2009). The 2008 eruption of the Chaitén Volcano, Chile: a preliminary report. Andean Geology, 36(1), 125–129. https://doi.org/10.4067/s0718-71062009000100009

Leggett, T. N., Befus, K. S., & Kenderes, S. M. (2020). Rhyolite lava emplacement dynamics inferred from surface morphology. Journal of Volcanology and Geothermal Research, 395. https://doi.org/10.1016/j.jvolgeores.2020.106850

Lescinsky, David T., Merle, O. (2005). Extensional and compressional strain in lava flows and the formation of fractures in surface crust. Geological Society of American Special Paper 396.

Maeno, F., & Taniguchi, H. (2006). Silicic lava dome growth in the 1934-1935 Showa Iwo-jima eruption, Kikai caldera, south of Kyushu, Japan. Bulletin of Volcanology, 68(7–8), 673–688. https://doi.org/10.1007/s00445-005-0042-5

Magnall, N., James, M. R., Tuffen, H., & Vye-Brown, C. (2017). Emplacing a cooling-limited rhyolite lava flow: Similarities with basaltic lava flows. Frontiers in Earth Science, 5(June). https://doi.org/10.3389/feart.2017.00044

Manga, M., Voltolini, M., & Wenk, H. R. (2018). Microlite orientation in obsidian flow measured by synchrotron X-ray diffraction. Contributions to Mineralogy and Petrology, 173(7). https://doi.org/10.1007/s00410-018-1479-9

Manley, C. R. (1996). Physical volcanology of a voluminous rhyolite lava flow: The Badlands lava, Owyhee Plateau, southwestern Idaho. Journal of Volcanology and Geothermal Research, 71(2–4), 129–153. https://doi.org/10.1016/0377-0273(95)00066-6

Manley, C. R., & Fink, J. H. (1987). Internal textures of rhyolite flows as revealed by research drilling. Geology, 15(6), 549–552. https://doi.org/10.1130/0091-7613(1987)15<549:ITORFA>2.0.CO;2

Merle, O. (1998). Internal strain within lava flows from analogue modelling. Journal of Volcanology and Geothermal Research, 81(3–4), 189–206. https://doi.org/10.1016/S0377-0273(98)00009-2

Miller, C. D. (1985). Holocene eruptions at the Inyo volcanic chain, California: Implications for possible eruptions in Long Valley caldera. Geology, 13(1), 14–17. https://doi.org/10.1130/0091-7613(1985)13<14:HEATIV>2.0.CO;2

Novakova, L., and Pavlis, T.L., 2019, Modern Methods in Structural Geology of Twenty-first Century: Digital Mapping and Digital Devices for the Field Geology, in Teaching Methodologies in Structural Geology and Tectonics: Springer, Singapore, p. 43-54.

Novakova, L., & Pavlis, T. L. (2017). Assessment of the precision of smart phones and tablets for measurement of planar orientations: A case study. Journal of Structural Geology, 97, 93–103. https://doi.org/10.1016/j.jsg.2017.02.015

Pallister, J. S., Diefenbach, A. K., Burton, W. C., Muñoz, J., Griswold, J. P., Lara, L. E., Lowenstern, J. B., & Valenzuela, C. E. (2013). The Chaitén rhyolite lava dome: Eruption sequence, lava dome volumes, rapid effusion rates and source of the rhyolite magma. Andean Geology, 40(2), 277–294. https://doi.org/10.5027/andgeoV40n2-a06

Park, S., & Iversen, J. D. (1984). Dynamics of lava flow: thickness growth characteristics of steady two-dimensional flow. Geophysical Research Letters, 11(7), 641–644.

Petroleum Experts, 2020, Fieldmove: Digital field mapping application for smartphone and tablet: https://www.petex.com/products/move-suite/digital-field-mapping/ (accessed July 2018).

Plaut, J. J., Anderson, S. W., Crown, D. A., Stofan, E. R., & van Zyl, J. J. (2004). The unique radar properties of silicic lava domes. Journal of Geophysical Research E: Planets, 109(3). https://doi.org/10.1029/2002je002017

Ramsey, M. S., & Fink, J. H. (1999). Estimating silicic lava vesicularity with thermal remote sensing: A new technique for volcanic mapping and monitoring. Bulletin of Volcanology, 61(1–2), 32–39. https://doi.org/10.1007/s004450050260

Reches, Z., & Fink, J. H. (1988). The Mechanism of Intrustion of the Inyo Dike, Long Valley Caldera, California. Journal of Geophysical Research, 93, 4321–4334.

Romine, W. L., & Whittington, A. G. (2015). A simple model for the viscosity of rhyolites as a function of temperature, pressure and water content. Geochimica et Cosmochimica Acta, 170, 281–300. https://doi.org/10.1016/j.gca.2015.08.009

Rust, A. C., Manga, M., & Cashman, K. v. (2003). Determining flow type, shear rate and shear stress in magmas from bubble shapes and orientations. Journal of Volcanology and Geothermal Research, 122(1–2), 111–132. https://doi.org/10.1016/S0377-0273(02)00487-0

Ryan, A. G., Russell, J. K., Heap, M. J., Kolzenburg, S., Vona, A., & Kushnir, A. R. L. (2019). Strain-Dependent Rheology of Silicate Melt Foams: Importance for Outgassing of Silicic Lavas. Journal of Geophysical Research: Solid Earth, 124(8), 8167–8186. https://doi.org/10.1029/2019JB018099

Saito, T., Ishikawa, N., & Kamata, H. (2004). Iron - Titanium oxide minerals in block-and-ash-flow deposits: Implications for lava dome oxidation processes. Journal of Volcanology and Geothermal Research, 138(3–4), 283–294. https://doi.org/10.1016/j.jvolgeores.2004.07.006

Sampson, D. E., & Cameron, K. L. (1987). The Geochemistry of the Inyo Volcanic Chain: Multiple Magma Systems in the Long Valley Region, Eastern California. Journal of Geophysical Research, 92, 403–421.

Schipper, C. I., Castro, J. M., Tuffen, H., James, M. R., & How, P. (2013). Shallow vent architecture during hybrid explosive-effusive activity at Cordón Caulle (Chile, 2011-12): Evidence from direct observations and pyroclast textures. Journal of Volcanology and Geothermal Research, 262, 25–37. https://doi.org/10.1016/j.jvolgeores.2013.06.005

Seaman, S. J., Dyar, M. D., & Marinkovic, N. (2009). The effects of heterogeneity in magma water concentration on the development of flow banding and spherulites in rhyolitic lava. Journal of Volcanology and Geothermal Research, 183(3–4), 157–169. https://doi.org/10.1016/j.jvolgeores.2009.03.001

Shields, J. K., Mader, H. M., Caricchi, L., Tuffen, H., Mueller, S., Pistone, M., & Baumgartner, L. (2016). Unravelling textural heterogeneity in obsidian: Shear-induced outgassing in the Rocche Rosse flow. Journal of Volcanology and Geothermal Research, 310, 137–158. https://doi.org/10.1016/j.jvolgeores.2015.12.003

Smith, J. v. (1996). Ductile-brittle transition structures in the basal shear zone of a rhyolite lava flow, eastern Australia. Journal of Volcanology and Geothermal Research, 72(3–4), 217–223. https://doi.org/10.1016/0377-0273(96)00009-1

Smith, J. v. (2002). Structural analysis of flow-related textures in lavas. Earth-Science Reviews, 57(3–4), 279–297. https://doi.org/10.1016/S0012-8252(01)00081-2

Smith, J. v., & Houston, E. C. (1994). Folds produced by gravity spreading of a banded rhyolite lava flow. Journal of Volcanology and Geothermal Research, 63(1–2), 89–94. https://doi.org/10.1016/0377-0273(94)90019-1

Sparks, Murphy, Lejeune, Watts, Barclay, & Young. (2000). Control on the emplacement of the andesite lava dome of the Soufriere Hills volcano, Montserrat by degassing-induced crystallization. Terra Nova, 12(1), 14–20. https://doi.org/10.1046/j.1365-3121.2000.00267.x

Stasiuk, M. V., Jaupart, C., & Sparks, S. J. R. (1993). Influence of cooling on lava-flow dynamics. Geology, 21, 335–338. http://pubs.geoscienceworld.org/gsa/geology/article-pdf/21/4/335/3514516/i0091-7613-21-4-335.pdf?casa_token=suCvnRp2bTAAAAAA:iSN4-C6mPFsZFMPrhfBvCbGFpH2Db8x9hOFSnB-owKxiOWdZEjEwS0Rzi6JA

Stevenson, R. J., Briggs, R. M., & Hodder, A. P. W. (1994). Physical volcanology and emplacement history of the Ben Lomond rhyolite lava flow, Taupo Volcanic Centre, New Zealand. New Zealand Journal of Geology and Geophysics, 37(3), 345–358. https://doi.org/10.1080/00288306.1994.9514625

Trede, C., Cardozo, N., & Watson, L. (2019). What is the appropriate sample size for strike and dip measurements? An evaluation from compass, smartphone and lidar measurements. Norwegian Journal of Geology, 99(3), 1–14. https://doi.org/10.17850/njg99-3-4

Tuffen, H., & Castro, J. M. (2009). The emplacement of an obsidian dyke through thin ice: Hrafntinnuhryggur, Krafla Iceland. Journal of Volcanology and Geothermal Research, 185(4), 352–366. https://doi.org/10.1016/j.jvolgeores.2008.10.021

Tuffen, H., James, M. R., Castro, J. M., & Schipper, C. I. (2013). Exceptional mobility of an advancing rhyolitic obsidian flow at Cordón Caulle volcano in Chile. Nature Communications, 4, 1–7. https://doi.org/10.1038/ncomms3709

Unwin, H. E., Tuffen, H., Phillips, E., Wadsworth, F. B., & James, M. R. (2021). Pressure-Driven Opening and Filling of a Volcanic Hydrofracture Recorded by Tuffisite at Húsafell, Iceland: A Potential Seismic Source. Frontiers in Earth Science, 9. https://doi.org/10.3389/feart.2021.668058

Vogel, T. A., Eichelberger, J. C., Younker, L. W., Schuraytz, B. C., Horkowitz, J. P., Stockman, H. W., & Westrich, H. R. (1989). Petrology and emplacement dynamics of intrusive and extrusive rhyolites of Obsidian Dome, Inyo craters volcanic chain, eastern California. Journal of Geophysical Research, 94(B12), 17937–17956.

Wadsworth, F. B., Llewellin, E. W., Vasseur, J., Gardner, J. E., & Tuffen, H. (2020). Explosive-effusive volcanic eruption transitions caused by sintering. In Sci. Adv (Vol. 6). http://advances.sciencemag.org/

Wadsworth, F. B., Witcher, T., Vossen, C. E. J., Hess, K. U., Unwin, H. E., Scheu, B., Castro, J. M., & Dingwell, D. B. (2018). Combined effusive-explosive silicic volcanism straddles the multiphase viscous-to-brittle transition. Nature Communications, 9(1), 1–8. https://doi.org/10.1038/s41467-018-07187-w

Watkins, N. D. , & Haggerty, S. E. (1967). Primary oxidation variation and petrogenesis in a single lava. Contributions to Mineralogy and Petrology, 15, 251–271.

Westoby, M. J., Brasington, J., Glasser, N. F., Hambrey, M. J., & Reynolds, J. M. (2012). “Structure-from-Motion” photogrammetry: A low-cost, effective tool for geoscience applications. Geomorphology, 179, 300–314. https://doi.org/10.1016/j.geomorph.2012.08.021

Wilson, L., Fagents, S. A., Robshaw, L. E., & Scott, E. D. (2007). Vent geometry and eruption conditions of the mixed rhyolite-basalt Námshraun lava flow, Iceland. Journal of Volcanology and Geothermal Research, 164(3), 127–141. https://doi.org/10.1016/j.jvolgeores.2007.04.005

Wood, S. H. (1977). Distribution, correlation, and radiocarbon dating of late Holocene tephra, Mono and Inyo craters, eastern California. Bulletin of the Geological Society of America, 88(1), 89–95. https://doi.org/10.1130/0016-7606(1977)88<89:DCARDO>2.0.CO;2

FIGURES

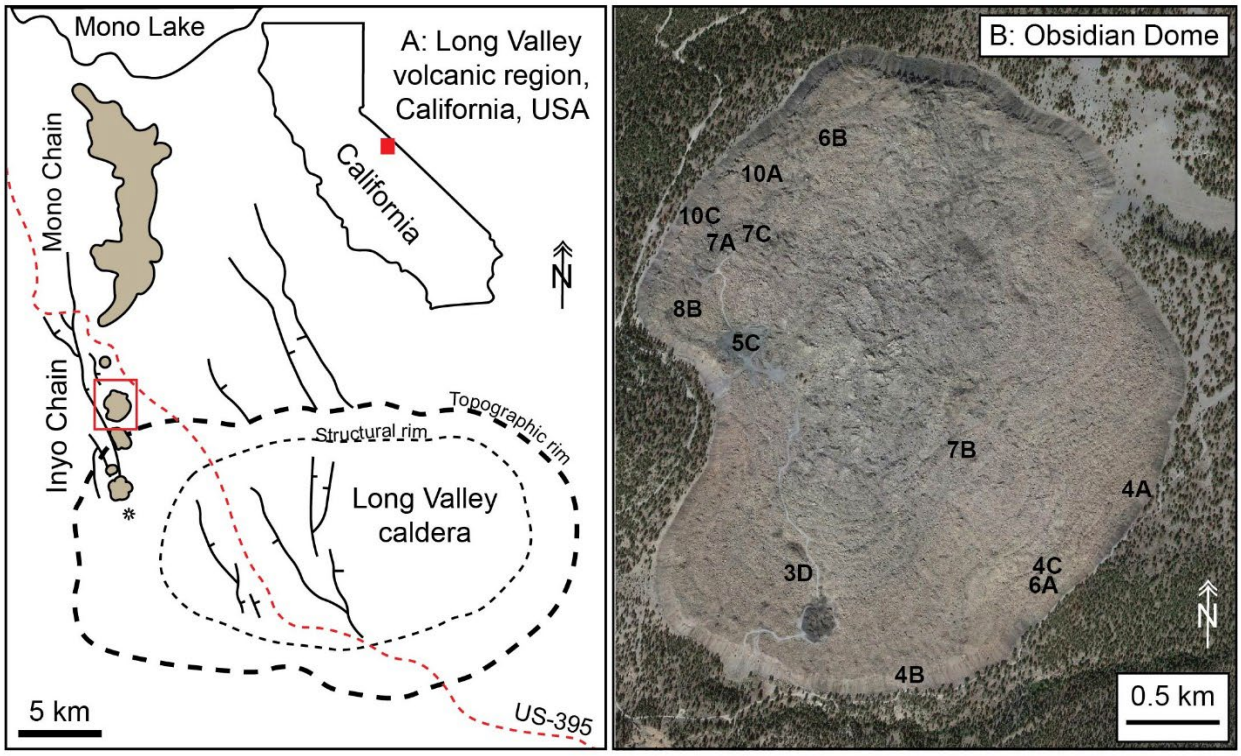

Figure 1. (A) The Long Valley volcanic region, California, USA after Hildreth (2004); Obsidian Dome is within the red rectangle. (B) Google Earth aerial image of Obsidian Dome. Numbers indicate the locations of the outcrop photos in the following figures.

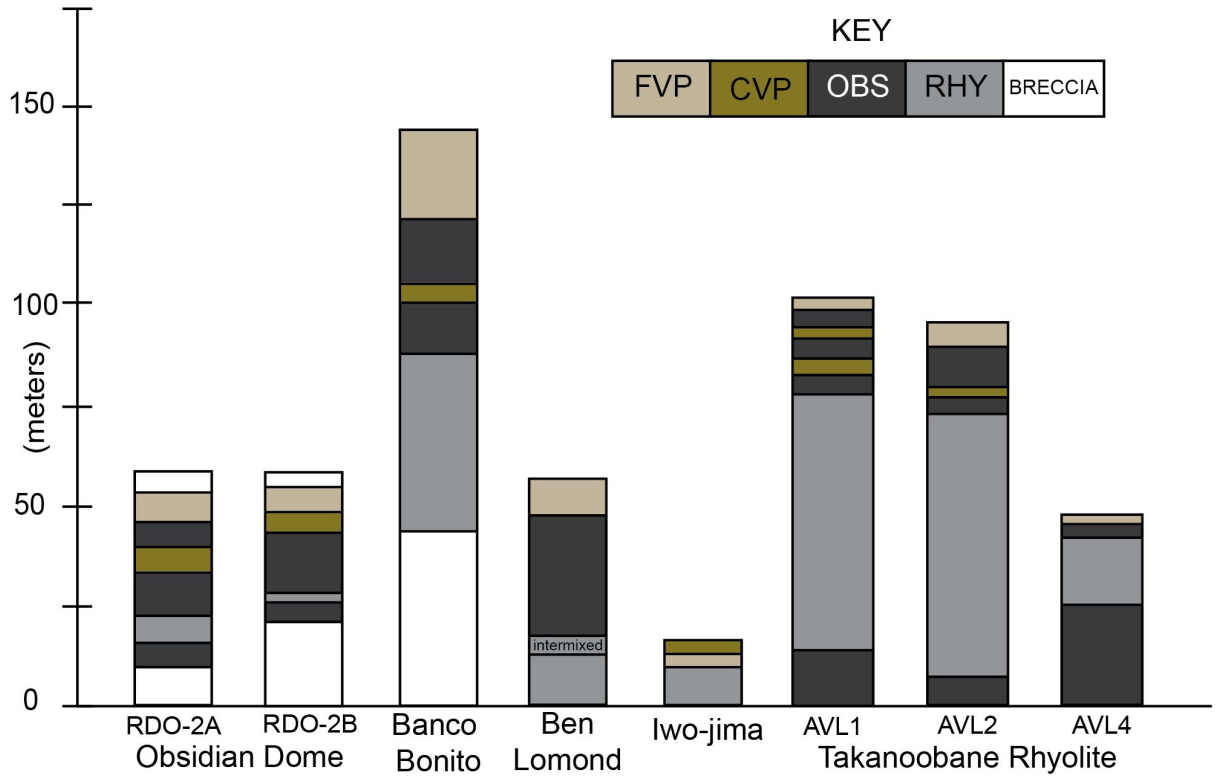

Figure 2. Compilation of observed lithostratigraphy across several silicic lavas. Obsidian Dome drill cores RDO-2A and RDO-2B from the Inyo Drilling Program and the Banco Bonito VC-1 drill core from the CSDP Valley Scientific Drilling Project taken from Manley & Fink (1987), the Ben Lomond core (Stevenson et al., 1994), the Showa Iwo-jima lava dome (Maeno & Taniguchi, 2006), and the Takanoobane rhyolite after Furukawa & Kamata (2004) and Furukawa & Uno (2015).

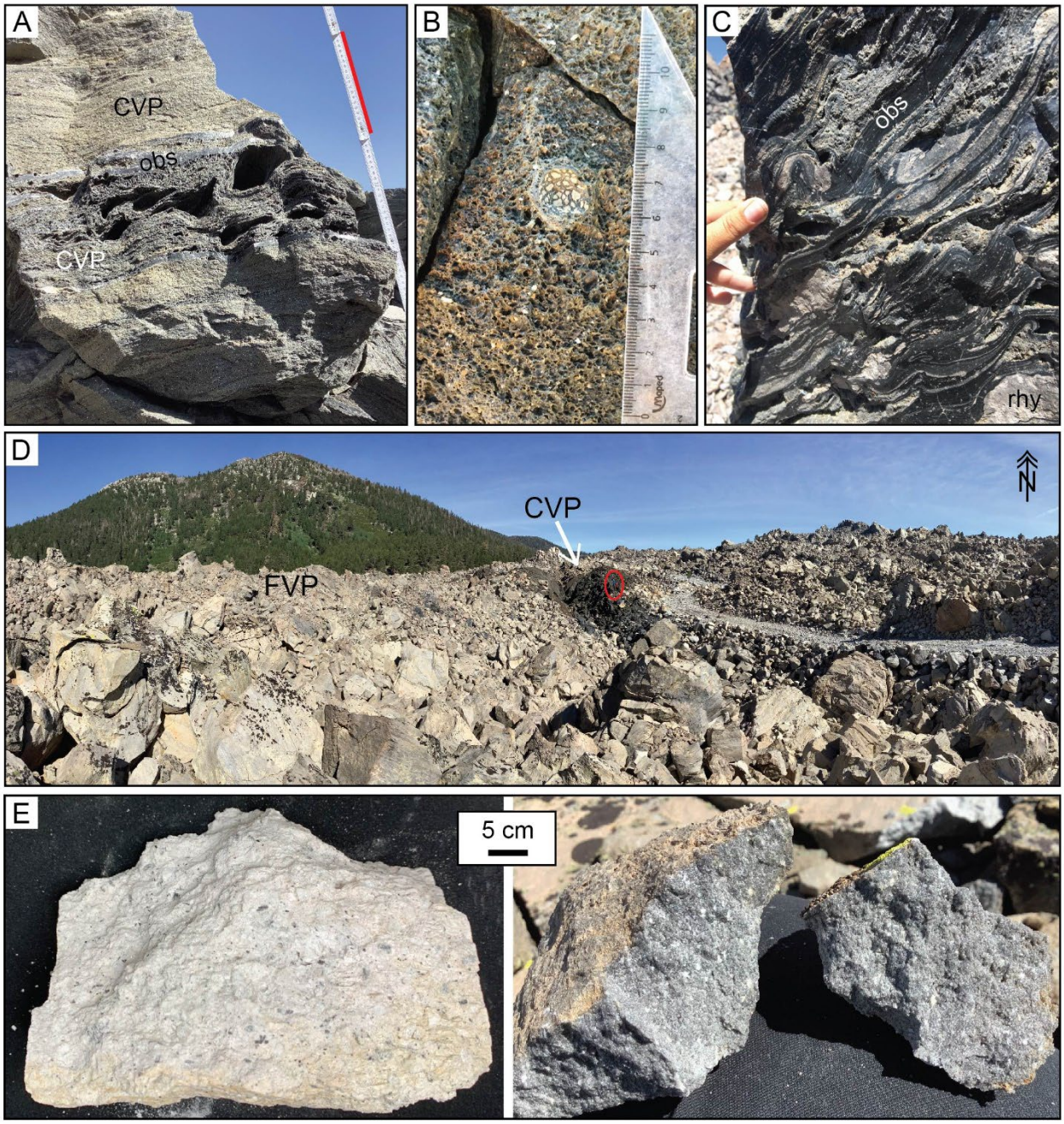

Figure 3. Lithofacies at Obsidian Dome. (A) Multiple layers of variable light and dark CVP with obsidian displaying stretched and interconnected vesicles, red line is 20 cm. (B) Close-up image of large vesicles in CVP. (C) Folded and banded sections of scoriaceous obsidian (grey), massive obsidian (dark black glassy: labeled 'obs'), and microcrystalline rhyolite. (D) Panorama looking north towards the center of Obsidian Dome highlighting the color contrast of CVP and FVP, geologist circled in red. (E) Hand samples displaying the pumiceous texture and variable colors of FVP.

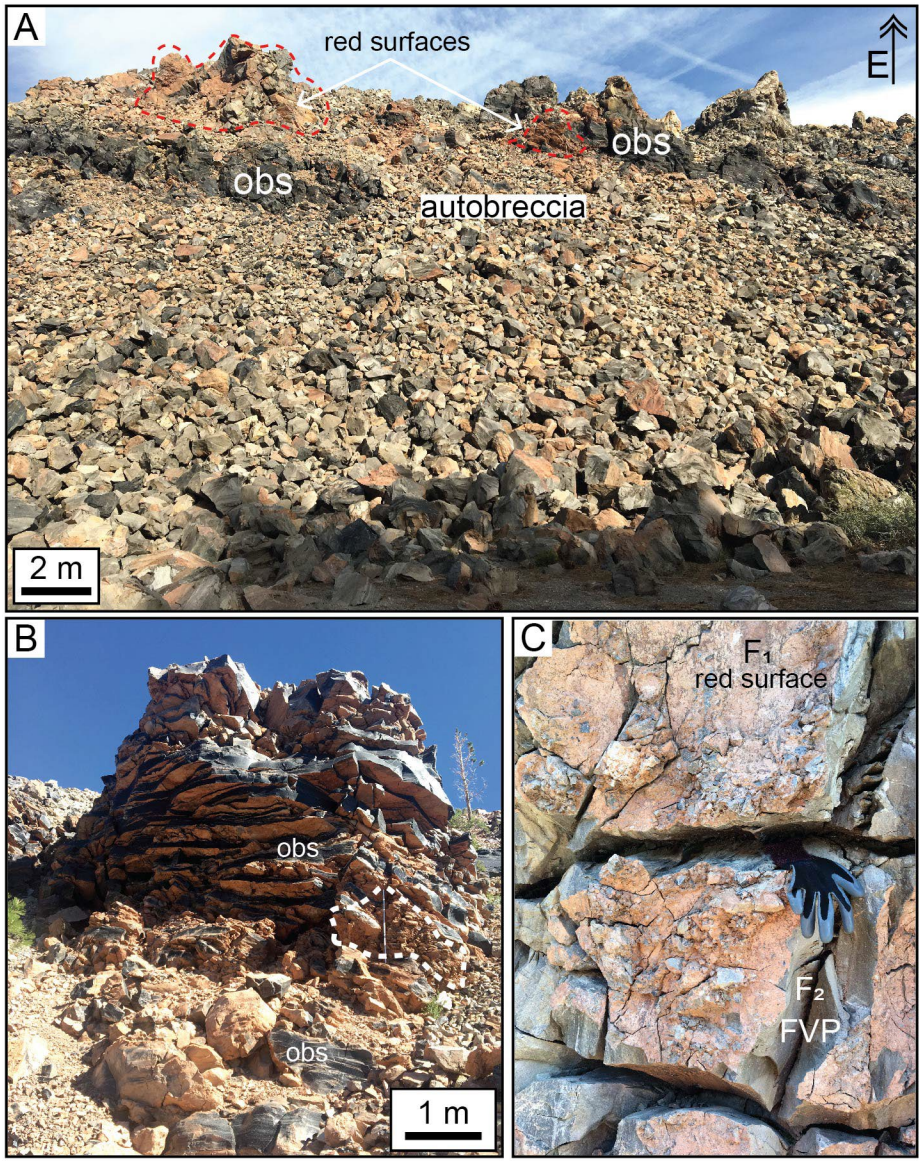

Figure 4. Red oxidized surfaces. (A) Flow front at the southeast of Obsidian Dome, approximately 20 meters tall. Dashed red lines circle red surfaces on obsidian (obs) and FVP. Autobreccia of FVP and obsidian make up the talus slope between the lenses of obsidian. (B) Breccia stained red between lenses of obsidian at the SE flow front of Obsidian Dome. White dashed line shows a cluster of breccia clasts. (C) Fracture surface (F1) on FVP coated with thin light red veneer and annealed lapilli-sized clasts. Secondary orthogonal fractures (F2) exposing the fresh FVP below.

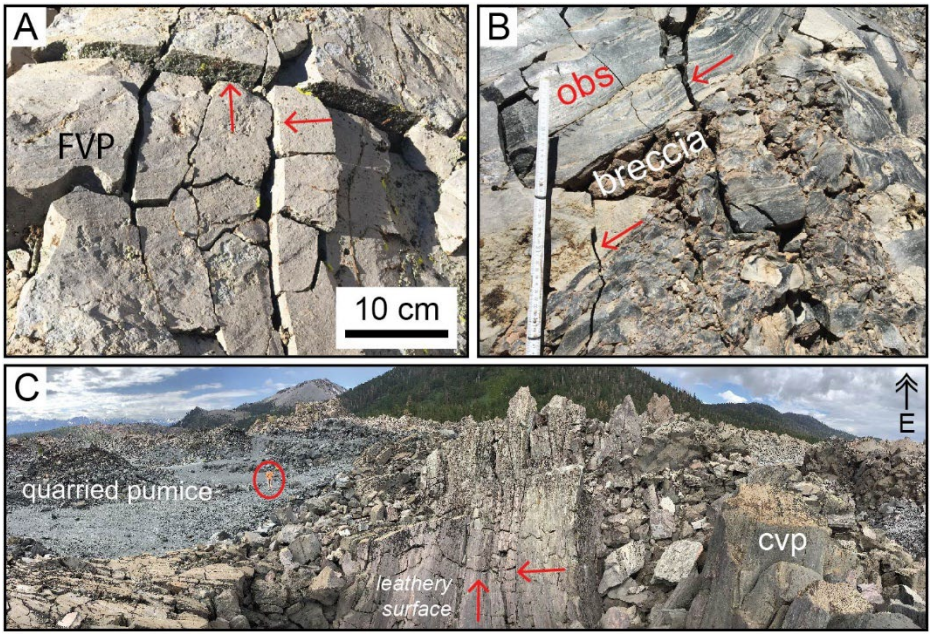

Figure 5. Cracks. (A) Orthogonal sets (red arrows) of vertical fractures, which widen upwards, in FVP. (B) Fractures (red arrows) cutting subhorizontal flow banded obsidian (obs) and breccia. (C) Image looking east towards a large, quarried section of Obsidian Dome, geologist circled in red. Leathery surfaces coat the CVP which is overprinted by orthogonal fracture sets (red arrows).

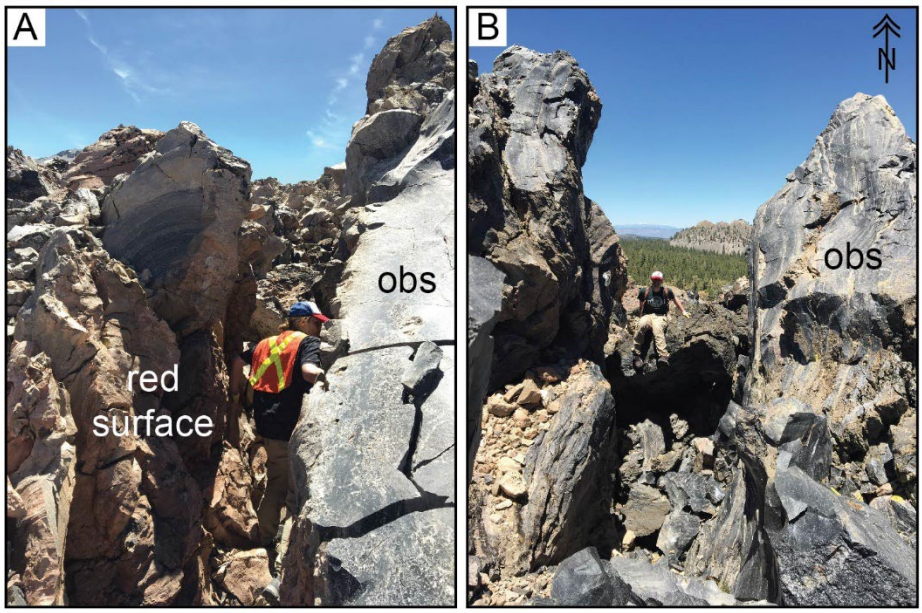

Figure 6. Clefts. (A) Large fracture (~4 m deep and 1 m wide) in obsidian (obs). Red surfaces coat the irregular fracture surface in the obsidian. (B) Deep, V-shaped cleft structure in obsidian.

Figure 7. Crevasses. (A) Red arrow indicates large crevasse in ~8-meter tall FVP. Fracture cuts through the cracked weathered surface of FVP exposing the fresh surface below. (B) V-shaped crevasse (red arrow) in FVP with fracture surfaces. (C) Red arrow indicates crevasse exposing fresh FVP at depth.

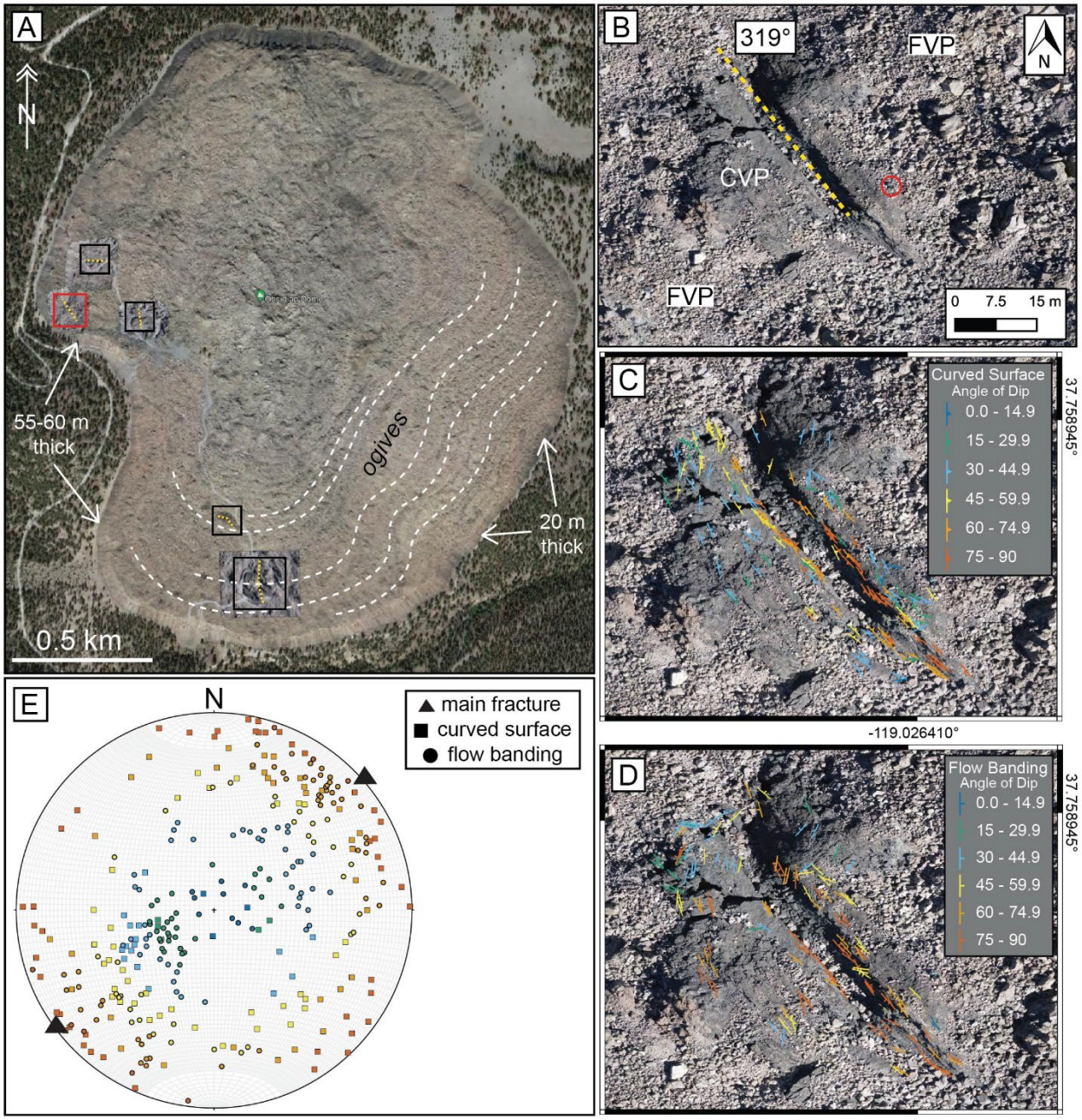

Figure 8. Crease structures. (A) Inset map of Obsidian Dome, rectangles outline the five major crease structures. Orthorectified aerial Images B-D are taken over the crease structure with the red rectangle. Yellow dashed lines indicate the orientation of the crease structures main fracture. Most of the crease structures occur in the thickest portion of the dome and often overprint ogives (white dashed line). (B) Orthorectified aerial image of crease structure in western area of Obsidian Dome, red circle denotes geologist and dashed yellow line indicates main fracture orientation, 319°. (C) Structure map displaying stike and dip measurements of the curviplanar surfaces and (D) flow banding orientation. (E) Stereonet of structural data, with poles representing curviplanar (curved) surface and flow banding with color reflecting the angle of dip used in the structure maps C and D.

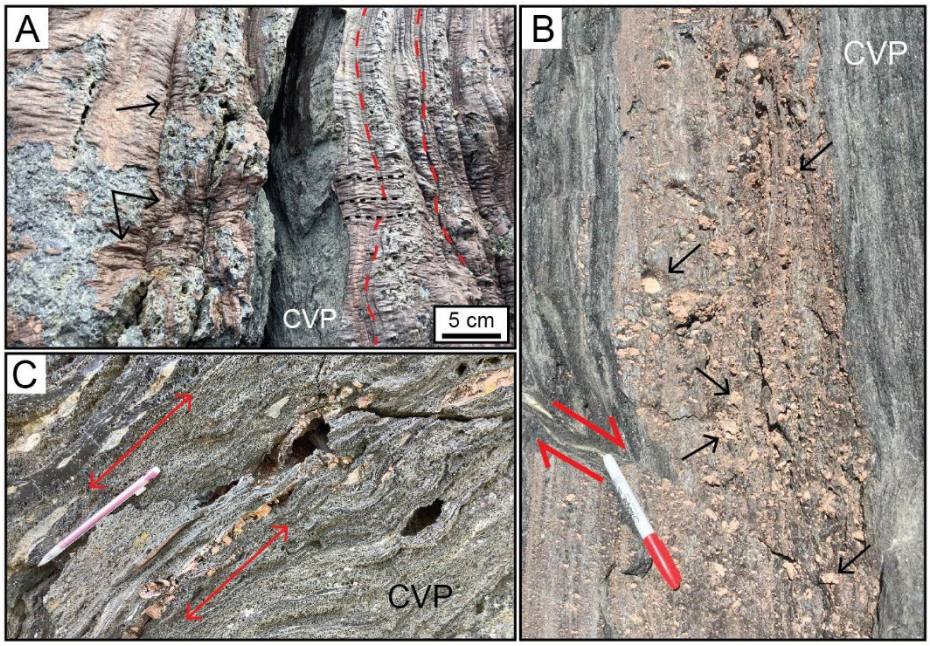

Figure 9. Leathery and tessellated surfaces. (A) Contorted and wrinkled red leathery surface coating CVP. Wrinkled veneer (black arrows and dashed line) runs perpendicular to the vertical flow banding (red dashed line). (B) Flow banded CVP coated in pink veneer with annealed tuff (black arrows). (C) Layers of stretched tesserae (pink tuff) within CVP. Individual tesserae are separated ~1-5 mm and red arrows indicate the orientation of stretching.

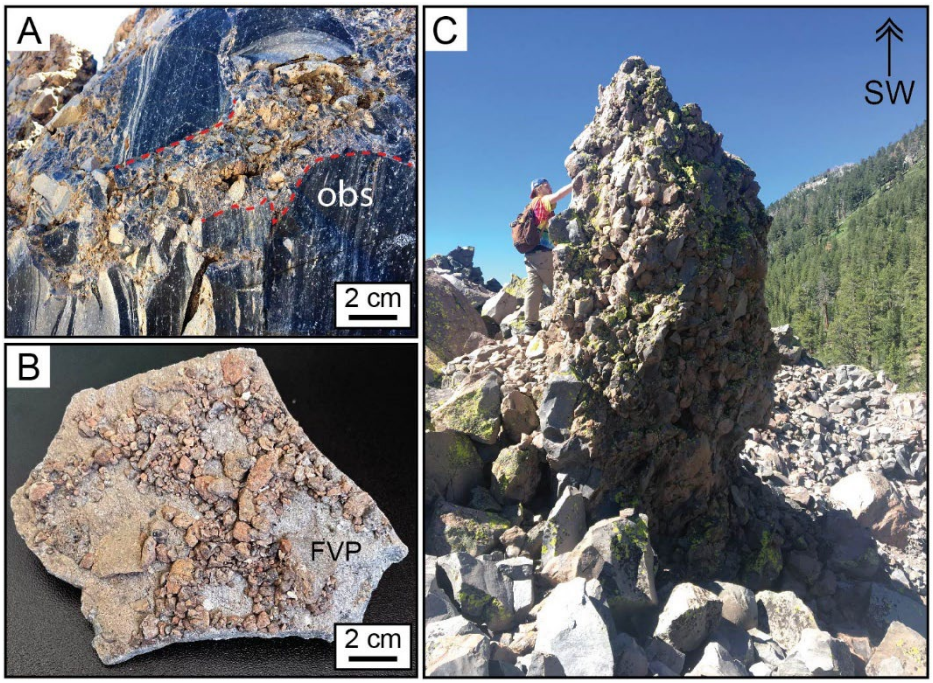

Figure 10. Welded breccias. (A) In situ angular lapilli-sized clasts within narrow fracture of obsidian (obs). (B) Handsample of FVP coated with reddish-orange veneer and annealed ash- to lapilli-sized rounded clasts. (C) 5 m-high pillar of tack-welded, angular, block-sized clasts atop the northwest flow front of Obsidian Dome.

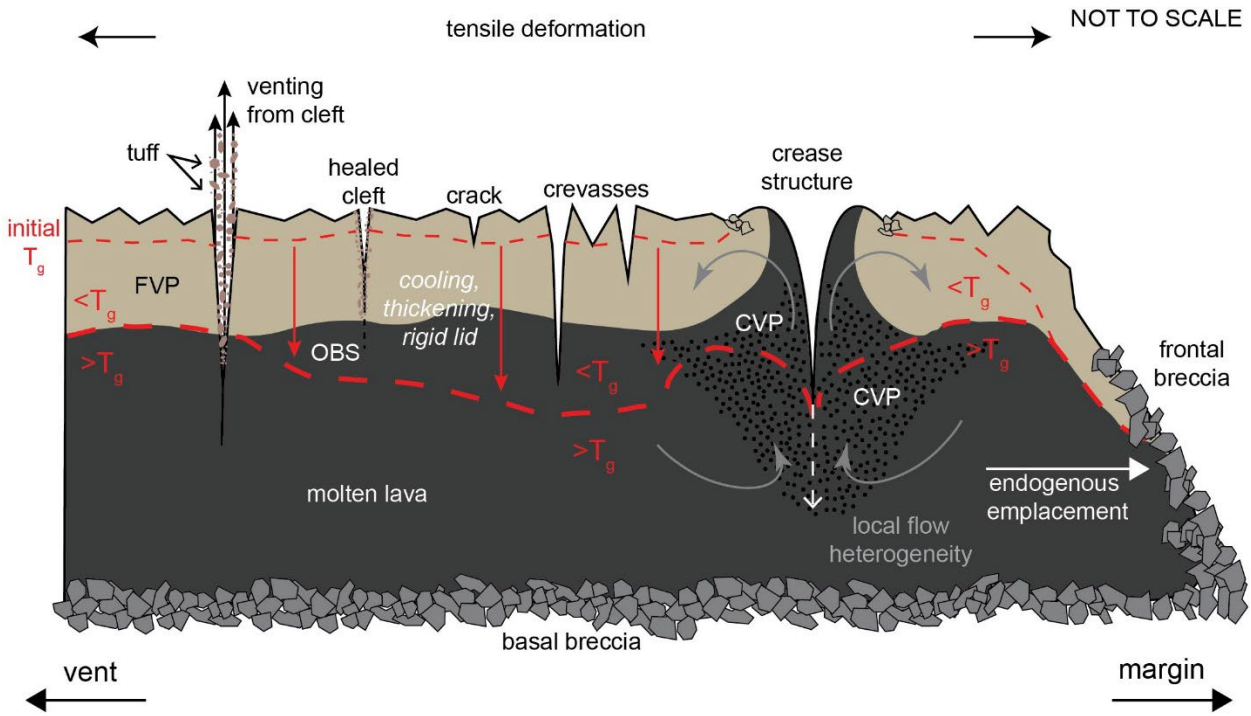

Figure 11. Conceptual diagram depicting the relationships between different fracture classes, the changing rheological conditions, and venting from hybrid behavior. The thin red dashed line approximates Tg when molten lava is first exposed and FVP begins to form. As the lava continues to spread and cool the Tg surface descends and a competent lid forms. Cracks initiate in FVP and grow into clefts that penetrate downwards into obsidian (rigid) or melt, in which case venting of gases and tephra may occur. Crevasses initiate at the upper surface of competent lid and penetrate downwards into obsidian or melt; in which case they evolve into crease structures due to return and upwards flow of melt.

Table 1. Fracture type schema for Obsidian Dome.

Fracture Type	*Planar Fractures*			*Crease Structures (Anderson & Fink, 1992)*
Fracture sub-type	*Cracks*	*Clefts*	*Crevasses*	
ubiquity	ubiquitous	very common	uncommon	uncommon
general scale	small	medium	large	large to very large
spacing apart	very close (≤0.2 m)	close (~1 - 2 m)	moderate (~10 – 20 m)	distant – far distant (≥100 m)
maximum fracture depth	shallow (≤1 m)	moderate (1 - 5 m)	deep (≥5 m)	deep (≥5 m)
maximum fracture length	short (≤2 m)	medium – long (2 – 10 m)	long (≥10 m)	long (≥10 m)
maximum fracture width	narrow (≤0.5 m)	medium (0.5 – 2 m)	wide (2 - 5 m)	very wide (≥5 m)
fracture profile shape	narrow V-shaped	V-shaped	wide V-shaped	wide and flared
fracture symmetry	symmetrical	symmetrical	symmetrical	symmetrical or asymmetrical
fracture surface	irregular or planar	irregular or planar	planar	curviplanar
fracture surface ornamentation	± red leather, ± convolute, ± welded breccia	± red leather, ± convolute, ± welded breccia	± red leather	± striations (Anderson & Fink, 1992) ± tesserae (tessellated surfaces)
topographic expression	no	no	minor	major
lithofacies association	all lithofacies – merges with FVP talus	all lithofacies – merges with FVP talus	FVP & obsidian	CVP & obsidian only – free of FVP talus
interpretation	mode-I tensile fracture	mode-I tensile fracture	mode-I tensile fracture	mode-I tensile fracture modified by viscous relaxation
interpreted relative age	early – late	early - late	middle - late	late only

CHAPTER 3: CHARACTERIZATION AND COMPARISON OF EMPLACEMENT PROCESSES: GLASS CREEK DOME AND OBSIDIAN DOME, CALIFORNIA, USA

Authors: Shelby L. Isom[1]* and Graham D.M. Andrews[1]

Corresponding author: Shelby L. Isom

Projected journal: Geochemistry, Geophysics, Geosystems or Volcanica (open-access international volcanology journal)

Keywords: Morphology, silicic lava, Inyo Domes, Jeffreys equation

Abstract

Analog models are often utilized to constrain the parameters under which certain processes occur. In the 1990s several models were constructed to describe the processes which create the morphological features observable on the surface of Holocene silicic lavas. These models produced morphological domains with associated effusion rates, eruption temperatures and calculated yield strengths. This study classifies the upper surface of 0.6 ka silicic lavas, Obsidian Dome and Glass Creek Dome, Inyo Domes, California using the morphological domains of Fink and Griffiths (1998). Additionally, the flow front structures observed at the active Cordón Caulle lava, Chile are compared to the structures observed at the margins of the two Inyo Domes. Finally, calculated yield strengths and flow advance rates, using Jeffrey's equation, are compared to previous work constraining rates of lava advance using different models (i.e., "Fold Theory"). We find that overall, the slowest advance rates are associated with the *platy* domains whereas the *lobate* domains advanced faster. Additionally, we identify a sequential pattern of emplacement with *platy* domains comprised of aphyric lava being the first to erupt and emplace, followed by the crystal-poor, crystal-rich, and microcrystalline mingled lava of the *lobate* domains. The last to erupt is the *spiny* domain, which is comprised of microcrystalline rhyolite. Additionally, we find an overall correlation between surficial morphology, flow front lithofacies and structures, and rates at which the Obsidian Dome and Glass Creek Dome lavas advanced.

1.0 INTRODUCTION

Prior to the first ever witnessed eruptions of two silicic lava flows, Chaitén and Cordón Caulle in Chile, all interpretations of silicic lava emplacement styles, longevity of the flow, and hazards associated with the eruptions came from observations of prehistoric silicic lavas and analog modeling. Morphological and structural observations, most notably, took place at the Holocene silicic lavas of California and Oregon (e.g., Fink, 1983). There is noted absence in the correlation between silicic lava morphology produced by analog modelling, structural observations of active flow fronts, and numerical models which calculate yield strength and flow rates (i.e., Magnall et al., 2019). This study characterizes the upper surface and flow fronts of two coeval lavas, using the morphology classification of Fink & Griffiths (1998) and the structural features of Magnall et al. (2019) observed at the 2011-2012 Cordón Caulle, Chile lava flow. With the aid of studies from active silicic lavas and laboratory experiments modeling silicic lava emplacement we attempt to constrain emplacement processes, yield strength, and 2D flow advance rate of two prehistoric silicic lava domes (Obsidian Dome and Glass Creek Dome) a part of the Inyo Chain, California, USA (Fig. 1). Obsidian Dome and Glass Creek Dome erupted simultaneously, ~0.6 ka, onto vastly different topographies and are comprised of variable amounts of chemically different lavas, providing an excellent case study to compare the control of underlying topography and composition (i.e., crystallinity) on the morphologies, flow front structures, and emplacements styles of effusive silicic lavas.

1.1 Observations from Active Silicic Lavas

There are two broad emplacement processes associated with silicic lavas: endogenous inflation and exogenous or tank track. Emplacement of lava through endogenous inflation occurs when the internal core remains hot and ductile allowing advance through inflation and break out lobes at the flow front (Tuffen et al., 2013). The movement of the lava through endogenous inflation relies on a hot ductile core. The core remains hot and ductile due to the insulating solidified carapace and base of the lava. As the core cools and solidifies (effectively increasing its yield strength) the lava ceases to move (Castruccio et al., 2010; Magnall et al., 2017).

Whereas the emplacement of lava through the exogenous or tank-track process occurs as young lava is supplied from the vent and is pushed onto the upper surface, rafting along until it falls down the flow front, and is cannibalized. This is typically observed in basaltic ’a’ā lavas

(Applegarth et al., 2010; Farquharson et al., 2015; Harris et al., 2002). This emplacement style is controlled by the flux and viscosity of the new erupted material at the vent. If the lava supplied becomes too viscous it has the potential to plug the vent and cease further emplacement (Castruccio et al., 2013; Farquharson et al., 2015; Magnall et al., 2017, 2019). Both emplacement processes (endogenous and exogenous) were documented for the first time to occur simultaneously during the 2011-12 eruption of Cordón Caulle, Chile (Tuffen et al., 2013; Farquharson et al., 2015). Most remarkably was the observation that after the eruption of fresh lava at the vent ceased the lava continued to move for eight more months.

1.2 Morphological Classification of Cordón Caulle Breakouts

It is observed that basaltic pahoehoe lavas advance through stages of inflation and break out, creating breakout lobes, but they behave more like a Newtonian fluid due to their low viscosities and crystal cargoes (McBirney & Murase, 1984). These more mafic lavas are dependent on active lava supply from the vent to drive their endogenous advance (Walker, 1991). On the other hand, silicic lava has several orders of magnitude higher viscosities and can act more as a Bingham fluid where there is a yield strength that first must be exceeded for them to flow (Griffiths & Fink, 1997). Recently, analog models and observations from active lavas show that both basaltic and rhyolitic lava flows may advance similarly, despite their different rheology (e.g., Ishibashi & Sato, 2010; Magnall et al., 2017).

During the 2011-12 eruption of the Cordón Caulle, Chile lava researchers noted that several lobes of the lava were active at one time. Furthermore, these “breakout lobes” were advancing similarly to pahoehoe lavas, through inflation and endogenous emplacement (Farquharson et al., 2015; Magnall et al., 2019; Tuffen et al., 2013). Detailed observations of the breakout lobes at the flow front revealed morphological properties associated with endogenous emplacement, local effusion rates, and inflation (Magnall et al., 2019). The morphology types described at the active flow fronts of Cordón Caulle are *domed*, *petaloid*, *rubbly*, and *cleft-split*, which develop in an evolutional continuum where *domed* morphology progresses to *cleft-split* with increasing inflation. The *domed* morphology is generally wider than tall, jig-saw fit dome-like structures which can grade into *petaloid* morphology as inflation upturns slabs resulting in steep spines (Magnall et al., 2019). The *rubbly* morphology results from disruption of slabs creating talus and block strewn rubbly covered surfaces. The *cleft-split* morphology is described

as resembling “lava-inflation clefts”, or splayed fracture surfaces which expose fresh lava, identified on Hawaiian basalts (e.g., Walker, 1991). These morphologies all indicate that advance of the Cordón Caulle lava occurred generally endogenously at the flow front with inflation driven by local vesiculation and flow front collapse (Magnall et al., 2019).

1.3 Insights from Modelling of Silicic Lavas

Analog experiments carried out in the late 1990s simulated the surficial morphology of silicic lavas and their relationship with emplacement styles (endogenous vs. exogenous) (Fink & Griffiths, 1998; Griffiths & Fink, 1997). Lava dome growth was modeled using a mixture of polyethylene glycol wax and kaolin powder injected into a tank of water. Experimental constraints such as tank water temperature and rate at which the mixture was injected into the tank were varied producing distinct morphological profiles (Fig. 2; Griffiths and Fink, 1997). The morphological classes defined by Fink and Griffiths (1998) modeled the dependence of growth rate with respect to rate of effusion, magma rheology, and thickness of the cooling surface. Each morphology yields a range in the dimensionless number Ψ_b, which allows the estimation of yield strengths associated with each morphology (Fig. 2A; Fink & Griffiths, 1998). There is a progressive increase in interior yield strength seen from the *platy* to *lobate* to the *spiny* morphologies, which is reflected by the relief produced (Fig. 2B-D; Fink & Griffiths, 1998; Griffiths & Fink, 1997).

The resulting morphologies were classified into four categories based on the effusion rate (injection rate) and the temperature of the tank water. High temperatures and effusion rates generated morphologies classified as *platy* and *axisymmetric* (Fig. 2B & E), while lowering the temperature and maintaining a high effusion rate resulted in the *lobate* morphology (Fig. 2C & F), and low effusion and low temperature created a *spiny* morphology (Fig. 2D & G). Morphological groups display a variation of endogenous, exogenous, and a combination of the emplacement processes during modeled eruptions. The *lobate* and *platy* morphology shows initial endogenous inflation generating discrete lobes which then advanced exogenously. The lobes display subhorizontal flow-parallel striations and in areas of extension paired, curviplanar fracture surfaces (crease structures) develop (Anderson & Fink, 1992). While the *spiny* morphology is entirely emplaced endogenously, generating tall, steep sided, subvertical spines

usually noted over the vent (Fink & Griffiths, 1998). The *axisymmetric* morphology is emplaced through a combination of endogenous and exogenous processes.

2.0 GEOLOGIC BACKGROUND

Punctuated and often simultaneous rhyolitic and basaltic volcanism has occurred over the last ~4.4 Ma in the Long Valley volcanic region, with some of the youngest eruptions occurring along the N-S trending Inyo Volcanic Chain (Bailey, 1989; Hildreth, 2004). Following the cataclysmic eruption of the Bishop Tuff, over the last ~750 ka, volcanism was concentrated within and to the west of the Long Valley caldera (Fig. 1A).

The youngest volcanism in the Long Valley volcanic region occurs along two, polygenetic, en-echelon lines of Holocene rhyolite - rhyodacite lavas and craters: the Inyo Chain and Mono Craters chain (Fig. 1B: Bailey, 1989). The Inyo Volcanic Chain is comprised of seven rhyolite – rhyodacite silicic lavas and several phreatic explosion craters. The oldest domes, North Deadman Dome (~4 ka) and Wilson Butte (~1.3 ka), are crystal-poor high silica rhyolites covered in vegetation (Miller, 1985). Two aphyric small domes (<0.001 km^3), Cratered Dome and Caldera Wall Dome erupted after Wilson Butte but neither have been age dated. Around ~600 years ago three silicic lavas erupted from a N-S trending dike within the Inyo Volcanic Chain (Blake & Fink, 1987). The two small domes are covered in tephra from the 600-year-old lava domes suggested they post-date at least 0.6 ka (Hildreth, 2004). From North to South the youngest simultaneous eruptions are Obsidian Dome, Glass Creek Dome, and Deadman Dome.

The 0.6 ka Inyo Domes display a complex compositional range with two textural and chemical endmember lavas erupted in variable amounts (Sampson, 1987; Sampson & Cameron, 1987). The textural distinct lavas are divided into crystal-poor and crystal-rich endmember groups with the crystal-poor lava containing <6 % crystals and the crystal-rich lava containing >12 % and up to 40 % crystals often with feldspar megacrysts (~5 to 25 mm) (Fig. 3A). Volumetrically the surface of Deadman Dome is dominantly composed of the crystal-rich lava (~50-70 %) while the only relic of the crystal-rich lava at Obsidian Dome is the occasional large feldspar megacryst found in the microcrystalline rhyolite over the center of the dome (Fig. 1B). Glass Creek Dome's surface is made up of ~30-50 % of the crystal-rich lava intermixed with the crystal-poor lava (Sampson, 1987). The emplacement of a density stratified dike is the potential

source of the variable amounts of the different chemical and textural lavas the 0.6 ka Inyo Domes erupted (Blake & Fink, 1987).

Four lithofacies, based on vesicularity, are described at the 0.6 ka Inyo Domes: coarsely vesicular pumice (CVP), finely vesicular pumice (FVP), avesicular obsidian, and microcrystalline rhyolite (Fink, 1983). The endmember textures (crystal-rich and crystal-poor) can be found in all lithofacies (Fig. 3A). CVP is dark olive green to dark brown with large, often stretched, vesicles and a porosity between 20-80 %. FVP is often beige to gray in color with small spherical vesicles and porosities between 30-40 % (Fink, 1983). Avesicular obsidian is glassy, dense, and not porous (Fig. 3B). The CVP, FVP, and obsidian readily grade from one another while the microcrystalline rhyolite is only found in discrete boudins in banded FVP and over the vent as dense spines.

3.0 METHODS

3.1 Field Data Collection

We collected textural and structural data at Obsidian Dome and Glass Creek Dome over two field campaigns in the summers of 2018 and 2019. A workflow following *Isom et al. (2022b)* was utilized to map the lithofacies, textures, and structures on the upper surface and at the flow fronts of Obsidian Dome and Glass Creek Dome. Images and strike and dip measurements were collected using the digital geological mapping software *FieldMove* (Petroleum Experts, 2020) operated on ruggedized Apple *iPad 4 mini* tablets. We documented structures observed at the upper surface and the flow fronts of both domes. A high-resolution (<10 cm^2/pixel-resolution) orthorectified basemap of Glass Creek Dome was provided by Tyler Leggett and allowed for precise mapping of the upper surface. Whereas the Landsat imagery was utilized as a basemap for Obsidian Dome as we did not have access to a high-resolution image.

3.2 Morphometric Analyses

We calculated the minimum yield strength of the margins of each dome based off estimated underlying topographic slope, using Google Earth (Fig. 4A). We defined four quadrants based on underlying slope and morphological domains at Obsidian Dome and Glass Creek Dome (Fig. 9). We took five height measurements using Google Earth from the flow fronts of each quadrant at each dome. We estimated underlying slopes using the rise and run of a

likely flow path from the center of the dome over the inferred conduit. Intersections between two slopes in different orientations were not considered (Fig. 4A).

Yield strength (Pa) estimates:

$$yield\ strength\ = \frac{h * g * \rho}{\sin(\alpha)}$$

Where *h* is thickness of the lava at the flow front or the height (m), ρ is density (kg*m^{-3}), and α is the slope angle. This equation yields a maximum down-slope stress on the lava.

To estimate rates at which Obsidian Dome and Glass Creek Dome were emplaced we used Jeffreys equation, which estimates the flow advance rate in 2D with known slope, viscosity, and density (Fig. 4B).

Flow advance rate using Jeffreys equation (Jeffreys, 1925):

$$v = \frac{\rho g h^2 \sin(\alpha)}{3\mu}$$

Where ρ is density (kg*m^{-3}), *g* is acceleration of gravity (m*s^{-2}), *h* is height (m), α is the slope angle, and μ is the viscosity (Pa s). The density of the Obsidian Dome lava is known and reported in Andrews et al. (2021), we used the density value, 2241 kg.m^{-3}, which considers that the lava was mainly (~90 %) obsidian with an upper FVP carapace (~10 %).

The viscosity of a magma is dependent upon the temperature, chemical composition (silica content), crystallinity, and volatile content (Harris & Rowland, 2009). We calculated viscosity considering an average crystallinity of 25% for the crystal-rich lava and 5% crystallinity for the crystal-poor lava using the "GRD" model of Giordano et al. (2008). The GRD model estimates viscosity using multicomponent chemical modelling to within an RMSE of ~0.4 log units (Table 1). We used the quantitative glass compositions of the crystal-poor and crystal-rich Obsidian Dome and Glass Creek Dome lavas from *Isom et al. (2022a).* Viscosity calculations of the crystal-rich glasses were ~5 times larger than that of the crystal-poor glasses. The viscosities calculated using the GRD model are a magnitude higher than the viscosities calculated using the crystal-poor obsidian and FVP from Obsidian Dome in Andrews et al.

(2021) (Table 1). We utilize both in estimates of flow advance rate to compare maximum and minimum rates of advance.

4.0 OBSERVATIONS & DATA

The 0.6 ka Obsidian Dome (OBD) and Glass Creek Dome (GCD) are post-glacial, and lidar imagery reflects the underlying topography on which they erupted. OBD was relatively unimpeded to the east as it flowed down a flat gently dipping slope. While the thickest ponded portions lie in the northeast and northwest flowing down a paleovalley and abutting against faulted Cretaceous granite and Pliocene basalt, respectively (Bailey, 1989). The Glass Creek marks a divide from OBD to the north and GCD to the south. GCD erupted on complex topography between the Cretaceous granite peak (White Wing Mountain: ~3000 m tall) and an elevated hilltop (~2500 m tall) made up of Pliocene basalts topped with till and pyroclastic fall and flow deposits (Fig. 4A). The lava of GCD flowed south constrained by its W-E topographic obstacles onto the Long Valley caldera floor, covering an older trachydacite lava and abutting against an older trachydacite dome (Bailey, 2004).

Utilizing Landsat imagery and the orthorectified base map of GCD we identify three morphological domains (*spiny*, *lobate*, and *platy)* on the surface of OBD and GCD, using the classification of Fink & Griffiths, (1998). Additionally, outcrop structural measurements and observations at flow fronts are discussed using the terminology of Magnall et al. (2019). Utilizing estimated slope measurements and calculated viscosities we discuss the yield strengths and advance flow rates of each domain.

4.1 Morphological Domains

4.1.1 Obsidian Dome

Three distinct morphological domains are observed from Landsat aerial imagery of OBD and confirmed with outcrop-scale observations, they are: *spiny*, *lobate*, and *platy*. The estimated area covered with respect to each domain exclude areas of pumice mining, visible as light-colored tracks winding across the surface (e.g., the western portion of OBD: Fig. 5A).

We define the center portion of OBD as *spiny*, which agrees with the observations of Fink & Griffiths (1998). Aerially the large coherent blocks forming the central domain are observed as the topographic high (~2,600 m asl) across the entire dome. A color difference is

also noted with the center appearing as light gray while the rest of the dome is dominated by pinks, beiges, and dark browns (Fig. 5A). The center of OBD is defined by tall, ~12 to 15 m, spines of microcrystalline rhyolite that are bounded by deep fractures (Fig. 5B). The large spines display vertical to subvertical flow banding and appear as coherent squeeze-ups through the talus. The microcrystalline rhyolite displays puffy flow banding and often contains feldspar antecrysts (~5 – 25 mm in length: *Isom et al., 2022a*). The central spiny domain makes up ~15 % of the upper surface.

The *platy* morphology dominates the eastern portion of OBD where the surface has the lowest relief, ~20 m-thick, and is most brecciated. This domain is characterized by 20 to 35 m-spaced, gently anastomosing, parallel ridges and intervening troughs of FVP (Fig. 5A). Obsidian is observed randomly on the upper surface, but is generally found at the eastern flow front, comprising ~5m thick outcroppings protruding from the talus slope. The relief between ridge axis and trough axis is ~3 – 10 m. Relief and spacing between adjacent ridges and troughs decrease toward the margins. The *platy* domain is the most aerially extensive morphological domain covering ~45 % of the upper surface and forming a continuous region fringing the central *spiny* domain from the northeastern clockwise to the southwest (Fig. 5E). Its highest elevation is ~2,554 m asl on the southeastern boundary and it slopes down gradually to a minimum elevation of ~2,475 m asl at the eastern and northeastern margins. When traversing the *platy* domain, the ridges and troughs seen aerially are felt by the exertion of traveling up over highs and down into lows, but one can only see large boulders and slabs chaotically positioned across the surface.

The morphological classification of the western fringe of OBD is *lobate*. The surface is less littered with small blocks, compared to the *platy* domain, and is instead composed of larger (≥5 m) subvertical pillars and domes (Fig. 5D). The more coherent pillars and dome structures are often comprised of banded FVP and microcrystalline rhyolite. Obsidian is generally found at the flow fronts and constitutes the lobe-like outcroppings. The *lobate* domain is the second most extensive covering ~40 % of the dome. Aerially, dark brown domal shapes cut by fractures are observed in this domain (Fig. 5A). Unlike the eastern margins, the flow front outcroppings are larger and more lobe-like sitting ~20 m above a talus slope. Only in this domain are CVP crease structures observed in outcrop (dark brown structures seen aerially) (Anderson & Fink, 1992).

Crease structures are paired curviplanar surfaces emerging from a central fracture and are characteristic of the *lobate* morphology (Fig. 5C; Fink & Griffiths, 1998). In this domain five discrete crease structures are observed, several have been heavily altered by mining operations in the last several decades (Eichelberger et al., 1984).

4.1.2 Glass Creek Dome

The central domain of GCD is characterized as *spiny*, consisting of ~30 % of the upper surface, which is significantly larger than the domain at OBD. Identifiable in aerial imagery is a four-leaf clover like distribution of the large spines protruding over the inferred NNE-SSW dike in a radial pattern, with the tallest being ~2615 m asl (Fig. 6A). In profile view the spines are conical in shape. In outcrop the scale of the spines at GCD are immensely larger (~15 m – 20 m) and structurally resemble the famous whaleback-shaped structure, erupted during the renewed activity at Mount St. Helens, Washington, USA in 2004-05 (e.g., Major et al., 2005). Small (<1 m^2) blocks and tephra fill in the areas between the spines. More tephra and lapilli-sized talus is noted at GCD relative to OBD, reflected in the large amount of vegetation on the surface of GCD (e.g., Fig 4C). The large spines are dominantly comprised of the crystal-rich lava that can be vesicular to dense. Where dense it is generally vertically flow banded and a bluish color (Fig. 6B).

The *platy* domain is constrained to the western margin of GCD where the lava abuts against the Cretaceous granite of White Wing Mountain. The *platy* domain makes up about 25 % of the upper surface. In profile there is an observable break in slope between the *spiny* and *platy* domains (Fig. 6C). In outcrop the domain is characterized by platy, broken blocks of crystal-rich and crystal-poor obsidian and FVP. Obsidian is also observed as discrete lobes banded with microcrystalline rhyolite. The western flow front is generally ≤6 m in height except for the southern margin, which is >6 and ≤ 30 m.

The north, eastern, and southeastern margin of GCD is classified as *lobate* constituting the remaining ~47 % of the dome. The domain is not rubble covered like the *platy* domain and instead in the west has large coherent blocks (~600 to 1000 m^2) with curviplanar surfaces protruding through the tephra and small block covered canopy. The coherent blocks are generally comprised of banded crystal-rich FVP and dense microcrystalline rhyolite. An E-W trending depression revealing the only CVP crease structure at GCD is bounded by ~10 m tall pillars and

uptilted blocks (Fig. 6D). The crease structure is ~200 m long with one well developed curviplanar surface which extends to the North.

4.2 Flow Front Structures

Detailed measurements of structural features and observations were done around the flow fronts of Obsidian Dome and Glass Creek Dome to identify morphological structures and attempt to classify advancement styles.

4.2.1 Obsidian Dome

The northeast and northwest flow front of OBD is ~20-50 m thick, with a large talus apron that grades into thick (~10-25 m) outcroppings of banded obsidian. The obsidian is horizontally to sub-horizontally flow banded with boudins of microcrystalline rhyolite and capped with FVP (Fig. 7C). Sitting atop the flow front, several meters in from the edge, large coherent blocks of vertically banded obsidian are identified. Additionally, *domed* and *petaloid* structures comprised of FVP are noted in this area. The northwestern flow front is the only region of OBD where spherulites have been identified in outcrop.

The east and southeastern flow front differs significantly from that of the north. The southeastern flow front is ~15-20 m thick with thin (≤5 m) outcrops of scoriaceous obsidian protruding from the talus fringe (Fig. 7B). Often noted are dark red veneers coating the obsidian and annealed tuff to lapilli-sized clasts (e.g., *Isom et al., 2022b*). *Domed* and *petaloid* structures are noted in FVP, which tops the obsidian. The obsidian is not banded with microcrystalline rhyolite and readily grades into the FVP carapace.

The *lobate* (west) and *platy* (east) morphological domains display vastly different flow front structures and lithofacies. Microcrystalline rhyolite is only observed banded with obsidian in the *lobate* domain, while *petaloid* structures are frequently noted in the FVP of both domains.

4.2.2 Glass Creek Dome

The northern flow fronts appear to be the thickest and are associated with the *lobate* domain. Lenses of obsidian (~5-10 m thick) outcrop above the talus, like the western flow front of OBD. The obsidian is often horizontally flow banded and displays *petaloid* structures (Fig. 8B). The flow fronts are generally capped in a FVP carapace. An abrupt change in lithofacies

and structures are observed as you travel from the northern flow front downslope along the western edge into the *platy* domain (Fig. 8F).

The western flow front of GCD is rarely thicker than 6 meters and often displays alteration as blocks are stained a variety of yellow, orange, and red colors (Fig. 8F). Overall, the flow front is a jumbled mess of obsidian and crystal-rich FVP, resembling the *rubbly* structure, with no coherent outcroppings of obsidian like that of the west and east flow fronts of OBD. The flow front structures shift again as you move further south, where the lava once traveled down slope to the caldera floor. Here *petaloid* obsidian and FVP structures are observed, and alteration is less prevalent. Coherent lenticular outcrops of obsidian are absent from the western flow front.

The eastern flow front has a maximum thickness of ~50 m at the southeastern edge where the lava advanced down the eastern topographic high and a minimum thickness of ~ 8 m at the northern extent, in a preserved tephra ring (e.g., Fig. 8A; Heiken et al., 1988). The outcrops are *domed* in structure and comprised of obsidian banded with microcrystalline rhyolite (Fig. 8C). The east facing obsidian surfaces are coated in a thin red veneer, possibly indicating alteration. Traveling from the tephra ring, south down the eastern margin the flow front structures begin to shift. The thickness of the lava increases to ~30 m and is generally comprised of upturned slabs (*petaloid* structures) of microcrystalline rhyolite banded with obsidian (Fig. 8D).

The southern flow front of GCD displays a gradation from base to top of scoriaceous obsidian, glassy obsidian banded with microcrystalline rhyolite, to crystal-rich FVP (Fig. 8D). *Petaloid* structures are noted at the top of the flow front. Regions of dark red tuff annealed to lithofacies surfaces, (e.g., *Isom et al., 2022b*) are often exposed at the southern flow front. Large blocks (~ 50 m^2 exposed) are observed precariously perched atop the talus scree, seemingly detached from the coherent flow front outcrop.

Much like that of OBD, the eastern and western flow fronts of GCD display opposing lithofacies and structures. At GCD banded obsidian and microcrystalline rhyolite are only identified at the flow front in the *lobate* domain. While the *platy* domain flow front is characterized by altered jumbled lithofacies.

4.3 Flow Advance Rate and Yield Strength Calculations

Yield strength calculations of the flow fronts of OBD and GCD reveal generally higher yield strengths for the *lobate* morphology, ~10^7 Pa for OBD, and ~10^6 Pa for GCD (Table 2). Whereas the *platy* morphology has generally lower yield strengths with OBD values ~10^6 Pa and ~10^5 Pa for GCD. The calculated yield strengths of this study are a magnitude larger than that of the morphological yield strengths of the *platy* and *lobate* domains constrained by Fink and Griffiths (1998) (Table 2).

Regardless of morphological domains, the calculated yield strength (Pa) differs between OBD and GCD, with maximum value of 2.5*10^7 Pa at OBD whereas at GCD the maximum yield strength is a magnitude lower at 5.5*10^6 Pa (Table 2). Although yield strength calculations do not factor-in chemical or textural (crystallinity) variations directly, this is an implicit reflection of the chemical and textural difference between OBD and GCD.

The rate of flow advance (m/day) calculated using Jeffreys equation, differs significantly with the viscosity measurements from this study and those of Andrews et al. (2021). This study takes into consideration the chemical and temperature variations between the crystal-rich and crystal-poor lavas of each dome, resulting in more accurately constrained viscosities (Table 1). Calculating advance rates using Jeffreys equation is often utilized to model the 2D advance of lava down a slope. However, Jeffreys equation mathematically models the flow of water through a rectangular channel. Thus, the equation does not take into consideration the temperature of the lava, the solidifying carapace, nor the flux from the vent. Therefore, the advance rates calculated in this study are a minimum estimate of the rate of advance of OBD and GCD. We find that overall, the E and W *platy* domains at OBD and GCD, respectively, advance the slowest at <2 m/day (Fig. 9). The *lobate* domains at each dome have faster advance rates, with an average of 6 m/day at OBD and 25 m/day at GCD (Fig. 9).

5.0 DISCUSSION

Overall, the upper surfaces of OBD and GCD display similar morphological domains. OBD has a larger *platy* region, which makes up the entire eastern portion of the dome whereas the *spiny* domain of GCD is more extensive and the individual spines have more surface area than that of OBD. The modeling of Fink & Griffiths (1998) estimated yield strengths associated with each morphology. The *spiny* morphology has the highest yield strength and *platy* with the

second lowest, this is reflected in our calculations as well (Fig. 2 & Table 2). The flow fronts of OBD and GCD are superficially similar, with obsidian being the dominant outcropping lithofacies often topped with FVP. Coherent lenses of obsidian are indicative of the flow fronts of OBD and less prevalent, except in the north, at GCD. The *petaloid* structures are identified at all flow fronts observed and *domed* structures are identified on the upper surface of both lavas.

5.1 Morphology Comparison and Emplacement Implications

The morphological domains of Fink & Griffiths (1998) are associated with different effusion rates, eruption temperatures, and emplacement styles. The *lobate* morphology is described as occurring initially exogenously as the lava is erupted onto the surface followed by noted inflation and a shift to endogenous emplacement of individual flow lobes (Fink & Griffiths, 1998). Whereas the *platy* morphology forms mainly by endogenous emplacement which stretches and fractures the upper surface during advance, creating the characteristic block strewn surface. The analog model parameters constrain *platy* morphologies to high effusion rates and eruption temperatures while *lobate* morphologies occur at lower temperatures and high effusion rates. The *spiny* morphologies occur at lower temperatures and effusion rates having the largest yield strengths. Our calculations agree with the effusion and temperature parameters of the *lobate*, *platy,* and *spiny* morphologies (Fig. 9).

The *lobate* domain at both domes is characterized by flow fronts of banded crystal-poor (and crystal-rich at GCD) obsidian and microcrystalline rhyolite. Furthermore, the *lobate* domains were emplaced upon steeper slopes resulting in faster calculated advance rates. The *platy* domain of both domes is dominated by crystal-poor lava, which has higher estimated eruption temperature and lower calculated viscosity (Table 1). The *platy* domains at both domes were emplaced upon relatively flat topography resulting in the slowest estimated advance rates (Fig. 9). The *spiny* morphologies at each dome occur over the inferred vent. We did not calculate yield strength of the *spiny* region, but modeling has shown that volcanic rocks with low porosities will have higher yield strengths (~17 MPa at porosities <10 %; Heap et al., 2021), which is potentially reflected in the dense microcrystalline spines within the *spiny* domain of each dome.

There appears to be a correlation between the flow fronts comprised of banded microcrystalline rhyolite and obsidian with the *lobate* morphology at both domes. The banded

obsidian is restricted to the northwestern flow front of OBD and found at all flow fronts within the *lobate* morphology of GCD. Conversely, the flow fronts within the *platy* domains lack the inclusion of microcrystalline rhyolite. Large coherent blocks of microcrystalline rhyolite are only found over the vents at each dome. Furthermore, drill cores penetrating the conduit of OBD show the dense microcrystalline lava extending hundreds of meters below the surface emphasizing that this lithofacies was the last to erupt (Eichelberger et al., 1984; 1985).

If OBD and GCD erupted from a density stratified dike, as is hypothesized (e.g., Blake & Fink, 1987), the first erupted material would be the crystal-poor lava, followed by and mixed with (at GCD) the crystal-rich lava with the microcrystalline rhyolite being the last to erupt. Therefore, we attempt to loosely place temporal constraints on the emplacement of each domain. We suggest the *platy* domain was the first erupted and emplaced, followed by the more long-lived emplacement of the *lobate* domain. The microcrystalline rhyolite is the last lithofacies erupted over the vent constituting the *spiny* domain. Furthermore, we suggest the *lobate* domain was emplaced after the *platy* domain based off the inclusion of microcrystalline rhyolite.

5.2 Emplacement Timescales

Calculating advance rates with Jeffreys equation omits the influence of mass flux from the vent that ultimately leads to the longevity of the eruption as well as the length at which the lava will travel (Walker, 1973) Whereas other studies suggest the importance of insulation provided by a thick carapace further extends the length in which the lava will travel (Harris & Rowland, 2009). Thus, the calculations of this study are first-order with qualitative correlations between morphology, flow front structures, and advance rates.

The timescales of emplacement calculated using Jeffreys equation at OBD and GCD show quick advancement recorded in the *lobate* domains and slower advancement recorded in the *platy* domains (Fig. 9). As Jeffreys equation is dependent on slope down which the lava travels this correlation is thus intuitive as the *lobate* domains were emplaced upon steeper slopes. Leggett et al. (2020) calculated timescales of emplacement for several silicic lavas using the surface-folding model of Fink (1980). Leggett et al., (2020) calculated a surface viscosity for OBD and GCD, which is five orders of magnitude higher than our GRD viscosity calculations (Table 1).

Overall, we calculate slower advance rates for OBD with respect to GCD, but our average emplacement rates are much quicker than that of Leggett et al. (2020). The discrepancy initiates from the vastly different calculated viscosities between the studies (Table 1). Leggett et al. (2020) calculated viscosity using the model of Fink (1980) resulting in a surficial viscosity calculation of $10^{12.8}$ and $10^{13.1}$ (Pa s) and interior viscosity of $10^{10.1}$ and $10^{11.4}$ (Pa s) for OBD and GCD, respectively (Table 1). Utilizing the estimated surficial viscosity in our advance rate calculations resulted in extremely slow advance rates for OBD and GCD on the order of <5 m/year. Advance rates calculated using the interior viscosities were quicker between 0.5 and 5 m/day (Table 2).

Furthermore, difference between our study and that of Leggett et al. (2020) could potentially be because we consider (and calculate) the domes to have four separate lobes (quadrants) that require individual calculations; in contrast, Leggett et al. (2020) models the advance of each dome as a single unit. Moreover, the surface-folding model (Fink 1980) is likely an inappropriate starting point because the upper surface is not folded (Andrews et al., 2021), and Biot's Law does not apply to extended, fractured media.

6.0 CONCLUSIONS

This study relates the upper surface morphology, flow front structures, and estimated rates of emplacement at Obsidian Dome and Glass Creek Dome. We note a correlation between morphology and lithofacies observed at the flow fronts, where *lobate* morphologies display banded obsidian and microcrystalline rhyolite and *platy* morphologies do not. A relationship between slope and morphology is noted where *lobate* develops on higher slopes while *platy* develops on lower slopes. Furthermore, rates at which the flow advances correspond to their morphological domains, with the quickest estimated emplacement occurring in *lobate* domains whereas slower rates were calculated for *platy* domains. This is the first study to combine the morphological domains characterized and modeled by Fink and Griffiths (1998), the structural observations from an active silicic lava's flow front, and calculations of the rate of advance for the Holocene Inyo Domes. Future work could apply these methods to silicic lavas with homogenous chemical and textural lavas to tease out if the correlation we see is more dependent on the underlying topography or the composition.

ACKNOWLEDGEMENTS

The authors sincerely thank the field assistance of Levi Fath and Holly Pettus. This research was supported by the National Science Foundation through awards EAR 1725131 and EAR 1935764 to GA and EAR 1724581 to AW, and the John C. and Mildred Ludlum Geology Endowment to SI.

REFERENCES

Anderson, S. W., & Fink, J. H. (1992). Crease structures: indicators of emplacement rates and surface stress regimes of lava flows. Geological Society of America Bulletin, 104(5), 615–625. https://doi.org/10.1130/0016-7606(1992)104<0615:CSIOER>2.3.CO;2

Applegarth, L. J., Pinkerton, H., James, M. R., & Calvari, S. (2010). Morphological complexities and hazards during the emplacement of channel-fed 'a'ā lava flow fields: A study of the 2001 lower flow field on Etna. Bulletin of Volcanology, 72(6), 641–656. https://doi.org/10.1007/s00445-010-0351-1

Bailey, R. A. (1989). Geologic map of Long Valley caldera, Mono-Inyo Craters volcanic chain, and vicinity, eastern California.

Bailey, R. A. (2004). Eruptive History and Chemical Evolution of the Precaldera and Postcaldera Basalt-Dacite Sequences, Long Valley, California: Implications for Magma Sources, Current Seismic Unrest, and Future Volcanism. U.S. Geological Survey Profession Paper, 1692, 0–75. http://pubs.usgs.gov/pp/pp1692/

Blake, S., & Fink, J. H. (1987). The dynamics of magma withdrawal from a density stratified dyke. Earth and Planetary Science Letters, 85(4), 516–524. https://doi.org/10.1016/0012-821X(87)90145-2

Castruccio, A., Rust, A. C., & Sparks, R. S. J. (2010). Rheology and flow of crystal-bearing lavas: Insights from analogue gravity currents. Earth and Planetary Science Letters, 297(3–4), 471–480. https://doi.org/10.1016/j.epsl.2010.06.051

Castruccio, A., Rust, A. C., & Sparks, R. S. J. (2013). Evolution of crust- and core-dominated lava flows using scaling analysis. Bulletin of Volcanology, 75(1), 1–15. https://doi.org/10.1007/s00445-012-0681-2

Eichelberger, J. C., Lysne, P. C., & Younker, L. C. (1984). Research Drilling at Inyo Domes, Long Valley Caldera, California. American Geophysical Union, 65(39), 723–725.

Farquharson, J. I., James, M. R., & Tuffen, H. (2015). Examining rhyolite lava flow dynamics through photo-based 3D reconstructions of the 2011-2012 lava flowfield at Cordón-Caulle, Chile. Journal of Volcanology and Geothermal Research, 304, 336–348. https://doi.org/10.1016/j.jvolgeores.2015.09.004

Fink, J. H. (1980). Gravity instability in the Holocene Big and Little Glass Mountain rhyolitic obsidian flows, northern California. Tectonophysics, 66, 147–166. https://doi.org/10.1016/0040-1951(80)90043-8

Fink, J. H. (1983). Structure and emplacement of a rhyolitic obsidian flow: Little Glass Mountain, Medicine Lake Highland, northern California (USA). Geological Society of America Bulletin, 94(3), 362–380. https://doi.org/10.1130/0016-7606(1983)94<362:SAEOAR>2.0.CO;2

Fink, J. H., & Griffiths, R. W. (1998). Morphology, eruption rates, and rheology of lava domes: Insights from laboratory models. Journal of Geophysical Research: Solid Earth, 103(1), 527–545. https://doi.org/10.1029/97jb02838

Giordano, D., Russell, J. K., & Dingwell, D. B. (2008). Viscosity of magmatic liquids: A model. Earth and Planetary Science Letters, 271(1–4), 123–134. https://doi.org/10.1016/j.epsl.2008.03.038

Griffiths, R. W., & Fink, J. H. (1997). Solidifying Bingham extrusions: A model for the growth of silicic lava domes. Journal of Fluid Mechanics, 347, 13–36. https://doi.org/10.1017/S0022112097006344

Harris, A. J. L., Flynn, L. P., Matías, O., & Rose, W. I. (2002). The thermal stealth flows of Santiaguito dome, Guatemala: Implications for the cooling and emplacement of dacitic block-lava flows. Bulletin of the Geological Society of America, 114(5), 533–546. https://doi.org/10.1130/0016-7606(2002)114<0533:TTSFOS>2.0.CO;2

Harris, A. & Rowland, Scott. (2009). Effusion rate controls on lava flow length and the role of heat loss: A review. Special Publications of IAVCEI. 10.1144/IAVCEl002.3.

Heap, M. J., Wadsworth, F. B., Heng, Z., Xu, T., Griffiths, L., Aguilar Velasco, A., Vairé, E., Vistour, M., Reuschlé, T., Troll, V. R., Deegan, F. M., & Tang, C. (2021). The tensile strength of volcanic rocks: Experiments and models. Journal of Volcanology and Geothermal Research, 418. https://doi.org/10.1016/j.jvolgeores.2021.107348

Heiken, G., Wohletz, K., & Eichelberger, J. (1988). Fracture Fillings and Intrusive Pyroclasts, Inyo Domes, California. Journal of Geophysical Research, 93, 4335–4350. https://doi.org/10.1017/CBO9781107415324.004

Hildreth, W. (2004). Volcanological perspectives on Long Valley, Mammoth Mountain, and Mono Craters: Several contiguous but discrete systems. Journal of Volcanology and Geothermal Research, 136(3–4), 169–198. https://doi.org/10.1016/j.jvolgeores.2004.05.019

Ishibashi, H., & Sato, H. (2010). Bingham fluid behavior of plagioclase-bearing basaltic magma: Reanalyses of laboratory viscosity measurements for Fuji 1707 basalt. Journal of Mineralogical and Petrological Sciences, 105(6), 334–339. https://doi.org/10.2465/jmps.100611

Jeffreys, H. (1925). The Flow of Water in an Inclined Channel of Rectangular Section. Philosophical Magazine, 49.

Leggett, T. N., Befus, K. S., & Kenderes, S. M. (2020). Rhyolite lava emplacement dynamics inferred from surface morphology. Journal of Volcanology and Geothermal Research, 395. https://doi.org/10.1016/j.jvolgeores.2020.106850

Magnall, N., James, M. R., Tuffen, H., & Vye-Brown, C. (2017). Emplacing a cooling-limited rhyolite lava flow: Similarities with basaltic lava flows. Frontiers in Earth Science, 5(June). https://doi.org/10.3389/feart.2017.00044

Magnall, N., James, M. R., Tuffen, H., Vye-Brown, C., Ian Schipper, C., Castro, J. M., & Davies, A. G. (2019). The origin and evolution of breakouts in a cooling-limited rhyolite lava flow. Bulletin of the Geological Society of America, 131(1–2), 137–154. https://doi.org/10.1130/B31931.1

Major, J. J., Scott, W. E., Driedger, C., & Dzurisin, D. (2005). Mount St. Helens Erupts Again. U.S. Geological Survey Fact Sheet, 3036.

McBirney, A. R., & Murase, T. (1984). Rheological Properties of Magmas. Annual Review of Earth and Planetary Sciences, 12, 337–357.

Miller, C. D. (1985). Holocene eruptions at the Inyo volcanic chain, California: Implications for possible eruptions in Long Valley caldera. Geology, 13(1), 14–17. https://doi.org/10.1130/0091-7613(1985)13<14:HEATIV>2.0.CO;2

Petroleum Experts, 2020, Fieldmove: Digital field mapping application for smartphone and tablet: https://www.petex.com/products/move-suite/digital-field-mapping/ (accessed July 2018).

Sampson, D. E. (1987). Textural heterogeneities and vent area structures in the 600-year-old lavas of the Inyo volcanic chain, eastern California. In Geological Society Special Publication (pp. 89–102). https://doi.org/10.1130/SPE212-p89

Sampson, D. E., & Cameron, K. L. (1987). The Geochemistry of the Inyo Volcanic Chain: Multiple Magma Systems in the Long Valley Region, Eastern California. Journal of Geophysical Research, 92, 403–421.

Schipper, C. I., Castro, J. M., Tuffen, H., James, M. R., & How, P. (2013). Shallow vent architecture during hybrid explosive-effusive activity at Cordón Caulle (Chile, 2011-12): Evidence from direct observations and pyroclast textures. Journal of Volcanology and Geothermal Research, 262, 25–37. https://doi.org/10.1016/j.jvolgeores.2013.06.005

Tuffen, H., James, M. R., Castro, J. M., & Schipper, C. I. (2013). Exceptional mobility of an advancing rhyolitic obsidian flow at Cordón Caulle volcano in Chile. Nature Communications, 4, 1–7. https://doi.org/10.1038/ncomms3709

Walker, G.P.L. (1973). Lengths of lava flows. Philosophical Transactions of the Royal Society, London, 274,107-118.

Walker, G. P. L. (1991). Structure, and origin by injection of lava under surface crust, of tumuli, “lava rises”, “lava-rise pits”, and “lava-inflation clefts” in Hawaii. Bulletin of Volcanology, 53, 546–558.

FIGURES

*Table 1. Viscosity values used in Jeffreys equation calculations. GRD viscosities calculated using the model of Giordano et al. (2008) and glass data from Isom et al., 2022a. Viscosity data indicated with * is from Andrews et al., 2021. Surface and interior viscosity measurements of OBD and GCD from Leggett et al., 2020.*

Method	Viscosity (Pa s)	Density (kg*m-3)	Avg. Eruption T ± 23°C
FVP1-Obs1*	9.85E+08	2242	-
GRD x-p OBD	9.33E+07		900
GRD x-p GCD	6.03E+07		876
GRD x-r GCD	3.02E+08		902
Leggett et al., 2020			
surface			
OBD	6.31E+12		
GCD	1.26E+13		
interior			
OBD	1.26E+10		
GCD	2.51E+11		

Table 2. Yield strength and Jeffreys equation calculations for the four morphological quadrants at Obsidian Dome and Glass Creek Dome. This study - crystal-poor (x-p) GRD viscosity value used for the platy domain at both domes whereas the crystal-rich GRD viscosity value used for the lobate domain at Glass Creek Dome. Columns indicating surface and interior* are advance rate calculations using the viscosities from Leggett et al., 2020 in Table 1.*

OBD					this study	surface*	interior*
Morphology	Location (N-S)	Thickness (m)	Slope (°)	(Pa)	Jeffreys Eqn. (m/day)	Jeffreys Eqn. (m/year)	Jeffreys Eqn. (m/day)
S lobate	S	31	0.08	8.48E+06	6	3	4
	S	35	0.08	9.57E+06	8	4	5
	S	29	0.08	7.93E+06	5	2	3
	S	36	0.08	9.85E+06	8	4	5
	S	44	0.08	1.20E+07	13	6	8
NE lobate	NE	46	0.04	2.32E+07	7	3	5
	NE	47	0.04	2.37E+07	8	4	5
	NE	39	0.04	1.97E+07	5	2	3
	NE	49	0.04	2.47E+07	8	4	5
	NE	47	0.04	2.37E+07	8	4	5
NW lobate	NW	20	0.05	8.36E+06	2	1	1
	NW	25	0.05	1.05E+07	3	1	2
	NW	33	0.05	1.38E+07	5	2	3
	NW	34	0.05	1.42E+07	5	2	3
	NW	28	0.05	1.17E+07	3	2	2
E platy	E	17	0.04	9.34E+06	1	0	1
	E	14	0.04	7.69E+06	1	0	0

	E	16	0.04	8.79E+06	1	0	1
	E	19	0.04	1.04E+07	1	1	1
	E	25	0.04	1.37E+07	2	1	1
		GCD			this study	surface*	interior*
Morphology	Location (N-S)	Thickness (m)	Slope (°)	(Pa)	Jeffreys Eqn. (m/day)	Jeffreys Eqn. (m/year)	Jeffreys Eqn. (m/day)
SE lobate	E	25	0.35	1.60E+06	17	4	0.5
	E	33	0.35	2.11E+06	30	7	0.9
	SE	50	0.35	3.20E+06	69	16	2.2
	SE	51	0.35	3.26E+06	72	16	2.2
	SE	52	0.35	3.33E+06	75	17	2.3
NE lobate	NE	19	0.16	2.56E+06	5	1	0.1
	NE	30	0.16	4.04E+06	12	3	0.4
	NE	33	0.16	4.44E+06	14	3	0.4
	NE	39	0.16	5.25E+06	20	5	0.6
	NE	41	0.16	5.52E+06	22	5	0.7
NW lobate	NW	20	0.20	2.24E+06	6	1	0.2
	NW	21	0.20	2.35E+06	7	2	0.2
	NW	19	0.20	2.13E+06	6	1	0.2
	NW	23	0.20	2.57E+06	8	2	0.3
	NW	32	0.20	3.58E+06	16	4	0.5
W platy	W	4	0.11	7.86E+05	0	0	0.0
	W	4	0.11	7.86E+05	0	0	0.0
	W	6	0.11	1.18E+06	1	0	0.0
	W	6	0.11	1.18E+06	1	0	0.0
	W	5	0.11	9.82E+05	1	0	0.0

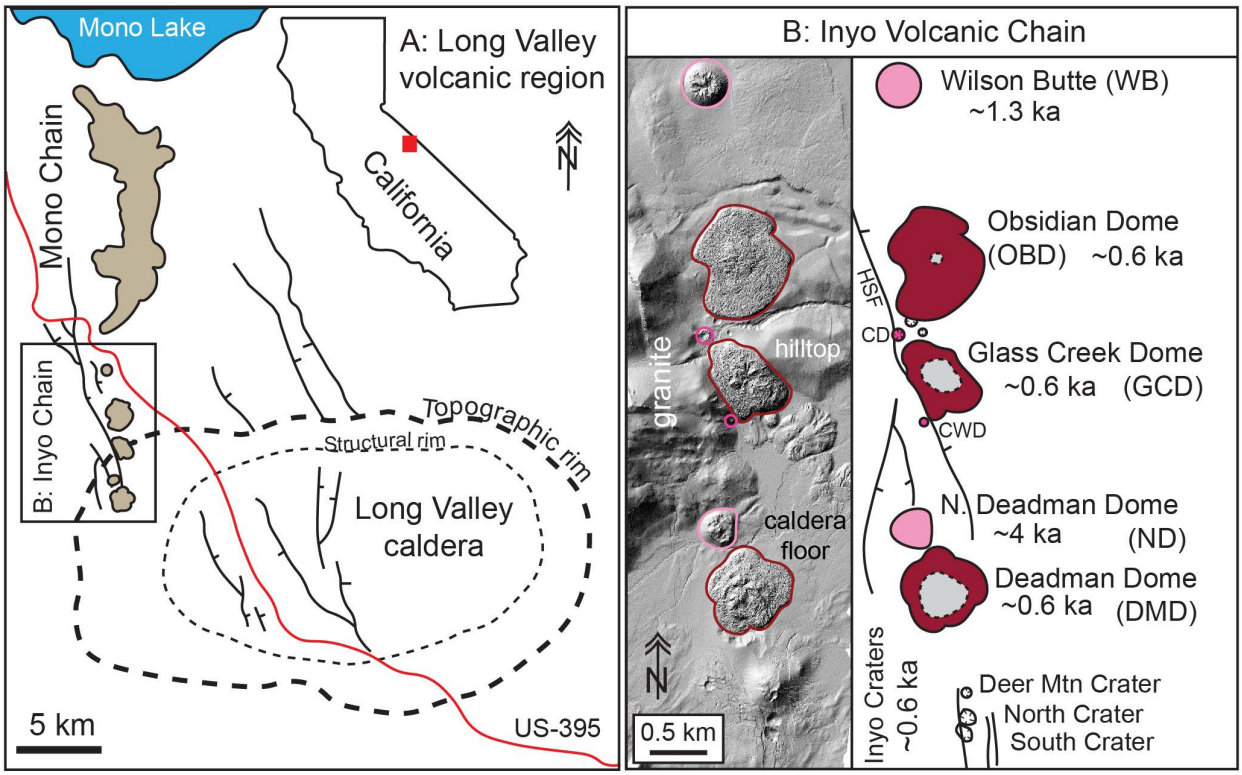

Figure 1. (A) The Long Valley volcanic region, California, USA (after Hildreth, 2004) and extents of the N-S trending, Holocene Mono and Inyo volcanic chains. (B) The Inyo Volcanic Chain (IVC). Left: lidar image with lavas outlined in red and pink. Right: sketch map of IVC lavas and their respective ages. Dashed grey patterns indicate the area covered by the crystal-rich lava at each dome, note the increased abundance to the south. HSF is the Hartley Springs Fault.

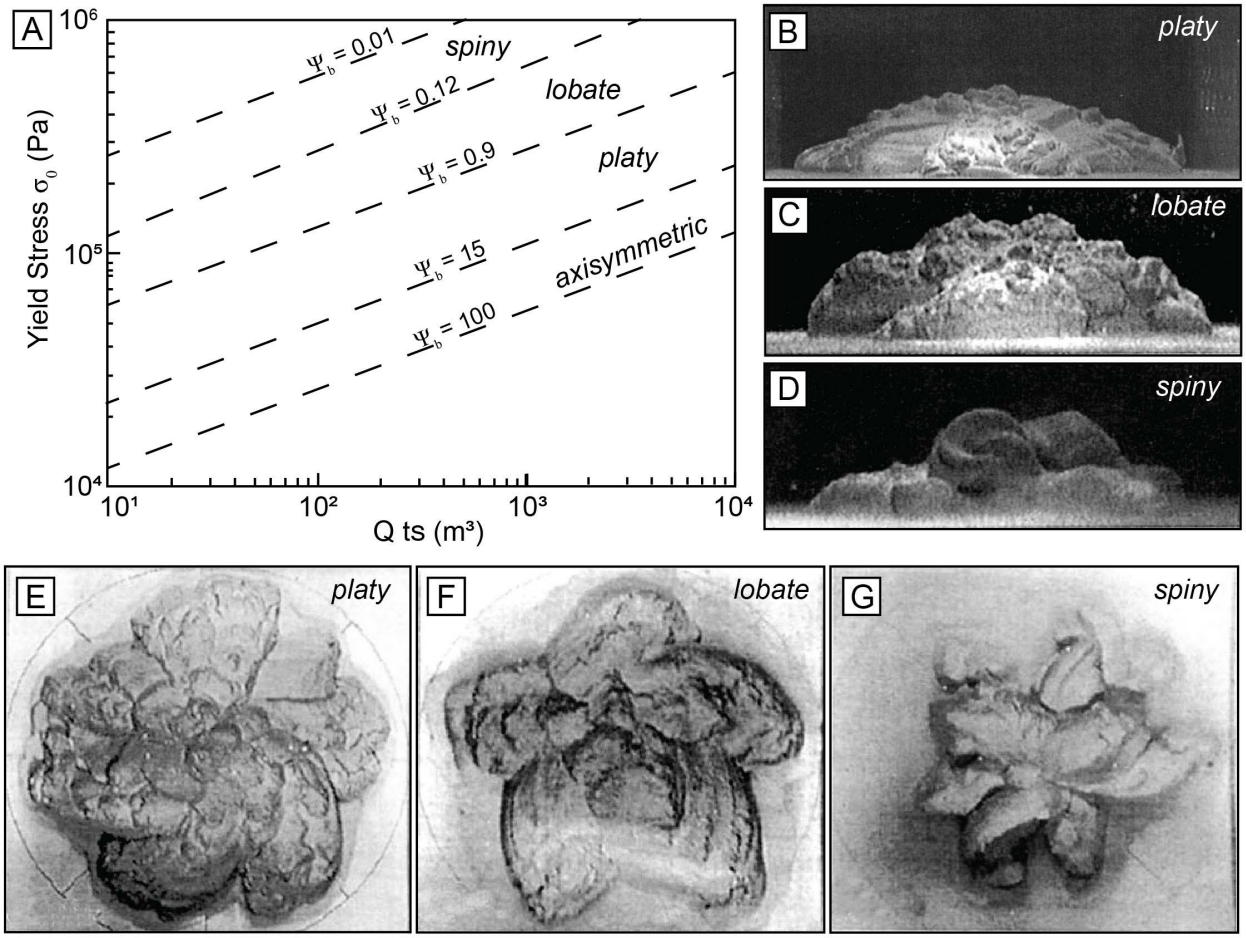

Figure 2. (A) Yield strength (Ψ_b) estimates for the morphologies (B-G) from Fink and Griffiths, 1998. Q ts is the quantity (volume) of the lava which erupted in one period or ts. (B-D) profile and (E-G) aerial views of the morphologies produced by analog modeling utilized in this study, images taken from Fink and Griffiths, 1998.

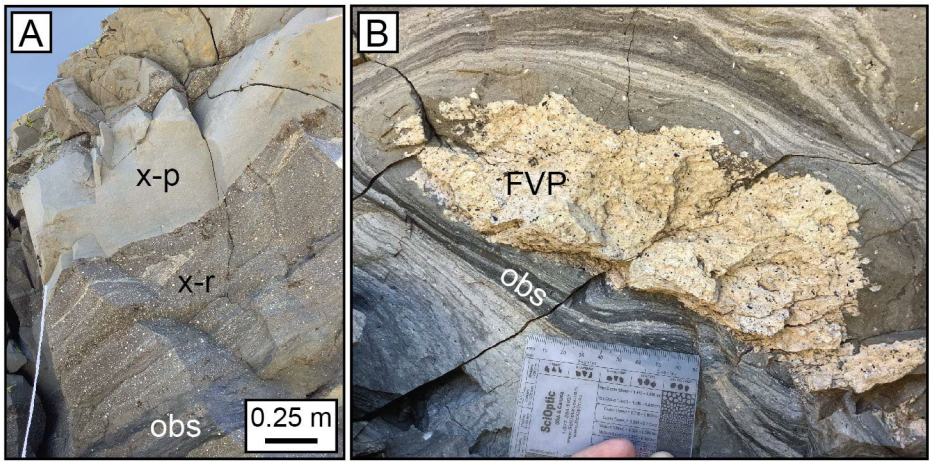

Figure 3. Textures (A) and lithofacies (B) at the Inyo Domes. (A) Field photo taken at Glass Creek Dome showing a contact between the aphyric crystal-poor (x-p) and crystal-rich (x-r) lava. (B) Photo taken at Glass Creek Dome displaying the pumiceous FVP lithofacies surrounded by bands of obsidian.

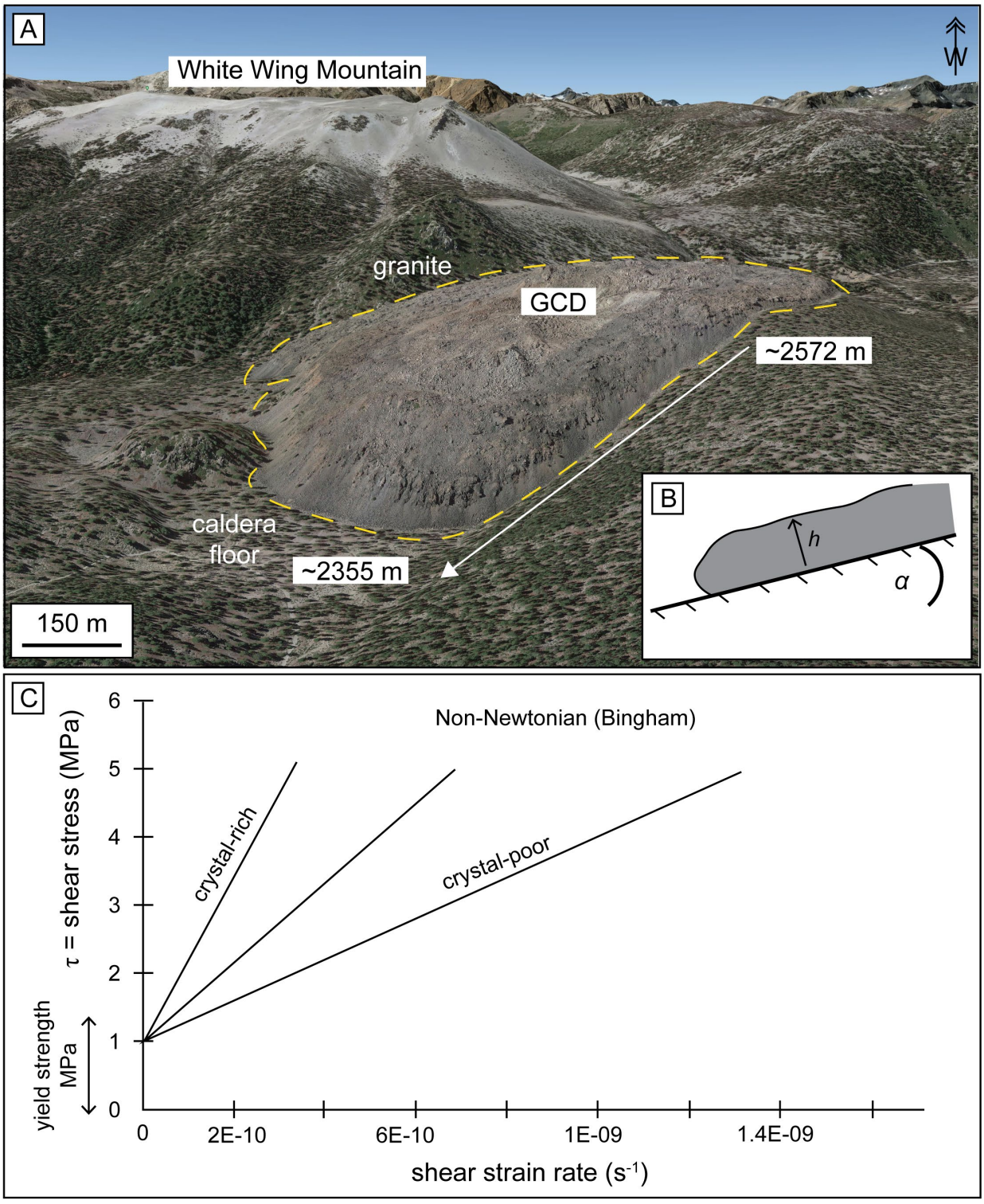

Figure 4. (A) Oblique Google Earth image of Glass Creek Dome (GCD). White arrow indicates likely flow path used to calculate the underlying slope the lava traveled over. (B) Jeffreys equation sketch of the lava (grey) traveling down a slope (black line), h is height (m), α is the slope angle. (C) Shear strain vs. shear stress graph. Slope of lines are calculated GRD viscosities.

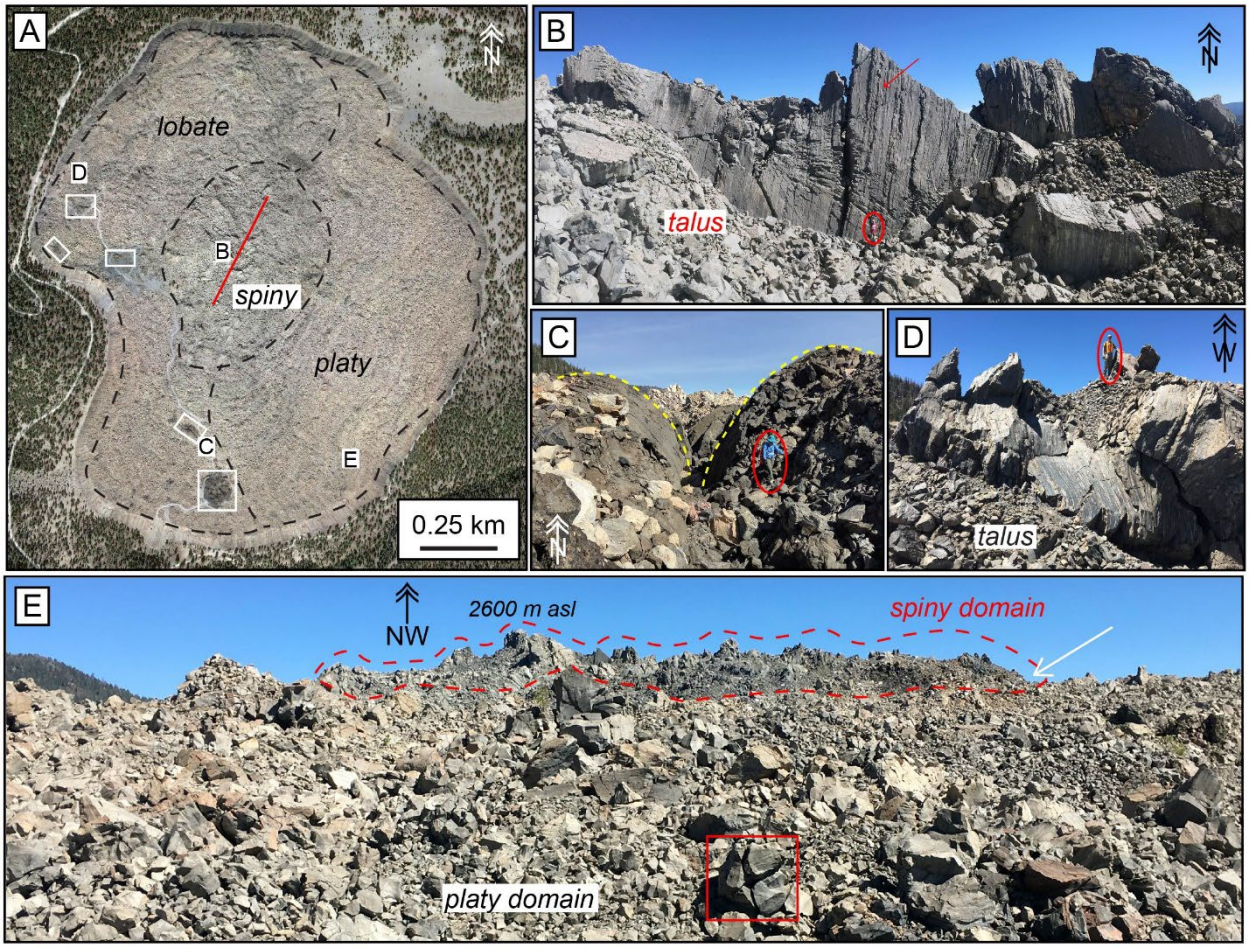

Figure 5. Morphological domains classified at Obsidian Dome. (A) Black dashed lines indicate the area of each domain. Letters mark the location of each outcrop photo included in this figure. Solid red line is the inferred orientation of the dike (Blake & Fink, 1987). White boxes indicate the five crease structures observed in the lobate domain. (B) Typical spiny domain exposure at the center of Obsidian Dome, featuring vertical, ~11 m-high spines emerging through talus. (C) Crease structure in the lobate domain. (D) Sub-horizontal to vertically flow-banded obsidian covered in talus within the lobate domain. (E) Typical platy domain surface in the foreground looking northwest towards the center of Obsidian Dome (spiny domain). The break-in-slope (white arrow) is inferred to be the boundary between the two domains.

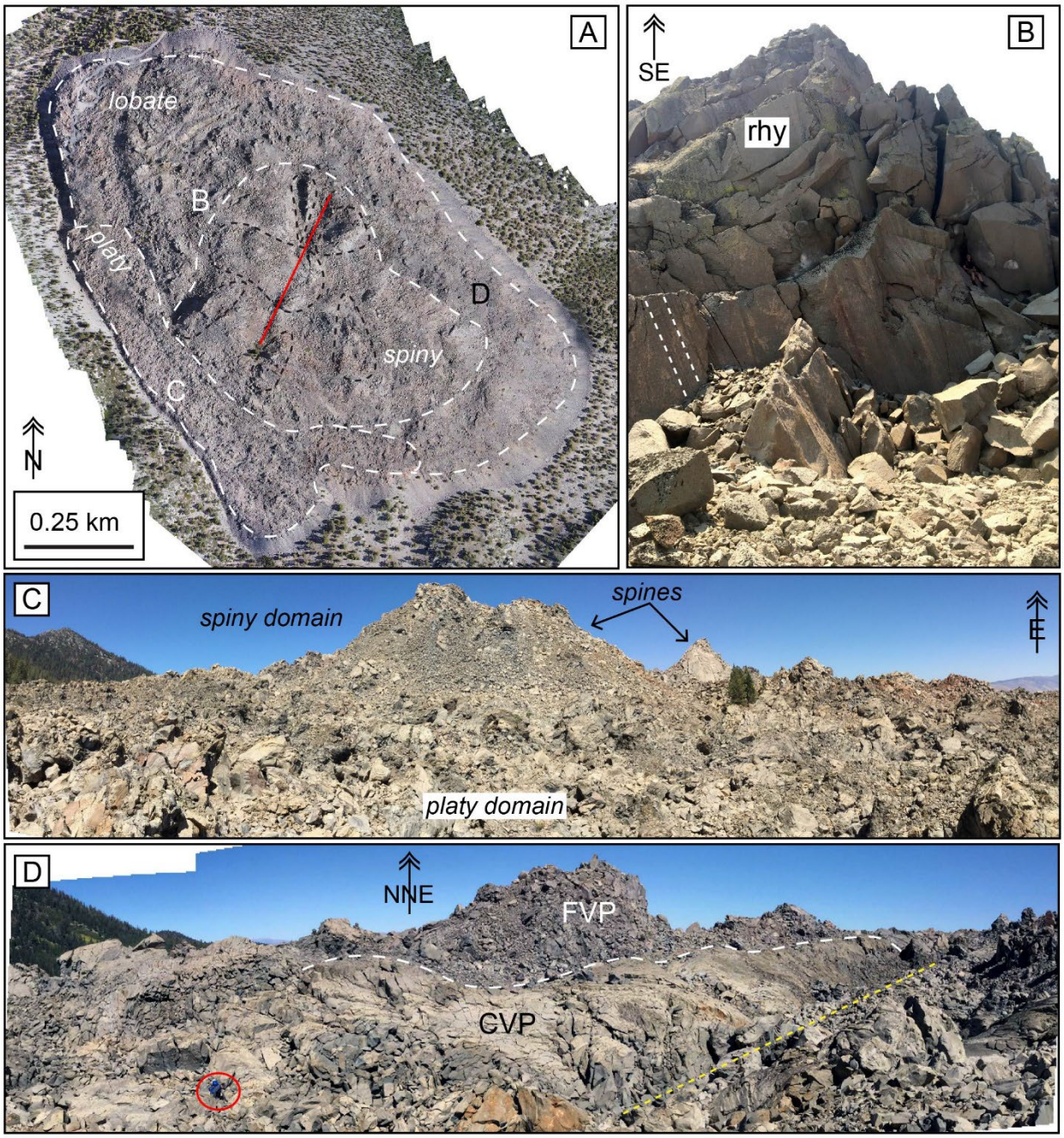

Figure 6. Morphological domains at Glass Creek Dome. (A) Red solid line is the approximate orientation of the dike with the black dashed lines indicating the orientations of individual spines within the spiny domain. Letters mark the location of each outcrop photo included in this figure. (B) A spine of vertically flow banded (white dashed line is ~1.5 m tall), crystal-rich, avesicular, microcrystalline rhyolite (rhy) at the margin of the spiny domain. Outcrop is approximately 18 m-high. (C) Panorama across the platy domain looking northeast toward spiny domain. The break-in-slope is inferred to the be boundary between the two domains. (D) ~100 m-long crease structure in the lobate domain, bounded by ~10 m-high masses of FVP rubbly blocks. White dashed line is the crease structure margin and yellow dashed line is the axial trace. Geologist circled in red for scale.

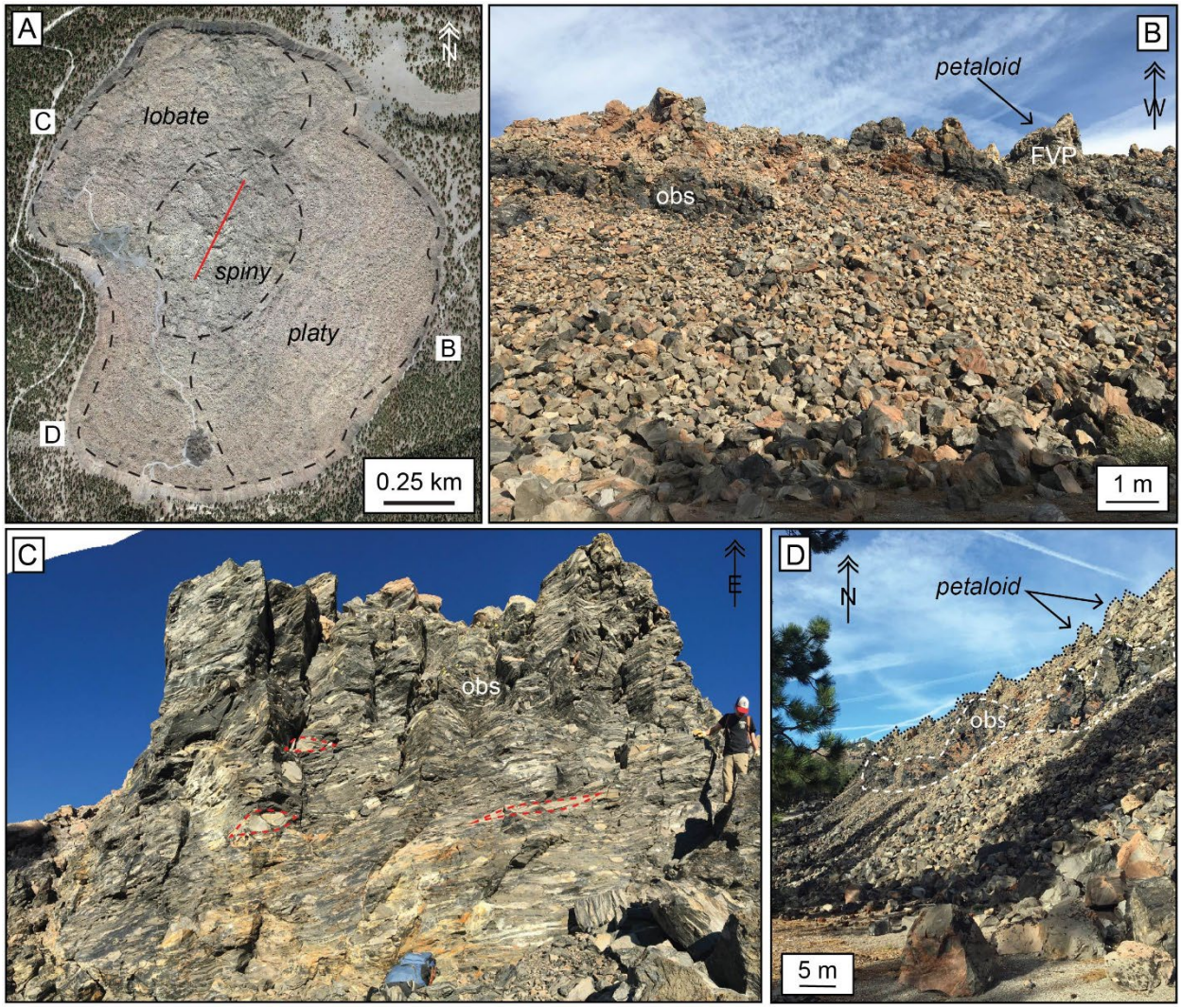

Figure 7. Flow front structures at Obsidian Dome. (A) Locations of images B-D and morphological domains. (B) Thin lenses of massive obsidian outcropping above a ~15 m-tall talus slope at the southeastern flow front (platy domain). The FVP atop the flow front is often petaloid. (C) ~10 m-high tower of horizontally banded obsidian and microcrystalline rhyolite (red dashed lines) at the northwest flow front (lobate domain). (D) Oblique view of the southwestern flow front showing an ~10 m-high obsidian ledge exposed within the talus slope and FVP petaloid features at the edge of the upper surface.

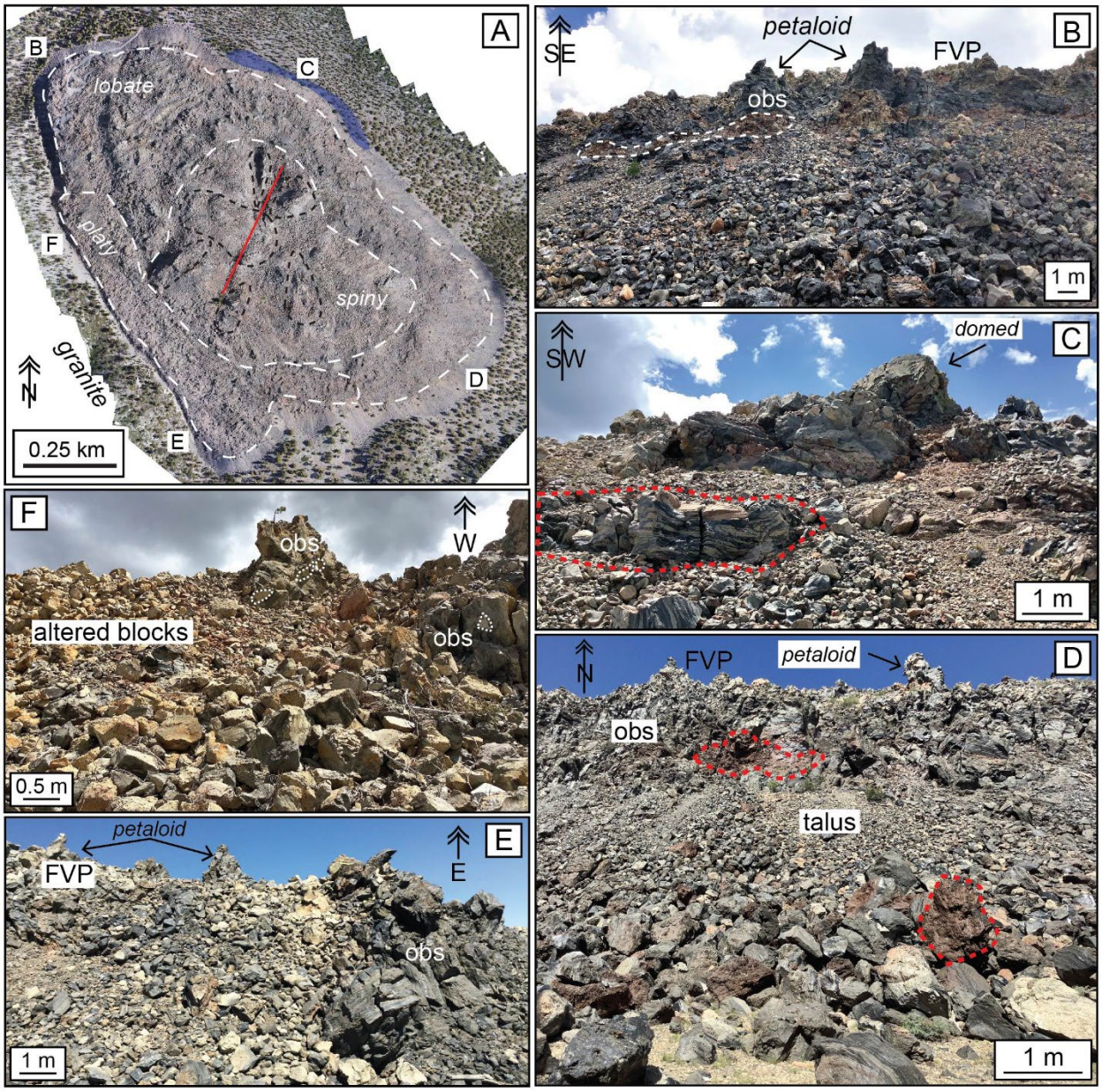

Figure 8. Flow front structures at Glass Creek Dome. (A) Locations of images (clockwise) B – F. Blue shaded region near the northeastern flow front shows the extent of the intact tephra ring described by Heiken et al (1988). (B) Thin lens of obsidian exposed at the northern flow front (lobate domain). (C) Parallel ledges of flow-banded microcrystalline rhyolite and obsidian at the western flow front (red dashed lines). (D) Ledges of flow-banded obsidian at the southeastern flow front grading upwards into glassy obsidian and then crystal-rich FVP. (E) Upturned obsidian outcrop bounded by FVP with petaloid features at the southwestern flow front (platy domain). (F) Orange-stained blocks of obsidian with inclusions of crystal-rich FVP (dashed white lines).

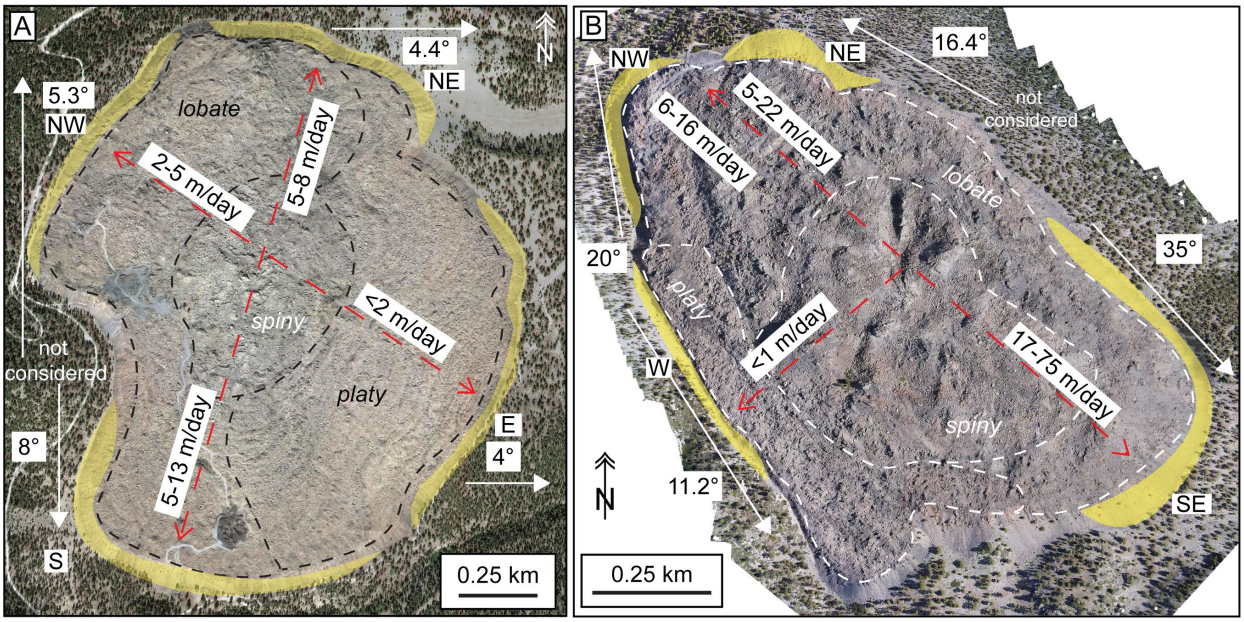

Figure 9. Slope measurements and calculated flow advance rates using Jeffreys equation for OBD (A) and GCD (B). Dashed red arrows on the upper surface suggest the flow path taken with labeled rates calculated from each quadrant. Large white arrows around the margins of the domes indicate the direction of the slope with calculated degree of slope. Yellow regions with orientations (i.e., "E" or "NW") indicate the four quadrants where flow front thickness was measured.

CONCLUSIONS

This dissertation attempts to constrain the magmatic and volcanic evolution of the three youngest Inyo Domes in California through a combination of extensive field work, digital field mapping, and quantitative petrology. This study concludes that the complex nature of the Inyo Domes magma system is also reflected in the morphology of the individual lavas.

We find that a convoluted array of mixing and mingling of at least three temporally long-lived magmas, which are not related to the Bishop Tuff magma system, generated the Inyo Domes. We envisage the shallow crust is comprised of several semi-contiguous magma reservoirs which have been re-energized through time by thermal recharge. Each lava (0.6 ka Inyo Domes; 41 ka Northwest dacites; 113 ka West Moat rhyolites) has sampled and incorporated different proportions of these magmas prior to their eruption. With the 0.6 ka Inyo Domes revealing the most complex and mixed proportions of the dichotomous magmas. We believe the emplacement of the dike cut through the individual reservoirs and promoted the mixing and distribution at each dome. The resulting erupted material (crystal-poor and crystal-rich) appear to rheologically behave differently at each of the 0.6 ka Inyo Domes.

We find that the upper surface of the crystal-poor Obsidian Dome is overprinted by a continuum of brittle and brittle-ductile fractures recording pervasive tensile fracturing during emplacement. The fractures characterized display two continua of formation where small cracks grow and link to form larger cracks and clefts throughout the lava's effusion. On the other hand, the largest fractures, crease structures, occur in one fracture event which penetrates deep enough to pass through the brittle-ductile transition into a volatile rich zone. If the fracture does not pass the brittle-ductile transition it does not promote vesiculation and instead results in a crevasse. Furthermore, we observe ornamentations on fracture surfaces that record explosive phenomenon and outgassing through the latter stages of lava emplacement.

The morphological domains classified at Obsidian Dome and Glass Creek Dome reveal similarities in lithofacies and structures observed at the flow fronts, calculated yield strengths, and advance flow rates. The *lobate* morphologies at each dome have thicker (≥20 m) flow fronts, higher yield strengths, and are comprised of obsidian with bands and boudins of microcrystalline rhyolite whereas the *platy* morphologies have thinner flow fronts, lower yield strengths, and thin (<5 m) outcrops of obsidian. The *spiny* morphologies are constrained to the center of each dome

dominated by the microcrystalline rhyolite. Overall, calculations reveal Obsidian Dome was emplaced quicker than Glass Creek Dome with the fastest advance rates noted in the *platy* morphologies. This study is the first to compare analog modeling morphologies with those recorded at active flow fronts and prehistoric lavas.

The major findings and contributions of this research include:

1. The crystal-rich endmember of the 0.6 ka Inyo Domes, 41 ka Northwest dacites, and 113 ka West Moat rhyolites is **not** related to a residual Bishop Tuff mush.
2. There is a strong correlation between surficial morphology, flow front structures, and calculated yield strengths and flow advance rates. This has long been proposed for silicic lavas generally, but is seldom and poorly quantified, and has not been measured before on lavas with mixed compositions.
3. The evolution of brittle structures records the thickening and stiffening of a mechanically strong lid during lava emplacement, such that some but not all fractures are within the lid. The exceptions are large-scale, late fractures that penetrate into ductile lava and cause splaying and rotation of the lid.
4. Brittle deformation is accompanied by localized but pervasive explosive behavior.
5. A digital field mapping workflow to produce orthorectified airphotos and DTMs to assist in mapping the structural features and lithofacies contacts of the upper surface of silicic lavas

These findings contribute to the overall understanding of the hazards and longevity of the eruption and emplacement of silicic lavas.

APPENDIX 1: ANALYTICAL METHODS

Table 1. Whole Rock Data – ICP-MS and XRF

Sample Name	SiO_2	TiO_2	Al_2O_3	FeO*	MnO	MgO	CaO	Na_2O	K_2O	P_2O_5	Original Total	L.O.I
OBD x-p	73.73	0.14	14.05	1.61	0.05	0.23	0.75	4.22	5.20	0.02	99.06	0.72
OBD x-p	73.80	0.14	14.12	1.62	0.05	0.10	0.73	4.19	5.22	0.02	99.40	0.26
OBD x-m	72.61	0.22	14.59	1.91	0.06	0.20	0.99	4.32	5.05	0.05	98.23	1.16
GCD x-r	71.42	0.42	14.77	2.36	0.06	0.64	1.82	4.19	4.19	0.12	98.69	0.68
GCD x-p	73.85	0.14	14.12	1.62	0.05	0.09	0.74	4.16	5.21	0.02	99.02	0.45
GCD x-p	71.60	0.26	15.01	2.11	0.06	0.27	1.12	4.50	5.00	0.06	99.40	0.14
DMD x-r	71.52	0.42	14.69	2.34	0.06	0.63	1.79	4.20	4.23	0.11	99.06	0.52
DMD x-p	71.27	0.38	14.89	2.38	0.06	0.50	1.52	4.37	4.52	0.10	98.84	0.51
DMD x-p	71.12	0.30	15.22	2.23	0.06	0.31	1.19	4.56	4.92	0.07	99.35	0.19
DM x-r	72.28	0.33	14.59	2.07	0.06	0.49	1.53	4.11	4.46	0.09	98.01	1.52
CD x-p	73.80	0.14	14.12	1.63	0.06	0.10	0.74	4.16	5.24	0.02	98.66	0.84
NWD x-r	66.35	0.62	16.65	3.50	0.07	0.85	2.35	4.41	5.00	0.18	98.66	0.75
CWD x-p	73.08	0.15	14.47	1.77	0.06	0.12	0.81	4.28	5.23	0.03	98.46	1.21

Table 1 cont.

(ppm)	OBD x-p	OBD x-p	OBD x-m	GCD x-r	GCD x-p	GCD x-p	DMD x-r	DMD x-p	DMD x-p	DM x-r	CD x-p	NWD x-r	CWD x-p
La	78.86	78.91	68.85	42.42	79.05	63.05	40.25	50.98	61.25	42.27	78.44	69.21	71.30
Ce	139.64	139.94	122.97	75.27	139.42	112.15	71.33	90.89	109.45	74.08	138.07	119.79	125.18
Pr	14.21	14.41	12.86	7.90	14.30	11.92	7.54	9.67	11.71	7.79	14.26	12.57	12.90
Nd	45.10	45.47	41.47	25.76	45.84	39.27	25.13	32.25	38.74	25.13	45.67	41.76	42.18
Sm	6.97	7.04	6.65	4.13	6.96	6.32	4.32	5.22	6.21	4.11	7.10	6.28	6.46
Eu	0.41	0.41	0.67	0.86	0.41	0.91	0.83	0.95	0.99	0.69	0.40	1.61	0.57
Gd	5.02	5.01	4.87	3.28	5.11	4.63	3.18	4.03	4.69	3.10	4.97	4.65	4.55
Tb	0.80	0.81	0.77	0.51	0.81	0.74	0.51	0.63	0.73	0.50	0.78	0.69	0.73
Dy	4.73	4.73	4.58	3.08	4.77	4.34	2.99	3.68	4.41	2.96	4.74	4.12	4.33
Ho	0.92	0.94	0.88	0.60	0.93	0.84	0.60	0.75	0.86	0.60	0.94	0.79	0.86
Er	2.65	2.66	2.55	1.70	2.62	2.42	1.70	2.03	2.43	1.72	2.60	2.14	2.41
Tm	0.40	0.40	0.38	0.26	0.40	0.37	0.26	0.32	0.37	0.26	0.40	0.32	0.37
Yb	2.60	2.57	2.41	1.68	2.58	2.39	1.75	2.09	2.36	1.70	2.63	2.17	2.40
Lu	0.41	0.43	0.40	0.27	0.40	0.39	0.28	0.34	0.39	0.28	0.41	0.34	0.38
Ba	341.84	344.54	653.84	820.19	349.62	975.45	866.51	966.60	1108.89	909.28	351.20	1570.46	629.82
Th	21.94	21.75	18.66	12.69	21.73	16.16	12.50	14.06	15.46	13.20	21.78	13.15	18.50
Nb	18.56	18.75	18.15	16.12	18.62	17.62	16.15	17.19	17.77	16.23	18.67	14.81	17.38
Y	25.19	25.48	24.24	16.59	25.46	23.39	16.63	20.12	23.40	16.54	25.30	21.00	23.45
Hf	7.02	7.10	7.49	5.81	7.01	8.20	5.81	7.46	8.78	5.69	7.06	8.81	7.50
Ta	1.64	1.61	1.52	1.49	1.60	1.44	1.46	1.43	1.41	1.50	1.59	1.09	1.46
U	5.47	5.52	4.97	3.67	5.50	4.54	3.71	4.09	4.46	3.82	5.55	3.26	4.88
Pb	26.20	26.26	25.15	24.11	26.31	24.86	24.29	24.11	24.68	24.78	26.34	20.44	25.93
Rb	159.56	161.93	147.77	116.41	162.83	134.69	114.84	123.42	131.65	116.36	159.85	106.78	144.48
Cs	4.08	4.12	3.65	2.93	4.11	3.25	2.94	3.02	3.15	3.06	4.09	2.47	3.66
Sr	40.52	41.68	103.82	284.29	42.30	144.58	286.81	227.18	164.94	250.47	42.14	335.83	68.60

Sc	3.32	3.35	3.71	3.80	3.31	4.12	3.66	3.96	4.18	2.89	3.37	5.99	3.53
Zr	246.87	250.42	287.68	227.22	247.83	327.84	229.70	304.98	359.57	205.43	246.54	392.17	276.57

Table 2. EPMA Analytical Conditions

Minerals	Elements Analyzed	Peak count time (s)	Background count times (s), when collected	Accelerating Voltage (keV)	Beam Current (nA)	Beam Diameter (μm)	Primary and secondary standards	Internal monitors	Crystal Used
oxides	Si	20	10	15	20	point	CPX - 1	ilmenite	TAP
	Al	20	10				Spinel	Tiebaghi Chromite	TAP
	Mg	40	20				Spinel		TAPL
	Ni	30	15				NiO		LIFL
	Mn	30	15				Mn2O3		LIFL
	Cr	20	10				Cr2O3		LIFL
	Fe	20	10				Hematite		LIFL
	V	30	15				V2O3		LIFL
	Ti	30	15				TiO2		PETL
	Ca	30	15				CPX - 1		PETL
feldspar	Si	20	10	15	10	5	Tiburon Albite	OR - 1	TAP
	Al	20	10				Tiburon Albite	Tiburon Albite	TAP
	Na	10	5				Tiburon Albite	AN 100	TAPL
	Mg	30	15				Springwater Olivine		TAPL
	Ba	40	20				Barite		LIFL
	Fe	20	10				Springwater Olivine		LIFL
	K	10	5				OR-1 (Orthoclase)		PETL
	Ca	20	10				Crystal Bay Bytownite		PETL
amphibole	Si	20	10	15	15	point	Springwater olivine		TAP
	Al	30	15				Tiberon Albite		TAP
	Na	20	10				Tiberon Albite		TAPL
	Mg	30	15				Springwater olivine		TAPL
	Mn	30	15				Mn2O3		LIFL
	Ti	30	15				TiO2		LIFL
	Fe	20	10				Springwater olivine		LIFL
	Cr	30	15				Cr2O3		LIFL

	K	20	10				OR-1		PETL
	Ca	20	10				CPX-1		PETL
glass	Si	20	10	15	3	5	Springwater olivine; Or-1; VG-2	VG-2	TAP
	Al	20	10				Tiburon Albite; Or-1;	RLS 75	TAP
	Na	10	5				Tiburon Albite	Wilburforce apatite	TAPL
	Mg	30	15				Springwater olivine; VG-2	Tiburon albite	TAPL
	Ti	40	20				TiO2	OR-1	PETL
	P	60	20				Wilburforce Apatite		PETL
	Fe	30	15				Hematite; VG-2		LIFL
	Mn	40	20				Mn2O3		LIFL
	K	10	5				Or-1		PETL
	Ca	20	10				CPX-1; VG-2		PETL

Table 3. Quantitative oxide compositions and monitors

No.	Sample ID	SiO_2	Al_2O_3	MgO	NiO	MnO	Cr_2O_3	FeO	V_2O_3	TiO_2	CaO	Total
16	DMD_11_pair1_b_1	0.039	0.075	1.091	0	1.876	0.006	49.968	0.132	47.82	0.024	101.031
17	DMD_11_pair1_b_2	0.037	0.076	1.094	0	1.814	0.004	49.785	0.178	48.125	0.009	101.122
18	DMD_11_pair1_b_3	0.034	0.072	1.065	0	1.812	0.008	49.889	0.167	47.693	0.008	100.748
19	DMD_11_pair1_b_4	0.047	0.073	1.086	0	1.773	0.012	49.833	0.161	47.628	0.036	100.649
20	DMD_11_pair1_b_5	0.047	0.066	1.089	0	1.79	0	49.571	0.171	47.894	0.025	100.653
21	DMD_11_pair2_a_1	0.063	0.075	1.064	0	1.821	0.001	49.378	0.178	47.324	0.077	99.981
22	DMD_11_pair2_a_2	0.054	0.063	1.066	0	1.792	0	49.447	0.172	47.172	0.063	99.829
23	DMD_11_pair2_a_3	0.048	0.066	1.056	0	1.855	0	49.724	0.178	47.273	0.046	100.246
24	DMD_11_pair2_a_4	0.053	0.066	1.052	0	1.834	0	49.327	0.193	47.335	0.054	99.914
25	DMD_11_pair2_a_5	0.079	0.064	1.036	0.008	1.751	0	49.29	0.173	46.807	0.086	99.294
31	DMD_11_pair3_a_1	0.063	0.071	1.113	0	1.81	0.011	48.974	0.16	47.403	0.041	99.646
32	DMD_11_pair3_a_2	0.062	0.064	1.12	0	1.844	0	48.81	0.176	46.92	0.07	99.066
33	DMD_11_pair3_a_3	0.037	0.066	1.093	0	1.84	0	49.273	0.182	47.32	0.047	99.858
34	DMD_11_pair3_a_4	0.038	0.073	1.103	0.017	1.838	0	49.089	0.185	47.513	0.081	99.937
35	DMD_11_pair3_a_5	0.079	0.079	1.119	0	1.815	0.006	48.724	0.18	47.133	0.09	99.225
41	DMD_11_Ox1_1	0.067	0.07	1.135	0	1.859	0	48.823	0.148	47.189	0.038	99.329
42	DMD_11_Ox1_2	0.101	0.072	1.116	0	1.82	0	48.887	0.161	46.976	0.023	99.156
43	DMD_11_Ox1_3	0.082	0.075	1.116	0	1.835	0	49.264	0.174	47.278	0.033	99.857
44	DMD_11_Ox1_4	0.111	0.086	1.13	0.01	1.808	0	48.984	0.161	46.971	0.073	99.334
45	DMD_11_Ox1_5	0.118	0.068	1.139	0	1.808	0	49.102	0.157	46.873	0.011	99.276
46	DMD_11_Ox2_1	0.157	0.107	1.107	0.019	1.883	0.027	49.058	0.183	46.557	0	99.098
47	DMD_11_Ox2_2	0.129	0.074	1.121	0.036	1.877	0.033	48.502	0.174	46.629	0	98.575
48	DMD_11_Ox2_3	0.092	0.083	1.13	0.01	1.868	0.011	48.9	0.167	46.844	0	99.105
49	DMD_11_Ox2_4	0.074	0.081	1.107	0.04	1.879	0.03	48.591	0.162	46.967	0	98.931
50	DMD_11_Ox2_5	0.133	0.078	1.118	0.005	1.879	0.015	48.364	0.173	46.68	0.01	98.455
51	DMD_11_Ox3_1	0.075	0.085	0.918	0.013	1.782	0	49.81	0.179	47.398	0	100.26

52	DMD_11_Ox3_2	0.085	0.084	0.944	0.022	1.819	0	49.808	0.188	47.303	0.014	100.267
53	DMD_11_Ox3_3	0.061	0.067	0.95	0.025	1.803	0.011	49.82	0.176	47.431	0	100.344
54	DMD_11_Ox3_4	0.035	0.067	0.935	0.011	1.767	0	49.976	0.175	47.636	0.019	100.621
55	DMD_11_Ox3_5	0.059	0.077	0.931	0	1.791	0	49.755	0.181	47.703	0.036	100.533
71	DMD_11_Ox4_1	0.038	0.061	1.138	0	1.873	0	50.012	0.167	47.604	0.087	100.98
72	DMD_11_Ox4_2	0.024	0.06	1.146	0	1.894	0	49.558	0.176	47.757	0.102	100.717
73	DMD_11_Ox4_3	0.011	0.057	1.117	0	1.836	0	49.693	0.184	47.713	0.051	100.662
74	DMD_11_Ox4_4	0.048	0.037	1.162	0	1.824	0	49.758	0.158	48.016	0.038	101.041
75	DMD_11_Ox4_5	0.014	0.061	1.134	0	1.844	0.001	49.985	0.178	48.122	0.007	101.346
6	DMD_11_pair1_b_1	0.055	0.049	1.199	0	1.633	0	49.743	0.197	47.329	0.041	100.246
7	DMD_11_pair1_b_2	0.058	0.052	1.215	0	1.631	0	49.572	0.198	47.631	0.064	100.421
8	DMD_11_pair1_b_3	0.074	0.036	1.216	0	1.621	0.01	49.502	0.188	47.558	0.05	100.255
9	DMD_11_pair1_b_4	0.083	0.044	1.209	0	1.65	0	49.482	0.179	47.474	0.087	100.208
10	DMD_11_pair1_b_5	0.068	0.039	1.22	0	1.667	0.001	49.338	0.181	47.564	0.072	100.15
16	DMD_11_pair2_b_1	0.048	0.059	1.118	0	1.789	0.01	49.853	0.161	47.76	0	100.798
17	DMD_11_pair2_b_2	0.029	0.074	1.1	0	1.831	0.023	49.845	0.178	47.691	0	100.771
18	DMD_11_pair2_b_3	0.069	0.055	1.115	0.01	1.761	0.041	49.996	0.184	47.856	0	101.087
19	DMD_11_pair2_b_4	0.024	0.055	1.134	0	1.829	0.02	49.807	0.186	47.905	0	100.96
20	DMD_11_pair2_b_5	0.03	0.076	1.098	0.017	1.772	0.045	49.609	0.172	47.898	0	100.717
12	DMD_11_pair4_a_2	0.079	0.084	1.053	0.089	1.837	0.032	50.026	0.218	47.438	0.088	100.944
13	DMD_11_pair4_a_3	0.072	0.094	1.078	0.068	1.837	0.037	50.122	0.208	47.638	0.083	101.237
14	DMD_11_pair4_a_4	0.074	0.094	1.081	0.08	1.806	0.041	50.045	0.199	47.807	0.115	101.342
15	DMD_11_pair4_a_5	0.078	0.082	1.079	0.084	1.845	0.029	49.918	0.211	47.562	0.181	101.069
21	DMD_11_pair5_a_1	0.037	0.065	1.044	0	1.723	0.008	50.023	0.201	47.313	0.087	100.501
22	DMD_11_pair5_a_2	0.017	0.055	1.035	0	1.728	0.003	49.856	0.207	47.251	0.102	100.254
23	DMD_11_pair5_a_3	0.028	0.049	1.068	0	1.771	0	50.126	0.193	47.481	0.091	100.807
24	DMD_11_pair5_a_4	0.023	0.081	1.084	0	1.684	0	50.226	0.195	47.4	0.071	100.764
25	DMD_11_pair5_a_5	0.016	0.081	1.087	0.006	1.697	0.015	50.143	0.171	47.387	0.057	100.66
6	DMD_11_OxPair4_b_1	0.008	0.064	1.09	0.002	1.8	0	49.694	0.179	47.218	0.032	100.087
7	DMD_11_OxPair4_b_2	0	0.06	1.063	0.001	1.791	0	49.846	0.181	48.198	0.049	101.189
8	DMD_11_OxPair4_b_3	0	0.061	1.072	0.001	1.777	0.004	50.235	0.172	48.108	0.01	101.44

9	DMD_11_OxPair4_b_4	0	0.058	1.066	0	1.837	0.002	50.217	0.176	48.053	0.018	101.427
10	DMD_11_OxPair4_b_5	0.018	0.055	1.077	0.003	1.788	0.035	50.422	0.196	48.198	0.014	101.806
16	DMD_11_OxPair5_b_1	0.013	0.062	1.119	0	1.774	0	49.908	0.194	48.175	0.12	101.365
17	DMD_11_OxPair5_b_2	0.007	0.075	1.124	0	1.772	0.009	49.701	0.175	47.985	0.23	101.078
18	DMD_11_OxPair5_b_3	0.032	0.065	1.104	0	1.721	0	50.191	0.194	47.828	0.237	101.372
19	DMD_11_OxPair5_b_4	0.014	0.07	1.113	0.006	1.784	0.021	50.123	0.199	48.054	0.034	101.418
20	DMD_11_OxPair5_b_5	0.028	0.059	1.123	0	1.783	0	50.193	0.195	48.058	0	101.439
1	GCD_41_Ox1_1	0.02	0.065	1.023	0	1.803	0.04	50.228	0.17	47.883	0.021	101.253
2	GCD_41_Ox1_2	0.021	0.077	0.99	0	1.803	0.028	50.039	0.171	47.79	0.052	100.971
3	GCD_41_Ox1_3	0.033	0.069	1.02	0	1.866	0.017	50.132	0.176	47.809	0.031	101.153
4	GCD_41_Ox1_4	0.017	0.058	1.023	0.005	1.844	0.018	50.007	0.184	47.892	0.051	101.099
5	GCD_41_Ox1_5	0.048	0.07	1.004	0	1.797	0.018	49.829	0.189	47.706	0.151	100.812
11	GCD_41_Ox3_1	0.061	0.03	1.249	0.007	1.787	0.018	49.689	0.202	46.767	0.238	100.048
12	GCD_41_Ox3_2	0.064	0.041	1.218	0.003	1.749	0.024	49.385	0.18	47.19	0.191	100.045
13	GCD_41_Ox3_3	0.103	0.041	1.23	0	1.798	0.014	49.331	0.189	47.167	0.159	100.032
14	GCD_41_Ox3_4	0.054	0.03	1.243	0.012	1.754	0	50.107	0.188	47.344	0.128	100.86
15	GCD_41_Ox3_5	0.084	0.035	1.273	0.004	1.758	0.013	49.758	0.19	47.198	0.171	100.484
31	GCD_41_Ox5_1	0.019	0.065	0.956	0	1.837	0.005	50.476	0.184	48.034	0.055	101.631
32	GCD_41_Ox5_2	0.018	0.07	0.913	0	1.847	0	50.127	0.199	48.115	0.051	101.34
33	GCD_41_Ox5_3	0.021	0.077	0.932	0	1.861	0.005	50.396	0.174	48.116	0.033	101.615
34	GCD_41_Ox5_4	0.05	0.056	0.983	0	1.798	0	50.315	0.185	47.949	0.068	101.404
35	GCD_41_Ox5_5	0.075	0.069	0.901	0	1.838	0.004	50.156	0.158	47.792	0.048	101.041
36	GCD_41_Ox6_1	0.01	0.049	1.095	0	1.793	0.006	50.209	0.212	48.262	0.054	101.69
37	GCD_41_Ox6_2	0.022	0.062	1.098	0	1.791	0.007	50.072	0.19	48.077	0.038	101.357
38	GCD_41_Ox6_3	0.02	0.065	1.103	0.007	1.79	0.006	50.168	0.197	48.045	0.074	101.475
39	GCD_41_Ox6_4	0.022	0.083	1.108	0.014	1.802	0	50.211	0.208	48.04	0.028	101.516
40	GCD_41_Ox6_5	0.005	0.063	1.131	0.001	1.852	0	50.367	0.207	48.08	0.015	101.721
41	GCD_41_Ox7_1	0.049	0.078	0.876	0	1.766	0.015	50.266	0.199	48.002	0.05	101.301
43	GCD_41_Ox7_3	0.129	0.08	0.81	0.01	1.744	0.01	50.204	0.186	48.011	0.022	101.206
44	GCD_41_Ox7_4	0.26	0.063	0.805	0.009	1.809	0	50.319	0.211	48.073	0.02	101.569
45	GCD_41_Ox7_5	0.02	0.061	0.841	0	1.763	0	50.464	0.19	48.446	0.091	101.876

16	OBD_61_OxPair2_b_1	0.016	0.054	0.744	0	1.423	0	51.031	0.197	47.843	0.065	101.373
17	OBD_61_OxPair2_b_2	0.03	0.058	0.742	0	1.413	0	51.119	0.186	47.81	0.066	101.424
18	OBD_61_OxPair2_b_3	0.012	0.041	0.733	0	1.402	0.001	51.109	0.186	47.78	0.096	101.36
19	OBD_61_OxPair2_b_4	0.006	0.042	0.731	0	1.36	0	50.933	0.183	47.925	0.024	101.204
20	OBD_61_OxPair2_b_5	0.014	0.058	0.721	0	1.422	0.003	51.084	0.178	47.595	0.18	101.255
12	OBD_61_Ox3_3	0.132	1.305	0.336	0	0.982	0.003	79.273	0.049	16.134	0	98.214
12	OBD_61_Ox6_2	0.103	1.285	0.412	0.004	0.794	0.01	78.944	0.066	16.437	0	98.055
13	OBD_61_Ox6_3	0.104	1.299	0.41	0.001	0.807	0	79.018	0.053	16.469	0	98.161
15	OBD_61_Ox6_5	0.089	1.368	0.404	0.024	0.827	0.004	78.737	0.057	16.597	0	98.107
16	OBD_61_Ox7_1	0.085	1.326	0.386	0.011	0.85	0	79.01	0.058	16.281	0	98.007
17	OBD_61_Ox7_2	0.094	1.313	0.388	0	0.848	0	79.009	0.06	16.313	0	98.025
28	OBD_61_Ox9_3	0.118	2.063	0.499	0.001	0.925	0.013	79.625	0.12	14.636	0	98
4	OBD_54_Ox1_4	0.104	1.301	0.409	0	0.866	0.007	78.956	0.048	16.49	0	98.181
14	OBD_54_Ox2_4	0.121	1.321	0.419	0	0.883	0	79.246	0.048	16.295	0	98.333
24	OBD_54_Ox4_4	0.102	1.341	0.42	0	0.801	0.02	79.432	0.056	16.212	0.018	98.402
25	OBD_54_Ox4_5	0.1	1.271	0.382	0	0.792	0.007	79.175	0.064	16.204	0.03	98.025
4	OBD_54_Ox1_4	0.104	1.301	0.409	0	0.866	0.007	78.956	0.048	16.49	0	98.181
14	OBD_54_Ox2_4	0.121	1.321	0.419	0	0.883	0	79.246	0.048	16.295	0	98.333
24	OBD_54_Ox4_4	0.102	1.341	0.42	0	0.801	0.02	79.432	0.056	16.212	0.018	98.402
25	OBD_54_Ox4_5	0.1	1.271	0.382	0	0.792	0.007	79.175	0.064	16.204	0.03	98.025
76	VR_1_IncOx2_1	0.091	2.496	1.467	0	0.679	0.045	76.254	0.258	16.91	0	98.2
77	VR_1_IncOx2_2	0.113	2.503	1.474	0	0.676	0.024	76	0.277	16.956	0	98.023
78	VR_1_IncOx2_3	0.078	2.488	1.471	0.012	0.679	0.037	76.228	0.271	16.846	0	98.11
79	VR_1_IncOx2_4	0.128	2.537	1.472	0	0.688	0.032	76.717	0.263	16.919	0	98.756
80	VR_1_IncOx2_5	0.097	2.467	1.465	0	0.68	0.04	76.169	0.274	16.865	0	98.057
1	VR_1_OxPair3_a_1	0.047	0.188	2.221	0	0.874	0	47.679	0.201	49.782	0.048	101.04
2	VR_1_OxPair3_a_2	0.054	0.178	2.17	0	0.858	0.012	47.899	0.205	50.031	0.038	101.445
3	VR_1_OxPair3_a_3	0.042	0.18	2.196	0	0.81	0	47.907	0.181	50.098	0.055	101.469
4	VR_1_OxPair3_a_4	0.058	0.194	2.163	0	0.824	0	48.105	0.206	50.309	0.009	101.868
5	VR_1_OxPair3_a_5	0.037	0.216	2.167	0	0.823	0.005	48.169	0.19	50.156	0.029	101.792
10	VR_1_OxPair3_b_5	0.109	2.302	1.432	0.008	0.669	0.025	76.65	0.238	16.627	0	98.06

21	VR_1_OxPair3_a_1	0.029	0.206	2.133	0	0.951	0.019	47.934	0.217	49.911	0	101.4
22	VR_1_OxPair3_a_2	0.041	0.206	2.157	0	0.935	0.023	47.983	0.233	49.685	0.014	101.277
23	VR_1_OxPair3_a_3	0.045	0.188	2.186	0	0.971	0.03	48.042	0.192	50.03	0	101.684
24	VR_1_OxPair3_a_4	0.077	0.2	2.194	0.013	0.984	0.017	47.671	0.208	49.91	0	101.274
25	VR_1_OxPair3_a_5	0.043	0.229	2.152	0	0.951	0.003	47.762	0.204	49.804	0	101.148
1	TbaghCr_4_1	0.069	9.247	14.944	0.147	0.228	61.559	13.056	0.057	0.099	0.013	99.419
2	TbaghCr_4_2	0.078	9.126	14.921	0.169	0.219	61.652	13.033	0.068	0.106	0.022	99.394
3	TbaghCr_4_3	0.046	9.126	14.908	0.172	0.219	61.536	13.057	0.051	0.121	0.026	99.262
4	TbaghCr_4_4	0.053	9.19	14.885	0.154	0.188	61.383	12.948	0.047	0.108	0.027	98.983
5	TbaghCr_4_5	0.044	9.171	14.963	0.167	0.212	60.849	12.952	0.048	0.121	0.017	98.544
6	Ilm_4_1	0.018	0.015	0.289	0.009	4.542	0.03	46.389	0.198	49.153	0	100.643
7	Ilm_4_2	0.022	0.017	0.294	0.016	4.557	0.022	46.762	0.223	49.033	0	100.946
8	Ilm_4_3	0.034	0.014	0.29	0.016	4.516	0.01	46.057	0.202	49.593	0	100.732
9	Ilm_4_4	0.022	0	0.293	0.002	4.499	0.022	46.404	0.217	49.51	0	100.969
10	Ilm_4_5	0.031	0.014	0.283	0.016	4.58	0.012	46.44	0.188	49.023	0	100.587
15	Ilm_1_1	0.049	0.014	0.286	0	4.562	0.008	45.743	0.188	49.356	0	100.206
16	Ilm_1_2	0.024	0.012	0.297	0.02	4.562	0.041	45.981	0.194	49.305	0	100.436
17	Ilm_1_3	0.028	0.012	0.299	0	4.484	0.033	46.158	0.197	49.47	0	100.681
18	Ilm_1_4	0.01	0.013	0.294	0.006	4.455	0.029	46.422	0.188	49.768	0	101.185
19	Ilm_1_5	0.009	0.012	0.293	0.009	4.539	0.036	46.623	0.212	48.915	0	100.648
76	TbaghCr_5_1	0.03	9.218	14.454	0.184	0.206	61.794	12.781	0.067	0.12	0	98.854
77	TbaghCr_5_2	0.049	9.091	14.542	0.179	0.219	61.504	12.881	0.062	0.129	0	98.656
78	TbaghCr_5_3	0.044	9.161	14.594	0.149	0.235	61.645	12.829	0.049	0.121	0.015	98.842
79	TbaghCr_5_4	0.058	9.246	14.554	0.172	0.227	61.329	13.006	0.051	0.114	0.009	98.766
80	TbaghCr_5_5	0.04	9.154	14.581	0.155	0.228	60.939	13.063	0.05	0.122	0.009	98.341
81	Ilm_5_1	0.012	0.014	0.29	0.006	4.522	0.021	46.019	0.216	48.779	0	99.879
82	Ilm_5_2	0.032	0.022	0.289	0	4.548	0.021	46.461	0.212	48.712	0	100.297
83	Ilm_5_3	0.025	0.028	0.299	0	4.579	0.019	46.231	0.196	48.934	0	100.311
84	Ilm_5_4	0.026	0.021	0.288	0	4.595	0	45.919	0.207	49.375	0	100.431
85	Ilm_5_5	0.027	0.026	0.301	0	4.618	0.013	45.74	0.194	48.989	0	99.908
57	TbaghCr_3_2	0.068	9.043	14.579	0.184	0.205	61.54	12.901	0.052	0.105	0.008	98.685

58	TbaghCr_3_3	0.061	9.122	14.724	0.176	0.214	61.157	13.041	0.059	0.101	0.008	98.663
59	TbaghCr_3_4	0.075	9.187	14.807	0.164	0.208	60.76	12.848	0.055	0.091	0.011	98.206
60	TbaghCr_3_5	0.084	9.064	14.795	0.183	0.215	61.093	12.948	0.054	0.096	0.001	98.533
61	Ilm_3_1	0.034	0.001	0.294	0.009	4.42	0.026	46.128	0.225	49.184	0	100.321
62	Ilm_3_2	0.033	0.002	0.287	0	4.554	0.044	45.959	0.201	49.275	0	100.355
63	Ilm_3_3	0.037	0.008	0.293	0	4.627	0.028	46.214	0.2	49.122	0	100.529
64	Ilm_3_4	0.024	0	0.286	0.005	4.34	0.044	47.001	0.204	48.382	0	100.286
65	Ilm_3_5	0.048	0.003	0.284	0.008	4.429	0.037	46.858	0.203	48.204	0	100.074

Table 4. Quantitative feldspar compositions and monitors

No.	Sample ID	SiO_2	Al_2O_3	Na_2O	MgO	BaO	FeO	K_2O	CaO	Total
6	DM_1_Alb1_core_1	64.218	22.838	8.598	0.004	0.075	0.158	1.063	4.12	101.074
7	DM_1_Alb1_core_2	63.382	22.912	8.626	0.012	0.03	0.144	1.02	4.133	100.259
8	DM_1_Alb1_core_3	63.781	22.947	8.746	0.004	0.098	0.16	1.048	4.23	101.014
9	DM_1_Alb1_core_4	63.595	23.032	8.552	0.014	0.063	0.142	1.034	4.287	100.719
10	DM_1_Alb1_core_5	64.209	22.873	8.718	0.004	0.058	0.167	1.054	4.047	101.13
11	DM_1_Kfeld1_core_1	66.59	18.985	3.51	0	0.178	0.066	11.486	0.16	100.975
12	DM_1_Kfeld1_core_2	66.187	18.802	3.501	0	0.178	0.105	11.639	0.152	100.564
13	DM_1_Kfeld1_core_3	66.53	19.009	3.562	0.003	0.208	0.074	11.543	0.156	101.085
14	DM_1_Kfeld1_core_4	66.556	18.988	3.482	0	0.249	0.124	11.468	0.172	101.039
15	DM_1_Kfeld1_core_5	66.989	18.809	3.505	0	0.188	0.095	11.621	0.153	101.36
16	DM_1_Kfeld2_core_1	66.387	18.928	3.493	0	0.359	0.115	11.534	0.124	100.94
17	DM_1_Kfeld2_core_2	66.689	18.72	3.408	0	0.417	0.11	11.537	0.118	100.999
18	DM_1_Kfeld2_core_3	66.157	18.768	3.497	0.004	0.268	0.107	11.665	0.139	100.605
19	DM_1_Kfeld2_core_4	66.252	18.875	3.37	0.003	0.387	0.044	11.538	0.171	100.64
20	DM_1_Kfeld2_core_5	66.46	18.609	3.38	0.002	0.386	0.094	11.661	0.15	100.742
21	DM_1_Alb2_core_1	64.408	22.768	8.683	0.012	0.032	0.144	1.094	3.941	101.082
22	DM_1_Alb2_core_2	64.609	22.511	8.997	0.001	0.032	0.132	1.12	3.793	101.195
23	DM_1_Alb2_core_3	64.15	22.962	8.819	0	0.01	0.14	1.009	4.171	101.261

24	DM_1_Alb2_core_4	65.058	22.396	9.015	0.001	0.07	0.177	1.172	3.625	101.514
25	DM_1_Alb2_core_5	65.097	22.631	9.003	0	0.022	0.124	1.147	3.697	101.721
31	DM_1_Kfeld3_core_1	66.068	19.274	3.469	0	1.109	0.073	11.155	0.212	101.36
32	DM_1_Kfeld3_core_2	65.873	19.21	3.395	0.002	1.096	0.076	11.309	0.227	101.188
33	DM_1_Kfeld3_core_3	66.103	19.12	3.372	0	1.09	0.092	11.338	0.213	101.328
34	DM_1_Kfeld3_core_4	66.049	19.056	3.339	0.004	0.954	0.081	11.392	0.188	101.063
35	DM_1_Kfeld3_core_5	65.97	18.924	3.367	0	0.894	0.055	11.399	0.189	100.798
41	DM_1_Kfeld4_core_1	66.008	19.366	3.457	0	1.271	0.112	11.064	0.206	101.484
42	DM_1_Kfeld4_core_2	65.793	19.2	3.445	0.005	1.251	0.093	11.197	0.205	101.189
43	DM_1_Kfeld4_core_3	65.861	19.219	3.395	0	1.324	0.094	11.106	0.209	101.208
44	DM_1_Kfeld4_core_4	65.777	19.206	3.475	0.004	1.31	0.096	11.104	0.211	101.183
45	DM_1_Kfeld4_core_5	66.006	19.467	3.528	0	1.294	0.081	11.22	0.201	101.797
46	DM_1_Alb3_core_1	78.306	12.719	3.523	0.039	0.068	0.674	4.893	0.577	100.799
47	DM_1_Alb3_core_2	78.487	12.606	3.523	0.051	0.005	0.628	4.922	0.578	100.8
48	DM_1_Alb3_core_3	78.584	12.541	3.527	0.045	0.075	0.608	4.806	0.559	100.745
49	DM_1_Alb3_core_4	78.847	12.659	3.561	0.04	0.08	0.61	4.909	0.579	101.285
50	DM_1_Alb3_core_5	78.173	12.641	3.596	0.041	0.045	0.566	4.951	0.56	100.573
51	DM_1_Kfeld5_core_1	67.077	19.058	3.462	0	0.258	0.054	11.536	0.164	101.609
52	DM_1_Kfeld5_core_2	67.116	18.898	3.473	0.006	0.313	0.056	11.539	0.144	101.545
53	DM_1_Kfeld5_core_3	66.746	18.95	3.403	0	0.286	0.085	11.554	0.139	101.163
54	DM_1_Kfeld5_core_4	67.126	19.156	3.417	0.007	0.358	0.076	11.549	0.163	101.852
55	DM_1_Kfeld5_core_5	66.748	18.952	3.391	0.006	0.278	0.083	11.616	0.147	101.221
56	DM_1_Kfeld6_core_1	66.908	18.983	3.597	0.005	0.3	0.087	11.585	0.17	101.635
57	DM_1_Kfeld6_core_2	67.307	18.914	3.509	0.007	0.15	0.114	11.488	0.143	101.632
58	DM_1_Kfeld6_core_3	67.049	19.041	3.534	0.001	0.163	0.118	11.703	0.166	101.775
59	DM_1_Kfeld6_core_4	67.226	19.153	3.546	0.003	0.22	0.057	11.519	0.165	101.889
60	DM_1_Kfeld6_core_5	67.246	19.007	3.708	0.004	0.245	0.074	11.175	0.147	101.606
62	DM_1_Alb4_core_2	63.008	24.026	8.07	0	0.005	0.158	0.737	5.453	101.457
63	DM_1_Alb4_core_3	63.819	23.553	8.432	0.003	0.082	0.164	0.875	4.804	101.732
64	DM_1_Alb4_core_4	63.843	23.174	8.482	0.009	0.142	0.182	0.97	4.435	101.237
1	VR_1_Alb1_core_1	64.55	22.132	8.783	0	0	0.124	1.295	3.535	100.419

2	VR_1_Alb1_core_2	64.941	22.217	8.752	0	0.018	0.082	1.237	3.462	100.709
3	VR_1_Alb1_core_3	64.097	22.442	8.808	0.008	0.035	0.123	1.197	3.815	100.525
4	VR_1_Alb1_core_4	64.568	22.104	9.098	0.005	0.045	0.114	1.272	3.517	100.723
5	VR_1_Alb1_core_5	64.348	22.33	8.906	0	0.03	0.114	1.206	3.687	100.621
6	VR_1_Alb1_rim_1	61.262	23.89	7.32	0.009	0.21	0.283	1.699	5.534	100.207
7	VR_1_Alb1_rim_2	62.558	22.612	6.801	0.051	0.108	0.548	2.133	5.126	99.937
9	VR_1_Alb1_rim_4	61.251	24.088	7.321	0.024	0.138	0.297	1.543	5.635	100.297
11	VR_1_Kfeld1_core_1	65.538	18.98	3.837	0.002	0.151	0.038	11.089	0.249	99.884
12	VR_1_Kfeld1_core_2	65.979	18.859	3.823	0	0.148	0.05	10.986	0.247	100.092
13	VR_1_Kfeld1_core_3	65.808	18.77	3.876	0	0.133	0.063	10.925	0.244	99.819
15	VR_1_Kfeld1_core_5	65.915	18.985	3.909	0.002	0.176	0.083	10.91	0.216	100.196
16	VR_1_Alb2_core_1	55.938	27.689	5.702	0.038	0.025	0.376	0.617	9.857	100.242
17	VR_1_Alb2_core_2	56.598	27.214	5.778	0.041	0.065	0.388	0.601	9.476	100.161
18	VR_1_Alb2_core_3	56.434	27.15	5.762	0.042	0.073	0.399	0.626	9.415	99.901
19	VR_1_Alb2_core_4	56.19	27.729	5.57	0.043	0.025	0.38	0.566	9.857	100.36
20	VR_1_Alb2_core_5	55.997	27.508	5.515	0.049	0.08	0.378	0.556	9.817	99.9
21	VR_1_Alb3_rim_1	62.983	23.271	8.067	0.005	0.065	0.266	1.621	4.566	100.844
22	VR_1_Alb3_rim_2	63.111	22.917	8.005	0.013	0.083	0.213	1.614	4.637	100.593
23	VR_1_Alb3_rim_3	62.529	23.201	8.04	0.01	0.09	0.242	1.551	4.897	100.56
24	VR_1_Alb3_rim_4	62.586	23.373	7.795	0.014	0.158	0.238	1.556	4.775	100.495
26	VR_1_Alb4_rim_1	56.106	27.446	5.73	0.048	0.103	0.381	0.551	9.759	100.124
27	VR_1_Alb4_rim_2	56.729	27.413	5.849	0.05	0.131	0.424	0.557	9.623	100.776
28	VR_1_Alb4_rim_3	56.405	27.242	5.854	0.04	0.163	0.433	0.539	9.551	100.227
29	VR_1_Alb4_rim_4	56.813	27.111	5.967	0.034	0.121	0.373	0.638	9.256	100.313
30	VR_1_Alb4_rim_5	57.461	27.13	6.084	0.037	0.151	0.361	0.632	8.961	100.817
31	VR_1_Kfeld2_core_1	66.039	18.898	3.884	0.003	0.133	0.076	10.737	0.352	100.122
32	VR_1_Kfeld2_core_2	66.18	19.091	3.962	0.009	0.083	0.115	10.95	0.367	100.757
33	VR_1_Kfeld2_core_3	66.121	19.042	3.863	0	0.033	0.112	10.94	0.34	100.451
34	VR_1_Kfeld2_core_4	66.378	19.058	3.999	0	0.025	0.135	10.743	0.34	100.678
35	VR_1_Kfeld2_core_5	66.125	19.06	4.012	0	0.148	0.13	10.766	0.351	100.592
36	VR_1_Alb5_core_1	60.775	24.406	7.285	0.002	0.178	0.256	1.407	5.851	100.16

37	VR_1_Alb5_core_2	61.119	24.222	7.315	0.012	0.173	0.245	1.369	5.878	100.333
38	VR_1_Alb5_core_3	60.757	24.264	7.424	0.003	0.188	0.288	1.357	5.901	100.182
39	VR_1_Alb5_core_4	60.504	24.686	7.109	0.013	0.226	0.258	1.232	6.309	100.337
40	VR_1_Alb5_core_5	60.979	24.337	7.407	0.012	0.211	0.237	1.4	5.883	100.466
41	VR_1_Kfeld3_core_1	66.018	18.764	3.775	0	0.143	0.08	11.052	0.212	100.044
42	VR_1_Kfeld3_core_2	65.787	18.784	3.722	0.01	0.154	0.101	11.058	0.216	99.832
43	VR_1_Kfeld3_core_3	66.054	18.795	3.656	0.012	0.199	0.076	11.154	0.23	100.176
44	VR_1_Kfeld3_core_4	65.88	18.819	3.697	0.002	0.174	0.102	11.202	0.212	100.088
45	VR_1_Kfeld3_core_5	66.109	18.934	3.794	0	0.133	0.081	11.057	0.229	100.337
1	OBD_6_Kfeld_core_1	65.726	18.61	3.474	0	0.196	0.085	11.605	0.168	99.864
2	OBD_6_Kfeld_core_2	65.775	18.759	3.411	0	0.153	0.106	11.57	0.171	99.945
3	OBD_6_Kfeld_core_3	65.67	18.808	3.422	0	0.156	0.076	11.542	0.185	99.859
4	OBD_6_Kfeld_core_4	65.789	18.901	3.506	0	0.128	0.102	11.52	0.168	100.114
5	OBD_6_Kfeld_core_5	65.623	18.681	3.458	0.004	0.176	0.083	11.508	0.174	99.707
6	OBD_6_Kfeld2_core_1	65.574	18.769	3.441	0	0.327	0.088	11.412	0.198	99.809
7	OBD_6_Kfeld2_core_2	65.461	18.745	3.456	0.004	0.389	0.116	11.352	0.194	99.717
8	OBD_6_Kfeld2_core_3	65.233	18.884	3.448	0	0.436	0.111	11.373	0.167	99.652
9	OBD_6_Kfeld2_core_4	65.036	18.792	3.512	0	0.361	0.075	11.585	0.166	99.527
10	OBD_6_Kfeld2_core_5	65.323	18.8	3.424	0	0.346	0.074	11.393	0.168	99.528
11	OBD_6_Alb1_core_1	63.293	22.646	8.388	0.015	0.002	0.151	1.473	4.008	99.976
12	OBD_6_Alb1_core_2	63.255	22.405	8.258	0	0.087	0.147	1.557	3.877	99.586
13	OBD_6_Alb1_core_3	63.629	22.441	8.329	0.003	0.085	0.128	1.645	3.885	100.145
14	OBD_6_Alb1_core_4	63.211	22.477	8.22	0	0.065	0.132	1.533	3.991	99.629
15	OBD_6_Alb1_core_5	63.496	22.421	8.318	0	0.095	0.122	1.712	3.796	99.96
16	OBD_6_Kfeld3_core_1	64.517	19.482	4.166	0.014	1.334	0.111	10.01	0.429	100.063
17	OBD_6_Kfeld3_core_2	64.714	19.611	4.171	0.001	1.332	0.08	9.821	0.467	100.197
18	OBD_6_Kfeld3_core_3	64.717	19.48	4.312	0	1.308	0.104	9.756	0.408	100.085
19	OBD_6_Kfeld3_core_4	64.791	19.297	4.194	0	1.042	0.074	9.982	0.417	99.797
20	OBD_6_Kfeld3_core_5	65.486	19.222	4.081	0.007	0.915	0.063	10.285	0.409	100.468
1	OBD_6_Alb2_core_1	58.629	25.812	6.688	0.028	0.185	0.259	0.678	7.787	100.066
2	OBD_6_Alb2_core_2	58.629	25.717	6.718	0.027	0.178	0.28	0.677	7.828	100.054

4	OBD_6_Alb2_core_4	58.039	26.468	6.347	0.038	0.123	0.356	0.598	8.332	100.301
5	OBD_6_Alb2_core_5	57.292	26.596	6.068	0.034	0.098	0.367	0.49	8.903	99.848
6	OBD_6_Alb2_rim_1	57.503	26.715	6.286	0.04	0.078	0.398	0.533	8.667	100.22
7	OBD_6_Alb2_rim_2	57.102	26.586	6.189	0.045	0.083	0.371	0.551	8.826	99.753
8	OBD_6_Alb2_rim_3	56.981	26.846	6.113	0.036	0.075	0.372	0.537	8.919	99.879
9	OBD_6_Alb2_rim_4	58.423	25.998	6.694	0.038	0.173	0.366	0.692	7.757	100.141
11	OBD_6_Kfeld_4_core_1	65.623	19.076	4.311	0	0.504	0.103	9.95	0.445	100.012
12	OBD_6_Kfeld_4_core_2	65.542	19.358	4.136	0.005	0.472	0.083	10.293	0.412	100.301
13	OBD_6_Kfeld_4_core_3	66.011	19.449	4.286	0	0.665	0.1	10.118	0.333	100.962
14	OBD_6_Kfeld_4_core_4	65.698	19.162	4.359	0	0.695	0.091	9.948	0.497	100.45
15	OBD_6_Kfeld_4_core_5	65.816	19.223	4.319	0	0.56	0.11	10.041	0.447	100.516
16	OBD_6_Alb3_core_1	63.149	22.734	8.295	0.002	0.068	0.204	1.519	4.156	100.127
17	OBD_6_Alb3_core_2	63.429	22.796	8.286	0	0.048	0.14	1.507	4.283	100.489
18	OBD_6_Alb3_core_3	63.122	22.662	8.283	0	0.045	0.134	1.586	4.065	99.897
19	OBD_6_Alb3_core_4	63.573	22.468	8.369	0	0.033	0.169	1.673	3.999	100.284
20	OBD_6_Alb3_core_5	63.529	22.617	8.277	0	0.058	0.15	1.486	4.091	100.208
21	OBD_6_Alb4_core_1	63.683	22.843	8.646	0.002	0.035	0.141	1.126	4.094	100.57
22	OBD_6_Alb4_core_2	63.496	22.95	8.712	0.002	0.065	0.195	1.119	4.22	100.759
23	OBD_6_Alb4_core_3	63.378	23.003	8.328	0.005	0	0.157	1.013	4.539	100.423
24	OBD_6_Alb4_core_4	62.954	23.317	8.399	0	0	0.18	0.968	4.724	100.542
25	OBD_6_Alb4_core_5	62.727	23.255	8.424	0.003	0.01	0.184	0.962	4.653	100.218
26	OBD_6_Kfeld5_rim_1	65.496	19.545	4.557	0.012	0.765	0.179	9.402	0.589	100.545
27	OBD_6_Kfeld5_rim_2	65.416	19.491	4.598	0.002	0.798	0.185	9.393	0.583	100.466
29	OBD_6_Kfeld5_rim_4	65.49	18.988	4.344	0.012	0.579	0.226	9.641	0.479	99.759
30	OBD_6_Kfeld5_rim_5	65.3	19.399	4.507	0	0.828	0.199	9.703	0.499	100.435
31	OBD_6_Kfeld5_middle_1	65.686	19.212	4.105	0	0.695	0.091	10.253	0.345	100.387
32	OBD_6_Kfeld5_middle_2	65.641	19.293	4.05	0	0.763	0.083	10.508	0.355	100.693
33	OBD_6_Kfeld5_middle_3	66.383	19.242	4.164	0.004	0.57	0.069	10.324	0.306	101.062
34	OBD_6_Kfeld5_middle_4	65.894	19.246	4.436	0.001	0.607	0.098	9.914	0.36	100.556
35	OBD_6_Kfeld5_middle_5	66.125	19.351	4.639	0	0.64	0.088	9.487	0.471	100.801
36	OBD_6_Kfeld5_core_1	64.04	22.266	8.444	0	0.033	0.17	1.813	3.582	100.348

37	OBD_6_Kfeld5_core_2	64.08	22.416	8.418	0.009	0.08	0.137	1.814	3.638	100.592
38	OBD_6_Kfeld5_core_3	64.19	22.284	8.389	0.011	0.063	0.161	1.884	3.649	100.631
39	OBD_6_Kfeld5_core_4	64.619	22.157	8.541	0	0.045	0.138	1.811	3.51	100.821
40	OBD_6_Kfeld5_core_5	64.269	22.342	8.43	0.009	0.053	0.164	1.802	3.505	100.574
41	OBD_6_Kfeld6_rim_1	65.171	19.32	4.298	0	0.858	0.15	9.84	0.494	100.131
42	OBD_6_Kfeld6_rim_2	65.239	19.433	4.214	0	1.043	0.111	9.861	0.472	100.373
43	OBD_6_Kfeld6_rim_3	65.241	19.517	4.266	0	1.091	0.083	9.995	0.464	100.657
44	OBD_6_Kfeld6_rim_4	65.563	19.356	4.092	0	1.146	0.1	9.938	0.407	100.602
45	OBD_6_Kfeld6_rim_5	65.29	19.475	4.283	0	1.273	0.115	9.792	0.399	100.627
46	OBD_6_Kfeld6_core_1	63.609	23.12	8.244	0.002	0.208	0.198	1.368	4.331	101.08
47	OBD_6_Kfeld6_core_2	63.62	22.966	8.471	0	0.145	0.193	1.545	4.083	101.023
48	OBD_6_Kfeld6_core_3	63.421	22.826	8.426	0.01	0.105	0.189	1.368	4.247	100.592
49	OBD_6_Kfeld6_core_4	63.075	23.01	8.318	0	0.05	0.171	1.396	4.332	100.352
50	OBD_6_Kfeld6_core_5	63.661	22.914	8.425	0.002	0.125	0.13	1.392	4.171	100.82
82	OBD_51_AlbGlom1_rim_2	63.166	23.346	8.37	0.002	0.06	0.246	0.963	4.637	100.79
83	OBD_51_AlbGlom1_rim_3	64.26	22.922	8.575	0	0.062	0.218	1.172	4.011	101.22
84	OBD_51_AlbGlom1_rim_4	63.531	23.038	8.46	0.013	0.042	0.201	1.125	4.357	100.767
85	OBD_51_AlbGlom1_rim_5	63.659	22.991	8.489	0	0.13	0.173	1.125	4.303	100.87
86	OBD_51_AlbGlom1_core_1	60.211	25.421	7.432	0	0.142	0.17	0.624	6.663	100.663
87	OBD_51_AlbGlom1_core_2	60.259	25.37	7.256	0.006	0.097	0.182	0.553	6.855	100.578
88	OBD_51_AlbGlom1_core_3	60.395	25.164	7.41	0.002	0.05	0.172	0.628	6.771	100.592
89	OBD_51_AlbGlom1_core_4	60.439	25.298	7.247	0	0.075	0.192	0.611	6.773	100.635
90	OBD_51_AlbGlom1_core_5	60.13	25.296	7.304	0.014	0.15	0.185	0.659	6.799	100.537
91	OBD_51_Alb1_core_1	54.152	29.729	4.711	0	0.005	0.214	0.225	11.898	100.934
92	OBD_51_Alb1_core_2	54.215	29.784	4.778	0.013	0.04	0.229	0.243	11.584	100.886
93	OBD_51_Alb1_core_3	53.686	29.869	4.654	0.001	0.02	0.152	0.232	12.136	100.75
94	OBD_51_Alb1_core_4	53.529	29.637	4.644	0.005	0.068	0.185	0.218	12.104	100.39
95	OBD_51_Alb1_core_5	55.396	28.498	5.314	0.011	0.06	0.14	0.254	10.671	100.344
96	OBD_51_Alb1_rim_1	62.962	23.27	8.444	0	0.025	0.174	0.965	4.503	100.343
97	OBD_51_Alb1_rim_2	63.259	23.033	8.337	0	0.097	0.19	0.993	4.472	100.381
98	OBD_51_Alb1_rim_3	62.985	23.52	8.425	0.008	0.03	0.203	0.871	4.805	100.847

99	OBD_51_Alb1_rim_4	62.659	23.816	8.329	0.009	0.06	0.15	0.852	5.041	100.916
100	OBD_51_Alb1_rim_5	63.545	22.999	8.451	0.009	0.107	0.213	1.019	4.381	100.724
101	OBD_51_Kfeld1_core_1	66.294	19.079	4.098	0	0.533	0.083	10.309	0.327	100.723
102	OBD_51_Kfeld1_core_2	65.932	18.918	4.107	0	0.448	0.103	10.402	0.337	100.247
103	OBD_51_Kfeld1_core_3	66.314	19.147	4.249	0.003	0.458	0.104	10.218	0.362	100.855
104	OBD_51_Kfeld1_core_4	66.015	19.217	4.178	0.002	0.697	0.096	9.943	0.399	100.547
105	OBD_51_Kfeld1_core_5	65.808	19.415	4.261	0	0.625	0.072	10.036	0.378	100.595
1	OBD_4_Kfeld1_core_1	65.971	19.508	4.228	0.008	1.243	0.117	9.92	0.445	101.44
2	OBD_4_Kfeld1_core_2	66.198	19.457	4.282	0	1.344	0.102	9.842	0.432	101.657
3	OBD_4_Kfeld1_core_3	66.21	19.415	4.277	0	1.014	0.052	9.918	0.451	101.337
4	OBD_4_Kfeld1_core_4	66.162	19.289	4.232	0	0.803	0.08	10.058	0.394	101.018
5	OBD_4_Kfeld1_core_5	66.319	19.006	4.265	0.002	0.604	0.083	10.121	0.364	100.764
6	OBD_4_Alb1_core_1	64.464	22.439	8.316	0.012	0	0.159	1.601	3.949	100.94
7	OBD_4_Alb1_core_2	64.192	22.538	8.319	0.005	0.045	0.186	1.664	3.942	100.891
8	OBD_4_Alb1_core_3	64.225	22.412	8.24	0.01	0.062	0.131	1.596	3.868	100.544
9	OBD_4_Alb1_core_4	64.569	22.704	8.241	0	0.07	0.17	1.519	3.925	101.198
10	OBD_4_Alb1_core_5	64.623	22.723	8.179	0.001	0.129	0.192	1.491	4.019	101.357
11	OBD_4_Alb2_core_1	64.426	22.728	8.447	0.003	0.065	0.153	1.615	4.045	101.482
12	OBD_4_Alb3_core_2	64.494	22.641	8.389	0.006	0.015	0.158	1.573	4.043	101.319
13	OBD_4_Alb3_core_3	64.374	22.531	8.438	0.013	0.057	0.139	1.646	3.869	101.067
15	OBD_4_Alb3_core_5	64.562	22.518	8.34	0.004	0.025	0.183	1.673	3.699	101.004
16	OBD_4_Kfeld2_core_1	65.479	19.481	4.47	0	1.144	0.103	9.769	0.575	101.021
17	OBD_4_Kfeld2_core_2	65.885	19.525	4.375	0	1.091	0.102	9.614	0.588	101.18
18	OBD_4_Kfeld2_core_3	65.719	19.357	4.351	0.004	1.1	0.102	9.656	0.564	100.853
19	OBD_4_Kfeld2_core_4	65.474	19.656	4.311	0.004	1.186	0.086	9.631	0.612	100.96
20	OBD_4_Kfeld2_core_5	65.437	19.431	4.305	0.005	1.167	0.101	9.802	0.454	100.702
22	OBD_4_Alb3_core_2	64.712	22.769	8.391	0	0.055	0.18	1.508	3.949	101.564
23	OBD_4_Alb3_core_3	64.647	22.612	8.377	0.006	0.027	0.163	1.459	3.952	101.243
24	OBD_4_Alb3_core_4	64.363	22.693	8.339	0.003	0.03	0.117	1.415	4.097	101.057
25	OBD_4_Alb3_core_5	64.373	22.715	8.371	0	0.065	0.141	1.451	4.082	101.198
26	OBD_4_Kfeld3_core_1	66.226	19.325	4.243	0.005	0.731	0.086	10.211	0.36	101.187

27	OBD_4_Kfeld3_core_2	66.315	19.477	4.325	0.009	0.803	0.086	9.738	0.535	101.288
28	OBD_4_Kfeld3_core_3	66.517	19.208	4.301	0.002	0.711	0.098	10.062	0.416	101.315
29	OBD_4_Kfeld3_core_4	66.156	19.372	4.226	0.003	0.581	0.113	9.985	0.462	100.898
30	OBD_4_Kfeld3_core_5	66.207	19.171	4.327	0	0.544	0.097	10.321	0.429	101.096
1	OBD_61_Alb1_core_1	63.609	22.818	8.362	0	0.062	0.14	0.993	4.274	100.258
2	OBD_61_Alb1_core_2	63.58	23.033	8.467	0.003	0.072	0.157	0.997	4.387	100.696
3	OBD_61_Alb1_core_3	64.237	22.741	8.498	0	0	0.157	1.046	4.045	100.724
4	OBD_61_Alb1_core_4	62.625	23.765	8.077	0.009	0.08	0.174	0.806	5.244	100.78
5	OBD_61_Alb1_core_5	62.299	23.873	7.982	0.012	0.142	0.258	0.775	5.261	100.602
6	OBD_61_Kfeld_core_1	65.722	18.837	3.331	0.002	0.962	0.096	11.293	0.183	100.426
7	OBD_61_Kfeld_core_2	65.282	18.956	3.346	0	1.123	0.098	11.323	0.195	100.323
8	OBD_61_Kfeld_core_3	65.411	19.146	3.369	0.011	1.305	0.117	11.3	0.201	100.86
9	OBD_61_Kfeld_core_4	65.402	19.122	3.288	0.007	1.242	0.125	11.283	0.211	100.68
10	OBD_61_Kfeld_core_5	65.221	18.889	3.24	0	1.361	0.107	11.303	0.175	100.296
11	OBD_61_Alb2_core_1	63.198	23.329	8.1	0	0	0.226	0.95	4.666	100.469
12	OBD_61_Alb2_core_2	63.446	23.479	8.288	0	0.022	0.134	0.956	4.701	101.026
13	OBD_61_Alb2_core_3	63.612	23.109	8.33	0.009	0.08	0.172	1.007	4.398	100.717
14	OBD_61_Alb2_core_4	64.002	22.338	8.509	0.001	0.065	0.164	1.185	3.905	100.169
15	OBD_61_Alb2_core_5	63.579	22.972	8.501	0.004	0.045	0.178	0.992	4.469	100.74
16	OBD_61_Kfeld2_core_1	66.382	18.786	3.355	0	0.35	0.112	11.594	0.152	100.731
17	OBD_61_Kfeld2_core_2	66.203	18.819	3.347	0.004	0.365	0.111	11.565	0.14	100.554
18	OBD_61_Kfeld2_core_3	66.162	18.862	3.399	0	0.402	0.088	11.531	0.182	100.626
19	OBD_61_Kfeld2_core_4	66.063	18.898	3.311	0	0.427	0.108	11.403	0.158	100.368
20	OBD_61_Kfeld2_core_5	65.742	18.896	3.389	0	0.827	0.07	11.47	0.195	100.589
31	GCD_6_Alb1_core_1	63.74	22.678	8.14	0	0.075	0.178	1.366	4.273	100.45
32	GCD_6_Alb1_core_2	63.918	22.781	8.272	0.007	0.035	0.16	1.38	4.211	100.764
33	GCD_6_Alb1_core_3	64.706	22.796	8.388	0.003	0.077	0.158	1.502	3.852	101.482
34	GCD_6_Alb1_core_4	63.679	22.642	8.257	0.01	0.052	0.176	1.489	4.091	100.396
35	GCD_6_Alb1_core_5	64.288	22.523	8.438	0.007	0.045	0.158	1.505	3.91	100.874
36	GCD_6_Kfeld1_core_1	66.532	19.324	4.224	0	0.526	0.06	10.116	0.38	101.162
37	GCD_6_Kfeld1_core_2	66.187	19.07	4.23	0.009	0.37	0.115	10.166	0.419	100.566

38	GCD_6_Kfeld1_core_3	66.336	19.34	4.195	0	0.427	0.123	10.229	0.37	101.02
39	GCD_6_Kfeld1_core_4	66.154	19.141	4.21	0.001	0.459	0.073	10.164	0.382	100.584
40	GCD_6_Kfeld1_core_5	66.396	19.198	4.247	0	0.412	0.077	10.218	0.383	100.931
41	GCD_6_Alb2_core_1	62.231	23.759	7.819	0.013	0.124	0.165	1.076	5.194	100.381
42	GCD_6_Alb2_core_2	62.607	23.581	7.905	0.001	0.157	0.206	1.171	4.977	100.605
43	GCD_6_Alb2_core_3	62.829	23.477	7.965	0.009	0.159	0.188	1.209	4.918	100.754
44	GCD_6_Alb2_core_4	62.282	23.721	8.017	0.009	0.097	0.206	1.106	5.302	100.74
45	GCD_6_Alb2_core_5	62.388	23.949	7.966	0	0.139	0.163	1.109	5.347	101.061
46	GCD_6_Kfeld2_core_1	66.082	19.361	4.241	0	0.42	0.082	10.03	0.434	100.65
47	GCD_6_Kfeld2_core_2	66.006	19.134	4.366	0	0.554	0.068	10.113	0.391	100.632
48	GCD_6_Kfeld2_core_3	66.322	19.313	4.215	0	0.616	0.077	10.154	0.408	101.105
49	GCD_6_Kfeld2_core_4	66.188	19.149	4.279	0	0.49	0.106	10.154	0.395	100.761
50	GCD_6_Kfeld2_core_5	66.478	19.223	4.424	0.003	0.524	0.087	9.967	0.452	101.158
41	GCD_10_AlbGlom_rim_1	62.856	23.612	8.352	0.003	0.105	0.187	0.963	4.712	100.79
42	GCD_10_AlbGlom_rim_2	63.229	23.552	8.362	0.003	0.082	0.222	0.942	4.719	101.111
43	GCD_10_AlbGlom_rim_3	63.389	23.067	8.404	0.003	0.002	0.182	1.008	4.432	100.487
44	GCD_10_AlbGlom_rim_4	63.42	23.308	8.325	0	0.085	0.193	0.994	4.586	100.911
45	GCD_10_AlbGlom_rim_5	63.288	23.3	8.561	0.013	0.06	0.159	0.977	4.568	100.926
46	GCD_10_AlbGlom_core_1	56.28	28.178	5.662	0.008	0.07	0.201	0.322	9.985	100.706
47	GCD_10_AlbGlom_core_2	56.168	27.991	5.684	0.004	0.008	0.175	0.293	9.942	100.265
48	GCD_10_AlbGlom_core_3	56.603	27.753	5.814	0	0.02	0.185	0.364	9.65	100.389
49	GCD_10_AlbGlom_core_4	56.527	27.72	5.834	0.046	0.01	0.232	0.399	9.584	100.352
50	GCD_10_AlbGlom_core_5	56.903	27.943	5.883	0.009	0.093	0.185	0.332	9.512	100.86
51	GCD_10_Alb1_core_1	62.857	23.369	8.396	0.001	0.047	0.204	0.901	4.778	100.553
52	GCD_10_Alb1_core_2	63.5	23.209	8.417	0.006	0.06	0.195	0.97	4.552	100.909
53	GCD_10_Alb1_core_3	62.445	23.965	8.137	0.007	0.06	0.18	0.779	5.335	100.908
54	GCD_10_Alb1_core_4	61.019	25.026	7.583	0	0	0.192	0.607	6.477	100.904
55	GCD_10_Alb1_core_5	60.989	25.22	7.562	0.007	0.04	0.205	0.552	6.557	101.132
56	GCD_10_Kfeld1_core_1	64.701	19.327	3.311	0	2.211	0.101	10.96	0.225	100.836
57	GCD_10_Kfeld1_core_2	64.443	19.227	3.341	0	2.114	0.113	10.809	0.219	100.266
58	GCD_10_Kfeld1_core_3	65.032	19.153	3.251	0	2.105	0.077	10.938	0.19	100.746

59	GCD_10_Kfeld1_core_4	64.852	19.437	3.345	0	2.005	0.105	11.011	0.203	100.958
60	GCD_10_Kfeld1_core_5	65.143	19.159	3.328	0.004	1.918	0.105	10.987	0.213	100.857
61	GCD_10_Kfeld2_core_1	66.131	18.975	3.324	0.011	0.89	0.114	11.434	0.192	101.071
62	GCD_10_Kfeld2_core_2	65.903	18.93	3.416	0.003	1.045	0.163	11.309	0.197	100.966
63	GCD_10_Kfeld2_core_3	66.08	19.044	3.32	0.004	0.8	0.084	11.36	0.181	100.873
64	GCD_10_Kfeld2_core_4	65.881	19.127	3.333	0	0.892	0.135	11.347	0.214	100.929
65	GCD_10_Kfeld2_core_5	66.126	19.181	3.362	0	0.88	0.113	11.376	0.18	101.218
66	GCD_10_Alb2_core_1	62.425	23.789	8.057	0	0.072	0.258	0.763	5.343	100.707
67	GCD_10_Alb2_core_2	62.421	24.123	8.023	0.009	0.032	0.181	0.831	5.359	100.979
68	GCD_10_Alb2_core_3	62.667	23.986	8.004	0	0.16	0.163	0.817	5.199	100.996
69	GCD_10_Alb2_core_4	63.99	22.875	8.557	0.009	0.052	0.19	1.04	4.109	100.822
70	GCD_10_Alb2_core_5	63.725	22.787	8.453	0.006	0.169	0.138	1.028	4.395	100.701
71	GCD_10_AlbGlom2_core_1	55.867	28.38	5.504	0.054	0.027	0.377	0.341	10.16	100.71
72	GCD_10_AlbGlom2_core_2	55.152	28.915	5.193	0.006	0.078	0.242	0.268	10.889	100.743
73	GCD_10_AlbGlom2_core_3	55.663	28.353	5.489	0.002	0.055	0.414	0.259	10.253	100.488
74	GCD_10_AlbGlom2_core_4	55.944	28.151	5.467	0	0.07	0.369	0.307	10.205	100.513
75	GCD_10_AlbGlom2_core_5	55.98	28.249	5.601	0.008	0.028	0.349	0.246	10.26	100.721
76	GCD_10_AlbGlom2_rim_1	58.284	26.743	6.572	0.011	0.07	0.246	0.47	8.439	100.835
77	GCD_10_AlbGlom2_rim_2	60.401	25.413	7.354	0.005	0.075	0.186	0.589	6.899	100.922
78	GCD_10_AlbGlom2_rim_3	56.296	28.043	5.746	0.004	0.038	0.217	0.302	9.847	100.493
79	GCD_10_AlbGlom2_rim_4	56.332	27.837	5.821	0.01	0.058	0.195	0.31	9.611	100.174
80	GCD_10_AlbGlom2_rim_5	55.431	28.564	5.232	0	0.083	0.29	0.278	10.501	100.379
1	GCD_41_Kfeld1_core_1	66.133	18.759	3.431	0.001	0.439	0.096	11.561	0.145	100.565
2	GCD_41_Kfeld1_core_2	65.468	18.744	3.44	0	0.584	0.109	11.507	0.181	100.033
3	GCD_41_Kfeld1_core_3	65.664	18.819	3.362	0	0.567	0.099	11.484	0.2	100.195
4	GCD_41_Kfeld1_core_4	65.431	18.997	3.39	0	0.729	0.122	11.419	0.203	100.291
5	GCD_41_Kfeld1_core_5	65.919	19.047	3.445	0	0.632	0.07	11.526	0.167	100.806
6	GCD_41_Alb1_core_1	56.418	27.412	6.016	0.01	0.143	0.289	0.321	9.383	99.992
7	GCD_41_Alb1_core_2	57.202	26.823	6.307	0.01	0.158	0.324	0.386	8.829	100.039
8	GCD_41_Alb1_core_3	56.822	27.078	6.223	0.009	0.118	0.356	0.336	9.11	100.052
9	GCD_41_Alb1_core_4	56.582	26.818	6.224	0	0.065	0.336	0.366	9.051	99.442

10	GCD_41_Alb1_core_5	56.576	27.053	6.151	0.013	0.1	0.401	0.35	9.226	99.87
11	GCD_41_Kfeld2_core_1	64.482	18.893	3.384	0	1.418	0.079	11.163	0.169	99.588
12	GCD_41_Kfeld2_core_2	64.521	19.145	3.328	0	1.4	0.098	11.162	0.148	99.802
13	GCD_41_Kfeld2_core_3	65.087	18.944	3.254	0.01	1.3	0.092	11.379	0.193	100.259
14	GCD_41_Kfeld2_core_4	64.79	19.026	3.436	0.002	1.57	0.116	11.196	0.216	100.352
15	GCD_41_Kfeld2_core_5	65.156	18.909	3.275	0	1.378	0.149	11.3	0.184	100.351
16	GCD_41_Alb2_rim1_1	63.723	22.977	8.55	0.002	0.04	0.161	1.04	4.284	100.777
17	GCD_41_Alb2_rim1_2	63.243	22.738	8.563	0.004	0.058	0.211	1.037	4.259	100.113
18	GCD_41_Alb2_rim1_3	63.506	22.606	8.689	0	0.11	0.168	1.075	4.043	100.197
19	GCD_41_Alb2_rim1_4	63.449	22.781	8.454	0	0.015	0.176	1.04	4.303	100.218
20	GCD_41_Alb2_rim1_5	63.361	22.999	8.648	0.011	0.057	0.15	1.051	4.295	100.572
21	GCD_41_Alb2_rim2_1	56.743	27.386	6.069	0.011	0.035	0.208	0.353	9.378	100.183
22	GCD_41_Alb2_rim2_2	56.511	27.197	6.188	0.003	0.06	0.245	0.358	9.358	99.92
23	GCD_41_Alb2_rim2_3	57.477	27.028	6.374	0	0.078	0.141	0.386	8.876	100.36
24	GCD_41_Alb2_rim2_4	57.766	27.046	6.487	0.002	0.08	0.183	0.403	8.786	100.753
25	GCD_41_Alb2_rim2_5	56.191	28.162	5.758	0.007	0.055	0.207	0.29	10.053	100.723
26	GCD_41_Alb2_core_1	63.132	22.906	8.62	0.009	0.045	0.218	1.061	4.261	100.252
27	GCD_41_Alb2_core_2	62.623	23.318	8.469	0.004	0.068	0.159	0.894	4.814	100.349
28	GCD_41_Alb2_core_3	62.017	24.066	8.245	0.008	0.03	0.237	0.769	5.46	100.832
29	GCD_41_Alb2_core_4	61.816	23.989	8.133	0	0.043	0.196	0.765	5.544	100.486
30	GCD_41_Alb2_core_5	62.14	23.838	8.198	0	0.028	0.175	0.789	5.29	100.458
31	GCD_41_Alb2_core2_1	62.205	23.521	8.334	0	0.028	0.133	0.861	5.15	100.232
32	GCD_41_Alb2_core2_2	63.431	23.119	8.791	0	0.058	0.196	0.985	4.362	100.942
33	GCD_41_Alb2_core2_3	63.059	23.052	8.641	0.002	0.007	0.156	0.941	4.565	100.423
34	GCD_41_Alb2_core2_4	62.44	23.336	8.361	0.003	0.078	0.175	0.86	5.094	100.347
35	GCD_41_Alb2_core2_5	63.555	22.932	8.559	0.007	0.057	0.15	0.982	4.255	100.497
36	GCD_41_Alb3_core_1	63.212	23.35	8.304	0.011	0.083	0.18	1.029	4.831	101
37	GCD_41_Alb3_core_2	63.053	23.129	8.433	0.006	0.07	0.242	1.087	4.539	100.559
38	GCD_41_Alb3_core_3	63.137	23.509	8.311	0.004	0.085	0.19	1.058	4.696	100.99
39	GCD_41_Alb3_core_4	63.322	23.182	8.335	0.009	0.075	0.18	1.065	4.587	100.755
40	GCD_41_Alb3_core_5	63.313	23.241	8.448	0	0.01	0.185	1.037	4.657	100.891

41	GCD_41_Ffeld3_core_1	65.538	19.147	3.344	0	1.606	0.11	11.22	0.159	101.124
42	GCD_41_Ffeld3_core_2	65.976	18.995	3.33	0.003	1.495	0.081	11.249	0.184	101.313
43	GCD_41_Ffeld3_core_3	65.568	19.026	3.315	0.006	1.243	0.075	11.332	0.156	100.721
44	GCD_41_Ffeld3_core_4	65.672	19.06	3.405	0.005	1.458	0.079	11.213	0.17	101.062
45	GCD_41_Ffeld3_core_5	65.428	19.067	3.432	0	1.292	0.127	11.213	0.17	100.729
46	GCD_41_Alb4_core_1	63.94	22.912	8.394	0.011	0.055	0.173	1.079	4.414	100.978
47	GCD_41_Alb4_core_2	63.925	22.9	8.551	0	0.105	0.172	1.053	4.23	100.936
48	GCD_41_Alb4_core_3	63.881	22.967	8.573	0.004	0.042	0.147	1.067	4.25	100.931
49	GCD_41_Alb4_core_4	64.044	22.896	8.517	0.004	0.13	0.175	1.038	4.268	101.072
50	GCD_41_Alb4_core_5	63.827	22.862	8.583	0.006	0.055	0.186	1.065	4.307	100.891
51	GCD_41_Alb5_rim_1	63.32	24.084	8.237	0.008	0	0.18	0.854	5.12	101.803
52	GCD_41_Alb5_rim_2	62.455	23.781	8.089	0.006	0.09	0.214	0.781	5.264	100.68
53	GCD_41_Alb5_rim_3	61.941	24.401	7.925	0	0.002	0.149	0.675	5.946	101.039
54	GCD_41_Alb5_rim_4	80.598	11.148	3.054	0.054	0	0.676	4.665	0.31	100.505
55	GCD_41_Alb5_rim_5	62.911	24.219	7.987	0.014	0.057	0.178	0.757	5.61	101.733
1	DMD_1.3_AlbKfeld_top_1	63.391	22.933	8.514	0.009	0.062	0.168	1.061	4.26	100.398
2	DMD_1.3_AlbKfeld_top_2	63.421	22.955	8.559	0.003	0.11	0.142	1.089	4.107	100.386
3	DMD_1.3_AlbKfeld_top_3	63.507	22.748	8.538	0	0.09	0.176	1.097	4.169	100.325
4	DMD_1.3_AlbKfeld_top_4	63.544	22.74	8.601	0.003	0.07	0.164	1.11	4.162	100.394
5	DMD_1.3_AlbKfeld_top_5	63.058	22.864	8.295	0.008	0.07	0.196	1.03	4.441	99.962
6	DMD_1.3_AlbKfeld_bottom_1	64.902	19.019	3.435	0.011	1.358	0.105	11.248	0.216	100.294
7	DMD_1.3_AlbKfeld_bottom_2	64.986	18.822	3.361	0	1.221	0.105	11.345	0.182	100.022
8	DMD_1.3_AlbKfeld_bottom_3	65.185	19.046	3.371	0.002	1.121	0.116	11.175	0.182	100.198
9	DMD_1.3_AlbKfeld_bottom_4	65.17	18.969	3.373	0.006	1.278	0.085	11.265	0.207	100.353
10	DMD_1.3_AlbKfeld_bottom_5	65.159	18.927	3.393	0	1.102	0.114	11.24	0.193	100.128
11	DMD_1.3_AlbKfeld2_top_1	63.174	22.888	8.626	0.002	0.01	0.148	1.05	4.383	100.281
12	DMD_1.3_AlbKfeld2_top_2	62.76	22.949	8.552	0	0.035	0.151	1.026	4.415	99.888
13	DMD_1.3_AlbKfeld2_top_3	63.428	22.782	8.493	0.004	0.027	0.156	1.044	4.335	100.269
14	DMD_1.3_AlbKfeld2_top_4	63.466	22.792	8.649	0.011	0.072	0.199	1.022	4.308	100.519
15	DMD_1.3_AlbKfeld2_top_5	63.616	22.578	8.614	0	0.067	0.176	1.06	4.05	100.161
16	DMD_1.3_AlbKfeld2_bottom_1	65.442	18.76	3.472	0	0.49	0.097	11.527	0.167	99.955

17	DMD_1.3_AlbKfeld2_bottom_2	65.327	18.754	3.419	0	0.498	0.096	11.388	0.186	99.668
18	DMD_1.3_AlbKfeld2_bottom_3	65.536	18.91	3.428	0	0.53	0.086	11.579	0.189	100.258
19	DMD_1.3_AlbKfeld2_bottom_4	65.421	18.795	3.379	0.001	0.5	0.119	11.547	0.198	99.96
20	DMD_1.3_AlbKfeld2_bottom_5	65.452	18.771	3.41	0.007	0.403	0.106	11.413	0.198	99.76
21	DMD_1.3_Alb1_core_1	57.18	26.843	6.279	0.031	0.125	0.315	0.397	8.873	100.043
22	DMD_1.3_Alb1_core_2	56.79	26.894	6.206	0.021	0.07	0.233	0.339	8.728	99.281
23	DMD_1.3_Alb1_core_3	56.883	27.354	6.064	0.011	0.12	0.322	0.33	9.262	100.346
24	DMD_1.3_Alb1_core_4	56.639	27.044	6.055	0.016	0.015	0.422	0.351	9.215	99.757
25	DMD_1.3_Alb1_core_5	57.076	26.943	6.193	0.008	0.07	0.335	0.369	8.786	99.78
26	DMD_1.3_Alb1_rim_1	77.849	11.988	3.324	0.04	0.04	0.606	4.845	0.52	99.212
27	DMD_1.3_Alb1_rim_2	77.102	11.991	3.307	0.05	0	0.729	4.792	0.487	98.458
28	DMD_1.3_Alb1_rim_3	77.413	12.177	3.35	0.048	0.032	0.651	4.805	0.54	99.016
29	DMD_1.3_Alb1_rim_4	77.754	11.839	3.227	0.034	0.02	0.657	4.833	0.466	98.83
31	DMD_1.3_Kfeld1_core_1	65.904	18.801	3.516	0	0.35	0.114	11.332	0.17	100.187
32	DMD_1.3_Kfeld1_core_2	65.761	18.718	3.558	0.001	0.238	0.095	11.369	0.186	99.926
33	DMD_1.3_Kfeld1_core_3	65.873	18.699	3.507	0.015	0.375	0.136	11.605	0.155	100.365
34	DMD_1.3_Kfeld1_core_4	65.939	18.906	3.436	0.006	0.353	0.084	11.563	0.169	100.456
35	DMD_1.3_Kfeld1_core_5	65.776	18.855	3.398	0.007	0.285	0.061	11.47	0.162	100.014
36	DMD_1.3_Alb2_core_1	60.016	25.482	7.302	0	0.045	0.2	0.588	7.168	100.801
37	DMD_1.3_Alb2_core_2	59.168	26.007	6.989	0.004	0.065	0.147	0.509	7.387	100.276
38	DMD_1.3_Alb2_core_3	59.178	25.905	7.023	0.002	0.035	0.126	0.487	7.59	100.346
39	DMD_1.3_Alb2_core_4	59.999	25.156	7.339	0.005	0.042	0.171	0.544	6.794	100.05
40	DMD_1.3_Alb2_core_5	60.319	24.742	7.52	0.002	0.055	0.19	0.593	6.361	99.782
52	DMD_3_Kfeld1_core_2	64.968	19.487	4.284	0.01	1.247	0.138	9.588	0.492	100.214
53	DMD_3_Kfeld1_core_3	65.154	19.253	4.175	0	1.34	0.117	9.751	0.464	100.254
54	DMD_3_Kfeld1_core_4	65.11	19.498	4.244	0.001	1.283	0.114	9.987	0.429	100.666
55	DMD_3_Kfeld1_core_5	65.181	19.383	4.39	0.005	1.35	0.087	9.733	0.426	100.555
56	DMD_3_Alb1_core_1	62.657	23.356	8.394	0.008	0.042	0.179	0.913	4.783	100.332
57	DMD_3_Alb1_core_2	62.874	23.587	8.18	0.002	0.067	0.189	0.912	4.776	100.587
58	DMD_3_Alb1_core_3	62.888	23.441	8.376	0.006	0.065	0.196	0.877	4.822	100.671
59	DMD_3_Alb1_core_4	63.329	23.278	8.395	0.016	0.097	0.187	0.906	4.83	101.038

60	DMD_3_Alb1_core_5	62.91	23.371	8.249	0	0.067	0.204	0.957	4.767	100.525
62	DMD_3_Kfeld2_core_2	65.448	19.398	4.404	0	1.056	0.091	9.636	0.54	100.573
63	DMD_3_Kfeld2_core_3	65.786	19.517	4.423	0	0.997	0.105	9.612	0.5	100.94
64	DMD_3_Kfeld2_core_4	65.886	19.525	4.472	0	0.999	0.112	9.596	0.553	101.143
65	DMD_3_Kfeld2_core_5	65.788	19.716	4.486	0	0.949	0.096	9.501	0.51	101.046
66	DMD_3_Alb2_core_1	63.603	22.854	8.144	0.012	0.099	0.17	1.705	4.11	100.697
67	DMD_3_Alb2_core_2	63.535	22.898	8.148	0.005	0.147	0.179	1.757	4.062	100.731
68	DMD_3_Alb2_core_3	63.447	22.987	8.104	0	0.007	0.19	1.582	4.392	100.709
69	DMD_3_Alb2_core_4	63.36	22.946	8.191	0.014	0.047	0.159	1.373	4.564	100.654
70	DMD_3_Alb2_core_5	63.376	22.962	8.158	0.001	0.082	0.188	1.491	4.379	100.637
1	DMD_11_Kfeld_core_1	66.366	18.919	3.287	0.001	0.597	0.088	11.553	0.168	100.979
2	DMD_11_Kfeld_core_2	66.51	19.053	3.373	0	0.687	0.056	11.408	0.166	101.253
3	DMD_11_Kfeld_core_3	66.382	18.868	3.42	0	0.657	0.113	11.558	0.167	101.165
4	DMD_11_Kfeld_core_4	66.34	18.889	3.379	0.001	0.64	0.088	11.567	0.165	101.069
5	DMD_11_Kfeld_core_5	66.323	19.085	3.425	0.005	0.662	0.131	11.457	0.174	101.262
6	DMD_11_Alb1_core_1	63.67	23.017	8.484	0.005	0.07	0.178	1.047	4.415	100.886
7	DMD_11_Alb1_core_2	63.795	23.098	8.548	0.007	0.042	0.163	1.009	4.435	101.097
8	DMD_11_Alb1_core_3	63.668	23.141	8.633	0.011	0.042	0.168	1.049	4.461	101.173
9	DMD_11_Alb1_core_4	63.657	23.175	8.502	0	0.025	0.205	1.041	4.443	101.048
10	DMD_11_Alb1_core_5	63.162	23.312	8.515	0.004	0.07	0.177	0.976	4.543	100.759
11	DMD_11_GlomAlb_core_1	62.517	23.947	8.083	0.014	0.133	0.153	0.828	5.345	101.02
12	DMD_11_GlomAlb_core_2	63.251	23.532	8.245	0.003	0.1	0.155	0.862	4.957	101.105
13	DMD_11_GlomAlb_core_3	62.176	23.851	8.156	0.002	0.077	0.189	0.782	5.363	100.596
14	DMD_11_GlomAlb_core_4	61.333	24.827	7.768	0.002	0.048	0.16	0.662	6.423	101.223
15	DMD_11_GlomAlb_core_5	62.767	23.896	8.307	0.003	0.067	0.159	0.804	5.297	101.3
16	DMD_11_GlomAlb_rim_1	63.196	23.905	8.259	0	0.165	0.16	0.846	5.069	101.6
17	DMD_11_GlomAlb_rim_2	62.695	23.582	8.237	0	0.07	0.223	0.886	4.988	100.681
18	DMD_11_GlomAlb_rim_3	62.862	23.71	8.367	0.002	0.108	0.169	0.822	5.09	101.13
19	DMD_11_GlomAlb_rim_4	62.966	23.527	8.436	0.011	0.112	0.152	0.884	4.922	101.01
20	DMD_11_GlomAlb_rim_5	61.144	24.655	7.617	0	0.103	0.17	0.655	6.253	100.597
21	DMD_11_GlomAlb2_core_1	58.331	26.849	6.458	0.002	0.095	0.182	0.427	8.523	100.867

22	DMD_11_GlomAlb2_core_2	58.234	26.849	6.44	0.008	0.13	0.19	0.408	8.634	100.893
23	DMD_11_GlomAlb2_core_3	58.359	27.031	6.421	0	0.148	0.209	0.371	8.652	101.191
24	DMD_11_GlomAlb2_core_4	58.11	26.863	6.349	0.007	0.103	0.201	0.396	8.647	100.676
25	DMD_11_GlomAlb2_core_5	58.356	27.212	6.364	0.005	0.128	0.193	0.342	8.712	101.312
26	DMD_11_GlomAlb2_rim_1	64.013	23.116	8.695	0.006	0.057	0.152	1.072	4.231	101.342
27	DMD_11_GlomAlb2_rim_2	64.773	22.65	8.71	0.005	0.022	0.192	1.192	3.857	101.401
28	DMD_11_GlomAlb2_rim_3	64.751	22.659	8.709	0.006	0.057	0.187	1.161	3.795	101.325
29	DMD_11_GlomAlb2_rim_4	64.494	22.694	8.585	0.007	0.13	0.153	1.189	3.854	101.106
30	DMD_11_GlomAlb2_rim_5	64.541	22.735	8.687	0.004	0.177	0.189	1.134	4.041	101.508
31	DMD_11_KfeldAlb1_core_1	62.576	23.291	8.199	0.007	0.142	0.226	0.923	4.721	100.085
32	DMD_11_KfeldAlb1_core_2	62.927	23.097	8.368	0.004	0.147	0.179	0.932	4.657	100.311
33	DMD_11_KfeldAlb1_core_3	63.123	23.298	8.467	0.011	0.072	0.188	0.988	4.592	100.739
34	DMD_11_KfeldAlb1_core_4	63.175	23.394	8.417	0	0.125	0.191	0.951	4.541	100.794
35	DMD_11_KfeldAlb1_core_5	63.274	23.01	8.225	0.003	0.209	0.186	0.967	4.444	100.318
36	DMD_11_KfeldAlb1_rim_1	65.874	18.923	3.377	0.002	0.566	0.087	11.344	0.194	100.367
37	DMD_11_KfeldAlb1_rim_2	65.945	19.012	3.453	0.01	0.561	0.116	11.572	0.185	100.854
38	DMD_11_KfeldAlb1_rim_3	66.004	18.91	3.497	0.012	0.558	0.109	11.361	0.218	100.669
39	DMD_11_KfeldAlb1_rim_4	65.894	18.945	3.413	0.011	0.663	0.095	11.503	0.262	100.786
40	DMD_11_KfeldAlb1_rim_5	66.023	18.783	3.502	0.007	0.661	0.129	11.459	0.171	100.735
21	DC_2_KfeldAlb_core_1	64.568	19.417	4.265	0.003	1.63	0.111	9.554	0.492	100.04
22	DC_2_KfeldAlb_core_2	64.785	19.545	4.311	0.001	1.593	0.159	9.671	0.507	100.572
23	DC_2_KfeldAlb_core_3	64.453	19.441	4.265	0.006	1.594	0.117	9.483	0.52	99.879
24	DC_2_KfeldAlb_core_4	65.132	19.844	3.997	0	1.553	0.122	9.316	0.53	100.494
25	DC_2_KfeldAlb_core_5	64.512	19.741	4.347	0	1.675	0.109	9.215	0.734	100.333
26	DC_2_KfelAlb_rim_1	63.76	22.355	8.22	0.003	0.269	0.185	1.82	3.628	100.24
27	DC_2_KfelAlb_rim_2	63.387	22.378	8.088	0	0.169	0.157	1.559	4.024	99.762
28	DC_2_KfelAlb_rim_3	63.781	22.473	8.174	0.009	0.14	0.161	1.707	3.789	100.234
29	DC_2_KfelAlb_rim_4	64.908	22.926	8.543	0.011	0.174	0.145	1.561	3.87	102.138
30	DC_2_KfelAlb_rim_5	64.005	22.337	8.188	0.001	0.155	0.167	1.881	3.637	100.371
31	DC_2_Alb1_core_1	63.678	22.564	8.307	0.004	0.1	0.145	1.7	3.694	100.192
32	DC_2_Alb1_core_2	64.329	22.474	8.43	0.003	0.097	0.199	1.74	3.615	100.887

33	DC_2_Alb1_core_3	64.543	22.078	8.401	0	0.065	0.171	1.78	3.606	100.644
34	DC_2_Alb1_core_4	64.098	22.034	8.262	0.011	0.087	0.158	1.743	3.656	100.049
35	DC_2_Alb1_core_5	63.212	22.541	8.083	0.005	0.242	0.189	1.665	3.922	99.859
36	DC_2_Kfeld1_core_1	65.213	19.077	4.064	0	0.62	0.04	10.283	0.386	99.683
39	DC_2_Kfeld1_core_4	65.784	19.194	4.14	0	0.64	0.068	10.159	0.383	100.368
40	DC_2_Kfeld1_core_5	65.29	19.159	4.051	0	0.621	0.086	10.069	0.369	99.645
41	DC_2_KfeldAlb2_left_1	64.203	22.251	8.361	0.002	0.067	0.178	1.65	3.583	100.295
42	DC_2_KfeldAlb2_left_2	63.702	22.245	8.378	0.001	0.107	0.175	1.626	3.737	99.971
43	DC_2_KfeldAlb2_left_3	63.758	22.661	8.329	0.007	0.067	0.15	1.532	3.856	100.36
44	DC_2_KfeldAlb2_left_4	63.273	22.145	8.153	0.013	0.065	0.204	1.641	3.735	99.229
45	DC_2_KfeldAlb2_left_5	64.237	22.208	8.314	0.005	0.012	0.138	1.895	3.421	100.23
46	DC_2_KfeldAlb2_right_1	65.816	19.186	4.16	0	0.647	0.1	10.165	0.408	100.482
47	DC_2_KfeldAlb2_right_2	65.593	19.309	4.258	0.006	0.692	0.107	10.027	0.42	100.412
48	DC_2_KfeldAlb2_right_3	65.651	19.051	4.206	0	0.562	0.097	10.143	0.377	100.087
49	DC_2_KfeldAlb2_right_4	66.216	19.36	4.339	0.009	0.807	0.109	9.821	0.414	101.075
50	DC_2_KfeldAlb2_right_5	65.811	19.133	4.251	0	0.797	0.111	10.107	0.421	100.631
51	DC_2_KfeldAlb3_core_1	64.125	22.106	8.326	0	0.007	0.143	1.641	3.631	99.979
52	DC_2_KfeldAlb3_core_2	63.639	22.417	8.321	0.008	0.04	0.089	1.557	3.788	99.859
53	DC_2_KfeldAlb3_core_3	63.564	22.723	8.391	0	0.055	0.136	1.587	4.056	100.512
54	DC_2_KfeldAlb3_core_4	63.349	22.55	8.154	0.002	0.042	0.177	1.544	4.08	99.898
55	DC_2_KfeldAlb3_core_5	63.576	22.674	8.121	0.006	0.055	0.137	1.552	4.155	100.276
56	DC_2_KfeldAlb3_rim_1	65.508	19.057	4.104	0	0.627	0.105	10.032	0.435	99.868
57	DC_2_KfeldAlb3_rim_2	65.01	19.82	4.805	0.014	0.631	0.091	9.186	0.441	99.998
58	DC_2_KfeldAlb3_rim_3	65.776	19.177	4.159	0	0.664	0.122	10.061	0.394	100.353
59	DC_2_KfeldAlb3_rim_4	65.485	19.138	4.22	0	0.617	0.089	10.079	0.42	100.048
60	DC_2_KfeldAlb3_rim_5	65.662	19.22	4.206	0	0.594	0.127	10.141	0.423	100.373
61	VR_5_Alb1_core_1	62.769	23.191	7.934	0.003	0.042	0.188	1.346	4.764	100.237
62	VR_5_Alb1_core_2	62.113	22.995	7.968	0	0.1	0.224	1.303	4.673	99.376
64	VR_5_Alb1_core_4	63.173	22.767	8.174	0.001	0.122	0.185	1.63	4.04	100.092
65	VR_5_Alb1_core_5	63.415	22.631	8.241	0.009	0.179	0.153	1.583	4.059	100.27
66	VR_5_Kfeld_core_1	66.032	19.144	4.29	0	0.594	0.097	10.023	0.366	100.546

67	VR_5_Kfeld_core_2	65.596	19.172	4.305	0	0.603	0.073	9.994	0.409	100.152
68	VR_5_Kfeld_core_3	65.83	19.15	4.299	0.006	0.601	0.092	10.036	0.385	100.399
69	VR_5_Kfeld_core_4	66	19.327	4.214	0.002	0.611	0.089	9.985	0.387	100.615
71	VR_5_Kfeld_rim_1	64.85	19.504	4.137	0	1.662	0.122	9.673	0.451	100.399
72	VR_5_Kfeld_rim_2	64.994	19.678	4.307	0	1.753	0.173	9.35	0.489	100.744
73	VR_5_Kfeld_rim_3	64.682	19.42	4.066	0.004	1.717	0.162	9.727	0.416	100.194
74	VR_5_Kfeld_rim_4	64.919	19.525	4.346	0	1.733	0.132	9.709	0.444	100.808
75	VR_5_Kfeld_rim_5	64.898	19.488	4.165	0	1.716	0.129	9.724	0.442	100.562
76	VR_5_Alb2_core_1	64.235	22.732	8.627	0.003	0.216	0.204	1.559	3.766	101.342
77	VR_5_Alb2_core_2	63.254	22.55	8.105	0.004	0.114	0.182	1.813	3.804	99.826
78	VR_5_Alb2_core_3	64.072	22.615	8.168	0.007	0.164	0.144	1.821	3.752	100.743
79	VR_5_Alb2_core_4	62.572	22.882	8.248	0.012	0.176	0.194	1.472	4.42	99.976
80	VR_5_Alb2_core_5	62.709	22.869	8.24	0.009	0.151	0.195	1.275	4.314	99.762
81	VR_5_Kfeld2_rim_1	65.762	19.217	4.215	0.003	0.537	0.122	10.072	0.368	100.296
82	VR_5_Kfeld2_rim_2	65.882	19.137	4.249	0.003	0.799	0.109	10.019	0.407	100.605
83	VR_5_Kfeld2_rim_3	65.74	19.157	4.193	0.003	0.645	0.118	10.016	0.394	100.266
84	VR_5_Kfeld2_rim_4	65.856	19.34	4.257	0	0.534	0.073	9.929	0.428	100.417
85	VR_5_Kfeld2_rim_5	65.788	19.155	4.224	0	0.792	0.121	10.293	0.4	100.773
41	OR1_2_1	64.399	18.343	1.054	0.003	0.963	0	15.041	0	99.803
42	OR1_2_2	64.035	18.598	1.025	0	0.941	0	14.864	0	99.463
43	OR1_2_3	63.543	18.39	1.073	0	0.859	0.002	14.947	0.006	98.82
44	OR1_2_4	64.571	18.764	1.045	0	0.873	0.003	14.838	0	100.094
45	OR1_2_5	64.324	18.652	1.032	0	0.926	0.009	14.973	0	99.916
46	TibAlb_2_1	68.354	19.441	11.746	0.006	0.042	0.012	0.022	0.001	99.624
47	TibAlb_2_2	68.785	19.552	11.968	0.001	0	0.015	0.029	0.006	100.356
48	TibAlb_2_3	68.597	19.323	11.937	0.001	0	0.035	0.007	0	99.9
49	TibAlb_2_4	68.454	19.361	11.77	0.003	0	0	0.042	0	99.63
50	TibAlb_2_5	68.515	19.579	11.931	0	0	0	0.011	0	100.036
51	AN100_2_1	43.69	36.644	0.015	0	0.01	0.074	0.006	20.154	100.593
52	AN100_2_2	43.846	36.793	0.025	0.002	0	0.047	0.01	20.223	100.946
53	AN100_2_3	43.776	36.897	0.016	0	0	0.003	0.011	20.058	100.761

54	AN100_2_4	43.815	36.968	0.03	0	0.05	0.039	0.008	20.177	101.087
55	AN100_2_5	43.761	36.763	0.003	0	0.058	0.048	0	20.187	100.82
66	OR1_2_1	64.978	18.642	1.053	0	0.814	0.017	14.933	0	100.437
67	OR1_2_2	64.937	18.731	1.026	0	0.804	0.016	14.93	0	100.444
68	OR1_2_3	65.072	18.686	1.055	0	0.944	0.018	14.913	0.006	100.694
69	OR1_2_4	64.745	18.721	1.01	0.008	0.812	0	14.873	0.006	100.175
70	OR1_2_5	64.546	18.588	1.094	0	0.772	0	14.999	0.018	100.017
71	TibAlb_2_1	69.077	19.4	11.839	0.018	0	0.016	0.017	0.002	100.369
72	TibAlb_2_2	69.457	19.508	11.882	0	0.057	0.006	0.012	0.001	100.923
73	TibAlb_2_3	69.51	19.596	11.842	0.001	0.027	0.001	0.018	0.008	101.003
74	TibAlb_2_4	69.374	19.534	11.873	0.002	0	0.006	0.009	0.015	100.813
75	TibAlb_2_5	69.227	19.644	11.759	0	0.045	0	0.008	0.014	100.697
76	AN100_2_1	44.036	36.762	0.04	0	0.071	0.05	0	20.139	101.098
77	AN100_2_2	43.024	37.221	0.03	0.001	0	0.085	0	19.992	100.353
78	AN100_2_3	43.612	36.863	0.007	0	0.068	0.074	0.004	20.22	100.848
79	AN100_2_4	43.669	37.004	0.011	0	0	0.06	0.009	20.345	101.098
80	AN100_2_5	43.779	36.539	0.018	0	0	0	0	20.3	100.636
86	OR1_3_1	63.878	18.53	1.074	0	0.899	0	15.052	0	99.433
87	OR1_3_2	64.473	18.669	1.019	0.011	0.909	0	14.882	0	99.963
88	OR1_3_3	64.223	18.752	1.138	0	0.862	0	14.835	0.015	99.825
89	OR1_3_4	64.439	18.665	1.128	0	0.909	0	14.882	0	100.023
90	OR1_3_5	64.293	18.475	1.072	0	0.846	0	14.94	0	99.626
91	TibAlb_3_1	68.75	19.311	11.816	0	0	0	0.017	0.016	99.91
92	TibAlb_3_2	68.452	19.314	11.991	0	0.039	0	0.032	0.001	99.829
93	TibAlb_3_3	68.558	19.492	11.732	0.006	0	0.022	0.034	0.007	99.851
94	TibAlb_3_4	68.44	19.414	11.687	0	0.002	0.02	0.016	0	99.579
95	TibAlb_3_5	68.835	19.472	11.961	0.002	0	0	0.028	0.008	100.306
96	AN100_3_1	43.423	36.708	0.013	0.001	0.008	0.022	0.009	20.107	100.291
97	AN100_3_2	43.217	36.562	0.007	0	0.005	0.077	0.008	20.147	100.023
98	AN100_3_3	43.492	36.708	0.023	0	0	0.06	0.015	20.138	100.436
99	AN100_3_4	43.444	36.644	0.015	0	0	0.029	0.004	20.183	100.319

100	AN100_3_5	43.305	36.69	0.001	0	0.04	0.063	0	20.171	100.27
66	OR1_2_1	64.951	18.642	1.053	0	0.814	0.017	14.933	0	100.41
67	OR1_2_2	64.91	18.731	1.026	0	0.804	0.016	14.93	0	100.417
68	OR1_2_3	65.045	18.686	1.055	0	0.944	0.018	14.913	0.006	100.667
69	OR1_2_4	64.718	18.721	1.01	0.008	0.812	0	14.873	0.006	100.148
70	OR1_2_5	64.519	18.588	1.094	0	0.772	0	14.998	0.018	99.989
71	TibAlb_2_1	69.048	19.401	11.839	0.018	0	0.016	0.017	0.002	100.341
72	TibAlb_2_2	69.429	19.508	11.882	0	0.057	0.006	0.012	0.001	100.895
73	TibAlb_2_3	69.481	19.596	11.842	0.001	0.027	0.001	0.018	0.008	100.974
74	TibAlb_2_4	69.345	19.534	11.873	0.002	0	0.006	0.009	0.015	100.784
75	TibAlb_2_5	69.199	19.645	11.759	0	0.045	0	0.008	0.014	100.67
76	AN100_2_1	44.018	36.762	0.04	0	0.071	0.05	0	20.139	101.08
77	AN100_2_2	43.007	37.222	0.03	0.001	0	0.085	0	19.992	100.337
78	AN100_2_3	43.594	36.863	0.007	0	0.068	0.074	0.004	20.22	100.83
79	AN100_2_4	43.651	37.005	0.011	0	0	0.06	0.009	20.344	101.08
80	AN100_2_5	43.761	36.539	0.018	0	0	0	0	20.3	100.618

Table 5. Quantitative amphibole compositions

No.	Sample ID	SiO_2	Al_2O_3	Na_2O	MgO	MnO	TiO_2	FeO	Cr_2O_3	K2O	CaO	Total
1	XR_DMD_11_amph1_rim1_1	45.45	7.29	1.94	11.92	0.61	1.62	16.49	0.01	0.91	10.98	97.23
2	XR_DMD_11_amph1_rim1_2	45.10	7.29	1.83	11.72	0.59	1.62	16.58	0.00	0.88	10.83	96.44
3	XR_DMD_11_amph1_rim1_3	45.56	7.36	1.95	11.88	0.60	1.59	16.61	0.02	0.89	11.00	97.47
4	XR_DMD_11_amph1_rim1_4	45.39	7.26	2.01	12.05	0.60	1.56	16.55	0.01	0.89	11.05	97.37
5	XR_DMD_11_amph1_rim1_5	45.83	7.31	1.94	11.92	0.62	1.61	16.71	0.00	0.89	10.88	97.71
6	XR_DMD_11_amph2_core_1	44.64	7.53	2.05	11.99	0.57	1.62	16.55	0.00	0.91	11.07	96.90
7	XR_DMD_11_amph2_core_2	44.85	7.58	2.02	11.94	0.57	1.62	16.69	0.00	0.95	11.04	97.26
8	XR_DMD_11_amph2_core_3	45.15	7.60	1.97	12.07	0.57	1.64	16.63	0.00	0.92	11.00	97.54
9	XR_DMD_11_amph2_core_4	45.02	7.55	1.96	12.11	0.57	1.62	16.67	0.00	0.88	11.05	97.44
10	XR_DMD_11_amph2_core_5	45.10	7.46	1.99	12.12	0.55	1.56	16.73	0.01	0.88	10.96	97.35
11	XR_DMD_11_amph2_rim_1	44.58	7.64	2.03	11.65	0.63	1.74	17.21	0.00	0.87	10.92	97.26
12	XR_DMD_11_amph2_rim_2	45.08	7.57	1.98	11.71	0.62	1.66	17.09	0.00	0.84	11.02	97.57
13	XR_DMD_11_amph2_rim_3	45.68	6.97	1.95	12.15	0.65	1.54	16.80	0.01	0.82	11.11	97.67
14	XR_DMD_11_amph2_rim_4	45.28	7.38	1.99	11.84	0.62	1.58	17.09	0.00	0.86	11.04	97.67
15	XR_DMD_11_amph2_rim_5	44.63	7.57	2.04	11.67	0.62	1.63	17.06	0.02	0.90	11.03	97.17
16	XR_DMD_11_pyx_1	45.01	7.46	2.00	11.80	0.66	1.55	17.62	0.00	0.92	11.37	98.39
17	XR_DMD_11_pyx_2	45.38	7.17	1.91	11.90	0.66	1.57	17.03	0.00	0.88	11.18	97.69
18	XR_DMD_11_pyx_3	45.05	7.35	2.01	11.79	0.64	1.58	17.02	0.01	0.87	11.14	97.46
19	XR_DMD_11_pyx_4	46.19	6.67	1.84	12.33	0.63	1.43	16.85	0.00	0.78	11.23	97.95
20	XR_DMD_11_pyx_5	46.35	6.49	1.82	12.46	0.61	1.35	16.61	0.00	0.73	11.19	97.62
1	XR_DMD_11_amp3_core_1	44.62	7.32	1.99	11.85	0.63	1.67	17.40	0.00	0.87	11.24	97.59
2	XR_DMD_11_amp3_core_2	44.57	7.39	1.99	11.84	0.65	1.61	17.33	0.00	0.85	11.25	97.48
3	XR_DMD_11_amp3_core_3	44.60	7.37	2.00	11.84	0.66	1.64	17.36	0.00	0.87	11.19	97.52
4	XR_DMD_11_amp3_core_4	44.59	7.46	2.03	11.84	0.68	1.62	17.37	0.00	0.84	11.17	97.60
5	XR_DMD_11_amp3_core_5	44.82	7.17	1.97	12.01	0.63	1.62	17.43	0.00	0.87	11.20	97.72
1	XR_DMD_11_amp4_core_1	46.06	6.49	1.79	12.72	0.60	1.35	16.57	0.00	0.72	11.21	97.50
2	XR_DMD_11_amp4_core_2	45.90	6.82	1.90	12.58	0.62	1.44	16.87	0.00	0.79	11.18	98.08
3	XR_DMD_11_amp4_core_3	45.44	6.73	1.84	12.58	0.62	1.37	16.64	0.00	0.77	11.27	97.25

4	XR_DMD_11_amp4_core_4	45.77	6.62	1.79	12.57	0.64	1.39	16.28	0.00	0.74	11.30	97.08
5	XR_DMD_11_amp4_core_5	45.61	6.91	1.88	12.39	0.60	1.49	16.77	0.00	0.77	11.29	97.68
6	XR_DMD_11_amp4_rim_1	46.33	6.10	1.74	12.76	0.64	1.26	16.15	0.00	0.68	11.23	96.89
7	XR_DMD_11_amp4_rim_2	46.74	5.99	1.74	12.90	0.67	1.20	16.19	0.02	0.63	11.26	97.35
8	XR_DMD_11_amp4_rim_3	46.12	6.37	1.77	12.62	0.67	1.29	16.47	0.01	0.72	11.19	97.23
9	XR_DMD_11_amp4_rim_4	46.71	6.12	1.75	12.85	0.61	1.27	16.28	0.01	0.66	11.20	97.46
10	XR_DMD_11_amp4_rim_5	46.48	6.19	1.71	12.75	0.66	1.27	16.35	0.00	0.66	11.21	97.29
11	XR_DMD_11_amp5_core_1	44.39	7.51	2.07	11.50	0.62	1.62	17.90	0.01	0.85	11.21	97.66
12	XR_DMD_11_amp5_core_2	44.81	7.44	1.98	11.64	0.68	1.44	17.73	0.01	0.83	11.15	97.70
13	XR_DMD_11_amp5_core_3	44.91	7.34	1.95	11.73	0.66	1.54	17.72	0.01	0.84	11.18	97.88
14	XR_DMD_11_amp5_core_4	44.68	7.48	2.02	11.61	0.65	1.59	17.90	0.00	0.87	11.17	97.97
15	XR_DMD_11_amp5_core_5	44.88	7.28	1.98	11.69	0.62	1.56	17.58	0.02	0.86	11.13	97.58
16	XR_DMD_11_amp5_rim_1	45.66	6.49	1.78	12.54	0.66	1.37	16.69	0.01	0.73	11.05	96.98
17	XR_DMD_11_amp5_rim_2	45.93	6.48	1.85	12.42	0.63	1.42	16.70	0.00	0.74	11.18	97.36
18	XR_DMD_11_amp5_rim_3	45.79	6.57	1.80	12.49	0.64	1.34	16.56	0.01	0.74	11.10	97.03
19	XR_DMD_11_amp5_rim_4	44.79	7.33	1.98	11.89	0.62	1.67	17.10	0.01	0.89	11.17	97.44
20	XR_DMD_11_amp5_rim_5	44.84	7.37	2.00	11.99	0.68	1.60	17.14	0.03	0.86	11.18	97.69
1	OBD_6_amph1_core_1	41.92	10.72	3.00	13.11	0.25	3.20	14.01	0.00	0.96	10.62	97.78
2	OBD_6_amph1_core_2	42.01	10.98	3.02	13.09	0.26	3.40	14.02	0.01	0.95	10.63	98.38
3	OBD_6_amph1_core_3	42.40	10.54	2.96	13.09	0.26	3.29	14.31	0.01	0.90	10.43	98.18
4	OBD_6_amph1_core_4	41.95	10.64	3.03	13.21	0.27	3.22	14.37	0.01	0.93	10.39	98.00
5	OBD_6_amph1_core_5	42.54	10.53	3.05	13.11	0.30	3.59	14.20	0.03	0.86	10.27	98.47
6	OBD_6_amph1_rim_1	41.90	10.86	3.00	11.27	0.36	3.56	16.26	0.01	1.09	10.56	98.85
7	OBD_6_amph1_rim_2	41.66	10.66	2.98	12.00	0.29	3.35	15.79	0.01	1.04	10.55	98.31
8	OBD_6_amph1_rim_3	41.85	10.60	3.01	11.74	0.31	3.55	16.12	0.01	1.05	10.56	98.80
9	OBD_6_amph1_rim_4	42.07	10.35	2.94	11.58	0.29	3.34	16.13	0.00	1.03	10.53	98.26
10	OBD_6_amph1_rim_5	42.38	10.47	2.99	10.35	0.36	3.36	17.09	0.00	1.11	10.54	98.64
6	DM_1_amph2_core_1	44.20	7.79	2.12	11.50	0.55	1.84	17.65	0.01	0.83	11.01	97.49
7	DM_1_amph2_core_2	44.46	7.38	1.99	11.67	0.63	1.71	17.51	0.02	0.83	11.00	97.20
8	DM_1_amph2_core_3	44.46	7.35	2.09	11.50	0.60	1.85	17.86	0.02	0.82	10.98	97.52
9	DM_1_amph2_core_4	44.50	7.37	2.01	11.57	0.58	1.75	17.34	0.01	0.82	10.95	96.88

10	DM_1_amph2_core_5	44.31	7.63	2.06	11.35	0.59	1.87	17.81	0.01	0.81	10.93	97.37
11	DM_1_amph3_core_1	45.33	6.61	1.95	11.94	0.61	1.51	17.80	0.00	0.76	10.91	97.43
12	DM_1_amph3_core_2	45.38	6.69	2.00	12.04	0.61	1.53	17.90	0.00	0.77	10.88	97.79
13	DM_1_amph3_core_3	45.49	6.64	1.95	11.99	0.61	1.60	17.76	0.00	0.76	10.86	97.66
14	DM_1_amph3_core_4	45.56	6.69	1.91	11.89	0.67	1.54	17.76	0.00	0.74	10.89	97.64
15	DM_1_amph3_core_5	45.12	6.84	1.96	11.86	0.65	1.62	17.88	0.00	0.76	10.91	97.58
16	DM_1_amph3_rim_1	44.82	7.09	1.97	11.59	0.61	1.73	17.63	0.00	0.83	10.96	97.22
17	DM_1_amph3_rim_2	44.90	7.12	2.05	11.60	0.61	1.74	18.00	0.00	0.81	10.97	97.80
18	DM_1_amph3_rim_3	44.73	7.14	1.92	11.28	0.60	1.58	18.63	0.00	0.80	10.78	97.46
19	DM_1_amph3_rim_4	44.41	7.01	1.96	10.74	0.70	1.59	18.97	0.00	0.82	10.85	97.06
20	DM_1_amph3_rim_5	44.66	7.11	1.91	10.96	0.69	1.49	18.66	0.00	0.83	10.98	97.29
21	DM_1_amph4_core_1	45.03	6.77	1.96	11.14	0.67	1.56	18.90	0.00	0.79	10.76	97.58
22	DM_1_amph4_core_2	45.17	6.88	1.96	11.21	0.69	1.58	18.79	0.00	0.78	10.81	97.88
23	DM_1_amph4_core_3	45.00	6.84	1.95	11.14	0.69	1.58	19.12	0.00	0.76	10.87	97.94
24	DM_1_amph4_core_4	45.15	6.95	1.89	11.24	0.70	1.48	19.33	0.01	0.75	10.80	98.29
25	DM_1_amph4_core_5	45.34	6.71	1.86	11.18	0.66	1.54	18.97	0.01	0.77	10.95	97.99
26	DM_1_amph4_rim_1	44.98	6.68	1.88	10.75	0.75	1.37	19.01	0.00	0.77	11.07	97.25
27	DM_1_amph4_rim_2	44.58	7.07	1.92	10.70	0.70	1.33	19.04	0.00	0.86	10.98	97.17
28	DM_1_amph4_rim_3	44.63	6.68	1.82	11.00	0.72	1.36	18.79	0.00	0.77	10.98	96.75
30	DM_1_amph4_rim_5	44.61	7.10	1.98	11.13	0.70	1.59	18.54	0.00	0.80	10.89	97.32
31	DM_1_amph5_core_1	45.07	6.85	1.94	11.37	0.62	1.44	18.81	0.00	0.79	10.81	97.71
32	DM_1_amph5_core_2	44.87	6.95	1.95	11.28	0.62	1.58	18.52	0.00	0.78	10.87	97.42
33	DM_1_amph5_core_3	44.96	6.72	1.96	11.49	0.65	1.68	18.64	0.02	0.73	10.83	97.67
34	DM_1_amph5_core_4	44.80	7.21	2.07	11.09	0.63	1.71	19.08	0.00	0.80	11.01	98.40
40	DM_1_amph5_core_5	45.05	6.95	1.97	11.27	0.64	1.56	18.70	0.00	0.78	11.08	98.00
35	DM_1_amph5_rim_1	45.11	6.89	1.83	10.96	0.73	1.33	19.60	0.00	0.77	11.14	98.35
36	DM_1_amph5_rim_2	44.90	6.75	1.87	10.89	0.72	1.41	19.36	0.00	0.75	10.97	97.61
37	DM_1_amph5_rim_3	44.78	6.81	1.82	10.86	0.70	1.45	19.41	0.00	0.79	10.97	97.60
39	DM_1_amph5_rim_5	45.02	6.76	1.89	10.79	0.74	1.35	19.74	0.00	0.76	10.96	97.99

Table 6. Quantitative pyroxene data

No.	Sample ID	SiO_2	Al_2O_3	Na_2O	MgO	MnO	TiO_2	FeO	Cr_2O_3	K2O	CaO	Total
1	VR_1_pyx1_1	48.81	1.40	0.04	21.96	0.68	0.39	22.35	0.00	0.00	1.41	97.03
2	VR_1_pyx1_2	48.83	1.51	0.04	22.14	0.69	0.42	22.07	0.00	0.00	1.58	97.28
3	VR_1_pyx1_3	49.13	1.51	0.04	22.35	0.68	0.38	21.45	0.00	0.00	1.66	97.20
4	VR_1_pyx1_4	49.05	1.78	0.04	23.12	0.61	0.42	20.61	0.00	0.00	1.58	97.21
5	VR_1_pyx1_5	48.39	2.42	0.07	22.14	0.56	0.56	20.36	0.00	0.00	2.86	97.35
6	VR_1_pyx2_1	49.46	1.19	0.05	22.29	0.70	0.45	22.07	0.01	0.01	1.47	97.71
7	VR_1_pyx2_2	49.84	1.16	0.05	22.48	0.72	0.38	21.56	0.02	0.01	1.47	97.68
8	VR_1_pyx2_3	49.54	1.06	0.05	22.17	0.73	0.31	22.17	0.00	0.00	1.48	97.51
9	VR_1_pyx2_4	50.96	1.29	0.03	21.57	0.75	0.33	22.34	0.02	0.01	1.50	98.80
10	VR_1_pyx2_5	49.21	1.11	0.05	21.61	0.80	0.29	22.76	0.01	0.00	1.51	97.35
1	VR_1_pyx3_core_1	49.39	2.23	0.05	23.39	0.55	0.42	20.60	0.00	0.00	1.60	98.22
2	VR_1_pyx3_core_2	51.23	2.04	0.02	24.78	0.42	0.40	18.71	0.01	0.00	1.45	99.06
3	VR_1_pyx3_core_3	49.17	1.55	0.02	24.40	0.49	0.32	19.25	0.00	0.00	1.45	96.65
4	VR_1_pyx3_core_4	49.42	2.14	0.04	23.35	0.55	0.43	20.32	0.00	0.00	1.55	97.79
5	VR_1_pyx3_core_5	50.28	1.68	0.03	24.71	0.48	0.36	18.99	0.00	0.00	1.39	97.91
6	VR_1_pyx3_rim_1	48.39	0.66	0.04	18.84	1.04	0.18	25.85	0.00	0.05	1.45	96.49
7	VR_1_pyx3_rim_2	48.98	0.73	0.04	19.68	1.06	0.20	24.86	0.00	0.02	1.46	97.02
8	VR_1_pyx3_rim_3	49.31	0.78	0.04	20.13	0.96	0.24	24.34	0.01	0.01	1.44	97.26
9	VR_1_pyx3_rim_4	49.68	0.87	0.04	21.02	0.89	0.22	23.61	0.00	0.01	1.42	97.75
10	VR_1_pyx3_rim_5	48.49	0.93	0.04	21.58	0.80	0.25	22.68	0.00	0.01	1.42	96.21
1	VR_1_pyx4_core_1	47.96	2.63	0.55	13.29	0.53	0.67	12.58	0.01	0.02	19.28	97.53
2	VR_1_pyx4_core_2	48.95	1.78	0.55	13.41	0.56	0.47	12.38	0.01	0.01	19.71	97.82
3	VR_1_pyx4_core_3	49.14	1.49	0.54	13.66	0.51	0.43	11.95	0.00	0.01	20.08	97.81
4	VR_1_pyx4_core_5	49.08	1.52	0.52	13.46	0.55	0.37	12.66	0.01	0.01	19.55	97.73
5	VR_1_pyx4_core_6	49.01	1.27	0.52	12.73	0.70	0.33	13.74	0.01	0.01	19.52	97.83
6	VR_1_pyx4_rim_1	49.49	1.59	0.53	13.72	0.57	0.43	12.45	0.02	0.03	19.83	98.67
7	VR_1_pyx4_rim_2	49.26	1.60	0.53	13.52	0.57	0.42	12.58	0.01	0.05	19.65	98.19
8	VR_1_pyx4_rim_3	49.05	1.41	0.52	13.54	0.57	0.35	12.66	0.01	0.03	19.57	97.71

9	VR_1_pyx4_rim_4	48.77	1.55	0.54	13.44	0.54	0.39	12.50	0.01	0.04	19.67	97.44
10	VR_1_pyx4_rim_5	48.86	1.09	0.51	12.47	0.73	0.30	13.89	0.00	0.04	19.48	97.37
1	VR_1_pyx5_core_1	49.93	1.85	0.46	14.08	0.58	0.42	13.06	0.00	0.01	18.40	98.80
2	VR_1_pyx5_core_2	46.75	5.06	0.75	11.95	0.53	1.50	13.21	0.02	0.01	19.22	98.99
3	VR_1_pyx5_core_3	47.31	4.72	0.68	11.96	0.51	1.32	12.69	0.03	0.01	19.61	98.85
4	VR_1_pyx5_core_4	50.00	2.11	0.60	12.88	0.53	0.49	12.29	0.00	0.01	20.34	99.25
5	VR_1_pyx5_core_5	47.10	5.10	0.61	13.61	0.36	1.38	11.61	0.06	0.01	18.82	98.65

No.	Sample ID	SiO_2	Al_2O_3	Na_2O	MgO	TiO_2	P_2O_5	FeO	MnO	K_2O	CaO	Total
1	DM_1_GMglass1_1	75.52	12.12	3.33	0.04	0.07	0.06	0.51	0.08	4.87	0.58	97.18
2	DM_1_GMglass1_2	75.95	12.05	3.45	0.04	0.07	0.05	0.62	0.02	4.75	0.59	97.59
3	DM_1_GMglass2_1	75.88	12.26	3.44	0.06	0.07	0.00	0.61	0.04	4.81	0.56	97.72
4	DM_1_GMglass2_2	75.77	12.27	3.29	0.03	0.07	0.03	0.58	0.03	4.71	0.57	97.35
5	DM_1_GMglass3_1	78.20	12.59	3.44	0.04	0.04	0.00	0.54	0.01	4.89	0.56	100.31
6	DM_1_GMglass3_2	77.26	12.07	3.42	0.06	0.07	0.00	0.71	0.07	4.79	0.55	98.98
7	DM_1_MIncBi1_1	76.11	12.91	3.92	0.06	0.09	0.00	0.70	0.00	5.02	0.33	99.14
8	DM_1_GMglass_4_1	76.99	11.56	3.28	0.05	0.08	0.00	0.56	0.08	4.83	0.49	97.92
9	DM_1_GMglass_4_2	76.74	11.75	3.17	0.03	0.08	0.00	0.58	0.00	4.82	0.52	97.68
10	DM_1_MIncAmph1_1	62.96	24.13	8.44	0.00	0.00	0.01	0.25	0.02	0.81	5.19	101.81
11	DM_1_MIncAmph1_2	62.53	24.52	8.28	0.01	0.02	0.02	0.17	0.01	0.71	5.87	102.13
12	DM_1_MIncAmph1_3	64.41	22.42	8.52	0.00	0.01	0.01	0.35	0.03	1.15	3.83	100.72
1	DM_1_GMglass5_1	78.71	12.23	3.69	0.04	0.08	0.01	0.64	0.06	4.87	0.62	100.94
2	DM_1_GMglass5_2	78.39	12.52	3.45	0.03	0.08	0.00	0.67	0.02	4.91	0.58	100.64
3	DM_1_GMglass6_1	77.39	12.51	3.45	0.02	0.06	0.01	0.66	0.05	4.82	0.56	99.53
4	DM_1_GMglass6_2	76.30	12.52	3.28	0.03	0.04	0.00	0.60	0.03	4.74	0.61	98.14
5	DM_1_GMglass7_1	76.06	11.90	3.64	0.04	0.05	0.00	0.61	0.03	4.86	0.52	97.72
6	DM_1_GMglass7_2	63.85	23.60	8.35	0.00	0.01	0.01	0.18	0.01	0.93	4.79	101.72
1	VR_1_MIncBi1_1	60.79	25.40	7.13	0.01	0.05	0.02	0.50	0.02	1.28	6.80	102.00
2	VR_1_MIncBi1_2	62.06	24.27	7.22	0.01	0.06	0.00	0.50	0.00	1.63	5.92	101.67
4	VR_1_GMglass1_2	63.58	20.50	5.90	0.01	0.03	0.03	0.29	0.01	5.50	2.23	98.07

5	VR_1_MIncBi2_1	70.20	15.57	4.19	0.31	0.25	0.03	2.12	0.11	5.95	1.01	99.73
6	VR_1_GMglass2_1	71.66	13.91	3.75	0.11	0.35	0.06	1.92	0.02	6.06	0.68	98.51
1	VR_1_GMglass3_1	68.50	13.97	3.75	0.05	0.35	0.09	1.55	0.02	6.16	0.71	95.14
2	VR_1_GMglass3_2	71.57	14.23	3.93	0.10	0.34	0.04	1.57	0.04	6.14	0.55	98.49
3	VR_1_GMglass4_1	62.76	23.13	7.48	0.01	0.01	0.01	0.25	0.00	1.72	5.22	100.60
4	VR_1_GMglass4_2	63.67	22.97	7.39	0.01	0.02	0.05	0.30	0.00	1.90	4.51	100.80
5	VR_1_GMglass5_1	61.97	24.09	7.05	0.01	0.05	0.04	0.30	0.06	1.96	5.05	100.59
6	VR_1_GMglass5_2	71.80	14.57	4.17	0.29	0.35	0.09	2.15	0.06	6.15	0.78	100.42
7	VR_1_GMglass6_1	70.89	15.36	4.40	0.08	0.30	0.17	1.43	0.04	5.66	1.03	99.35
9	VR_1_GMglass7_2	62.37	23.07	7.20	0.01	0.02	0.03	0.36	0.00	2.53	4.45	100.03
10	VR_1_GMglass7_3	71.95	14.66	3.95	0.16	0.35	0.06	1.77	0.00	6.08	0.63	99.61
1	OBD_4_GMglass1_1	75.21	14.05	4.34	0.04	0.11	0.00	1.16	0.04	5.24	0.57	100.75
2	OBD_4_GMglass2_1	75.43	14.12	4.05	0.04	0.12	0.02	1.31	0.00	5.37	0.66	101.12
3	OBD_4_GMglass3_1	76.47	14.18	4.20	0.04	0.11	0.02	1.14	0.03	5.29	0.57	102.03
4	OBD_4_GMglass4_1	74.76	13.86	4.04	0.02	0.08	0.00	0.92	0.03	5.33	0.59	99.62
5	OBD_4_GMglass5_1	75.93	13.28	3.99	0.05	0.10	0.02	1.10	0.01	5.48	0.52	100.47
6	OBD_4_GMglass6_1	74.53	14.05	4.01	0.04	0.09	0.00	1.29	0.03	5.26	0.62	99.91
1	OBD_51_MIncBi1_1	76.24	13.76	2.60	0.10	0.27	0.01	0.89	0.05	5.72	0.58	100.21
2	OBD_51_MIncBi1_2	75.91	13.57	2.42	0.06	0.24	0.00	0.93	0.02	5.81	0.49	99.44
3	OBD_51_GMglass1_1	78.04	13.16	2.63	0.06	0.09	0.00	1.26	0.04	4.78	0.64	100.70
1	OBD_51_GMglass3_1	74.61	11.05	2.98	0.03	0.07	0.02	0.80	0.02	4.74	0.30	94.61
2	OBD_51_GMglass3_2	74.38	12.12	3.66	0.01	0.08	0.01	0.78	0.03	4.76	0.36	96.19
3	OBD_51_GMglass6_1	65.25	21.78	7.94	0.00	0.00	0.03	0.20	0.02	3.14	2.62	100.99
4	OBD_51_MIncBi3_1	76.23	12.77	2.78	0.27	0.48	0.03	1.31	0.03	5.02	0.75	99.66
5	OBD_51_GMglass7_1	78.07	12.31	3.25	0.03	0.11	0.05	1.04	0.03	5.28	0.40	100.56
6	OBD_51_GMglass8_1	76.60	11.83	3.05	0.03	0.17	0.02	1.40	0.04	4.97	0.37	98.47
7	OBD_51_MIncBi4_1	76.41	13.50	2.40	0.07	0.20	0.02	0.84	0.08	5.78	0.50	99.79
1	OBD_51_MIncBi2_1	77.17	13.09	1.58	0.06	0.13	0.02	1.24	0.02	4.63	0.64	98.58
2	OBD_51_MIncBi2_2	77.92	13.49	1.62	0.08	0.16	0.00	1.25	0.07	4.93	0.59	100.10
3	OBD_51_GMglass2_1	77.77	12.78	2.81	0.07	0.20	0.02	1.25	0.04	5.76	0.41	101.11
4	OBD_51_GMglass9_1	76.01	12.53	3.61	0.01	0.09	0.00	0.94	0.03	4.96	0.45	98.63

1	OBD_6_GMglass1_1	76.65	13.07	3.60	0.02	0.09	0.00	0.90	0.03	4.92	0.65	99.93
2	OBD_6_GMglass1_2	75.05	12.54	3.36	0.02	0.15	0.01	1.03	0.04	5.50	0.47	98.15
3	OBD_6_GMglass2_1	64.38	22.97	8.32	0.00	0.02	0.00	0.25	0.01	1.39	3.90	101.22
4	OBD_6_GMglass3_1	78.76	11.45	2.88	0.02	0.07	0.00	0.90	0.06	5.56	0.33	100.02
5	OBD_6_GMglass4_1	78.09	12.02	3.32	0.06	0.11	0.02	1.19	0.11	5.42	0.40	100.74
6	OBD_6_GMglass5_1	77.54	11.64	2.96	0.02	0.11	0.00	0.98	0.05	5.46	0.37	99.11
7	OBD_6_GMglass5_2	79.19	11.70	2.96	0.03	0.11	0.00	1.06	0.04	5.58	0.35	101.02
8	OBD_6_GMglass6_1	77.08	11.75	3.09	0.02	0.08	0.00	0.91	0.08	5.75	0.41	99.16
9	OBD_6_GMglass7_1	78.37	12.24	3.38	0.03	0.08	0.02	0.84	0.02	5.56	0.35	100.88
10	OBD_6_GMglass7_2	78.20	11.05	2.91	0.00	0.10	0.01	0.91	0.00	5.18	0.33	98.69
11	OBD_6_GMglass8_1	80.28	11.58	2.90	0.03	0.08	0.01	0.89	0.06	5.66	0.35	101.83
7	GCD_6_GMglass1_1	75.72	13.98	4.11	0.06	0.07	0.01	1.22	0.04	5.09	0.64	100.94
8	GCD_6_GMglass2_1	75.32	13.67	4.04	0.03	0.10	0.00	1.11	0.09	5.36	0.55	100.27
9	GCD_6_GMglass3_1	74.29	13.92	4.13	0.03	0.10	0.00	1.07	0.04	5.02	0.68	99.29
10	GCD_6_GMglass4_1	74.35	13.85	4.22	0.04	0.09	0.01	1.26	0.02	5.40	0.65	99.88
1	GCD_10_MIncBi1_1	77.50	13.08	4.04	0.01	0.17	0.01	0.85	0.04	4.70	0.40	100.79
2	GCD_10_MIncBi1_2	77.83	12.97	2.02	0.01	0.14	0.01	0.90	0.05	4.68	0.44	99.04
3	GCD_10_GMglass1_1	77.29	12.95	3.34	0.04	0.08	0.03	0.59	0.01	4.75	0.56	99.63
4	GCD_10_GMglass1_2	77.90	12.81	3.75	0.04	0.09	0.00	0.68	0.03	4.87	0.60	100.77
5	GCD_10_MIncBi2_1	77.54	12.78	3.46	0.04	0.16	0.03	0.87	0.00	4.93	0.58	100.40
6	GCD_10_MIncBi2_2	76.89	12.86	3.62	0.04	0.13	0.01	0.82	0.00	4.97	0.60	99.94
7	GCD_10_MIncBi2_3	77.44	12.76	3.40	0.04	0.14	0.00	0.91	0.04	5.00	0.58	100.30
8	GCD_10_MIncBi3_1	77.89	13.15	3.51	0.03	0.14	0.00	0.92	0.07	4.91	0.55	101.18
9	GCD_10_MIncBi3_2	78.33	12.90	3.41	0.04	0.12	0.02	0.88	0.06	4.84	0.59	101.18
10	GCD_10_MIncBi3_3	77.85	13.02	3.36	0.04	0.14	0.03	0.81	0.04	4.75	0.60	100.64
11	GCD_10_MIncOx1_1	77.55	12.82	3.73	0.05	0.41	0.00	1.38	0.07	4.82	0.57	101.39
12	GCD_10_MIncOx2_1	77.92	12.96	3.79	0.04	0.47	0.06	1.39	0.09	4.68	0.59	101.99
13	GCD_10_MIncOx3_1	78.77	12.88	3.80	0.04	0.14	0.01	2.31	0.06	4.83	0.52	103.35
14	GCD_10_GMglass2_1	77.71	12.80	3.78	0.03	0.09	0.02	0.80	0.04	4.81	0.51	100.59
15	GCD_10_GMglass2_2	78.05	12.73	3.52	0.04	0.11	0.00	0.74	0.07	4.81	0.60	100.65
16	GCD_10_MIncBi4_1	77.88	12.98	3.63	0.02	0.15	0.02	0.92	0.06	5.14	0.57	101.36

17	GCD_10_MIncBi4_2	78.30	13.09	3.56	0.01	0.14	0.00	0.93	0.03	5.02	0.62	101.68
1	GCD_10_GMglass3_1	78.94	13.09	3.66	0.06	0.09	0.01	0.65	0.03	4.86	0.60	102.01
2	GCD_10_MIncBi5_1	79.27	12.86	3.65	0.02	0.10	0.00	0.73	0.03	4.94	0.58	102.17
3	GCD_10_GMglass4_1	78.86	12.66	3.53	0.04	0.09	0.00	0.68	0.06	4.84	0.55	101.30
4	GCD_10_GMglass4_2	79.08	12.50	3.60	0.04	0.13	0.01	0.65	0.07	4.85	0.57	101.50
5	GCD_10_GMglass5_1	79.03	13.12	3.50	0.03	0.09	0.03	0.56	0.05	4.88	0.61	101.89
6	GCD_10_GMglass6_1	77.77	12.89	3.74	0.04	0.07	0.02	0.66	0.03	4.64	0.56	100.41
7	GCD_10_MIncBi6_1	78.33	12.98	3.21	0.05	0.11	0.03	0.67	0.00	5.18	0.60	101.15
8	GCD_10_MIncBi7_1	63.99	23.51	8.22	0.00	0.03	0.02	0.45	0.03	1.01	4.49	101.75
9	GCD_10_MIncBi7_2	65.65	22.86	8.90	0.00	0.06	0.02	0.48	0.07	1.34	3.64	103.00
10	GCD_10_GMglass7_1	77.71	12.85	3.53	0.05	0.04	0.00	0.65	0.04	4.66	0.58	100.10
11	GCD_10_GMglass7_2	70.59	11.81	3.52	0.05	0.09	0.00	0.65	0.00	4.50	0.53	91.74
1	DMD_11_GMglass1_1	77.23	12.52	3.39	0.04	0.08	0.02	0.60	0.06	4.92	0.61	99.47
2	DMD_11_GMglass1_2	77.42	12.83	3.66	0.04	0.07	0.00	0.65	0.02	4.99	0.64	100.32
3	DMD_11_GMglass2_1	76.80	12.56	3.53	0.07	0.07	0.02	0.68	0.03	4.90	0.65	99.31
4	DMD_11_MIncBi1_1	73.84	12.61	3.13	0.04	0.17	1.52	0.44	0.04	5.39	2.59	99.77
5	DMD_11_MIncBi1_2	77.27	13.06	3.39	0.06	0.13	0.00	0.54	0.07	5.26	0.61	100.39
6	DMD_11_MIncBi1_3	77.40	12.99	3.30	0.04	0.13	0.00	0.70	0.01	5.11	0.55	100.22
7	DMD_11_MIncBi2_1	77.49	12.94	3.44	0.03	0.12	0.00	0.57	0.01	4.92	0.59	100.11
8	DMD_11_GMglass3_1	77.19	12.71	3.49	0.05	0.07	0.02	0.65	0.08	4.61	0.57	99.46
9	DMD_11_GMglass3_2	77.39	12.68	3.57	0.02	0.10	0.00	0.67	0.00	4.91	0.56	99.90
10	DMD_11_GMglass4_1	77.35	12.59	3.56	0.04	0.07	0.00	0.64	0.03	4.81	0.60	99.69
11	DMD_11_GMglass4_2	77.29	12.59	3.46	0.08	0.10	0.00	0.61	0.04	4.75	0.57	99.49
12	DMD_11_GMglass5_1	78.08	12.75	3.80	0.04	0.08	0.00	0.62	0.05	4.68	0.54	100.65
13	DMD_11_GMglass5_2	77.93	12.88	3.70	0.05	0.06	0.03	0.50	0.00	4.94	0.55	100.64
14	DMD_11_GMglass5_3	77.61	12.86	3.51	0.05	0.11	0.02	0.66	0.00	4.85	0.57	100.24
15	DMD_11_MIncBi3_1	77.93	12.80	3.55	0.02	0.13	0.00	0.63	0.06	4.69	0.62	100.43
16	DMD_11_MIncBi3_2	77.70	12.61	3.55	0.04	0.11	0.03	0.71	0.00	4.79	0.59	100.13
17	DMD_11_GMglass6_1	77.37	12.86	3.59	0.03	0.04	0.00	0.69	0.04	4.56	0.57	99.74
18	DMD_11_GMglass6_2	76.96	12.84	3.67	0.08	0.08	0.00	0.59	0.02	4.99	0.59	99.82
19	DMD_11_GMglass7_1	77.16	12.87	3.56	0.05	0.06	0.00	0.70	0.05	4.76	0.59	99.80

20	DMD_11_GMglass7_2	76.34	12.56	3.59	0.04	0.06	0.03	0.61	0.02	4.66	0.53	98.43
22	DMD_11_MIncBi4_2	74.22	10.66	2.60	2.04	0.09	0.01	2.77	0.22	4.16	4.33	101.10
23	DMD_11_MIncBi4_3	77.09	12.59	3.51	0.00	0.12	0.01	0.64	0.03	4.99	0.54	99.51
24	DMD_11_GMglass8_1	77.08	12.71	3.65	0.06	0.10	0.00	0.60	0.01	4.98	0.62	99.81
11	DMD_3_GMglass1_1	70.53	14.57	4.94	0.13	0.22	0.04	1.63	0.10	4.76	1.06	97.98
12	DMD_3_GMglass2_1	69.99	14.32	4.57	0.13	0.20	0.00	1.51	0.05	5.20	0.82	96.78
13	DMD_3_GMglass3_1	69.90	13.95	4.44	0.12	0.19	0.01	1.38	0.06	5.22	0.77	96.04
14	DMD_3_GMglass4_1	72.13	13.93	4.44	0.07	0.10	0.06	1.60	0.08	5.28	0.73	98.41
15	DMD_3_GMglass4_2	71.61	13.71	4.24	0.06	0.08	0.00	1.48	0.07	5.21	0.72	97.17